

Phase-Change Materials:

Structure, vibrational states and thermodynamics of crystallization

Von der Fakultät für Mathematik, Informatik und Naturwissenschaften der RWTH Aachen University zur Erlangung des akademischen Grades eines Doktors der Naturwissenschaften genehmigte Dissertation

vorgelegt von
Diplom-Physiker
Peter Erhard Zalden
aus Münster

Berichter: Univ.-Prof. Dr. rer.-nat. Matthias Wuttig
Dr. rer.-nat. Christophe Bichara

Tag der mündlichen Prüfung: 11.09.2012

Diese Dissertation ist auf den Internetseiten der Hochschulbibliothek online verfügbar.

Kurzfassung

Abstract

Phase-change materials (PCM) offer the potential to be employed as active switching material in novel, non-volatile memory devices. These devices allow for faster read- and write operations as compared to common Flash memory and are superior to state-of-the-art DRAM due to their ability to retain information even when the external power supply is removed. The application of such phase-change memory in various fields (e.g. automotive and home use) requires the adaptation to specific external conditions and hence can be realized only if systematic design rules are available to tune the material's properties. These design rules can be derived from a microscopic theory for their properties and transitions. Data storage in these devices is generally based on the distinct properties of their amorphous and crystalline phases, from which the present state can be read. Information is written by heating the active material either above the crystallization temperature or above the melting temperature for vitrification. Therefore, research on these materials can be classified into three areas: The static properties of the amorphous phase, those of the crystalline phase and the nature of the quasi-reversible transition. Progress in the systematic understanding of phase-change materials has to be based on an atomistic picture of both, transitions and properties, in particular since only compounds containing some few elements – mostly chalcogenides – show the necessary properties.

The atomic short range order has a crucial impact on the property contrast and was investigated here by means of x-ray absorption spectroscopy, total and inelastic neutron scattering. The resulting atomic pair distribution functions revealed that all investigated materials (i.e. GeSb_2Te_4 , $\text{Ge}_2\text{Sb}_2\text{Te}_5$, In_3SbTe_2 , Sb_2Te , AIST, GeTe und $\text{Ge}_{15}\text{Sb}_{85}$) show 5% to 15% longer average interatomic distances in the crystalline phase. Also their coordination number was found to increase. This increase is particularly pronounced in the case of $\text{Ge}_2\text{Sb}_2\text{Te}_5$, where the average bond length increases from 2.72(1) Å by 11% upon crystallization, while at the same time the coordination number increases from 2.8(1) by 88(5)%. This modification of the local atomic structure indicates a change in the bonding mechanism and increases the contrast e.g. in optical reflectivity. In GeSb_2Te_4 and $\text{Ge}_2\text{Sb}_2\text{Te}_5$, however, also the variance of interatomic distances increases upon crystallization. This observation is surprising, since a larger variance of bond lengths in the crystalline phase as compared to that of the amorphous phase at equal temperatures indicates a softening of the interatomic potentials upon crystallization. Measurements of the mechanical stress, however, show that the crystalline phase is mechanically harder than the amorphous phase. Measurements of the density of vibrational states were performed to resolve this discrepancy. They confirmed that the crystalline phase consists of softer bonds. The changes of the interaction potential are accompanied by a change in the bonding mechanism: While the coordination numbers of the amorphous phase of all investigated phase-change materials is well described by the 8-N rule, the coordination numbers of the respective crystalline phases is generally higher and in good agreement with resonance bonding, which is accompanied by a particularly large optical dielectric constant. This transition from stiffer bonds in the amorphous and softer bonds in the crystalline phase is favorable for the switching properties of memory devices.

Recently, a metal-insulator transition was reported for various compounds from the pseudo-binary line $\text{GeTe-Sb}_2\text{Te}_3$ (GST), whose order parameter is the atomic disorder. This transition can be controlled by changing the annealing temperature of amorphous phase-change materials above the crystallization temperature. At low annealing conditions, the material behaves semiconducting and becomes metallic after heating to higher temperatures. Motivated by these results, the local

atomic disorder of the crystalline phase was investigated. First, different sources of atomic disorder are discussed. This revealed that the chemical disorder on one of the two sublattices induces pronounced static atomic displacements, whose amplitude reduces with increasing annealing temperature. This is a manifestation of a decrease of the amplitude of the Peierls mechanism, which then reduces its energy gap. These changes, however, leave the alloy in a semiconducting state. At even higher annealing conditions, the majority of intrinsic vacancies is arranged on layers. Nevertheless, it was shown that the materials still remain in a semiconducting phase. A comparison of measured and calculated EXAFS suggests that even in this phase, the Ge and Sb atoms are chemically disordered on their sublattice. These atoms are only ordered at even higher temperatures and on long time scales, where also stacking faults are removed. A unique atomic model for the metal-insulator transition cannot be derived from these data, since as few as 7% of the atoms remaining on the layers of vacancies suffice to localize the charge carriers. This low number of atoms in their quasi-regular arrangement is insufficient for detection by most present techniques of atomic structure determination.

The crystallization process of phase-change materials was investigated calorimetrically in order to describe its thermodynamic and kinetic properties. This description will help to reveal the characteristics of the crystallization mechanism in this class of materials. Even here, the disorder of the crystalline is of importance. The phase transition itself reduces the enthalpy by only 40–50 meV/atom, which indicates a remarkably small driving force as compared to the crystallization of Ge or Si, where the enthalpy is reduced by approx. 120 meV/atom. This becomes even more important, when the additional change in entropy is taken into account, which has to be subtracted from the change in enthalpy in order to calculate the driving force of crystallization via $\Delta G = \Delta H - T\Delta S$. Hence, the pronounced disorder of crystalline phase-change materials reduces the change in entropy ΔS and thereby increases the driving force of crystallization ΔG . In order to quantify ΔS , the full entropies of both, the amorphous and the crystalline phases have to be known. Two facts make these measurements very complicated: Firstly, crystallization occurs so rapidly upon cooling the melt, that it is not possible to measure the specific heat of the undercooled liquid phase. Secondly, in the case of GST, the specific heat of the liquid phase – even if it were known – could not be extrapolated to the amorphous phase, since a change in the local atomic coordination was observed for the Ge atoms: While there are only octahedrally coordinated atoms in the liquid phase, a non-negligible fraction of Ge atoms transforms to a tetrahedral geometry upon cooling. This change in bonding could also influence the thermodynamic properties of the system. Nevertheless, the specific heat of the undercooled liquid and the crystalline phases of AIST could be measured. An extrapolation of the differences in specific heat to the amorphous phase could be performed and allowed quantifying the change in free enthalpy due to the decrease of entropy upon crystallization, which is $\Delta S = -16(6)$ meV/atom, so that the total driving force of crystallization ΔG amounts to only 30(9) meV/atom. Hence, the driving force of crystallization in phase-change materials is surprisingly low. The implications of this result on the fundamental processes of nucleation and growth is discussed for different materials.

Phasenwechselmaterialien können als aktive Komponente in neuartigen nicht-flüchtigen Datenspeichern genutzt werden. Diese Speicher erlauben höhere Schreib- und Lesegeschwindigkeiten als herkömmliche Flash-Speicher und sind gleichzeitig vorteilhaft gegenüber schnelleren DRAMs, da ihre Informationen selbst dann erhalten bleiben, wenn die externe Spannungsversorgung entfernt wird. Für die Anwendung von Phasenwechselmaterialien in Speichermedien ist es erforderlich, sie auf die jeweiligen Anwendungsgebiete anzupassen, so dass Designregeln für die Eigenschaften nötig sind. Diese Designregeln können über ein fundamentales Verständnis der Materialien auf atomarer Skala gewonnen werden. Für die Datenspeicherung werden der amorphen und der kristallinen Phase die verschiedenen Zustände des Speichers zugeordnet. Der Speicher kann somit über die verschiedenen optischen und elektrischen Eigenschaften dieser Phasen ausgelesen werden. Daher sind also die Untersuchungen in drei Gebiete zu unterteilen: Die Eigenschaften der amorphen Phase, die der kristallinen Phase und der Übergang zwischen beiden Phasen – für deren Verständnis jeweils Modelle erforderlich sind, die bis auf die mikroskopische Ebene reichen.

Die atomare Nahordnung ist entscheidend für den Eigenschaftskontrast beider Phasen und wurde daher im Rahmen dieser Arbeit untersucht, indem mittels Röntgenabsorptionsspektroskopie und Neutronenstreuung die Paarverteilungsfunktionen gemessen wurden. Ein charakteristisches Merkmal aller untersuchten Phasenwechselmaterialien (das sind GeSb_2Te_4 , $\text{Ge}_2\text{Sb}_2\text{Te}_5$, In_3SbTe_2 , Sb_2Te , AIST , GeTe und $\text{Ge}_{15}\text{Sb}_{85}$) ist, dass der mittlere atomare Abstand bei der Kristallisation um mindestens 5%, maximal um 15% zunimmt. Gleichzeitig nimmt auch die Koordinationszahl zu. Am Beispiel von $\text{Ge}_2\text{Sb}_2\text{Te}_5$ wird dieser Unterschied besonders deutlich: Die Bindungslänge nimmt von $2.72(1) \text{ \AA}$ um 11% zu, die Koordinationszahl von 2.78 um 88(5)%. Diese starke Änderung der lokalen Struktur unterstützt den Eigenschaftskontrast von Phasenwechselmaterialien, indem sie z.B. den optischen Reflektivitätskontrast vergrößert. Bei $\text{Ge}_2\text{Sb}_2\text{Te}_5$ und GeSb_2Te_4 erhöht sich allerdings bei der Kristallisation auch die Verteilungsbreite der Bindungslängen. Diese Beobachtung wirkt zunächst überraschend, weil eine breitere Verteilung in der kristallinen Phase i.d.R. auf weichere Wechselwirkungspotentiale zurückzuführen ist, obwohl aber aus mechanischen Spannungsmessungen bekannt ist, dass die kristalline Phase härter ist als die amorphe. Daher wurden die atomaren Schwingungsmoden beider Phasen untersucht. Diese Messungen zeigen eindeutig, dass die kristalline Phase weichere Bindungen besitzt als die amorphe. Diese Änderung der Bindungsverhältnisse wird auch von einem Wechsel des Bindungsmechanismus begleitet: Während die amorphe Phase aller Phasenwechselmaterialien überwiegend der 8-N-Regel folgt, tritt in der kristallinen Phase eine Resonanzbindung auf, die mit einer hohen dynamischen Ladung der Atome einhergeht. Dieser Übergang von härteren zu weicheren atomaren Wechselwirkungspotentialen ist für die Eigenschaften als Phasenwechselmaterial von Vorteil.

In der kristallinen Phase von verschiedenen Legierungen des $\text{GeTe-Sb}_2\text{Te}_3$ - (GST)-Systems wurde kürzlich ein Metall-Isolator Übergang gefunden, der lediglich von der atomaren Unordnung abhängt, nicht aber von der lokalen Koordination. Dieser Übergang wird durch eine Variation der Heiztemperatur gesteuert, so dass die kristalline Phase nach geringer Heiztemperatur halbleitend, nach höherer Heiztemperatur metallisch ist. Motiviert durch diese Erkenntnis wurde die Unordnung der kristallinen Phase im Detail untersucht. Zunächst werden die verschiedenen Ursachen für atomare Unordnung diskutiert. Dabei zeigt sich, dass besonders die chemische Unordnung auf einem kristallographischen Untergitter der Kochsalzstruktur zu starken Auslenkungen der Atome führt. Die Amplitude dieser statischen Auslenkungen verkleinert sich zunächst mit der Heiztemperatur und spiegelt sich in einer Verkleinerung der Bandlücke wider. Selbst nach dieser Umordnung ist das Material allerdings noch in einem halbleitenden Zustand – mit etwas verringertem elektrischen Widerstand. Bei noch höheren Heiztemperaturen ordnet sich die Mehrheit der intrinsischen Leerstellen auf Lagen. Dennoch wurde gezeigt, dass die Materialien noch in einer halbleitenden

Phase sind. Ein Vergleich von gemessenen und berechneten EXAFS Daten legt nahe, dass auch in dieser Phase die Ge und Sb Atome noch unsortiert das Untergitter bilden. Diese Atome werden bei noch höheren Heiztemperaturen geordnet und gleichzeitig werden Stapelfehler ausgeheilt. Eine eindeutige Identifikation des für den Metall-Isolator-Übergangs relevanten Mechanismus ist aus diesen Messungen nicht möglich, da bereits 7% verbleibender Atome auf den Leerstellenebenen zu einer Lokalisierung der Elektronen führen – eine Größe die unterhalb der Detektionsschwelle der meisten strukturauflösenden Methoden liegt.

Die thermodynamischen und kinetischen Aspekte des Kristallisationsvorgangs wurden kalorimetrisch untersucht. Es zeigt sich, dass auch hier die Unordnung der kristallinen Phase eine Rolle spielt. Der Phasenübergang geht mit einer verglichen mit Ge oder Si (ca. 120 meV/Atom) kleinen Enthalpieänderung von nur 40-50 meV/Atom einher. Dies wird besonders deutlich, wenn die treibende Kraft der Kristallisation – d.h. die Reduktion der freien Enthalpie untersucht wird, da im Vergleich zur Enthalpieänderung noch der mit einer Entropieänderung verbundene Beitrag abgezogen werden muss. Somit erhöht die Unordnung der kristallinen Phase deren Entropie, die wiederum die treibende Kraft der Kristallisation vergrößert. Folglich muss die gesamte Entropie des Systems bekannt sein, um den Einfluss dieser zusätzlichen Konfigurationsentropie der kristallinen Phase zu quantifizieren – allerdings lässt sich dieser Wert aus mindestens zwei Gründen nicht mit herkömmlicher Kalorimetrie messen: Zum einen findet die Kristallisation zu schnell statt, so dass die Wärmekapazität der unterkühlten Schmelze nicht gemessen werden kann. Zum anderen lässt sich auch die Wärmekapazität der flüssigen Phase bei GST-Systemen nicht zur amorphen Phase extrapolieren, da eine Änderung des Bindungsmechanismus beobachtet wurde: Während in der flüssigen Phase, keine tetraedrischen Ge-Atome gefunden werden konnten, so befindet sich in der amorphen Phase ein nicht vernachlässigbarer Anteil der Atome in dieser lokalen Konfiguration. Es kann also nicht ausgeschlossen werden, dass dieser Wechsel des Bindungsmechanismus einiger Atome auch die Wärmekapazität beeinflusst. Dennoch wird in dieser Arbeit eine Methode vorgestellt, mit deren Hilfe der Beitrag der Unordnung quantifiziert werden kann. Am Beispiel von AIST wurde eine solche Messung der spezifischen Wärme der flüssigen und kristallinen Phasen durchgeführt. Der resultierende Beitrag zur Änderung der freien Enthalpie beträgt bei der Kristallisationstemperatur -16(6) meV/atom, so dass die gesamte Enthalpieänderung nur noch 30(9) meV/atom beträgt. Die treibende Kraft der Kristallisation ist also bei Phasenwechselmaterialien erstaunlich gering, wird aber durch die Unordnung der kristallinen Phase bei GST weniger stark durch die Entropieänderung reduziert. Die Auswirkungen der treibenden Kraft auf die verschiedenen Kristallisationsprozesse, Nukleation und Wachstum, werden ebenfalls für verschiedene Materialien diskutiert.

Contents

1	Introduction	1
1.1	Motivation for a new memory technology	1
1.2	Non-volatile data storage with phase-change materials	3
1.3	What is a phase-change material?	5
1.4	Design-rules and Motivation for this thesis	6
1.5	Phase-change compounds	14
1.6	Structure of this thesis	16
2	Methods of microscopic structure analysis	18
2.1	General scattering theory	19
2.2	General Neutron scattering	20
2.3	Inelastic Neutron Scattering	23
2.4	Total Neutron Scattering	29
2.5	General X-ray scattering	33
2.6	The structure factor	35
2.7	X-ray Absorption Spectroscopy	38
2.8	Atomic displacements probed by XRD and EXAFS	48
3	Disorder in crystalline GeSb_2Te_4: Modifications along the MIT	53
3.1	Disorder in solids	53
3.2	Motivation	55
3.3	Previous investigations	57
3.4	Experimental details for XRD	61
3.5	Annealing dependence of the lattice constant in cubic GeSb_2Te_4	61
3.6	Annealing dependence of the lattice constants in hexagonal GeSb_2Te_4	62
3.7	The layer distances in hexagonal GeSb_2Te_4	64
3.8	Reflex broadening in XRD patterns of hexagonal GeSb_2Te_4	65
3.9	Conclusions from Annealing trends in GeSb_2Te_4 from reciprocal space	68

3.10	EXAFS analysis of meta-stable cubic GeSb_2Te_4	69
3.11	Annealing dependence of the crystalline phase from EXAFS analysis	74
3.12	Annealing dependence of the PDF of crystalline GeSb_2Te_4	78
3.13	Conclusions from Annealing trends in GeSb_2Te_4 from real space	83
4	Structure contrast between amorphous and crystalline phase-change materials	86
4.1	Motivation	86
4.2	Amorphous and Crystalline GeSb_2Te_4 and $\text{Ge}_2\text{Sb}_2\text{Te}_5$	88
4.3	Amorphous and Crystalline GeTe	98
4.4	Amorphous and Crystalline AlSbTe and Sb_2Te_3	102
4.5	Amorphous and Crystalline In_3SbTe_2	103
4.6	Conclusions from the study of atomic order	109
5	Vibrational properties of phase-change materials	112
5.1	Mössbauer Effect	113
5.2	Nuclear Inelastic Scattering	113
5.3	Results and Conclusion	115
6	Thermodynamic properties of phase-change materials	118
6.1	Crystallization / Motivation	118
6.2	Thermodynamics of glass forming systems	120
6.3	Calorimetry	126
7	Phase transitions and Entropy	129
7.1	Sample preparation	129
7.2	Differential Scanning Calorimetry	130
7.3	Thermodynamics of the phase transitions	133
7.4	Measurements of specific heat/entropy	139
7.5	Comparison of GST and Sb_2Te_3 -based phase-change materials	141
8	Summary and conclusions	143
A	Drift in phase-change materials: A study of the model system GeTe-SnTe	146
A.1	Amorphous Phase	147
A.2	Conclusions for the structural relaxation during the drift	151
A.3	Crystalline phase	152
B	Data compilation of phase-change materials	159
B.1	Density of phase-change materials	159
B.2	Compilation of structural investigations of amorphous GST-based PCMs . .	161
	Acknowledgements	163
	Bibliography	165

List of Figures

1.1	Correlation between information technology and economic competitiveness	2
1.2	Thermal program for the SET and RESET operation of a PCM	4
1.3	GST and AIST: TEM images of crystallized spots: Nucleation and Growth .	10
2.1	Scattering parabola for neutron scattering experiments	21
2.2	Structure factor $S(Q)$ for neutron scattering	31
2.3	Schematics of the EXAFS setup at beamline C, Hasylab	39
2.4	EXAFS: Interference of scattered and backscattered wave	42
2.5	K- and L_{III} -edge energy vs. Z	43
2.6	EXAFS data treatment steps	47
2.7	Debye-Waller factor or displacement parameter in EXAFS	51
3.1	GeSb_2Te_4 : Disorder induced insulator-metal transition in resistivity	56
3.2	Crystal structures of rock-salt and hexagonal GeSb_2Te_4	58
3.3	XRD patterns of an annealing series of GeSb_2Te_4 from amorphous to 748 K	59
3.4	XRD patterns of an annealing series of GeSb_2Te_4 from amorphous to 748 K	60
3.5	Reflex width vs. annealing condition in GeSb_2Te_4	66
3.6	Baseline effect on the EXAFS at the Ge K-edge	70
3.7	EXAFS results of meta-stable cubic GeSb_2Te_4 annealed at 378 K for 60 h .	71
3.8	Effect of vacancies on EXAFS and XRD	73
3.9	EXAFS data of crystalline GeSb_2Te_4 for different annealing temperatures .	75
3.10	EXAFS fitting results of crystalline GeSb_2Te_4 at different annealing tem- peratures	76
3.11	Avg. atomic displacement in GeSb_2Te_4 vs. optical band gap and diel. const.	77
3.12	RDF of crystalline GeSb_2Te_4 at 300 K for diff. annealing temperatures . . .	79
3.13	Interblock atomic distances in GeSb_2Te_4	81
3.14	RDF of crystalline $\text{Ge}_2\text{Sb}_2\text{Te}_5$ at 10 K	82
3.15	Calculated EXAFS data of mixed and ordered Ge/Sb in hex. GeSb_2Te_4 . . .	84

4.1	EXAFS data of as-deposited amorphous GeSb_2Te_4 at 10 K	91
4.2	RDF of amorphous GeSb_2Te_4 at 300 K decomposed to partial bond contri- butions	92
4.3	RDF of amorphous $\text{Ge}_2\text{Sb}_2\text{Te}_5$ at 10 K decomposed to partial bond contri- butions	93
4.4	Amorphous and crystalline GST-compounds: EXAFS and PDF analysis . .	95
4.5	EXAFS spectra of the Te K-edge of GeSb_2Te_4 measured at different tem- peratures	97
4.6	Displacement parameter σ^2 of $\text{Ge}_2\text{Sb}_2\text{Te}_5$ vs. temperature	98
4.7	Refined EXAFS data of amorphous GeTe at 10 K	99
4.8	Amorphous and crystalline GeTe: EXAFS and PDF analysis	102
4.9	Amorphous and crystalline Sb_2Te_3 : EXAFS data and PDF analysis	104
4.10	EXAFS-data of crystallized In_3SbTe_2 at 10 K, annealed at 533 K	106
4.11	EXAFS-data of as-deposited amorphous In_3SbTe_2 at 10 K	108
4.12	Comparison of EXAFS of amorphous and crystalline In_3SbTe_2 at 10 K . . .	110
5.1	NIS: Experimental setup	114
5.2	Partial density of phonon states in GeSb_2Te_4	117
6.1	Schematic: Free enthalpy of glass forming substances	122
6.2	Schematic: Entropy of glass forming substances	123
6.3	Configurational entropy in the GeTe-Sb ₂ Te ₃ -system	125
7.1	3-step method for measuring specific heats: $\text{Ge}_2\text{Sb}_2\text{Te}_5$ at 528 K	132
7.2	Molar specific heat reference measurements on Al_2O_3 and sputter deposited Sb	133
7.3	Technical drawing of the coupled DSC and EXAFS experiment.	134
7.4	DSC and in-situ EXAFS scan of $\text{Ge}_{15}\text{Sb}_{85}$: Phase separation	135
7.5	DSC scan on crystallization and melting of $\text{Ag}_4\text{In}_3\text{Sb}_{67}\text{Te}_{26}$ from 323 K to 843 K	136
7.6	DSC scan of amorphous $\text{Ge}_3\text{Sb}_2\text{Te}_6$ at 5 K min^{-1}	137
7.7	Phase diagram GeTe-Sb ₂ Te ₃ including meta-stable phases	139
7.8	Specific heat of amo., cryst., and liquid AIST	140
7.9	Entropy of AIST in the amo., cryst. and liquid phases	141
A.1	EXAFS measurements on amorphous Ge_3SnTe_4 at 10 K	148
A.2	EXAFS measurements on amorphous GeSnTe_2 at 10 K	150
A.3	EXAFS data on crystalline SnTe at 10 K	154
A.4	EXAFS data of crystalline Ge_3SnTe_4 at 10 K	155
A.5	EXAFS data of crystalline GeSnTe_2 at 10 K	157

CHAPTER 1

Introduction

1.1 Motivation for a new memory technology

The progress of a society depends on its ability to obtain, preserve and provide information wherever and whenever necessary. This can be seen e.g. from the correlation between the information and communication technology (ICT) index with the Global Competitiveness Index (GCI). Both factors are regularly reported by the World Economic Forum [1]. In Fig. 1.1, both indices are plotted against each other for various countries and a striking correlation is found. Therefore, the efficient use of information technology directly correlates with the competitiveness of a society. Data storage is naturally a key technology to enable the use of information and therefore leads to economic competitiveness by itself.

The insight of the importance of preserving knowledge dates back to the invention of the Sumerian cuneiform script (first evidence from 3150 BC [2], p. 47), whose writing process is based on mechanically engraving wet clay. The data retention of these clay tablets is enhanced by the pronounced change in the viscosity of clay as a function of annealing (more precisely as a function of the amount of water between the clay particles [3]): In wet condition, the clay particles can be easily rearranged, so that the cuneiforms can be written. Heating the clay tablets reduces the content of water, so that the shape of the clay becomes mechanically protected by its significantly higher fragility. This allows the long-term storage of information in clay tablets. Surprisingly, there is a direct analogy to phase-change memory, where also a change in viscosity is used to store information: In phase-change materials, it is the change of the microscopic, atomic structure and not just the surface topology, which contains the information. Nevertheless, also in phase-change materials the low atomic mobility at room temperature allows to preserve the information, whereas the high atomic mobility at elevated temperatures facilitates the writing process. Therefore, the crucial parameter, which was the water content in clay tablets is the temperature in phase-change materials. Naturally, the details of both processes are very different, given alone the

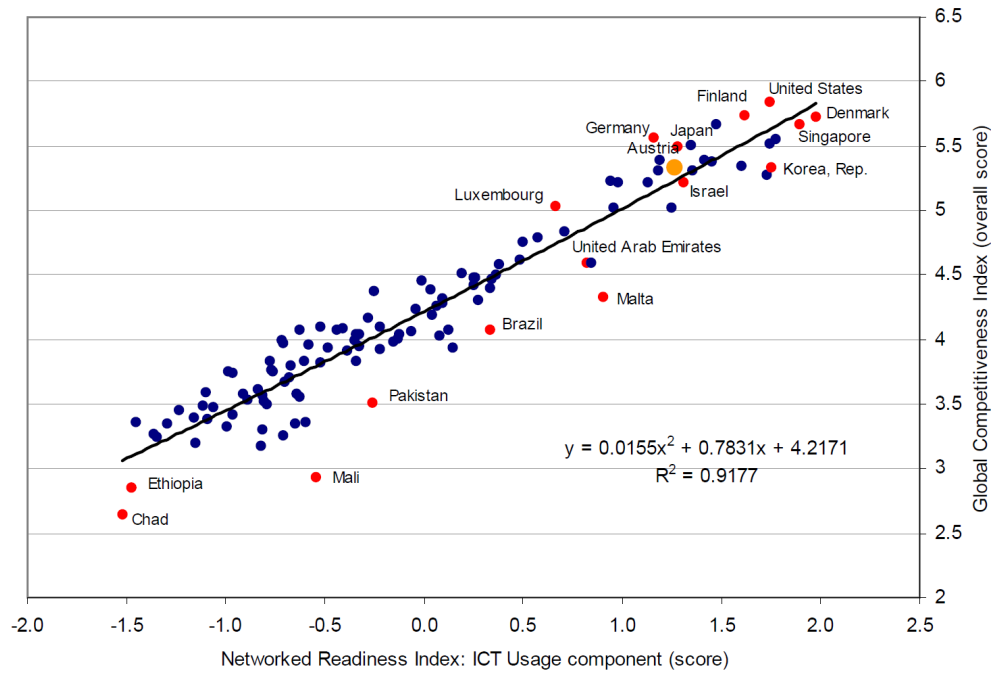


Figure 1.1: Correlation between information technology and economic competitiveness, showing that more efficient use of information technology goes along with faster economic progress. Taken from [1].

fact that a single bit of information is stored in some $(30 \text{ nm})^3$ of phase-change material, whereas at least $(1 \text{ mm})^3$ of clay is necessary to store the same amount of information. This corresponds to a storage density, which is 10^{13} times higher.

Almost together with the invention of the cuneiform, the first competitive product was developed: The Egyptian hieroglyphs, which were based on writing symbols with ink on papyrus. From this point in time, writing was continuously refined until finally electro-mechanical data storage was developed together with the first programmable computer – the Zuse Z3 in 1941. In the early 1970's, the first semiconductor memories were developed and started an enormous progress in data storage density and access times. The following digital revolution, well described by Moore's law [4], created a large demand for storage technology.

Not only the economic progress, but also the pleasure of personal entertainment generated this demand for data storage technology. Several technologies have been developed to fulfill the various requirements. On the one hand, large amounts of electronic storage capacity are necessary for data backup and -protection purposes. These data should better not be stored on mobile devices, but rather in safe buildings (data centers). There, technologies like magnetic tapes and magnetic hard disk drives are employed to retain the information. These technologies have random access times of milliseconds to seconds [5] but reasonable transfer rates once the device is positioned. There, information are stored in the different orientation of the remanent magnetic field of ferromagnetic domains on tapes or discs. These data are even retained without supply of power so that this memory is called non-

volatile. These properties make it perfectly suitable for data backup. On the other hand, there is an enormous market for mobile data storage: "Mobile DRAM Market to Grow 71 Percent in 2011" to 2.9 billion gigabits [6] with about 20 US-\$ per gigabit in 2010. Here, light-weight memory is required with large capacity, low power-consumption and short random access times. Currently, the ideal memory with all these properties is missing: Either very fast dynamic random-access memory (DRAM) can be used, which is volatile, i.e. the stored information are lost if the voltage supply is interrupted. Therefore, these memories consume a significant amount of power even without operation. Alternatively, Flash memory [7] can be used, which is non-volatile but significantly slower than current DRAM [8]. Therefore, combinations of this memory are used in most mobile devices – sometimes even in combination with a hard disc drive, thereby creating an additional level of storage in a single device. This combination of technologies is complex and therefore expensive and power-consuming and the unification of the different memory types in a single device is highly desirable from the perspective of both, manufacturer and consumer, because it allows for the cheaper manufacturing of products with higher storage density and therefore higher mobility.

One potential concept of such a unified memory technology is the phase-change random access memory (PCRAM), which is based on the cycling of a so-called phase-change material (PCM) between its amorphous and crystalline phases. Its invention dates back to 1968, when S. Ovshinsky published the first proof of principle [9]. This switching process is non-volatile in nature, very fast [8] (less than 1 ns) and works even in small volumes [10] (films as thin as 2 nm). Thus, the most fundamental requirements for a unified memory technology have been shown and the production of working devices is based on an optimization of the materials' properties. Therefore, it is the aim of this thesis to contribute to the understanding of the fundamental physical mechanisms, involved in the switching of PCMs.

This introductory first chapter will continue by explaining the non-volatile switching (or phase-change) mechanism in more detail in Sec. 1.2, followed by a discussion of the necessary properties of the materials employed (cf. Sec. 1.3). These properties will be brought in the framework of previous scientific work in Sec. 1.4, from which questions for scientific work are derived.

1.2 Non-volatile data storage with phase-change materials

PCMs are a rare class of compounds, which can be rapidly cycled between an amorphous and a crystalline phase. These different atomic arrangements induce changes in the macroscopic properties, like the optical reflectivity and electronic resistivity [11]. The change in optical reflectivity is commonly employed in rewritable optical discs, while the contrast in electronic resistivity is utilized to develop resistive random access memory devices (PCRAM). These are beneficial as compared to common Flash memory due to their faster switching times [12], but also due to their inertness against external sources of radiation [13] (p. 84). Since they are non-volatile, they can bridge the gap between fast, but volatile

DRAM and non-volatile, but slower Flash memory.

The fundamental physical mechanisms involved in the switching are a crystallization transition from the amorphous phase (SET operation) and a quenching process, upon which the material is vitrified (RESET operation) [12], cf. Fig. 1.2. These two operations and the scientific challenges related to their optimization will be discussed in the following. The RESET operation is based on the vitrification and is mainly limited by the heating and cooling rates of the device. The most significant properties of the phase-change material influencing the vitrification are the melting temperature T_m , the thermal conductivity κ and the specific heat C_p . These mostly thermodynamic properties of phase-change materials will be discussed in Sec. 7. The design of memory devices and their improvement is discussed e.g. in the review article by Wong et al. [12]. The fast crystallization mechanism (SET operation) on the other hand strongly depends on the employed material. It is the process, which usually limits the switching speeds of phase-change memories [12]. Its optimization involves the selection of specific materials, i.e. design-rules are necessary, which can be derived from a systematic analysis of macroscopic and microscopic properties and should finally reveal, which atomic mechanisms control the speed of the crystallization process. Therefore, this thesis will focus on the investigation of microscopic properties and in particular on the atomic structure of both, amorphous and crystalline phase-change materials (cf. Chpt. 4) and on the influence of thermodynamic properties on the crystallization mechanism (cf. Chpt. 7). From a scientific point of view, "the deepest and most interesting unsolved problem in solid state theory is probably the theory of the nature of glass and the glass transition" [14], borrowing Nobel price winner P.W. Anderson's words. Phase-change materials are an extreme case of glass forming systems, whose properties can be used to verify existing models and to extend our understanding of glass formation.

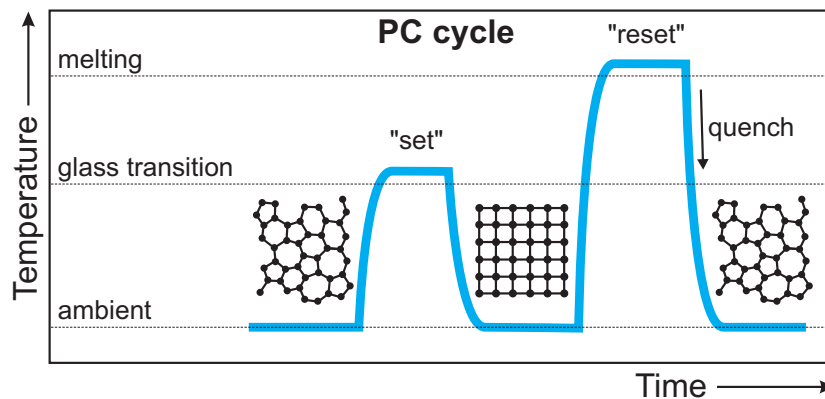


Figure 1.2: Thermal cycling of a phase-change material is accomplished by applying different heating pulses. A low intensity pulse crystallizes the amorphous material by heating it above the crystallization temperature (which roughly equals the glass transition temperature in phase-change materials [15]). A pulse of high intensity can melt the material locally, so that it is vitrified upon cooling.

1.3 What is a phase-change material?

Before we can turn to a discussion of the physical properties and the scientific questions related to phase-change materials, it should be clearly defined, what requirements exist for a phase-change material. These criteria are essentially derived from the expectations towards a phase-change memory device and therefore, this discussion will not go into the details of the complex challenges, which occur when a cost optimized mass production of PCRAM shall be started for the first time.

This collection of requirements is summarized in Tab. 1.1, where every property is supported by the value for the most common phase-change material, $\text{Ge}_2\text{Sb}_2\text{Te}_5$. The most crucial feature of every phase-change material is certainly the large difference between the crystallization rates at ambient conditions and high temperature. The crystallization rate at ambient conditions is usually too low to be experimentally accessible and is therefore extrapolated from the crystallization rate at higher temperature by assuming an Arrhenius-like behavior. For $\text{Ge}_2\text{Sb}_2\text{Te}_5$, the temperature at which the material crystallizes after 10 y is extrapolated as 343 K [16]. This value is sufficiently above ambient temperature for most purposes (except e.g. automotive application). The maximum crystallization rate is usually too high in order to follow the transition in-situ by common experimental techniques. A valuable parameter to describe the crystallization speed is the critical cooling rate. It measures the lowest cooling rate, with which the liquid phase of the PCM needs to be quenched in order to reach the glass transition temperature without crystallization. This critical cooling rate can be estimated from the switching characteristics [17] to be approx. $3.4 \cdot 10^9$ K/s. This high value ensures that the crystallization process can take place in only some nanoseconds, which enables fast data storage. It further points out that most time-resolved experimental techniques are at their limit of time resolution and that pump-probe experiments are the most feasible technique to characterize the crystallization in-situ.

The specific heat up to the melting temperature and the additional latent heat of melting define the amount of heat, which has to be released in the active material in order to perform the RESET operation. It is desirable to reduce both, melting temperature and latent heat, because the RESET operation requires the highest amount of electric energy. In order to develop a device with low power consumption, these values have to be kept as low as possible.

There are several further parameters related to the ability to retain the written information over a longer time. These are the resistance drift of the amorphous phase, which is related to a structural relaxation [18]. The relaxation towards the ideal glassy state is driven by a reduction of the free enthalpy and is accompanied by a change in the electronic conductivity. This change could be neglected, if the contrast between the amorphous and crystalline conductivity is sufficiently large and if only two levels of conductivity need to be distinguished in a phase-change memory cell. But in order to increase the storage density of phase-change memory, multi-level storage is desired. Then, many more levels need to remain distinguishable over long times so that resistance drift becomes an important param-

Table 1.1: Materials research related requirements for phase-change materials. All properties are given for $\text{Ge}_2\text{Sb}_2\text{Te}_5$, the material of choice for CD-RWs.

Property	Requirements	Value for $\text{Ge}_2\text{Sb}_2\text{Te}_5$	Reason
Crystalliz. rate (elevated temp.)	High crit. cooling rate	$3.4 \cdot 10^9 \text{ K/s}$ [17]	Fast crystallization
Crystalliz. rate (ambient temp.)	As low as possible	10 y at 343 K [16]	Long term data retention
Crystallization temperature	Signific. above 423 K [12]	428 K (cf. Chpt. 7)	Data retention
Melting temperature	As low as possible	900 K [19]	Energy for RESET operation
Resistance drift	Low drift index ν at 323 K	0.14 [20]	Long term data retention
Property contrast	Large ratio σ_c/σ_a	> 1000 [21]	Read-out & multi-level storage

eter to reduce in order to allow for higher storage densities. The results from a study of the model system GeTe-SnTe are presented in Chpt. A.

1.4 Design-rules and Motivation for this thesis

The aim of materials research on phase-change materials is to develop design rules, which predict new compounds with equal or even more suitable properties. Also the design of specialized materials, e.g. for higher operating temperatures, could be possible by such rules. These are usually derived from experimental and calculated data of microscopic and macroscopic properties. Several such design rules have been proposed, which are focused on one or two specific properties. They will be summarized in the following, since in particular the combination of these results will provide a scheme, on which the prediction of new materials can be based.

1.4.1 T_g/T_m rule

The crystallization rate, \dot{x} , where x is the fraction of crystalline volume, of an undercooled liquid material has a specific temperature dependence. In phase-change materials, this crystallization rate has to depend significantly on temperature in order to combine the two aspects of fast switching times and long data retention. We can therefore wonder, which physical properties describe this behavior and how they can be used to identify phase-change materials. Crystallization rates are usually depicted in the so called TTT-diagram, where temperature and time are plotted on the axes and contour lines give the time it takes to crystallize a specific fraction x_0 of the undercooled liquid material at a given temperature. Below the glass transition temperature T_g and above the melting temperature T_m , no transformation occurs. A rough estimate was derived by Kauzmann in 1948 [22], that the width of this transformation window is given by

$$T_g/T_m \approx 0.66. \quad (1.1)$$

This estimate was roughly confirmed by a compilation of the glass transition temperatures of 108 compounds by Gutzow et al. [23]. Between T_g and T_m , however, the transformation

Table 1.2: T_{rg} rule for several glass forming materials. The table shows that indeed T_{rg} is particularly low for phase-change materials.

Compound	T_{rg}
SiO ₂	0.84 [26]
GeO ₂	0.65 [26]
Se	0.61 [26]
Fe ₄ B	0.49 [26]
Ag ₆ In ₆ Sb ₅₉ Te ₂₉	0.56 [25]
Ge ₂ Sb ₂ Te ₅	0.49 [25]

time depends strongly on temperature (cf. Sec. 6.1.1 for details). It was proposed that this region, limited by T_g and T_m is very broad for a material that has a large nucleation rate¹, i.e. $T_{rg} = T_g/T_m$ is very low. Turnbull simplified an expression for the nucleation rate and predicted that the nucleation rate is largest in those materials, where the ratio T_g/T_m is lowest [24], i.e. where the temperature window between T_g and T_m is large. These materials would need to be cooled very rapidly to obtain a glass. Materials with large T_{rg} could even be vitrified at slower cooling rates and therefore crystallize more slowly. Kalb et al. could show that indeed the value of T_{rg} for the phase-change materials Ag₆In₆Sb₅₉Te₂₉ and Ge₂Sb₂Te₅ is rather low [25], cf. Tab. 1.2.

Glass forming materials can be classified additionally by their kinetic fragility² m , which is defined as the deviation of the temperature dependence of viscosity from the Arrhenius behavior, i.e. [28]

$$m = \left. \frac{\partial \log_{10} \eta(T)}{\partial \left(\frac{T_g}{T}\right)} \right|_{T=T_g}. \quad (1.2)$$

Unfortunately, no clear relationship can be found between the T_g/T_m value and the fragility m [27], as also the collection of data by Nascimento and Aparicio suggests [29]. Up to now, only one measurement of the fragility of a phase-change materials has been published and a strong deviation from the Arrhenius behavior was obtained with a fragility of $m \approx 90$ for Ge₂Sb₂Te₅. From the knowledge of thermodynamic properties like the excess specific heat at the glass transition $\Delta C_p(T_g)$ and the latent entropy of melting ΔS_m , the fragility can be calculated [27].

$$\frac{\Delta C_p(T_g)}{\Delta S_m} = \frac{m - m_{\min}}{m(1 - T_{rg}) + m_{\min} T_{rg}}, \quad (1.3)$$

where $m_{\min} = \log_{10} 0(\tau_g/\tau_\infty)$ is the minimum slope of the viscosity curve, taking into account the shortest relaxation times, $\tau_\infty \approx 10^{-14}$ s and the relaxation times at the glass transition, $\tau_g = 100$ s. Further, the driving force of crystallization is the change in free enthalpy ΔG . Therefore, measurements of thermodynamic properties can be used to classify phase-change

¹Nucleation refers to the formation of crystalline grains (nuclei) in an amorphous matrix and is followed by the continuous growth of these grains.

²The kinetic fragility can differ from the thermodynamic fragility of the undercooled liquid [27], which will not be discussed here.

materials further. Such measurements have been performed in the framework of this thesis and will be discussed in Chpt. 7.

1.4.2 Atomic structure contrast

The transition process in PCMs is based on the (meta-)stability of an amorphous and crystalline phase at ambient conditions. These structures must have different macroscopic properties, to allow for an easy reading of the stored information. This contrast is not usually observed upon crystallization in glass forming systems (cf. e.g. the crystalline modifications of silicate glasses). In PCMs, this property contrast is large and in conclusion it is natural to wonder, whether also the microscopic, atomic structures are different in both phases. This question will be addressed in Chpt. 4 and in the following, previous results for phase-change materials are briefly summarized.

Many amorphous semiconductors like Si, Ge, but also III-V compounds like GaAs and GaSb are well described in the continuous-random-network (CRN) model [30, 16]. This model for an amorphous material has many features in common with the crystal lattice: Coordination numbers, nearest-neighbor distances and the average bond angle. The only difference lies in the larger variance of bond angles and, of course, in the absence of long range order.

An investigation of the local order in GeSb_2Te_4 revealed that the local atomic environment changes upon crystallization even in those aspects, which are considered to remain unchanged in common semiconductors. This local environment can be probed by extended x-ray absorption fine structure (EXAFS) independently for each element contained. Specifically, nearest neighbor distances were found to increase significantly upon crystallization from 2.61 Å to 2.83 Å [31] (values for the Ge-Te distances from EXAFS analysis). EXAFS necessarily relies on the comparison with a theoretical model, if quantitative information like atomic distances shall be obtained. The analysis of EXAFS data is very accurate only if the correct model for the local atomic configuration is chosen. The choice of this model has been a matter of constant debate and it can be easily shown that the models used so far are unable to reproduce the average nearest neighbor spacing, that is observed in scattering experiments combined with pair distribution function (PDF) analysis. In their analysis of the amorphous phase, Kolobov et al. [31] obtained nearest neighbor distances of 2.61 Å for Ge-Te and 2.85 Å for Sb-Te distances. In the crystalline phase, on the other hand, bond lengths of 2.83 Å and 2.91 Å were obtained for Ge-Te and Sb-Te distances, respectively. The resulting average bond lengths are compared to the results of a PDF analysis in Tab. 1.3. The data show a significant deviation – 2% in the amorphous and 4% in the crystalline phase. This deviation is clearly larger than the precision of both techniques, which is better than 1%. Since the PDF analysis technique is not based on comparison with some structural model, it can be considered reliable. In Chpt. 3, this deviation between EXAFS data and PDF analysis will be explained and a different data analysis will be presented, which accurately reproduces the average nearest neighbor distances from EXAFS data.

It was further proposed that a specific switching mechanism could be responsible for the

Table 1.3: Average nearest neighbor spacings in amorphous $\text{Ge}_2\text{Sb}_2\text{Te}_5$, measured at ambient conditions. A significant deviation is found between the values obtained by EXAFS and PDF analysis. In Chpt. 3, the origin of this deviation will be explained and an EXAFS analysis will be presented, which is in line with the PDF analysis.

Phase	EXAFS [31]	EXAFS [32]	PDF [33]
Amorphous	2.73 Å	2.73 Å	2.78 Å
Crystalline	2.87 Å	n/a	2.99 Å
Contrast	+5%	n/a	+8%

fast crystallization of Ge-based phase-change materials [31]. This mechanism is based on the assumption that the Ge atoms are tetrahedrally coordinated in the amorphous phase and switch to an octahedral coordination in the crystalline phase. The basic structural features will be re-investigated in this thesis, but it is stressed that the derivation of structural models alone cannot explain the kinetics of the transition and therefore cannot explain the speed of the crystallization – just like the knowledge of the final and initial states are insufficient in Fermis golden rule [34] to predict the transition time. This becomes possible only if the interaction operator is known as well. In the case of crystallization, this interaction operator must be based on thermodynamic (e.g. the driving force ΔG) and kinetic properties (e.g. the viscosity η) of the system, but no such operator is known so far.

The analysis presented throughout this thesis does not go so far as to derive a crystallization mechanism from the static structures of both phases. The atomic structures of phase-change materials are only used to identify a unique property contrast between the local atomic structure of both phases, which is not observed in other glass forming materials. It can be stated already that all investigated phase-change materials changed their local atomic configuration upon crystallization. This thesis will therefore focus on systematic differences between the atomic rearrangement of various phase-change materials.

Some differences among phase-change materials can be observed from their crystallization behavior. It is often written that some phase-change materials like GeTe and $\text{Ge}_2\text{Sb}_2\text{Te}_5$ crystallize in a nucleation dominated way, whereas Sb-based materials like $\text{Ag}_4\text{In}_3\text{Sb}_{67}\text{Te}_{26}$ crystallize growth dominated. This difference is indeed suggested by TEM images, which are depicted in Fig. 1.3. They were obtained by laser-recrystallizing the respective material under various external conditions. On these length scales, however, the dominant mechanism can be observed from the many tiny crystallites in $\text{Ge}_2\text{Sb}_2\text{Te}_5$, which imply that the crystal nucleation rate is very high. In $\text{Ag}_4\text{In}_3\text{Sb}_{67}\text{Te}_{26}$, on the other hand, larger crystallites are observed – indicating that only few nucleation events were necessary for the nuclei to grow all over the heated volume. Therefore, a distinction is commonly made between nucleation- and growth dominated materials. It has to be kept in mind, however, that the

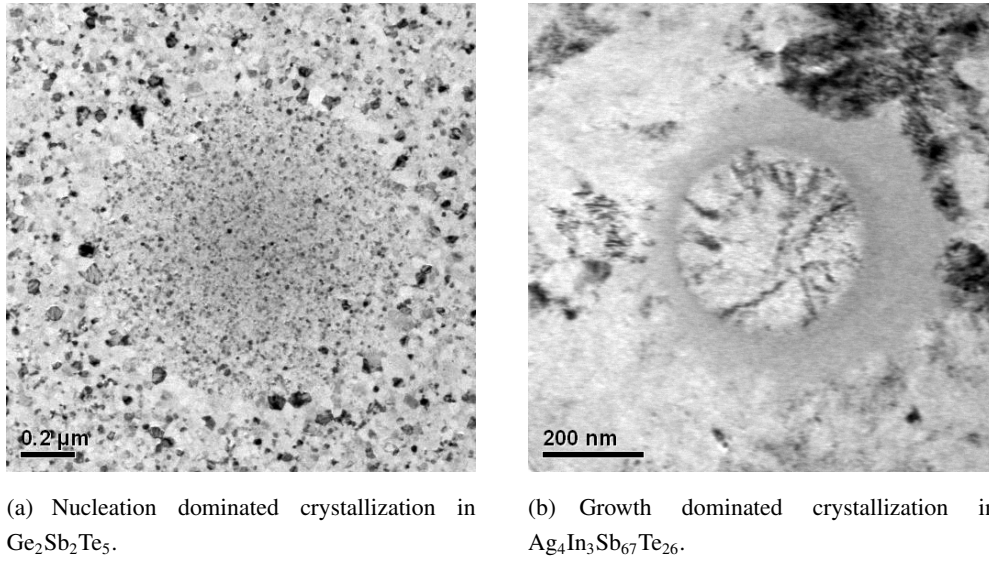


Figure 1.3: TEM images of crystallized spots in GST and AIST: Nucleation and Growth. Images from [35]

dominating mechanism inside a phase-change memory cell depends on the geometry of the cell – most significantly on the ratio of interfaces to volume. In this way, even in the nucleation dominated material GeTe, features of growth dominated crystallization were observed [8]. This observation, however, does not affect the basic crystallization mechanism with nucleation and growth processes, which can be clearly distinguished from optical switching experiments as shown in Fig. 1.3. This seemingly different crystallization mechanism motivates further investigation of the local atomic property contrast in those compounds.

1.4.3 Resonance Bonding

Since the atomic arrangement in crystalline phase-change materials differs from that of the amorphous phase, it is reasonable to suspect that a change in the bonding mechanism might occur, which might be responsible for the contrast in many properties – most directly for the contrast in optical reflectivity. Indeed, resonant covalent bonds were found in the crystalline phase as compared to the ordinary covalent bonds of the amorphous phase.

The concept of resonance bonding was first discussed by Pauling in 1939 [36]: He proposed the concept to describe the bonding in a benzene ring, where the average distance between C atoms lies between that of single- and double-bonds. Therefore, Pauling interpreted the bonding in benzene as a resonance between single- and double-bonds between adjacent atoms. Therefore, he suggested to add two quantum mechanical wavefunctions of the electronic configuration: One, where the alternation of single and double bonds starts to the one direction along the ring and another configuration, where the alternation starts to the opposite direction. The description of the electronic state by the superposition of these degenerate states lowers the energy by the so-called resonance energy ΔE_r .

The resonance bonding in phase-change materials is based on the same concept, except that it takes place in three dimensions: Most PCMs crystallize in a cubic rock-salt like structure with three p-electrons per atom. These electrons form covalent bonds to the six neighboring atoms, but there are too few electrons to saturate all six bonds. Hence, the electronic configuration can be described as a superposition of saturated covalent bonds in opposite crystallographic directions. This superposition again reduces the energy of the total system and the bonds remain unsaturated. In contrast to the benzene ring, where both wavefunctions remain perfectly degenerate, static atomic displacements occur in crystalline PCMs. These displacements can be described as an unequal superposition of wavefunctions. They are driven by an additional reduction of the electronic energy in a Peierls-like mechanism in three dimensions. Thereby, they localize electronic charge and lift the local octahedral symmetry. The atomic displacements therefore limit the effect of resonance bonding and will be studied extensively in this thesis (cf. Chpt. 3). The atomic displacements can also generate configurational entropy, which is relevant to the driving force of crystallization $\Delta G = \Delta H - T\Delta S$ (cf. Chpt. 6).

Resonance bonding in phase-change materials was first observed by their large optical dielectric constant ϵ_∞ [37], which is the most direct experimental evidence. Lucovsky and Littlewood mention three additional criteria, by which resonance bonding can be observed: These are the energy gap E_g [38], the transverse electric charge e_T^* [38] and the transverse optical phonon frequency ω_{TO} [39]. The transverse electric charge will be referred to in this thesis as dynamic charge Z^* , since both terms are used synonymously [40] although their definitions are somewhat different. However, the latter term is much more directly related to the features of resonance bonding, cf. eq. 1.4. The mathematical definition of the dynamic charge is introduced for a rock-salt crystal with covalent bonding, where a distortion of atomic planes along the 111-direction is modeled by u , the short bond length, and an opposite long bond length u_2 , which is related to u via the average bond length \bar{u} : $u = 2\bar{u} - u_2$. Then, the dynamic charge of the solid $Z^*(u)$ is given by the change of the electronic dipole moment of the diatomic bonds, ∂p for a variation of the atomic distance,

$$Z^*(u) = \frac{\partial p(u)}{\partial u}. \quad (1.4)$$

The transverse effective charge also contains the contribution from the static charge [41], i.e. the different charge of the atomic cores, which is negligible in all materials studied here [42]. Therefore, it must be the dynamic charge, which dominates the transverse effective charge. The effect of a large dynamic charge can be described as follows: If an atom is displaced in such a solid, a particularly large amount of electronic charge is reorganized (shifted) due to this atomic displacement. This leads to a large increase of the dipole moment associated with the asymmetric distribution of electronic charge. It is therefore not surprising that also the electronic polarizability, $\epsilon_\infty - 1$ is large in these systems. Lucovsky et al. showed that indeed the relationship

$$(Z^*)^2 = a(\epsilon_\infty - 1) \quad (1.5)$$

holds within good approximation of $a \approx 1$ [38]. The best indicator for resonance bonding

is the experimentally accessible optical dielectric constant, and since it occurs only in the crystalline phase, where neighboring p-orbitals are aligned, a large contrast in ϵ_∞ is observed between the amorphous and crystalline phases.

Experimentally, a large optical dielectric constant was found for all investigated crystalline phase-change materials. The electric field E in the optical regime excites the electronic system in the solid. In the optical frequency regime, the atoms will not significantly follow this excitation, so that only the electronic system is displaced. It was found by density functional theory (DFT) calculations that static atomic displacements from the high-symmetry rock-salt lattice site reduce the optical dielectric constant [42]. This trend can be understood from the more significant localization of charge in the more covalent bond. The static atomic displacements therefore reduce the effect of resonance bonding. These displacements can be of different nature, because the atoms can be displaced in a random direction (e.g. in the cubic phase of GeSb_2Te_4) or along a specific crystallographic direction (e.g. in α - GeTe and in the hexagonal phase of GeSb_2Te_4). The nature of these displacements will be investigated throughout this thesis and will be related to the Peierls effect and distortions originating from chemical disorder.

As mentioned before, also the energy gap and the frequency of transverse optic (TO) phonons are related to resonance bonding. In particular the scaling of the energy gap with the optical dielectric constant is given by [38]

$$\epsilon_\infty = 1 + \frac{\hbar\omega_p^2}{E_g}. \quad (1.6)$$

This leads to the rare situation, in which the crystalline phase has a smaller band gap than the amorphous phase. In common semiconductors (e.g. Si) the energy gap of the amorphous phase is usually smaller due to tail states in the gap (caused by disorder). The criterion of TO phonon modes is experimentally most challenging, since it relies on the softening of the TO mode. This softening is observed in many IV-VI compounds, where an atomic distortion along the cubic 111-direction is 'frozen in' at low enough temperatures. This instability is a direct cause of the unsaturated bonds [38]. Although this mode softening is a fingerprint of resonance bonding, it is the only criterion, which cannot be transferred to the amorphous phase without extending the definition of an LO mode ³.

1.4.4 Map for phase-change materials

The aim of creating a "treasure" map to identify the most suitable PCM for a specific application was brought one step closer, when a coordinate scheme was applied to categorize those materials, which have on average 3 p -electrons and crystallize in a (distorted) rock-salt structure. It was found that all phase-change materials are located in a specific region of this map. The coordinate scheme is based on purely atomic parameters, which gives

³A vibrational mode in a crystal is labeled LO, when the vibrations take place in the direction of the wave vector of the excitation. However, wavenumber is not a well-defined quantity in amorphous materials so that no clear definition of TO and LO is yet established for amorphous materials.

the map a quite significant predictive power over the class of materials to which it can be applied.

The axes of the map are hybridization and ionicity of a material. The hybridization is related to the difference of the radii of s and p -electrons at the same atom. A strong hybridization implies that this difference is particularly small. The ionicity on the other hand is related to the difference of the radius of the p -electrons on the anion and cation sublattice. A large ionicity implies a large difference of these radii. Phase-Change materials are located in a corner of this map, where both, ionicity and hybridization are very low. Indeed, no phase-change materials with a significant ionicity are known so far. It is nevertheless desirable to develop a coordinate scheme for materials with more or less than 3 p -electrons per lattice site.

1.4.5 Transport properties of phase-change materials

It is well known that amorphous solids have a very low thermal conductivity, because the topological disorder leads to a strong phonon scattering and reduces their mean free path (cf. [43], p. 58). Therefore, it is no surprise that amorphous phase-change materials have a low thermal conductivity as well [44]. The thermal conductivity of amorphous $\text{Ge}_2\text{Sb}_2\text{Te}_5$ was found to be $0.14 \text{ W (K m)}^{-1}$. Even more surprising is the fact, that even crystalline phase-change materials have a rather low thermal conductivity of only $0.39 \text{ W (K m)}^{-1}$ [44]. In addition, they have a significant electronic conductivity so that they resemble the ideal properties of thermoelectric materials, i.e. 'phonon glass, electron crystal' quite closely.

The low thermal conductivity in crystalline phase-change materials might be related to the significant sources of disorder due to substitutional disorder on the one hand (disorder of the occupation of lattice sites, cf. Secs. 1.5 and 3.1) and the resulting atomic displacements from their ideal lattice sites. This argument, however, was not yet proven because the situation in the crystalline phase with its translational symmetry of lattice sites is in principle different from that encountered in amorphous materials. However, the random sequence of strongly varying masses (vacancies and heavy atoms) in these crystals might impose significant challenges for thermal conduction by phonons. Acoustic phonon modes are usually responsible for thermal conductivity of the lattice. Therefore, changes in the thermal conductivity are caused by changes in the local atomic structure. Even in those rare cases, where the optical modes significantly reduce the thermal conductivity by a strong anharmonic coupling mechanism [45], measurements of the atomic structure and its thermal expansion can explain transport properties. This coupling was found in the rock-salt phase of the IV-VI compound PbTe , which is not too different from the crystalline phase-change materials investigated here. Therefore, also the lattice dynamics of phase-change materials will be discussed in Chpt. 5.

Furthermore, also the electronic properties of the crystalline $\text{GeTe-Sb}_2\text{Te}_3$ -based PCMs show surprising features: It is the first three-dimensional crystal in which a metal-insulator transition occurs entirely due to changes in atomic disorder [21]. This atomic disorder in turn is irreversibly controlled by the annealing temperature. At lowest annealing conditions,

the crystalline phase contains several sources of atomic disorder: Local atomic displacements, substitutional disorder and a large concentration of vacancy. This phase is semiconducting. At higher annealing temperatures, all these sources of disorder are removed. It is not yet clear, which of these sources of disorder is (or are) responsible for the transition. Therefore, the annealing temperature dependence of this disorder will be investigated by probing the local atomic environment as well as the lattice symmetry (cf. Chpt. 3). Further influences on thermodynamic properties will be discussed in Chpt. 7.

1.4.6 Resistance drift

An important challenge in the large scale application of phase-change memory devices is the control of the resistance drift in the amorphous phase. The crystalline phase, on the other hand, does not show such drifting behavior at the commonly observed temperatures up to 350 K. The term resistance drift refers to the change of the electrical resistivity with time even at room temperature [46]. It can become critical, if the states involved in the memory operation have very similar resistances. This is particularly the case, when several bits are encoded as different resistances – so called multi-level storage. Several technological mechanisms have been proposed in order to reduce the impact of resistance drift on the operation, e.g. by encoding information only in the resistance difference between neighboring cells, which show a similar drift behavior. The resistance drift phenomenon is based on a structural relaxation mechanism [18] in the amorphous phase, but since the atomic structure of many phase-change materials has been described controversially, it is not yet possible to identify this relaxation mechanism. Therefore, the structural model for the amorphous phase of several phase-change materials has been investigated in the framework of this thesis. It was shown in particular that the resistance drift of amorphous GeTe can be reduced by substituting several percent of the Ge atoms by Sn [20]. These compounds were shown to have a more stable resistance and their structural differences will be discussed in Chpt. A.

1.5 Phase-change compounds

From the discussion presented so far, one can derive already that the atomic bonding mechanism in phase-change materials is very complex: As covalency and ionicity are both very low, the materials are just at the transition between semiconductors and metals. This critical state of bonding ensures that large property differences can be expected from small variations of the local order. Furthermore, the directional bonding of covalent bonds is necessary to stabilize the amorphous network and prevent the atomic structure to relax to closest packing. It is therefore not surprising that all phase-change materials consist of those elements, which are at the transition between metals and non-metals, also known as metalloids (sometimes also referred to as semimetals). Of these metalloids, Ge, Sb and Te are the most commonly employed materials – sometimes with the addition of metallic elements like Ag, In and Sn. In the following the known classes of phase-change materials will be discussed.

Compounds from the GeTe-Sb₂Te₃-system are commonly employed in CD-RWs. Since

the crystallization temperature of Sb_2Te_3 is too low for applications, only those materials with a sufficient content of GeTe can be employed as phase-change materials. Therefore, $\text{Ge}_2\text{Sb}_2\text{Te}_5$ is employed in CD-RWs. Most materials from this pseudobinary system possess a meta-stable cubic phase, which is composed of two sublattices like in a rocksalt structure (cf. [47] for GeSb_4Te_7 , [48] for GeSb_2Te_4 and [49] for $\text{Ge}_2\text{Sb}_2\text{Te}_5$). One sublattice is fully occupied with Te atoms, while the other contains some Ge and Sb atoms and the remaining lattice sites are empty. The empty sites (vacancies) are in fact energetically favorable, because they reduce the average number of p -electrons per lattice site to three and therefore shift the Fermi energy in the band gap. Therefore, these vacancies are intrinsic [50] (in contrast to those non-intrinsic defects, which are formed due to the entropic contribution $-TS$ to the free enthalpy G). The disorder of the occupation of the second sublattice induces a significant amount of configurational entropy (cf. Sec. 6.2.3), but at the same time creates large atomic distortions. This can be seen from the large Debye-Waller factor even at very low temperatures, as well as from the splitting of atomic nearest neighbor spacings to short and long distances, which is observed from an analysis of EXAFS data.

Another class of phase-change materials is based on Sb_2Te_3 , whose crystallization temperature is too low (383 K [51]) for application. Substituting 4% Te with Ag and 3% Te with In increases the crystallization temperature to 451 K (cf. Sec. 7). Due to its higher optical contrast at shorter wavelengths, $\text{Ag}_4\text{In}_3\text{Sb}_{67}\text{Te}_{26}$ is a well known phase-change material used in DVD-RWs.

Sb-based phase-change materials are probably the structurally most simple phase-change materials. Of this class, $\text{Ge}_{15}\text{Sb}_{85}$ is the most well-investigated material. Although it crystallizes rapidly [52] and has a high crystallization temperature of 512 K [53], the material might be difficult to employ in phase-change devices, because it phase separates upon crystallization at a heating rate of 5 K/min. It is not yet clear, if this phase-separation also takes place upon rapid switching in electronic or optical devices.

Several other compounds have been investigated as well, which are possibly phase-change materials as well: In_3SbTe_2 (IST) is a glass forming compound as well and crystallizes rather rapidly at about 515(10) K, depending on the film thickness. Thinner films crystallize at higher temperature, which is beneficial for scaling properties. Upon crystallization, the electronic resistivity is changed by more than seven orders of magnitude [54]. Crystallization times of 100 ns were also observed in phase-change cells [55], so that in principle all requirements for a phase-change material are fulfilled. It is well known, that IST crystallizes in a cubic structure, but it will be shown that also IST consists of a rocksalt-like crystal structure with one sublattice fully occupied with In, while the second sublattice contains Sb and Te atoms (cf. Chpt. 4.5). Therefore, also IST might contain significant atomic displacements and will be studied here. IST also phase separates at higher annealing temperatures, where crystalline InSb is formed [56].

Another potential phase-change material is SnSe_2 , which is exceptional because it is based on Se, not on Te. Indeed, the crystallization times observed are significantly longer than those of Te-based materials [57], p. 126. SnSe_2 crystallizes at 493(5) K [58] into a

layered, hexagonal structure and changes its electronic resistivity by about five orders of magnitude. No phase separation was observed even after annealing at higher temperatures. There is, however, a large change in density upon crystallization, which could hamper its application in phase-change memory. The amorphous phase has a density of 4.77 g cm^{-3} , which increases upon crystallization by 21% to 5.75 g cm^{-3} in the crystalline phase [58]. It was shown from the analysis of EAXFS data that this change in density is a result of the significant increase of nearest neighbor spacing and coordination number upon crystallization, [59], p. 108.

The previous summary of different phase-change compounds shows that there is no obvious universal property. An analysis of the local atomic structure in those various materials might reveal a universal structural motif. The identification of such a structural motif might help to understand the universal properties of phase-change materials, i.e. the property contrast and the thermodynamic properties. Furthermore, several studies of the crystallization mechanism are based on ab-initio molecular dynamics (AIMD) methods and rely on a model of the atomic arrangement in the amorphous phase [60, 61]. Both, the initial and the final crystalline structure should be in good agreement with experimental data so that highly accurate data are necessary to confirm the calculated models. Therefore, the atomic structure of both phases is discussed in Chpts. 4 and 7.

1.6 Structure of this thesis

This thesis will start with an analysis of the static structure of amorphous and crystalline phase-change materials. To reveal these, scattering and spectroscopic experiments were performed. These technique will be explained first in Chpt. 2 of this thesis in order to put the following data treatment on a solid mathematical framework. This theory will be referred to in the data treatment in Chpts. 3 and 4. Chpt. 3 focussed entirely on the annealing dependence of the crystalline phase of GeSb_2Te_4 . It will also introduce the application of all different techniques of structure determination to one specific compound. The aim of that chapter is to reveal the changes in atomic disorder during the disorder-induced metal-insulator transition (MIT). The following Chpt. 4 discusses the structural contrast between the amorphous and crystalline phases for a variety of phase-change materials. Based on an understanding of the microscopic structure, this thesis continues with an analysis of the interatomic forces in a prominent phase-change material, GeSb_2Te_4 , cf. Chpt. 5. This analysis is based on the density of phonon states (DOPS), which was obtained from nuclear inelastic scattering (INS) experiments. The DOPS allows calculating several thermodynamic quantities, like the Debye temperature or the interatomic force constants. These results will help to find out why the interaction potentials in a crystalline phase are stiffer than those of the respective amorphous material. These results will be combined with a discussion of the thermodynamics of glass forming materials Chpt. 6, which focuses in particular on the role of entropy upon crystallization. Calorimetric analyses are presented in Chpt. 7, which presents a method to determine the entropy difference in glass-forming systems. Finally,

the knowledge of atomic disorder and thermodynamic data will be combined to discuss the nucleation and growth mechanisms of the crystallization.

CHAPTER 2

Methods of microscopic structure analysis

It was shown in the introduction (cf. Sec. 1.4) that the difference in atomic structures and the corresponding property contrast is the fundamental principle of data storage in phase-change materials. Therefore, an investigation of material properties and stoichiometric trends in these materials should start from a detailed analysis of the atomic structure. From a knowledge of the atomic structure on different lengths scales, many macroscopic properties of a material can be determined by empirical laws and/or by complex quantum mechanical calculations. Therefore, the atomic structure of phase-change materials will be investigated by several different techniques, which focus on different lengths scales of the atomic ordering. Diffraction e.g. probes the short and long range order of materials, whereas spectroscopic techniques like EXAFS probe the short range order with a special sensitivity for chemical ordering. These complimentary techniques have been employed and their theory will be explained in the following. Wherever possible, the theories behind all techniques will be brought in relation.

In order to put the analysis of experimental data on a solid mathematical framework, the theory of the applied methods will be summarized in this chapter. Several techniques have been employed also because the atomic structure of phase-change materials is rather complex due its different types of disorder depending on the investigated length scales. Furthermore, many methods of structural analysis rely on the periodicity of the investigated structures, which is simply absent in the amorphous phase. Therefore, different techniques have to be employed, like pair-distribution function (PDF) analysis of X-ray and neutron scattering experiments and X-ray Absorption Spectroscopy (XAS). Even after switching to the crystalline state, many phase-change materials do not possess the kind of translational symmetry which is desired for a Rietveld refinement of X-ray diffraction patterns: Many materials consist of two sublattices, of which both have significant atomic displacements

even at 0 K. Furthermore, one of the sublattices is almost randomly occupied by a fraction of more than 10% vacancies. This high degree of disorder motivates the use of methods, which do not rely on translational symmetry also for the analysis of the crystalline phase. This chapter begins with a fundamental treatment of X-ray and neutron scattering and continues to discuss the differences between elastic and inelastic scattering. Inelastic scattering contains information on the density of vibrational states and will become important later. Finally, also x-ray absorption spectroscopy is discussed as a complimentary method of structural analysis. The formulae given in this chapter will be of use during the data analysis presented in Chpts. 3 and 4.

2.1 General scattering theory

Let an incident particle (either photon or neutron in this study) of \vec{k}_i be scattered to the state \vec{k}_f . This situation has six free parameters - neglecting any other property of the scattered particle, like e.g. the spin state. Since this combination of vectors, including the scatterer can be rotated in any direction without changing the scattering condition, only four parameters remain free to chose. These can be expressed in terms of the momentum transfer

$$\vec{Q} = \vec{k}_i - \vec{k}_f \quad (2.1)$$

for both neutron and x-ray scattering and the energy transfer $\Delta E = E_i - E_f = E$

$$E = \frac{\hbar^2}{2m} \cdot (\vec{k}_i^2 - \vec{k}_f^2) \quad \text{for neutron scattering,} \quad (2.2)$$

$$E = \hbar c (|\vec{k}_i| - |\vec{k}_f|) \quad \text{for x-ray scattering.} \quad (2.3)$$

If, in addition, the sample has no preferential orientation, which is the case for amorphous and poly-crystalline samples, only two parameters, e.g. $|\vec{Q}|$ and E need to be varied to obtain all available information about the scattering sample. In this case, it suffices to count the number of particles scattered per unit time to a small solid angle $d\Omega = dS/r^2$ (r is the distance from the sample to the detector, $r^2 \gg dS$, dS the area of the detector) with an energy $E + dE$ per incident particle per unit time. This is called the double differential cross section,

$$\frac{d^2\sigma}{d\Omega dE}, \quad (2.4)$$

which is of unit m^2J^{-1} and is usually given in unit of barns per eV with $1\text{barn} = 10^{-24} \text{cm}^2$. The double differential cross section, being the experimentally accessible quantity differs significantly for the cases of neutron and x-ray scattering. This expression is related to the scattering potential (i.e. the sample) via (cf. [62], p. 17)

$$\frac{d^2\sigma}{d\Omega dE} = \frac{1}{N} \frac{k_f}{k_i} \frac{m}{2\pi\hbar^2} \sum_{\lambda_i} p_{\lambda_i} \sum_{\lambda_f} \left| \langle \vec{k}_f \lambda_f | V(\vec{r}) | \vec{k}_i \lambda_i \rangle \right|^2 \delta(E + E_{\lambda_i} - E_{\lambda_f}). \quad (2.5)$$

In this equation, N is the number of scattering atoms, m the mass of the scattering particle, λ numerates all possible states of the sample and $V(\vec{r})$ is the interaction potential. E_λ is

the energy of the sample in state λ . p_λ is the probability for the sample to be in the state λ before the scattering event. Here, $V(\vec{r})$ is the scattering potential, which is different for x-ray and neutron scattering, but contains the crucial information about the structure of the investigated sample. The techniques of neutron and x-ray scattering will be discussed in the following, based on the approach given in Eq. 2.5.

2.2 General Neutron scattering

The full double differential cross section, Eq. 2.4, of isotropic (amorphous or poly-crystalline) PCMs can be measured with a time-of-flight (TOF) spectrometer. Large quantities of sample mass (approx. 1 g) are necessary for these experiments to be possible at high-flux spectrometers. Nevertheless, these experiments could be performed and the theory of these experiments will be discussed first, because they nicely reveal the difference between coherent and incoherent scattering and the relation to different scattering cross sections. Later in this thesis, total scattering experiments will be presented, which are a special, energy transfer averaged case of neutron scattering. There, only $d\sigma/d\Omega$ is measured (by some specific experimental integration over E).

In the scattering geometry used here, the direction of the incident beam \vec{k}_i is always kept constant and only the kinetic energy of the incoming neutrons is varied. For a more convenient theoretical description, the wave vectors should be replaced by scalar quantities. Therefore, k_i is defined as $\vec{k}_i = \vec{e}_x \cdot k_i$. Taking into account only the scattering angle θ , it follows that

$$\vec{k}_f k_i \vec{e}_x = k_f k_i \cos(2\theta). \quad (2.6)$$

Then, the so called *scattering parabola* can be derived, which determines the maximum energy and momentum transfers for a specific scattering angle 2θ and incident energy E_i ,

$$\frac{E}{E_i} = \left(2 - \frac{Q^2}{k_i^2}\right) - 2 \cdot \left(\cos(2\theta) \pm \sqrt{\cos^2(2\theta) + Q^2/k_i^2 - 1}\right). \quad (2.7)$$

A plot of this scattering parabola for the conditions used in various experiments can be seen in Fig. 2.1. For inelastic scattering, it is desirable to resolve the excitations with the best energy resolution possible. Therefore, at low temperatures, where the excitations have to be created (Stokes side), the energy is chosen to be slightly higher than the most energetic excitation. A large number of excited states exists at ambient or high temperature conditions so that it is sufficient to measure with neutrons of lower kinetic energy the annihilation of these excited states (anti-Stokes side). The latter condition is even advantageous because a better energy resolution can be obtained because of the higher final kinetic energy of the neutrons. In total scattering experiments, on the other hand, a high momentum transfer is desired to probe over a large range in reciprocal space so that neutrons of a short wavelength (0.5 Å) have been chosen in this study.

Neutron scattering offers different insights to the structure of matter than x-ray scattering, because the interaction of neutrons with matter is mediated by (cf. [63], Chpt. 11)

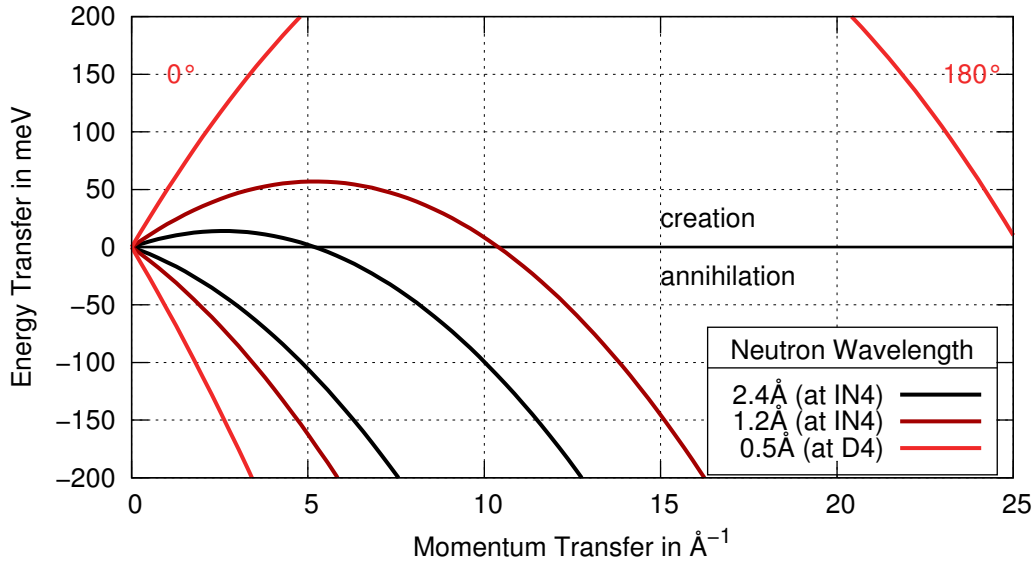


Figure 2.1: Energy and momentum transfer in a neutron scattering experiment. The lines show the maximum absolute energy transfer upon creation or annihilation of an excitation, so that the area enclosed by them is accessible using neutrons of the given wavelengths. The momentum transfer is further limited by the available angular range of the detectors.

(1) scattering at atomic nuclei and (2) scattering from magnetic moments. The investigated atoms (Ge, Sb and Te) typically possess only small magnetic moments and hence only nuclear scattering has to be taken into account. In particular, the scattering by unpaired magnetic moments of electrons is neglected. Therefore, the scattering at atomic nuclei is discussed in the following. When the neutron has a wavelength comparable to interatomic distances, it has about the kinetic energy of ambient temperature – hence the name “thermal” neutron. A quick way to transform energy (and temperature) to wavelength is given by $\lambda = 0.286 \cdot E^{-1/2} \text{ \AA}$ with the kinetic energy E of neutrons given in eV without unit. With a wavelength of this order of magnitude, the neutron scattering can resolve interatomic distances, but is not sensitive to the inner structure of nuclei, which is on the order of 10^{-5} \AA . This means that no inner features of the nuclei can be resolved and accordingly that no dependence of scattering length on momentum transfer is expected for thermal neutron scattering (so-called s-wave scattering). It suffices to describe the scattering nucleus as a point particle with a scattering length $b = (\sigma/4\pi)^{1/2}$ of some fm. This scattering length goes into scattering theory via the application of the so called Fermi pseudo potential (cf. [64], p. 15),

$$V(\vec{r}) = \frac{2\pi\hbar^2}{m} \sum_j b_j \delta(\vec{r} - \vec{R}_j). \quad (2.8)$$

This potential contains the mass of the neutron m and a sum over all atoms j in the scattering sample with their scattering lengths b_j at position R_j . In order to calculate the wavefunction of the scattered neutron ψ_f , given the wavefunction of the incoming neutron

$\psi_i = \exp(i \cdot (\vec{k}_i \vec{r} - \omega_i t))$, a lot more information is necessary. In typical samples with some 10^{23} atoms, the number of parameters in Eq. 2.8 is huge. Therefore, a way was worked out to analyze the experimental scattering cross sections based on fundamental properties, like interatomic distances and densities of phonon states. To realize this, the potential is inserted into the formula for the double differential cross section, Eq. 2.5 (not taking into account polarization effects. The resulting formula can be simplified to (cf. [62], p. 20)

$$\frac{d^2\sigma}{d\Omega dE} = \frac{1}{N} \frac{k_f}{k_i} \sum_{dd'} \sum_{j \in d, j' \in d'} \langle b_j^* b_{j'} \rangle S_{jj'}(\vec{Q}, E), \quad (2.9)$$

Where the sums d and d' run over all kinds of elements in the sample and j and j' run over all atoms of element d and d' , respectively. The average, $\langle \dots \rangle$, refers to an averaging over spin and isotope distributions of the corresponding pair of atoms. This equation allows discussing the origin of coherent and incoherent scattering, which is the aim of the following paragraphs. Finally, it is desirable to explain the derivation of the density of phonon states from inelastic neutron scattering and the influence of the different cross sections. Eq. 2.9 contains the structure factor $S_{jj'}(\vec{Q}, E)$, which will be discussed later. For an uncorrelated distribution of isotopes, it holds that $\langle b_j^* b_{j'} \rangle = \langle b_j^* \rangle \cdot \langle b_{j'} \rangle$, with

$$\langle b_j^* \rangle \cdot \langle b_{j'} \rangle = \langle b_d^* \rangle \cdot \langle b_{d'} \rangle + (\langle b_d^2 \rangle - \langle b_d \rangle^2) \delta_{jj'} \delta_{dd'}. \quad (2.10)$$

Introducing this equation into Eq. 2.9, the delta functions allow separating the sum over all atoms in two contributions (cf. [62], p. 20):

$$\frac{d^2\sigma}{d\Omega dE} = \underbrace{\frac{1}{N} \frac{k_f}{k_i} \sum_{dd'} \langle b_d^* \rangle \cdot \langle b_{d'} \rangle \sum_{jj'} S_{jj'}}_{\text{coherent scattering}} + \underbrace{\frac{1}{N} \frac{k_f}{k_i} \sum_d (\langle b_d^2 \rangle - \langle b_d \rangle^2) \sum_j S_{jj}}_{\text{incoherent scattering}} \quad (2.11)$$

The first term represents a sum over all distinct pairs of atoms, where each term stands for the correlation of atom j at time 0 with atom j' at time t and therefore contains the interference terms, which make the coherent scattering. The coherent cross section for bound nuclei is defined as $\sigma_c = 4\pi \langle b \rangle^2$. It can replace $\langle b_j^* \rangle \cdot \langle b_{j'} \rangle$, when the sample contains only one element and its isotopes are distributed randomly. σ_c is usually only slightly smaller than σ_s , given in Tab. 2.1.

The second term on the right side of Eq. 2.11 represents the sum over all atoms and contributes the correlation between atom i at time 0 with itself at time t . It is called the incoherent cross section and since it only depends on one single species at a time, can be replaced by the incoherent cross section for bound nuclei: $\sigma_i = 4\pi (\langle b^2 \rangle - \langle b \rangle^2)$.

It is common to define two additional quantities: The total scattering cross section for bound nuclei: $\sigma_s = 4\pi \langle b^2 \rangle$ and the absorption cross section for bound nuclei: $\sigma_a = 4\pi b''/k_i$, where k_i is the magnitude of the incoming neutron wave vector and b'' is the imaginary part of the scattering length, defined as $b = b' - ib''$. For the experiments presented throughout this thesis, b'' is of negligible magnitude. Scattering lengths are measured in

Table 2.1: Bound coherent scattering lengths b , total cross sections for bound atoms σ_s and coherent cross sections σ_c of the most common elements of phase-change materials [62]

Element	b in fm	σ_s in b	σ_c in b
Ge	8.193	8.60(6)	8.435(4)
Sb	5.641	4.3(1)	3.99(2)
Te	5.43	3.7(2)	3.71(5)

fm, while cross sections are usually give in unit barns, i.e. $1 \text{ b} = 100 \text{ fm}^2$. A list of bound coherent scattering lengths can be found in Tab. 2.1.

The scattering function is defined as (cf. [62], p. 20)

$$S_{jj'}(\vec{Q}, E) = \frac{1}{2\pi\hbar} \int_{-\infty}^{\infty} \left\langle e^{-i\vec{Q}\vec{R}_j(0)} e^{i\vec{Q}\vec{R}_{j'}(t)} \right\rangle e^{-iEt/\hbar} dt \quad (2.12)$$

From a single experiment, the partial scattering functions $S_{jj'}$ cannot be obtained, because just one total scattering function $S(\vec{Q}, E)$ is measured, as shown in Eq. 2.5. It is possible, at least in principle, to prepare isotopically enriched samples with the same structure, which have different scattering lengths. Taking the differences of these structure factors for enriched and non-enriched samples allows obtaining the partial structure factors as well. But since the necessary amounts of sample material are rather large in neutron scattering, these experiments are not regularly performed. We will return to the discussion of structure factors in more detail in the data treatment of total scattering experiments, where only the $|\vec{Q}|$ -dependence of S is measured. For the general purpose of the following data treatment, the structure factor S will be related to the experimentally obtained double differential cross section via

$$\frac{d^2\sigma}{d\Omega dE} = \frac{k_f}{k_i} S(\vec{Q}, E). \quad (2.13)$$

2.3 Inelastic Neutron Scattering

2.3.1 Density of Phonon States

Eq. 2.11 describes the scattering function, which can be partially obtained from an experiment with neutrons. The accessible range is limited by the scattering parabola shown in Fig. 2.1 for creation ($E > 0$) or annihilation ($E < 0$). The density of phonon states (DOPS) describes the vibrational features of a sample and is of high interest for many materials because it allows deriving macroscopic properties like the Debye temperature, for example, and microscopic properties like atomic force constants from one measurement. It is a rare occasion, that such a multitude of length scales can be probed with a single experiment. The DOPS can be obtained from the partial structure factor, if the measured Q -range fulfills the criterion [65]:

$$(Q_{\max} - Q_{\min}) \gg \frac{2\pi}{d}, \quad (2.14)$$

where d is the average atomic spacing in the sample. In order to obtain the density of vibrational states, the double differential cross section obtained from experiment, Eq. 2.13, is multiplied by $\sin(\theta)$ and integrated over the scattering angle θ [65]:

$$\frac{d\sigma}{dE} = \int_{\theta_{\min}}^{\theta_{\max}} \frac{d^2\sigma}{dE d\Omega} \sin(\theta) d\theta. \quad (2.15)$$

This expression is linked to the density of one-phonon states $f(E)$ for a sample containing only one element by [65]

$$\frac{d\sigma}{dE} = \frac{\hbar^2}{8\pi k_i^2} \frac{1}{E \left(\exp\left(-\frac{E}{k_B T}\right) - 1 \right)} (Q_{\max}^4 - Q_{\min}^4) \frac{\sigma_s}{m} f(E). \quad (2.16)$$

2.3.2 Partial Density of Phonon States

It was shown that the so-called incoherent approximation can be applied even to polycrystalline samples [66]. It takes into account one-phonon scattering only, i.e. the phonons are considered to be uncorrelated. Then, the total scattering cross sections σ_s of the specific elements can be used to sum the partial elemental DOPS in order to obtain Eq. 2.16.

Eq. 2.16 can be generalized for a compound of n atomic species (elements, not isotopes) with atomic fraction c_j by [65]

$$\frac{d\sigma}{dE} = \frac{\hbar^2}{8\pi k_i^2} \frac{1}{E \exp\left(\frac{-E}{k_B T}\right) - 1} (Q_{\max}^4 - Q_{\min}^4) \sum_j^n \frac{c_j \sigma_{s,j}}{m_j} f_j(E), \quad (2.17)$$

where f_j is the partial DOPS and m_j is the molar mass of species j , c_j its atomic fraction and σ_j its total cross section for bound atoms. The generalized density of phonon states $g(E)$, which is measured in inelastic neutron scattering, is obtained by

$$g(E) = \sum_j^n \alpha_j f_j(E), \quad (2.18)$$

with

$$\alpha_j = \frac{c_j \sigma_{s,j} / m_j}{\sum_l c_l \sigma_{s,l} / m_l}. \quad (2.19)$$

Therefore, light elements with a large cross section contribute most to the total density of phonon states, which is obtained directly from experiment.

2.3.3 The density of phonon states

In the previous section, the measurement of $g(\omega)$ by inelastic neutron scattering has been described, but neither was $g(\omega)$ defined, nor was explained what exactly the DOPS represents. In the framework of this thesis, the partial elemental DOPS $f_j(E)$ of amorphous and crystalline phase-change materials was measured by nuclear inelastic scattering. Since this

technique is based on the absorption and not on the scattering of particles, it is not discussed here, but is discussed separately in Chpt. 5. The corresponding results and data analysis will be presented in Chpt. 5 as well. In the following paragraphs, the means of analyzing the DOPS from both techniques will be explained.

The number of allowed frequencies of atomic vibrations in the range ω to $\omega + d\omega$ for a system of $3N$ atoms is $3Ng(\omega)d\omega$, so that the normalization condition

$$\int_0^\infty g(\omega)d\omega = 1 \quad (2.20)$$

holds for $g(\omega)$. In a perfectly ordered polycrystalline system, the DOPS can be separated into well defined, sharp features from the limited number of allowed vibrational modes, which is 3 times the number of atoms per unit cell. In disordered polycrystalline or in amorphous samples, however, the DOPS becomes rather featureless, except for some general properties, which always remain valid. These general properties will be discussed in the following.

The first peak in the DOPS corresponds to acoustic modes, which probe macroscopic properties of a sample due to their large wavelengths. In particular, the Debye temperature can be obtained exactly from the density of states in the regime of acoustic modes. To do so, it is necessary to observe all phonon modes in the density of states. This is surely the case for a polycrystalline sample, where many equal Brillouin zones are covered by the scattering parabola. In topologically disordered, amorphous materials however, there is no periodicity in reciprocal space, so that the acoustic modes at low wave-number k are smeared out at higher k . Therefore, the scattering parabola should contain only the acoustic modes, i.e. the wavelength should be sufficiently large – a condition that can be met experimentally. From the measured Debye temperatures, elastic properties of the isotropic and homogeneous samples can be obtained to a good approximation (cf. Sec. 2.3.4)

The total number of acoustic modes is related to the number of bonds within the atomic network: The N atoms, within a sample have in general $3N$ degrees of freedom. If every atom has only 2 bonds, which have to be kept of fixed length, $3N - 2N = N$ displacement directions stay free so that no restoring force applies and therefore these must be zero frequency modes [67]. Thus, the ratio of acoustic to optic modes is related to the formation of the atomic network. The above discussion neglects the influence of bond bending constraints, but delivers a useful estimate for the fraction of acoustic modes in the amorphous phase.

2.3.4 Debye temperature

From the low-frequency regime of the density of phonon states, the Debye temperature θ_D can be obtained. According to Ashcroft and Mermin [68], the Debye temperature should only be derived from specific heat measurements at low temperatures, where the Debye relation $C_V \propto T^3$ holds. Due to this difficulty, we will use the Debye temperature as an approximate number only and try to suggest trends in the resulting values. From a possible

trend in the Debye temperature, we can then derive trends in other properties. This functional relationship shall be discussed in the following. The Debye temperature θ_D is obtained from the definition of the Debye phonon spectrum with the cut-off frequency $\omega_D = k_B\theta_D/\hbar$,

$$g(\omega) = \begin{cases} \frac{3\omega^2}{\omega_D^3}, & 0 \leq \omega \leq \omega_D \\ 0, & \omega > \omega_D \end{cases}, \quad (2.21)$$

by fitting the low-frequency behavior to the experimental DOPS $g(\omega)$.

From the Debye temperature θ_D , we can derive the mean velocity of sound v_m . To do so, we start from the assumption that the Debye model describes well the acoustic phonon modes of a given compound. Then, the longitudinal mode has to be distinguished from the two transverse modes with velocities v_l and v_t , respectively. The total number of modes is then made up as ([69] p. 239)

$$3N = \frac{4\pi}{3}V \left(\frac{1}{v_l^3} + \frac{2}{v_t^3} \right) \cdot \left(\frac{k_B}{h} \theta_D \right)^3. \quad (2.22)$$

Since only one quantity can be obtained from the Debye temperature, a mean velocity of sound v_m is defined as [70]

$$v_m = 3^{1/3} \left(\frac{1}{v_l^3} + \frac{2}{v_t^3} \right)^{-1/3}, \quad (2.23)$$

This leads to the relation

$$\theta_D = \frac{h}{k_B} \left(\frac{3N}{4\pi V} \right)^{1/3} v_m. \quad (2.24)$$

The atomic number density N/V in this equation can be obtained from the compilation in Tab. B.1.

The velocity of sound, in turn, can be used to estimate the bulk modulus B if the shear modulus G and the mass density ρ are known (cf. Tab. B.1) via [71]

$$v_l = \sqrt{\frac{B + 4/3G}{\rho}}. \quad (2.25)$$

2.3.5 Vibrational entropy

Some macroscopic parameters are linked to the acoustic phonon modes of a system and are well described within the Debye model. These parameters were discussed in the previous section. Furthermore, some properties are linked to the exact shape of the total DOPS. These are the specific heat C_{vib} (which is independent of pressure and volume), the entropy S_{vib} and the interatomic force constant F , which will be derived from the DOPS in this section.

In a crystal, the different eigenmodes can be considered as independent harmonic oscillators. This also applies to the localized atomic vibrations in an amorphous solid. For such a system of independent harmonic oscillators, the partition function can be used to calculate the vibrational entropy from the DOPS directly ([69], p. 237),

$$Z = \sum_{n(\vec{k}\sigma)} \exp\left(-\frac{E[n(\vec{k}\sigma)]}{k_B T}\right), \quad (2.26)$$

where $n(\vec{k}\sigma)$ denotes the occupation number of states with momentum \vec{k} and phonon branch σ . By applying the common thermodynamic relations, the free energy of the vibrations can be calculated by $F_V = -k_B T \ln Z$,

$$F_V = k_B T \sum_{k\sigma} \ln \left(2 \sinh \left(\frac{E[n(\vec{k}\sigma)]}{2k_B T} \right) \right) \quad (2.27)$$

The sum over $k\sigma$ in Eq. 2.27 can be replaced by the integral $g(\omega)d\omega$ and allows calculating the specific heat and the entropy using the common thermodynamic relations. The resulting expressions are [72]

$$C = \frac{\partial E}{\partial T} = \frac{\partial}{\partial T} \left(F_V - T \frac{\partial F_V}{\partial T} \right) = 3Nk_B \int_0^\infty \left(\frac{\hbar\omega}{2k_B T} \right)^2 \left(\sinh^2 \left(\frac{\hbar\omega}{2k_B T} \right) \right)^{-1} g(\omega) d\omega, \quad (2.28)$$

for the specific heat, where N is the number of unit cells in the sample.

The entropy is given by

$$S_V = -\frac{\partial F_V}{\partial T} = 3Nk_B \int_0^\infty \left[\frac{\hbar\omega}{2k_B T} \coth \left(\frac{\hbar\omega}{2k_B T} \right) - \ln \left(2 \sinh \left(\frac{\hbar\omega}{2k_B T} \right) \right) \right] g(\omega) d\omega. \quad (2.29)$$

Finally, also the interatomic force constants F can be approximated based on the DOPS. To this end, the second moment of the DOPS has to be calculated [73]

$$F = \bar{m} \int_0^\infty g(\omega) \omega^2 d\omega, \quad (2.30)$$

where \bar{m} is the average mass of the atoms in the sample. The origin of this relation will be discussed again at the end of the following section, where the situation for a crystalline structure is discussed.

2.3.6 Dynamical Matrix

After this presentation of general properties of the DOPS, the discussion should be extended to well-ordered crystalline systems, which can be considered a limiting case of disordered crystals. It was already mentioned in the introduction that many phase-change materials resemble a rock-salt type atomic structure with a significant amount of chemical disorder, which is introduced by the random occupation of at least one lattice site (e.g. by vacancies and Ge or Sb atoms in the meta-stable phase of GeSb_2Te_4 and $\text{Ge}_2\text{Sb}_2\text{Te}_5$). A fully analytic and therefore very instructive calculation of the lattice vibrations in the sodium chloride structure can be found e.g. in the work by Kellermann [74]. The quantitative analysis of the density of phonon states in crystalline samples is most commonly performed by the construction of the dynamical matrix. From this, the eigenmodes of a crystalline solid can

be derived and can explain its vibrational properties. In the following, the general features of the dynamical matrix will be discussed. We will use this model later in order to compare it to the experimentally obtained DOPS.

An ideal lattice consists of atoms n , which are displaced by u_i^n from their equilibrium sites n_i , where i denotes the cartesian component x , y or z . The potential energy of the configuration in harmonic approximation is given by

$$\Phi = \frac{1}{2} \sum_{nn'} \sum_{ii'} \Phi_{ii'}^{nn'} u_i^n u_{i'}^{n'}. \quad (2.31)$$

The coefficients are defined as

$$\Phi_{ii'}^{nn'} = \frac{\partial^2 \Phi}{\partial u_i^n \partial u_{i'}^{n'}}. \quad (2.32)$$

Due to translational invariance, the potential for the relative displacement of n vs. n' is the same as that of n' vs. n , so that

$$\Phi_{ii'}^{nn'} = \Phi_{ii'}(\vec{n} - \vec{n}') \quad (2.33)$$

From this expression, we can write down the equations of motion for atom n ,

$$-\bar{m} \ddot{u}_i^n = \sum_{n'} \sum_{i'} \Phi_{ii'}(\vec{n} - \vec{n}') u_{i'}^{n'} \quad (2.34)$$

This set of equations conveniently describes the oscillations of the atoms along the cartesian axis, but it is usually energetically favorable for the atoms to oscillate along different directions, which are denoted $\epsilon_{i,\vec{k}}$, where the index \vec{k} is due to the definition of new coordinates $Q_{\vec{k}}$, by employing the lattice periodicity,

$$u_i^n = \frac{1}{\sqrt{Nm}} \sum_{\vec{k}} \epsilon_{i\vec{k}} Q_{\vec{k}} \exp(i\vec{k}\vec{n}) \quad (2.35)$$

$$-\ddot{Q}_k \epsilon_{i,k} = Q_k \sum_{i'} D_{ii'}(\vec{k}) \epsilon_{i',\vec{k}}, \quad (2.36)$$

which as compared to 2.34 does no longer depend on all other coordinates.

The new matrix, $D_{nn'}(\vec{k})$, is called the dynamical matrix, which is written as

$$D_{ii'}(\vec{k}) = \frac{1}{\bar{m}} \sum_n \Phi_{ii'}(\vec{n}) \exp(i\vec{k}\vec{n}) \quad (2.37)$$

The frequencies of the vibrations are now the eigenvalues of the dynamical matrix and the polarization vector $\epsilon_{i,\vec{k}}$ defines the displacement of the atom i due to the vibrational mode \vec{k} ,

$$\sum_{i'} D_{ii'}(\vec{k}) \epsilon_{i',\vec{k}} = \omega^2 \epsilon_{i,\vec{k}} \quad (2.38)$$

Now, the squared frequencies are the elements on the diagonal of $D_{ii'}(\vec{k})$ so that the second moment of the distribution of frequencies in the DOPS, 2.30, is nothing else than

$$F = \frac{\bar{m}}{3N} \sum_{\vec{k}} \text{tr} [D_{ii'}(\vec{k})]. \quad (2.39)$$

For a crystal of the rock-salt type, like meta-stable $\text{Ge}_2\text{Sb}_2\text{Te}_5$, it is now possible to refine the experimentally observed DOPS with a model for the dynamical matrix, using the analytical model by Kellermann [74]. Even without such detailed refinement, the measured DOPS allows calculating parameters of the atomic interaction and macroscopic properties at the same time. This is a great opportunity for PCMs, where the partial DOPS of Sb and Te can be measured by nuclear inelastic scattering.

2.4 Total Neutron Scattering

In the previous section, the scattering cross section was averaged over the momentum transfer and it was shown that it allows deriving the DOPS. The energy-average of the scattering cross section on the other hand contains information on the atomic structure of a solid. It can be shown that at higher incident neutron energies and for sufficiently large systems of N atoms, the total scattering is dominated by the elastic contribution (scales with N^2) and furthermore that the inelastic contribution (scales with N) can be removed to a very good approximation. The remaining elastic contribution to the scattering contains both, the Bragg reflections, as well as the diffuse scattering underneath the Bragg reflections, which originates from atomic disorder. Therefore, total scattering allows obtaining structural information on disordered materials, where Bragg reflections are absent. Short and long range correlations of atomic positions can be probed with total scattering. In the following, the treatment of such measurements of $d\sigma/d\Omega$ will be discussed.

2.4.1 Instrumentation

Total neutron scattering measurements are based on the counting of scattering events at fixed scattering angles without energy resolution. This, of course, increases the count rate as compared to the energy resolved TOF measurements presented earlier, since in TOF, the chopper necessarily absorbs some fraction of the incoming neutrons. For the total scattering measurements presented in this thesis, monochromatized neutrons with 0.498 \AA were employed. The monochromator was a Cu 220 surface, which creates an energy resolution of approximately $\Delta\lambda/\lambda \approx 10^{-2}$, which implies a coherence length L for neutron scattering of [75]

$$L = \frac{1}{2} \frac{\lambda^2}{\Delta\lambda}, \quad (2.40)$$

which equates to 25 \AA under the conditions given above. This is approximately the largest real space distance, over which correlations can be observed. It should not remain unmentioned that this value is smaller than the lattice constant c_h of the hexagonal phase of

GeSb₂Te₄, but since a PDF analysis and no Rietveld refinement is performed, this is not of further relevance.

2.4.2 The Static Approximation

In order to successfully evaluate the results from total scattering experiments, we have to investigate how the energy insensitive counting influences the structure factor $S(Q)$. The experimental conditions imply that we have to mathematically describe the transformation of the double differential cross section

$$\frac{d^2\sigma}{d\Omega dE} \rightarrow \frac{d\sigma}{d\Omega}. \quad (2.41)$$

The static approximation is the common theoretical framework for this transformation and its basic assumptions will be discussed in the following.

Mathematically, the transformation is performed by [62]

$$\left. \frac{d\sigma}{d\Omega} \right|_{\vec{Q}} = \int_{-\infty}^{E_0} \frac{d^2\sigma}{d\Omega dE} dE, \quad (2.42)$$

where E_0 denotes the maximum energy transfer for a specific value of \vec{Q} . In a real experiment, however, this integration is performed for constant scattering angles θ – not for constant \vec{Q} – so that scattering intensity for different momentum transfers is averaged. Furthermore, the pre-factor k_i/k_f has been neglected in the integrand and E_0 should be ∞ for the transformation to be correct. Neglecting the errors involved in these limitations is called the static approximation, which is commonly used in the analysis of total scattering data. Its name "static approximation" becomes obvious by investigating the van-Hove correlation function, giving the probability to find atoms at distance \vec{r} after time t ,

$$G(\vec{r}, t) = \frac{1}{(2\pi)^3} \int d\vec{Q} \exp(-i\vec{Q}\vec{r}) \int_{-\infty}^{\infty} d\omega \exp(i\omega t) S(\vec{Q}, \omega). \quad (2.43)$$

Here, $t = 0$ corresponds to a static snapshot of the atomic structure and is based on integrating $S(\vec{Q}, \omega)$ over ω without transformation – just as the integration over energy transfers in experiment.

The differential scattering cross section resulting from Eq. 2.42 is considered equal to the experimental result and in case of a monoatomic sample with N atoms equals

$$\frac{d\sigma}{d\Omega} = \underbrace{\left\langle \sum_{i,j \neq i}^N e^{i\vec{Q}\vec{R}_{ij}} \right\rangle}_{\text{distinct}} \langle b \rangle^2 + \underbrace{N \langle b^2 \rangle}_{\text{self}}, \quad (2.44)$$

with the first term on the right side resulting from scattering at different atoms (*distinct scattering*) at positions \vec{R}_{ij} and $\langle \dots \rangle$ over the exp-function denoting a time average over thermal vibrations and the second term resulting from so-called *self-scattering*. It is nicely seen that only the first term depends on \vec{Q} . It can also be seen that the second term does not correspond to the incoherent scattering due to its different scattering cross section.

2.4.3 Structure factor

The energy-integrated structure factor is usually extracted from scattering experiments and it is defined as

$$S(\vec{Q}) = \frac{1}{N} \left\langle \sum_{i,j}^N e^{i\vec{Q} \cdot \vec{R}_{ij}} \right\rangle. \quad (2.45)$$

The second term in Eq. 2.44, however, does not depend on atomic correlations and has to be subtracted from the experimental differential cross section. Furthermore, there is a difference between the first term in Eq. 2.44 and the common definition of the (static) structure factor, Eq. 2.45. By comparison, one obtains

$$\frac{1}{N} \frac{d\sigma}{d\Omega} = \underbrace{S(\vec{Q}) \langle b \rangle^2}_{\text{elastic}} + \underbrace{(\langle b^2 \rangle - \langle b \rangle^2)}_{\text{inelastic}}. \quad (2.46)$$

This differential scattering cross section contains the sum of the elastic and inelastic contributions. It is obvious that - in order to extract the structure factor $S(Q)$ from the experimental differential scattering cross section - the full inelastic scattering of the sample has to be subtracted. These different contributions to the experimental data are nicely depicted in Fig. 2.2. The influence of thermal vibrations on the structure factor, Eq. 2.45, will be discussed in Sec. 2.8.1.

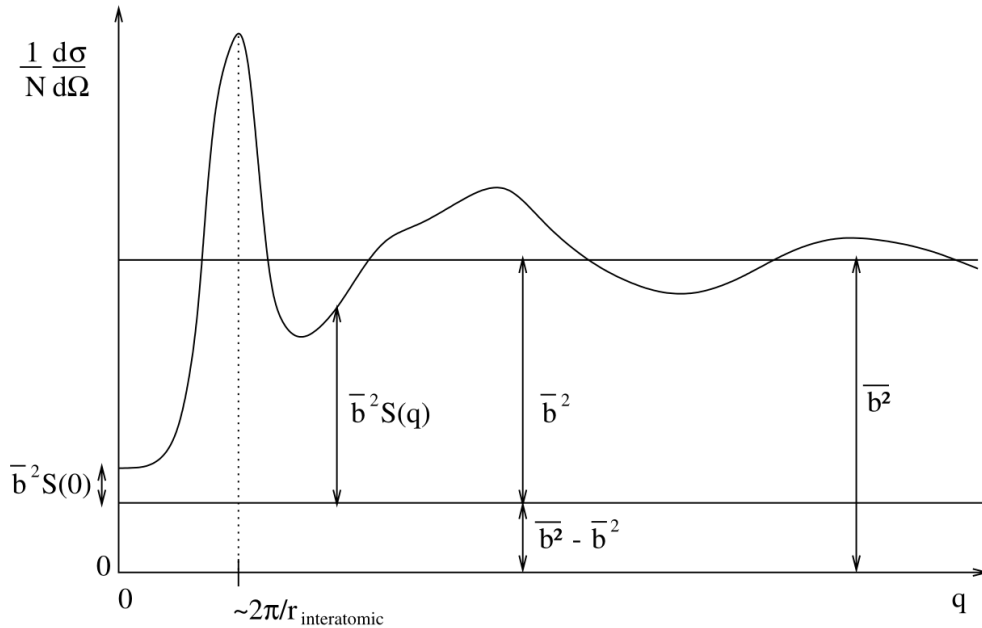


Figure 2.2: Contributions to the structure factor $S(\vec{Q})$ are shown. The flat background from inelastic scattering, $(\langle b^2 \rangle - \langle b \rangle^2)$, can be subtracted and the self-scattering remains on top of the inelastic contribution at $Q = 0$. Figure taken from [76].

2.4.4 Polyatomic samples

The previous theory was developed for monoatomic samples, but usually the local structure of polyatomic samples is of interest in materials research. In the following, it will be shown

that this formalism can be easily extended to systems containing n different elements, each with an atomic fraction c . Therefore, one defines an average scattering length

$$\langle \sigma \rangle = \sum_j^n c_j (\sigma_{c,j} + \sigma_{i,j}). \quad (2.47)$$

The resulting expression reads

$$\frac{d\sigma}{d\Omega} = NF(\vec{Q}) + N\langle \sigma \rangle, \quad (2.48)$$

where $F(\vec{Q})$ is called *total interference function*. From this quantity, the *total pair-correlation function* $G(r)$ can be obtained by means of Fourier transformation:

$$G(r) = \frac{1}{2\pi^2 r \rho_0} \int_0^\infty q F(q) \sin(qr) dq. \quad (2.49)$$

This function is composed of the partial pair-correlation functions $g_{ij}(r)$, weighted by the scattering lengths of the atomic species involved:

$$G(r) = \sum_{i,j}^n c_i c_j \langle b \rangle_i \langle b \rangle_j^* [g_{ij}(r) - 1]. \quad (2.50)$$

In practice, also related functions are frequently investigated. These are the *radial distribution function* (RDF), defined by

$$\text{RDF}(r) = 4\pi r^2 \rho_0 G(r), \quad (2.51)$$

where ρ_0 is the atomic number density, usually given in $\text{atoms} \cdot \text{\AA}^{-3}$. The radial distribution function oscillates around a curve given by $4\pi r^2 \rho_0$, i.e. around the average number of atoms in a sphere with radius r .

2.4.5 Data treatment

All total scattering experiments were performed at D4, ILL, Grenoble. The resulting data are the differential scattering cross section, Eq. 2.48, i.e. the scattering events under the angle of each detector element. The data treatment procedure will be described in the following in order to achieve maximum reproducibility. First, the number of scattering events is divided by the number of incoming neutrons. This compensates for time-dependent changes of the source intensity. The scattering angles between the incoming flux and each detector element with respect to the sample is calibrated with a measurement of pure Ni, whose diffraction pattern is corrected for a constant offset in the scattering angle 2θ . Also the exact wavelength of neutrons coming from the monochromator is obtained from this experiment and turned out to be 0.4976 \AA . The sample environment was varied with respect to the desired temperature conditions. For low temperature measurements at 10 K, the powdery specimen was filled in vanadium cans, whose inner diameter (4.88 mm) and outer diameter (5.08 mm) are known. Then, the stacking height of the powder and its weight are used to calculate the packing fraction from the well known density of amorphous PCMs (cf. Sec.

B.1). From the beam profile of 20 x 7.8 mm and the fact that the stacking height was slightly larger than 20 mm, the amount of scattering atoms in the neutron flux is well known. The samples for measurements under ambient conditions were prepared in the same way, except that quartz capillaries were employed instead of the vanadium sample containers. These had a outer diameter of 1.9 mm with a wall thickness of 0.01 mm and were filled with 40–45 mm of powdrous specimen. The packing fraction of the scratched powder after shaking the container was about 0.30(5).

A scan of the empty instrument and of the instrument with an empty vanadium can was performed for background subtraction. Subsequently, samples were measured and the resulting data were treated with the software CORRECT [77], which takes into account the quantity and geometry of the atoms in the container and the same geometric properties of the sample. It subtracts the scattering events of the container and transforms the resulting data to meaningful units of barns per sr per atom. Subsequently, the Placzek correction is employed to remove the angular dependence of the self-scattering term. Therefore, the data are fitted by a polynomial in powers of \vec{Q}^2 , which is subsequently subtracted so that the final data oscillate symmetrically around 0 (giving the $F(Q)$ of Eq. 2.48). The data are then Fourier transformed and scaled with $\langle b \rangle^2$ according to Eq. 2.48. Number densities ρ_0 can be found in Sec. B.1 for the as-deposited amorphous phases. The resulting $G(r)$ and the derived RDF(r) will be discussed in detail in Chpt. 3.

2.5 General X-ray scattering

Due to the significantly higher availability of intense sources of X-rays than neutron sources, more experiments and -series can be performed based on x-ray scattering. There are significant differences between x-ray and neutron scattering, but the fundamental concepts are the same, so that this section continues from the discussion presented in Chpt. 2.1. It aims at highlighting the differences and similarities between both techniques.

The scattering length for X-rays is far more complex than that of neutrons and this makes a PDF analysis more complicated. The fundamental reason is that X-rays are scattered dominantly by the electronic charge in the sample and the distribution of charge has features on the same length scale as the interatomic distances, so that those photons, which probe the atomic structure are necessarily modified by the electronic structure as well. The absence of purely s-wave scattering induces an additional momentum dependence of the scattering length. The scattering length for X-rays furthermore depends both on the momentum transfer Q and on the incoming X-ray energy E_0 . Although, this complexifies data treatment, the understanding of these dependencies is so well progressed, that it opens new opportunities: The scattering lengths of different atoms depend differently on the incident energy, which enables a technique called "anomalous scattering". There, specific energies E_0 are selected for the incoming x-rays, where the scattering of a specific element is significantly increased.

2.5.1 Scattering length for x-rays

Let us first write the scattering length for X-ray scattering in the same framework as the scattering length of neutron scattering was treated [76],

$$b(Q, E_0) = r_e [f(Q) + f'(E_0) + if''(E_0)], \quad (2.52)$$

where the last two terms are referred to as anomalous scattering, which originates from the inner electrons, so that these terms do not have a significant Q -dependence. $r_e = 2.818$ fm is the classical radius of the electron. The most significant contribution originates from $f(Q)$, which goes from the atomic number, Z , at $Q = 0$ to 0 as $Q \rightarrow \infty$. It is given by the electronic charge distribution ρ around an atom,

$$f(\vec{Q}) = \int_{\text{atomic site}} \rho(\vec{r}) \exp(-i\vec{Q}\vec{r}) d^3r. \quad (2.53)$$

The anomalous scattering coefficients are negligible if the x-ray energy is clearly above all absorption edges. If this is not the case, the so-called dispersion corrections, f' and f'' can become significant. For Cu K- α radiation used on Sb and Te, f'' can be as high as 5-6, while it is negligible for Ge. f' is slightly negative (-1) for all elements (cf. [78], p. 22). A quantum mechanical treatment has been elaborated, but it is beyond the scope of this document. Here it suffices to say that the real contribution from the charge of static electrons, $f(\vec{Q})$ suffices to describe the scattering, whereas extra dispersion effects come in strongly, when vibrations of the core electrons are excited.

In order to refer to the general scattering theory, the scattering potential of elastic x-ray scattering $k_i = k_f$ is simply $U(\vec{Q}) = f(\vec{Q})$ in Eq. 2.5. In X-ray scattering, there are two basic contributions to the scattered intensity: Elastic scattering and Compton scattering, of which the latter is inelastic and since the scattered photons have a different wavelength, there is no coherence and no interference [78], p. 12.

2.5.2 Interference conditions

Due to the physics behind Compton scattering, at $\theta = 0$ there is no Compton scattering, only coherent scattering with the atomic scattering factor equal to the number of electrons in the sample plus anomalous contributions. At large angles, there is only Compton scattering left, since the atomic structure factor converges to zero. It is therefore important to know, which of these mechanism dominates the total scattered intensity. For a sample, which consists of N atoms, the Compton intensity increases with N , while the coherent scattering increases with N^2 due to constructive interference conditions ([78], p. 20).

The ratio of scattered X-ray intensity I over incident X-ray intensity I_0 is given by (cf. [78] p. 103f)

$$\frac{I(Q)}{I_0} = r_e^2 \underbrace{\frac{1 + \cos^2 2\theta}{2}}_{\text{Polarization factor}} \underbrace{\frac{1}{16\pi r \sin^2 \theta \cos \theta}}_{\text{Lorentz factor}} \lambda^3 F_{hkl}^2(Q) \frac{n}{V_e^2} D(Q) dV, \quad (2.54)$$

where r is the distance of the detector from the scattering object, r_e is the classical radius of the electron, $F_{hkl}(Q)$ is the structure factor, n is the multiplicity factor for the planes (hkl), V_e is the volume of the unit cell, D is the temperature- or Debye-factor, dV is the volume of the diffracting powder. The scattered intensity can be described equally by its dependence on the momentum transfer Q or on the scattering angle θ , given by Eq. 2.6. Eq. 2.54 nicely enables a summary of the following discussion: The scattered intensity in X-ray scattering contains a yet unknown influence of thermal vibrations $D(Q)$, which reduces the scattered intensity. In addition, the diffraction pattern $I(Q)$ is strongly influenced by the structure factor $F_{hkl}(Q)$. These two factors will be discussed in the following.

Thermal vibrations around the equilibrium position are described by

$$D = \exp\left(-\frac{16\pi^2 \sin^2 \theta \sigma^2}{\lambda^2} \frac{1}{3}\right). \quad (2.55)$$

σ^2 is the root mean square of the distance of the atoms from their equilibrium lattice sites. It depends strongly on temperature, since the vibrations are thermally excited. Usually, the temperature dependence is given in the Debye Model as:

$$\sigma^2 = \frac{9h^2}{4\pi^2 mk\theta_D} \frac{T}{\theta_D} \left[\frac{1}{4} \frac{\theta_D}{T} + \frac{T}{\theta_D} \int_0^{\theta_D/T} \frac{y}{\exp(y-1)} dy \right], \quad (2.56)$$

where $y = \hbar\omega/k_B T$. The residual displacement σ^2 at $T = 0$ refers to atomic zero point motion alone. However, the framework holds equally well for additional static atomic displacements σ_0^2 , which are isotropic and do not displace the time- and space-averaged atomic positions. X-ray scattering is always a time- and space-average, so that we can wonder how static atomic displacements will influence the displacement parameter. If these displacements are of a random direction, then they can be described in the same framework as thermal vibrations, since after averaging over space, the average atomic position does not differ from its lattice position. Therefore, we will observe in crystalline PCMs displacement parameters σ^2 significantly larger at $T = 0$ K than those predicted by Eq. 2.56.

2.6 The structure factor

The structure factor of x-ray and neutron scattering $F_{hkl}^2(Q)$ first occurred in Eq. 2.54. It contains the information on the structure of the investigated specimen. The following discussion will be limited to the case of powder diffraction, which holds for any isotropic distribution of crystal orientations and therefore can be applied to crystalline PCMs as well. Since the PCMs are as-deposited amorphous, they do not contain any preferred orientation after deposition. The crystallization of the films starts from the surface of the films, which has a significant roughness and therefore no preferred orientation is observed even in crystalline PCMs. Furthermore, the crystal grains (< 40 nm) are much smaller than the film thickness (> 500 nm) in all studies presented here. The structure factor (for x-rays) of a crystal with N atoms is given by (cf. [78] p. 104)

$$F_{hkl} = \sum_{i=1}^N f_i(hkl) \exp[-2\pi i (hx_i + ky_i + lz_i)], \quad (2.57)$$

where x_i , y_i and z_i are the cartesian coordinates of atom i and f_i its atomic form factor.

The constructive interference of x-ray photons creates a maximum of intensity at a specific scattering angle θ . These maxima of order n can occur at the angles given by the Bragg equation,

$$2d \sin \theta = n\lambda. \quad (2.58)$$

The intensity of these reflections is then obtained from the structure factor F_{hkl} .

The angular width $\Delta 2\theta$ of these maxima depends on several properties of the solid. These contributions to $\Delta 2\theta$ will be discussed, starting from the most common, i.e. the reflex broadening $\Delta 2\theta_{gs}$ due to the finite size of the crystallites (grain size) [78], from which the X-rays are scattered coherently. Another source of broadening is stress induced strain in the atomic structure, $\Delta 2\theta_{strain}$ [79]. Usually, also an instrumental broadening $\Delta 2\theta_{instr}$ has to be taken into account, but already $\Delta 2\theta_{gs} \gg \Delta 2\theta_{instr}$. Both remaining terms sum up to the total reflex width,

$$\Delta 2\theta = \sqrt{\Delta 2\theta_{gs}^2 + \Delta 2\theta_{strain}^2}. \quad (2.59)$$

Both contributions will be discussed in sequence. A large crystal of N lattice planes will create a reflection with a sharp angular distribution of intensity

$$I(\phi) = \left| \frac{1}{N^2} \frac{\sin N\phi}{\sin \phi} \right|^2. \quad (2.60)$$

The width of the peak created by this function is expressed by the Scherrer equation, which therefore gives a lower limit for the reflex broadening in the case of ideal constructive interference. This can be used to obtain an approximate value for the average size of the scattering (unstrained) crystals in a polycrystalline sample. The Scherrer equation for a sample with an average crystallite size L reads

$$\Delta 2\theta_{gs} = \frac{\lambda}{L \cos \theta_0}, \quad (2.61)$$

where the reflections are centered at θ_0 . In order to obtain the total width of a reflex, $\Delta 2\theta$, usually Voigt peak functions are fitted to the profile. They are a superposition of a Lorentzian contribution due to finite crystal size and a Gaussian contribution due to microstrain. Then, $\Delta 2\theta$ denotes the full angular width at half maximum of these profile functions. Additional broadening is caused by microstrain in the sample, caused e.g. by stress due to the density change upon crystallization. This contribution is described by

$$\Delta 2\theta_{strain} = 4e \tan \theta_0, \quad (2.62)$$

where the parameter e is related to the average strain in the sample $\langle \epsilon \rangle$ in case of a Gaussian distribution of strain on a lateral average via $\langle \epsilon \rangle = \sqrt{2/\pi} e$ [80]. Both contributions to the reflex broadening are conveniently described by the formula of Caglioti [81], which is based on the different θ -dependence of the strain and size-broadening. Then, the total broadening is parametrized by U , V , W , X and Y as

$$\sigma_G^2 = U \cdot \tan^2(\theta_0) + V \cdot \tan(\theta_0) + W \quad (2.63)$$

for the Gaussian contribution and

$$\sigma_L = X \cdot \tan(\theta_0) + Y \cos^{-1}(\theta_0). \quad (2.64)$$

A detailed analysis of the structure factors of the phase-change material GeSb_2Te_4 and the reflex broadening in particular will be presented in Chpt. 3.

Reports on both contributions of reflex broadening can be found in the literature. The strain induced broadening after crystallization has been discussed by Rimini et al. [82] by TEM and XRD experiments. In particular, they compare the grain size of crystallized phase-change material observed by applying the Scherrer formula and by direct study using TEM. They find that the crystallites are significantly larger than predicted by the Scherrer formula - due to the strain, which allows the Bragg condition to be fulfilled only for a fraction of the bended crystalline grain. However, they investigate only the meta-stable cubic phase and the question remains how the strain evolves upon further annealing. Without taking into account strain-induced broadening, the grain-size was investigated as a function of the annealing temperature [83]. It was found that the grain size within the meta-stable cubic phase is increased continuously. The result of including both effects over the full transformation range of GeSb_2Te_4 from the meta-stable cubic to the stable rhombohedral phase will be discussed in Sec. 3.8.

2.7 X-ray Absorption Spectroscopy

X-ray Absorption Spectroscopy (XAS) is complimentary to scattering techniques in the field of microstructure analysis, since it is readily capable of determining partial atomic correlation functions in polyatomic samples. It does not rely on translational symmetry and can therefore resolve atomic correlations in amorphous structures as well. This study will focus on the analysis of the extended absorption fine structure (EXAFS) only, which is based on the absorption spectrum above the absorption edge. The EXAFS contains information about the partial atomic pair distribution functions and can thereby resolve the short range order around a specific element. This makes it a valuable tool, which can be employed to both, amorphous and crystalline phase-change materials. Due to the inherent necessity to tune the energy in the X-ray regime around the absorption edges (between 10 and 32 keV for the K-edges of Ge, Sb and Te), the experiments have to be performed at synchrotron beam lines. Since an energy resolution of some eV is usually sufficient, the monochromatized radiation from a bending magnet is used for EXAFS measurements.

The absorption features around the K-edge were measured in this work, but also L or M edges are frequently used for heavier elements. Several textbooks have already been published about this technique, some of which will be cited in the following [84, 63]. Quite generally, XAS refers to the precise ¹ measurement of the absorption μ as a function of energy as defined by Lambert Beer's law,

$$\frac{I(E)}{I_0(E)} = \exp[-\mu(E) \cdot d]. \quad (2.65)$$

I and I_0 are the incoming and transmitted intensities, respectively, and d is the thickness of the sample. When the energy is increased above a specific absorption edge of one of the elements inside the sample, the absorption increases significantly. This increase is attributed to the fact that now electrons from the K, L or M shell (hence the name K, L or M-edge) can be promoted from a localized core orbital to an unoccupied electronic state. An example is shown in Fig. 2.6 (a) for the K edge of Ge. The short region in k-space from the absorption edge to $1/\text{\AA}$ above the edge is usually called XANES (X-ray Absorption Near Edge Structure), whereas the region more than 50 eV [84, 63] above the absorption edge is attributed to EXAFS. Therefore, XANES features contain information on the density of electron states some eV above the Fermi level. This density of states differs from that of the unexposed sample due to the presence of a core hole in the 1s state and has to be compared to calculated electronic structures. The electronic states in this energy regime are usually delocalized, so that their calculation requires large atomic models. These models usually contain more information on the atomic structure, than the XANES features can provide. Therefore, this method is usually used for a fingerprint-type analysis. The so-called EXAFS states on the other hand, which are at least 50 eV above the absorption edge, scatter more strongly at the surrounding atoms. Single scattering dominates here and the information contained mostly regards atomic distances and the total electronic charge found at the scattering atom.

¹The adjective precise is added here, since the oscillatory changes in μ are usually at least a factor 100 lower than the height of the absorption edge.

In the following, the experimental setup will be described first, followed by a derivation of the most important formula in the theory of EXAFS.

2.7.1 Experimental Setup

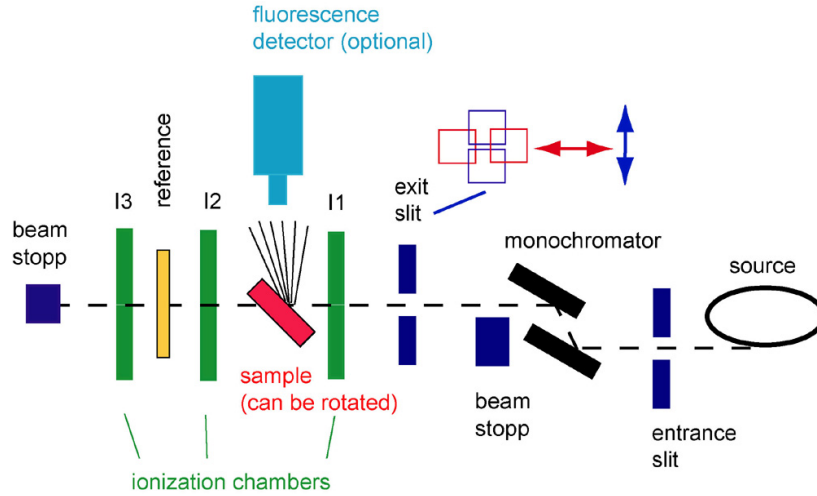


Figure 2.3: Schematics of the EXAFS setup at beamline C, Hasylab. Ionization chambers (green) measure the intensity of the radiation as a function of energy in front of and behind the sample (red). Details on the setup can be found in the text. Taken from [85]

All measurements have been performed at beamline C [86] of DORIS III at HASYLAB (Hamburger Synchrotronstrahlungslabor). A schematic drawing of the beamline setup is depicted in Fig. 2.3. The white beam of x-rays coming from the bending magnet enters from the right, passes a collimator slit and is reflected by a double-crystal monochromator crystal. This double-crystal monochromator uses a double Si(111) or Si(311) crystal set, allowing for a total energy range of 2.3 to 43.4 keV behind the exit slit [86]. It is installed at 19.3 m from the bending magnet source. The construction of this advanced monochromator is described in detail in [87]. The second crystal is usually detuned (i.e. rotated out of reflection geometry) in order to exclude higher order Bragg reflections with a different energy from the beam. This is possible, because higher-order reflections have narrower angular widths and thus loose coherent scattering conditions at lower angles of detuning. However, a loss of usually 50% in intensity is inevitable [88, 84].

The beam is again collimated by a rotational slit, which is located 28.8 m from the source. As controlled by this slit, the beam usually has a cross section of 5×8 mm. The intensity of the monochromatic, collimated beam is then measured in ionization chamber 1, which is usually filled - like all three ionization chambers - with an inert gas like nitrogen, argon or krypton. The beam propagates through the sample and is partly absorbed according to Eq. 2.65. This remaining intensity is measured by ionization chamber 2 and passes a reference sample of the pure element under investigation and its intensity is measured again in ionization chamber 3. The edge energy of that sample is then used as a reference for the

Table 2.2: Filling of ionization chambers with inert gas for EXAFS experiments on specific edges

Element	K-edge energy	Ioniz. chamb. 1	Ioniz. chamb. 2
Ge	11103 eV	0.13 bar Ar	0.88 bar Ar
Sb	30491 eV	0.17 bar Kr	approx. 1 bar Kr
Sn	29200 eV	0.15 bar Kr	0.99 bar Kr
Se	12658 eV	0.20 bar Ar	0.72 bar Kr

calibration of the x-ray energy setting of the monochromator.

The type and pressure of the gas in the ionization chambers during these experiments was calculated by using the software *XAFSmass* [89]. Usually, the pressures are chosen in order to absorb 10% of the beam intensity in the first ionization chamber and about 50% of the intensity in the second chamber. The rest of the beam (about 90%) is subsequently absorbed in chamber 3. The filling of the chambers for each measured edge is presented in Tab. 2.2. The average error on the filling amounts to 0.01 bar. Data concerning the edge energy were taken from the Elam database [90].

2.7.2 EXAFS Sample preparation

All samples except In_3SbTe_2 were prepared by sputter depositing a layer of approximately $1.5\,\mu\text{m}$. The exact conditions of the sputter system are described elsewhere [91] and the films were obtained after a deposition time of 4 h at 20 W. This layer was subsequently scratched to powder using another silica substrate. During this mechanical scratching process, usually some silica was unintentionally admixed to the sample, but EXAFS is only sensitive to the direct environment of a specific element, so that the silica will not influence the data. The powder was in some cases annealed at elevated temperature under a constant flow of Ar to prepare the desired phase. Subsequently, the powder was admixed with cellulose and processed to pellets of 13 mm diameter for use in the sample holder [86]. Usually, about 20 to 100 mg of phase change material and 100 mg of cellulose are necessary for one pellet. The ideal mass can be determined by maximizing the edge step $\Delta\mu d$, while simultaneously taking care that the total absorption μd remains below approximately three. Only then, the count rates in the first and second ionization chambers produce a similar count rate, which minimizes the experimental error on μd .

Samples of amorphous In_3SbTe_2 had to be prepared in a different manner than other phase-change compounds, since the scratched powder turned out to be crystalline after preparing the pellet for EXAFS measurements. The crystallinity of the material was tested only after the preparation of the pellet so that it might have crystallized already during the long sputter deposition process. This suggests a significant thickness dependence of In_3SbTe_2 films, which was indeed observed from a strongly decreasing crystallization tem-

perature with increasing film thickness [92]. 37 nm thick layers of In_3SbTe_2 crystallized at 535 K, whereas 285 nm thick films crystallized already at 483 K. Amorphous layers of about 150 nm thickness were sputter deposited on Al foil of $10\mu\text{m}$ thickness. About 140 of these foils were subsequently stacked to obtain $\Delta\mu \cdot d \approx 1$ and measured in transmission geometry. No Bragg reflections of Al were observed in the relevant EXAFS energy spectrum.

During the EXAFS experiments the spectra have been measured two or three times for every sample (approx. 40 min each). If no significant differences could be observed, these measurements were averaged to improve the counting statistics.

2.7.3 Theory of EXAFS

In Fig. 2.6 (a)&(b), oscillations can be seen above the absorption edge. They are caused by a quantum mechanical effect, which will be explained in the following.

In this heuristic derivation, a central atom absorbs the X-ray photons, whose energy is transferred to photoelectrons, which are then scattered at the neighboring atoms and form spherical waves. This mechanism is depicted in Fig. 2.4. For simplification, scattering processes are treated only to first order in the derivation presented here. Additionally, scattering of the spherical waves of the photoelectrons at other neighboring atoms - often termed multiple scattering - is not taken into account here for simplicity. Some articles were published about EXAFS formula for multiple scattering [93] and the resulting formalism will be included later in this derivation.

The origin of the oscillations can be described as follows: As a function of the energy, constructive or destructive interference conditions of the outgoing and backscattered electron-wave are observed at the absorbing atom. These interference conditions modify the probability to find the electron at the absorbing site and thereby also modify the transition probability from the core level. This concept will be written down in a mathematical form in the following.

The EXAFS structure function is usually defined by the absorption μ from Lambert Beer's law as

$$\chi(E) = \frac{\mu(E) - \mu_{\text{spline}}(E)}{\mu_{\text{spline}}(E)} \quad (2.66)$$

Here, $\mu_{\text{spline}}(E)$ is a smooth background function representing the absorption of an isolated atom, which will be discussed in more detail in Sec. 2.7.4. Transforming $\chi(E)$ to $\chi(k)$ in order to be able to describe the wave character of the photoelectron, one usually applies the relation

$$k = \sqrt{\frac{2m_e(E - E_0)}{\hbar^2}} \quad (2.67)$$

For plotting, one usually compensates for the fact that the oscillations are damped at higher wave vectors by plotting $k^n \cdot \chi(k)$, where n usually equals 3.

Fermi's Golden rule describes absorption quantum mechanically [34] and is therefore

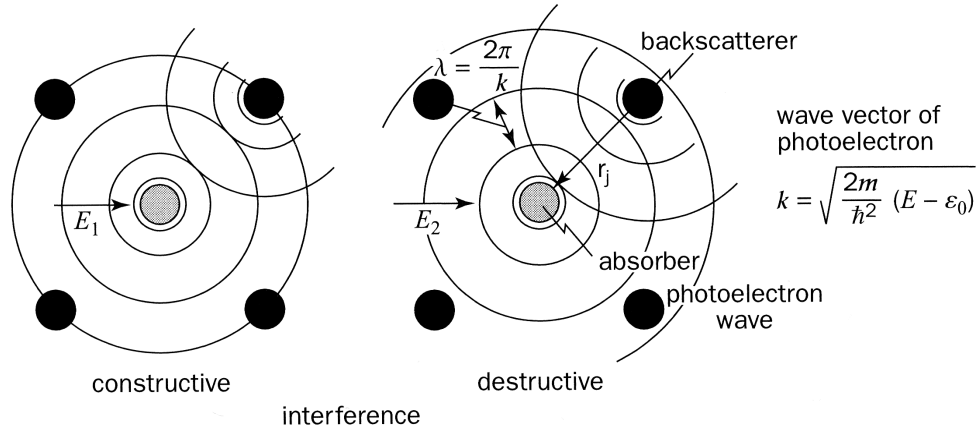


Figure 2.4: Origin of the EXAFS: Incoming, continuous waves of different energies E_1 and E_2 are absorbed and generate a free electron with different wavelengths λ . The photoelectron is scattered back from adjacent atoms and interferes with the generation of a subsequent electron, which leads to oscillations in the absorption as a function of energy E_i . Taken from [63].

the starting point for deriving $\mu(E)$ based on atomic properties:

$$R_{i \rightarrow j} = \frac{2\pi}{\hbar} \sum_j |\langle j | \hat{H}_{\text{int}} | i \rangle|^2 \delta(E_j - E_i - \hbar\omega) \quad (2.68)$$

$R_{i \rightarrow j}$ is the transition rate from initial state $|i\rangle$ to final state $|j\rangle$, where the initial state consists of a photon and an atomic structure with an electronic system in its ground state, whereas the final state describes the same atomic structure with an ionized atom and a photo electron with $E_{\text{kin}} > 0$. The absorption of the photon is included in the equation by the term $-\hbar\omega$. Therefore, only the electronic system has to be described by those two states. $|i\rangle$ is a 1s-like state of the electron localized at the atom and $|j\rangle$ is the state of a spherical electron wave. E_i and E_j are the respective eigenenergies and \hat{H}_{int} (int. stands for interaction) mediates the transition between the states. In the end, the transition rate $R_{i \rightarrow j}$ is obtained. How is this transition rate related to the absorption μ ? Therefore, one has to take the x-ray beam as a continuous wave described by a vector potential \vec{A} , like

$$\vec{A}(\vec{x}, t) = 2 \vec{A}_0 \cos(\vec{k}\vec{x} - \omega t) \quad (2.69)$$

$$= \vec{A}_0 \left[\underbrace{\exp(+i(\vec{k}\vec{x} - \omega t))}_{\text{incoming wave}} + \underbrace{\exp(-i(\vec{k}\vec{x} - \omega t))}_{\text{outgoing wave}} \right] \quad (2.70)$$

For the process of the photoeffect, only the incoming wave has to be taken into account. The energy density $u = dE/dV$ can be directly evaluated using the common definition of \vec{E} and \vec{B} in terms of \vec{A} reads

$$u = \frac{dE}{dV} = \frac{1}{2} \left(\frac{\vec{E}^2}{8\pi} + \frac{\vec{B}^2}{8\pi} \right) = \frac{1}{2\pi} \frac{\omega^2}{c^2} |\vec{A}_0|^2. \quad (2.71)$$

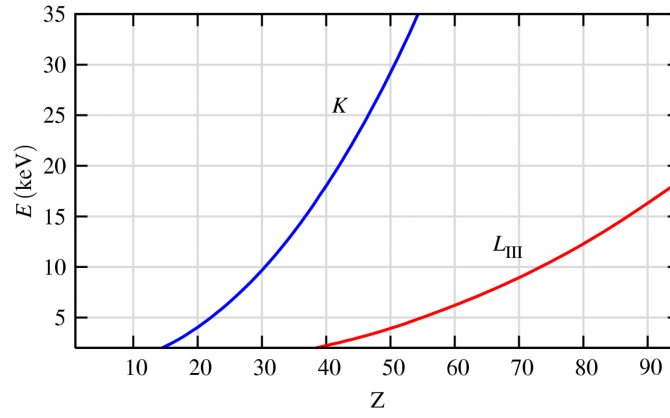


Figure 2.5: This figure shows the energies of K- and L_{III} absorption edges as a function of atomic number Z . For heavier elements, also the L_{III}-edge can be used to observe oscillations. Taken from [94].

For a continuous wave (i.e. continuous in time), the energy density u is proportional to the intensity I of the beam. Therefore, the differential equation of absorption can be slightly modified

$$\frac{d}{dx}I(x) = -\mu I(x) \quad (2.72)$$

$$\rightarrow \frac{d}{dx}u(x) = -\mu u(x) \quad (2.73)$$

$$\Rightarrow \mu = -\frac{1}{u} \frac{d}{dx}u(x) \quad (2.74)$$

The energy absorbed from the beam per unit time (the beam propagates with the speed of light c) is given by the expression

$$\frac{d}{dx}u(x) = -n_{\text{at}} \hbar\omega \frac{R_{i \rightarrow j}}{c} \quad (2.75)$$

n_{at} is the number of absorbing atoms per unit volume and $R_{i \rightarrow j}$ the transition rate given by Fermis Golden Rule. Finally, by inserting 2.68 in 2.75 and 2.75 in 2.74, we obtain an expression for the absorption:

$$\mu = 4\pi^2 \frac{N_{\text{at}}}{|\vec{A}_0|^2} \frac{c}{\omega} \sum_j |\langle j | \hat{H}_{\text{int}} | i \rangle|^2 \delta(E_j - E_i - \hbar\omega) \quad (2.76)$$

A more detailed evaluation of Eq. 2.76 can be found in [84], but is too complex for the framework of this thesis. Therefore, a different derivation will be presented here, which lacks some mathematical rigor but gives the crucial insight to the technique. The sum in Eq. 2.76 runs over all possible final states.

The following simpler expression will be used at the beginning of this derivation:

$$\mu \propto |\langle j | \hat{H}_{\text{int}} | i \rangle|^2 \quad (2.77)$$

The final state $|j\rangle$ is essentially the photo-electron, leaving the atom as a spherical wave $|j_0\rangle$ and returning as a scattered wave $|\delta j\rangle$. The ansatz $|j\rangle = |j_0\rangle + |\delta j\rangle$ will be the basis of

an expansion in terms of small effects by the scattered wave:

$$\mu(E) \propto |\langle j_0 | \hat{H}_{\text{int}} | i \rangle|^2 \cdot \left[1 + \frac{\langle j_0 | \hat{H}_{\text{int}} | i \rangle \langle j_0 | \hat{H}_{\text{int}} | i \rangle^*}{|\langle j_0 | \hat{H}_{\text{int}} | i \rangle|^2} + \text{compl. conj.} \right] \quad (2.78)$$

Comparing this expression with Eq. 2.66, one can see that $\mu_0 = |\langle j_0 | \hat{H}_{\text{int}} | i \rangle|^2$ corresponds to the bare atom, while the interaction with neighboring atoms is included by:

$$\chi(E) \propto \langle j_0 | \hat{H}_{\text{int}} | i \rangle. \quad (2.79)$$

This expression can be written more clearly for the purpose of understanding the principle. Evaluating the interaction operator from a classical radiation field is maybe the most difficult task. The important part of that operator is $\vec{A} \cdot \vec{p}$, which is proportional to $\exp(i\vec{k} \cdot \vec{r})$ (for a detailed derivation cf. [34], p. 340f). The initial state can – due to its extension of just a_0/Z – be roughly approximated by a delta function centered around the atomic core. This results in a very simple expression for the EXAFS:

$$\chi(k) \propto \int d^3r \delta(r) e^{ikr} \psi_{\delta j}(r) = \psi_{\delta j}(r=0). \quad (2.80)$$

We can see that the EXAFS is proportional to the probability of finding the scattered photoelectron at the absorbing atom. This is nicely compatible with what has been described earlier by Fig. 2.4.

The above expression can be developed further by simple arguments. The outgoing photoelectron can be described as a spherical wave

$$\psi(k, r) = \frac{e^{ikr}}{kr}. \quad (2.81)$$

During traveling a distance R , a phase shift of kR occurs and the amplitude decreases by a factor of $(kR)^{-1}$. When the photoelectron reaches the nearest neighbor, it enters the electric field of that atom and is scattered again. Thereby, the phase is shifted by $\delta(k)$ and the amplitude of the wave varies by a factor of $2kf(k)$. These two functions $\delta(k)$ and $f(k)$ strongly depend upon the nuclear charge Z of the neighboring atom. This is essentially why different neighboring elements can be distinguished in EXAFS. Upon multiplying all factors, including an additional phase shift and reduction of amplitude for the way back to the absorbing atom, the result is:

$$\chi(k) = \psi_{\delta j}(r=0, k) = \frac{e^{ikR}}{kR} \left[2kf(k)e^{i\delta(k)} \right] \frac{e^{ikR}}{kR} + \text{compl. conj.} \quad (2.82)$$

$$= \frac{f(k)}{kR^2} \sin(2kR + \delta(k)) \quad (2.83)$$

This expression considers only one absorbing atom and one scattering atom. As there are usually N_i (coordination number of shell i) atoms in a shell, the EXAFS has to be multiplied by this factor. Measurements are not performed at zero Kelvin but slightly above, so the remaining vibrational energy and some displacements will occur. They are accounted for by introducing an additional factor, where σ^2 is the mean-square-displacement of the atoms

of the shell at distance R . As it is not just a single shell that contributes, but also higher shells, i.e. next-nearest neighbors, the EXAFS simply has to be summed over all shells in the system:

$$\chi(k) = \sum_i \frac{N_i f_i(k) e^{-2k^2 \sigma_i^2}}{k R_i^2} \sin(2k R_i + \delta_i(k)) \quad (2.84)$$

If there are different kinds of atoms in each shell, as is sometimes the case, then an additional sum has to be introduced. There is one more correction that still has to be incorporated: It was always assumed that the photoelectron scatters elastically at the neighbors and the finite lifetime of the core-hole has not been taken into account. It could also happen that the photoelectron scatters at other electrons or phonons. Thus, it is reasonable to use a spherical wave, which is damped by a factor $\exp(-r/\lambda(k))$ instead of 2.81. Additional damping effects are taken into account by a pre factor S_0^2 . The resulting and final EXAFS equation is:

$$\chi(k) = S_0^2 \sum_j \frac{N_j F_j(k)}{2k R_j^2} e^{-2k^2 \sigma_j^2} e^{(-2R_j/\lambda(k))} \sin(2k R_j + \pi - \delta(k)) \quad (2.85)$$

The factor $1/R^2$ reduces the EXAFS strongly for shells that are far away from the absorbing atom. This is why EXAFS can only resolve the short range order in condensed matter. Usually, the EXAFS can be evaluated up to a distance of about 6 Å. The functions $f(k)$ and $\delta(k)$ can be calculated using first-principles methods. In the framework of this thesis, *FEFF* [95] has been used to determine those functions. Also analytical models for these functions exist, but they are not accurate enough to allow for a quantitative evaluation. If the two functions are known, the scattering paths in Eq. 2.85 can be calculated and some of the parameters in the formula can be obtained from a fit of $\chi(k)$ to the experimental data.

It can be seen that oscillations with different frequencies contribute to the EXAFS. This is why we will continue with a Fourier transform of this equation. Fourier transforming the EXAFS $\chi(k)$ gives additional insight into the experiment, which is necessary for an understanding of the plots shown later in section 4. The Fourier transform is defined as

$$\mathcal{F}(\chi(k)) = \tilde{\chi}(r) = \frac{1}{\sqrt{2\pi}} \int_0^\infty \chi(k) e^{ikr} dk \quad (2.86)$$

The principle of superposition also holds for Fourier transforms, $\mathcal{F}(f+ag) = \mathcal{F}(f) + a\mathcal{F}(g)$, i.e. to transform the EXAFS in Eq. 2.85 it is sufficient to transform the contribution of a simplified single shell j :

$$\chi_j(k) = \exp\left(\frac{(k - k_{j,0})^2}{\Delta k_j}\right) \sin(2k R_j + \pi - \delta(k)) \quad (2.87)$$

$$= \Im \left[\exp\left(\left(\frac{k - k_{j,0}}{\Delta k_j}\right)^2 + i(\delta_0 + k \cdot \delta_1)\right) \exp(2ik R_j) \right] \quad (2.88)$$

The envelope of this oscillation is centered around k_0 and its width amounts to Δk . A linear behavior $\delta(k) = \pi - \delta_0 - k \cdot \delta_1$ is assumed for the phase shift. Generally, the coefficient δ_1 will be negative [96]. The Fourier transform of Eq. 2.87 is [84]

$$\tilde{\chi}(r) = \frac{\Delta k}{2i} \exp\left(i\delta_0 + ik_0\delta_1 + 2ik_0r - \frac{\Delta k^2}{4}(2r - 2R - \delta_1)^2\right) \quad (2.89)$$

As this is an imaginary function, usually its magnitude is plotted in real space. The expression then reads:

$$|\tilde{\chi}(r)| = \frac{\Delta k}{2} \exp\left(-\Delta k^2 \left(r - R - \frac{\delta_1}{2}\right)^2\right) \quad (2.90)$$

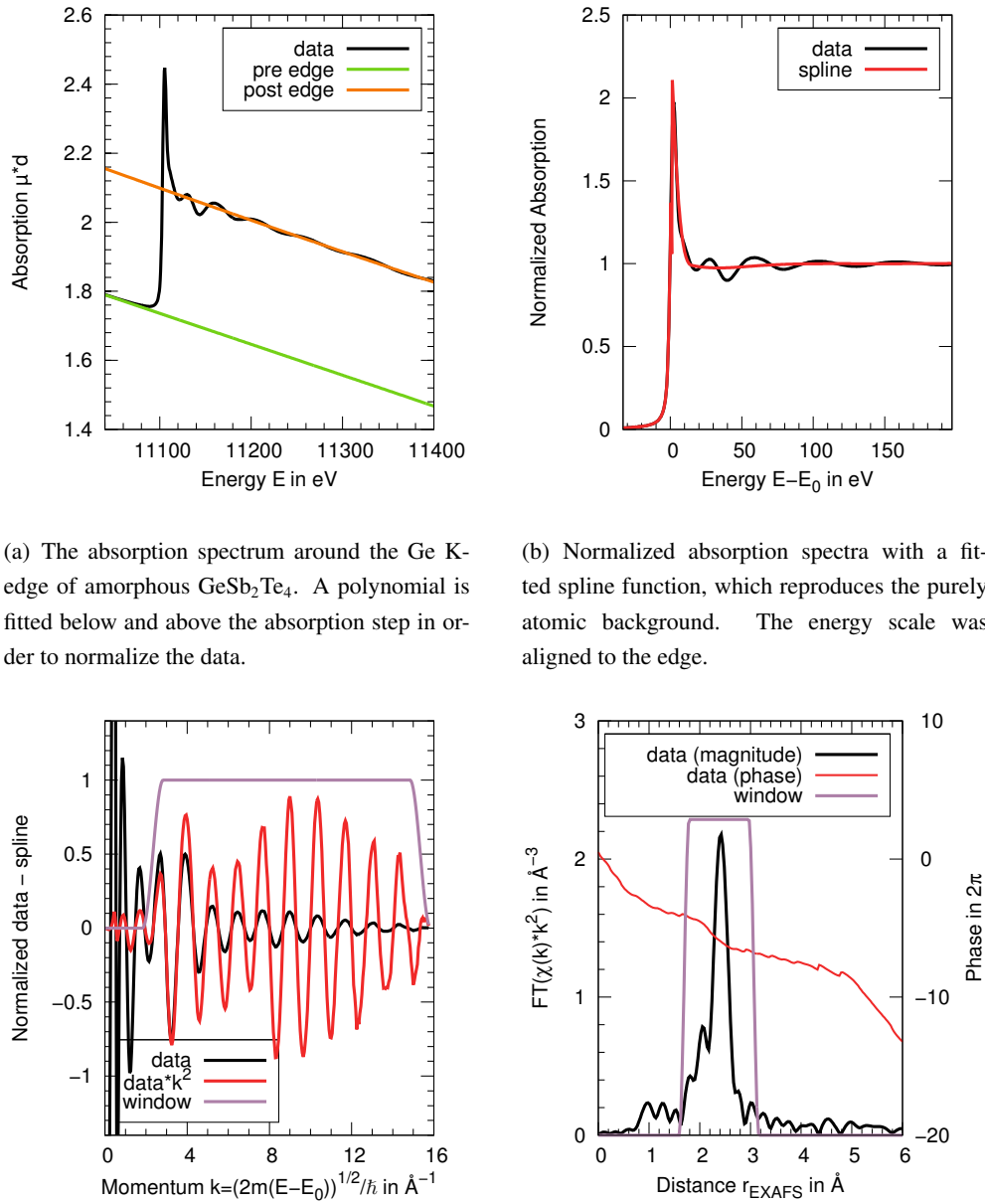
It is obviously a Gaussian function, which is centered around $R + \delta_1/2$ and as $\delta_1 \leq 0$ it is shifted to lower radii. This shift is a general attribute of real-space distributions obtained by EXAFS and has to be considered during data treatment.

2.7.4 Data treatment

The EXAFS, $\chi(k)$, can be extracted from a measurement of $\mu(E) \cdot d$. Subsequently, the EXAFS is fitted based on a path expansion as shown in Eq. 2.85. The method behind these two steps will be explained in the following in order to allow for a reproducible data analysis.

Raw data of $d \cdot \mu(E)$ can be seen in Fig. 2.6 (a), black curve. Polynomials are fitted to the pre-edge region below the absorption energy (green curve) E_0 and to the post-edge region (orange curve). These functions are necessary for data normalization, defining the pre-edge polynomial μ_{pre} as zero and the post-edge polynomial μ_{post} as one. These polynomials cannot follow the oscillations and therefore, the normalized EXAFS oscillates closely around one (cf. Fig. 2.6, right). Therefore, a spline function μ_{spline} is fitted to the data, according to an algorithm published by Newville [97]. The spline contains $(2/\pi) \Delta k R_{\text{bkg}}$ data points, where Δk is the interval, in which oscillations are clearly visible in k-space. The parameter R_{bkg} depends on the shortest possible bond length in the sample, since it filters out all low-frequency oscillations. As a rule of thumb, R_{bkg} should be not larger than half the distance to the next-nearest neighbor in order to avoid interferences with the physically relevant oscillations. Applying Eq. 2.66 and 2.67 gives the correct experimental $\chi(k)$, which will be extensively investigated in this thesis.

In order to extract physical quantities from the EXAFS, a path expansion has to be applied, which is based on Eq. 2.85. This procedure is discussed in the following for a binary sample, where data sets of the two K-edges are assumed to exist. It can be easily extended to a ternary system. First, each data set is refined independently using all structural information, which are already available. If nothing is known, a good start is to assume heteropolar bonds only with bond lengths given by the sum of the covalent radii of the atoms involved. This refinement has to start from the most dominant contribution, i.e. from the first coordination shell, which can be separated from higher coordination shells in r -space so that refinements are usually performed on this Fourier transform of the EXAFS. The additional parameters in Eq. 2.85 are obtained from FEFF calculations, which introduce an energy shift ΔE between experiment and calculation. This is an additional fitting parameter. During the refinement, parameters like atomic distance and the nature of the backscattering atoms are modified until the best possible refinement is obtained. If the refinement has a low residual (roughly below 0.05), the next coordination shell is refined. If no correspondence between refinement and data can be obtained, a second scattering path has to be added to



(a) The absorption spectrum around the Ge K-edge of amorphous GeSb_2Te_4 . A polynomial is fitted below and above the absorption step in order to normalize the data.

(b) Normalized absorption spectra with a fitted spline function, which reproduces the purely atomic background. The energy scale was aligned to the edge.

(c) The EXAFS function $\chi(k)$ is plotted: It is the difference between the normalized absorption and the spline function as a function of the momentum of the photoelectron. Commonly $\chi(k) \cdot k^2$ (red curve) is plotted.

(d) Fourier transform of $\chi(k) \cdot k^2$. Its imaginary result is given as magnitude and phase. The magnitude allows deriving atomic distances, taking into account the phase shift, which reduces r_{EXAFS} as compared to r . The phase function contains information on the nuclear charge of the backscattering atoms.

Figure 2.6: Treatment of X-ray absorption spectra around the Ge K-edge of amorphous GeSb_2Te_4 . The extraction of the EXAFS $\chi(k)$ is shown in Fig. (c) and its Fourier transform in Fig. (d).

the same coordination shell. Finally, a good (and stable ²) fit of the full data set should

²Stable means that all fitting parameters are at least in a local minimum of the residual landscape.

be obtained. The same procedure is applied to the data set of the other edge and in the ideal case (which occurs quite frequently), the fitting results are in good agreement for the various data sets. For a system containing atoms A and B, this means that the parameters for A-B scattering paths obtained from the absorption data of element A are equally obtained from the data of element B. Then, both data sets can be refined simultaneously by using the same variables for both data sets. If the fit remains stable, then the refinement is finished if the final residual is below approximately 0.02. If the result is not satisfactory at this stage, additional contributions from homopolar A-A or B-B bonds can be tested, but if this does not significantly improve the refinement, most likely the model was not correct or the sample was not homogeneous. The method described above has been employed for the refinement of all EXAFS data throughout this thesis. The results and conclusions from the local atomic arrangement of PCMs will be presented in Chpts. 3 and 4.

2.8 Atomic displacements probed by XRD and EXAFS

Thermal vibrations of atoms are inherently present in matter and can be observed in EXAFS and XRD data, where they reduce the amplitude of oscillations and intensity of reflections, respectively. Indeed, large atomic displacements have been observed in the crystalline PCM $\text{Ge}_2\text{Sb}_2\text{Te}_5$ [98] at room temperature. At this temperature, it is not possible to verify if the displacements are of thermal or of static nature. In a perfect crystalline solid, thermal vibrations can be described by coupled equations of oscillatory motion around the ideal lattice sites (cf. Sec. 2.3.6). If, however, the center of the oscillation is shifted with respect to the ideal lattice site, we call this static disorder. Large static displacements would be mainly due to substitutional disorder, whereas large amplitudes of thermal vibration would indicate soft phonon modes. Whereas the soft phonon modes could indicate a low thermal conductivity [98], the substitutional disorder might be responsible for the recently observed disorder induced localization [21]. In this section 2.8, two essential questions shall be answered: **How can we use X-ray absorption spectroscopy and/or scattering techniques to distinguish thermal from static disorder?** and it should be further discussed, **Which thermal vibrations influence the results from X-ray absorption spectroscopy and/or which influence scattering techniques?**

When thermal vibrations are considered, the time scales of the different experiments should be mentioned as well. It is well known that atomic vibrations in phase change materials have less than about 30 meV [73] which corresponds to a frequency of about 7 THz, i.e. one oscillation period takes roughly 100 fs. Since scattering occurs instantaneously, the diffraction pattern consists of a sum of snapshots, which are then averaged over both, time and space. In EXAFS spectroscopy, the time dependence of the interference pattern originates from the lifetime of the core hole, which is of the order of a fs for K edges [84], p. 11. Thus, EXAFS equally probes the instantaneous local structure. The space and time average is then imposed by a large absorption volume and a large number of subsequent absorption events. In conclusion, both methods, scattering and absorption spectroscopy are unable to

distinguish static from thermal disorder from a single measurement. However, the temperature dependence of the atomic displacements can resolve those two contributions, since at very low temperature, amplitudes of thermal vibration are very low (zero point motion, cf. Eq. 2.56) and can be approximated by a model of harmonic oscillators. Therefore, **temperature dependent measurements of the displacement parameter can distinguish static from thermal atomic displacements.**

2.8.1 Atomic displacements in XRD

In XRD, the structure factor defines the observed diffraction pattern. Thermally induced displacements of the i -th atom $\Delta \vec{r}_i$ lead to a modified scattering amplitude $F(\vec{Q})$ with the modified scattering amplitude given by

$$F_{\text{thermal}}(\vec{Q}) = \sum_i f_i \exp(-i\vec{Q}(\vec{r}_i + \Delta \vec{r}_i)), \quad (2.91)$$

where $\vec{Q} = \vec{k}_f - \vec{k}_i$ is the momentum transfer and \vec{r}_i is the average position of the atom i , which is displaced at a specific point in time of the snapshot by $\Delta \vec{r}_i$. Now the Debye Waller factor shall be derived and factorized from the unperturbed scattering amplitude,

$$F(\vec{Q}) = \sum_i f_i \exp(-i\vec{Q}\vec{r}_i). \quad (2.92)$$

For small displacements, $(\Delta \vec{r}_i \ll |\vec{r}_i - \vec{r}_j|) \forall j \neq i$, the additional term can be developed as follows (it is assumed here, that this expansion indeed converges):

$$\exp(-i\vec{Q}\Delta \vec{r}_i) = 1 - i\vec{Q}\Delta \vec{r}_i - \frac{1}{2}(\vec{Q}\Delta \vec{r}_i)^2 + \dots \quad (2.93)$$

Taking the time-average of this expression over the timescale of an experiment $\tau \approx \text{minutes}$ and assuming purely thermal vibrations (no static contribution!) yields

$$\langle \vec{Q}\Delta \vec{r}_i \rangle_{\tau, \text{exp}} = \vec{Q} \langle \Delta \vec{r}_i \rangle_{\tau, \text{exp}} = 0. \quad (2.94)$$

This, however, is not the case for the second order term, which can be written with the simplifying assumption of isotropic displacements:

$$F_{\text{thermal}}(\vec{Q}) = \sum_i f_i \cdot \exp(-i\vec{Q}\vec{r}_i) \cdot \left(1 - \frac{\vec{Q}^2}{6} \langle \Delta \vec{r}_i^2 \rangle \right). \quad (2.95)$$

Due to the scattering at different sets of lattice planes, XRD is sensitive to the anisotropy of the atomic displacements. A precise discussion of anisotropic displacements requires an individual description of every observed reflex. While this is possible, the resulting formula could not be easily compared for XRD and EXAFS.

Long-wavelength phonon modes induce atomic deviations from the lattice sites, which hardly affect the local interatomic distances, observed in EXAFS. On the other hand, they contribute significantly to the displacement parameter obtained from XRD analysis, where

the number of probed lattice sites is limited by the coherence length of the scattering X-rays, which in the case of PCMs is larger than the grain size. **The displacement parameter obtained from XRD is therefore sensitive to both, short wavelength optic and long wavelength acoustic phonons and measures the root mean square of the atomic displacement from the high-symmetry lattice site.** It should be mentioned further, that the condition in Eq. 2.94 is not necessarily legitimate in the case of static displacements without further justification. This justification comes from the fact that the observed static displacements are considered to be randomly distributed, so that for the space average over all atoms,

$$\sum_i \Delta \vec{r}_i = 0 \quad (2.96)$$

holds.

2.8.2 Atomic displacements in EXAFS

The EXAFS displacement parameter differs somewhat from the displacement parameter observed in scattering experiments. In EXAFS, the distribution of atomic distances is measured, while the absorbing atom is always located exactly at $\vec{r} = 0$. By refining a specific peak in EXAFS, the variance of this atomic distance σ^2 can be obtained, assuming a Gaussian distribution of bond lengths centered around r_0 [99],

$$\rho(r) = (2\pi\sigma^2)^{-1/2} \exp\left(-\frac{(r-r_0)^2}{2\sigma^2}\right). \quad (2.97)$$

This expression can be included in the general EXAFS equation [100],

$$\chi(k) = \frac{NS_0^2}{k} \cdot \Im \left[F(k) e^{i\delta_1} \int_0^\infty \frac{\rho(r)}{r^2} \exp\left(-\frac{2r}{\lambda(k)}\right) e^{2ikr} dr \right] \quad (2.98)$$

and after a lengthy solution of this integral, one obtains the commonly employed EXAFS Eq. 2.85:

$$\chi(k) = \frac{NS_0^2}{kr_0^2} \cdot F(k) \exp\left(-\frac{2r}{\lambda(k)}\right) e^{-2k^2\sigma^2} \sin(2kr_0 + \delta_1). \quad (2.99)$$

Now, it is still necessary to understand how σ^2 is obtained from the variance of atomic distances for a given set of atomic positions. An example for the first coordination shell in an arbitrary system is depicted in Fig. 2.7. While the ideal lattice positions with an arbitrary reference point are \vec{u}_0 and \vec{u}_1 , the atoms are displaced to the new position $\vec{u}_{0,i} = \vec{u}_0 + \Delta\vec{u}_0$ and $\Delta\vec{u}_{1,j}$. Therefore, the atomic distance $r_0 = |\vec{u}_0 - \vec{u}_1|$ is modified by oscillations of the absorber by its displacement direction projected on the normed atomic distance $(\vec{u}_{0,i} - \vec{u}_0) \cdot (\vec{u}_1 - \vec{u}_0)/r_0$ and by those of the scattering atom $(\vec{u}_{1,j} - \vec{u}_1) \cdot (\vec{u}_1 - \vec{u}_0)/r_0$. Therefore, the displacement parameter amounts to:

$$\sigma_{\text{EXAFS}}^2 = \langle u^2 \rangle_\tau = \left\langle \left[(\vec{u}_{0,i} - \vec{u}_0 + \vec{u}_{1,j} - \vec{u}_1) \cdot (\vec{u}_1 - \vec{u}_0)/r_0 \right]^2 \right\rangle_\tau, \quad (2.100)$$

which can be inspected more easily by letting $\vec{u}_0 = 0$:

$$\sigma_{\text{EXAFS}}^2 = \left\langle \left[(\vec{u}_{0,i} + \vec{u}_{1,j} - \vec{u}_1) \cdot \vec{u}_1/r_0 \right]^2 \right\rangle_\tau. \quad (2.101)$$

The EXAFS displacement parameter contains only the displacement along the direction of the atomic distance and is therefore referred to as mean squared relative displacement (MSRD) parameter. This reduces the contribution of transverse optic modes and due to the local probe also the influence of long wavelength modes.

2.8.3 Conclusions on the difference of displacement parameters

Two differences can be observed between the two displacement parameters: The first (1) concerns the contribution of anisotropic thermal and static displacements, the second (2) concerns the weighting of thermal vibrational modes with different wave lengths.

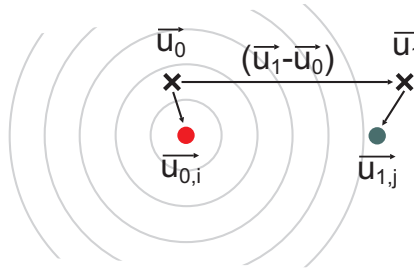


Figure 2.7: In EXAFS, the absorbing atom (red) at position $\vec{u}_{0,i}$ emits a photo-electron, which is scattered at a neighboring atom (green) at position $\vec{u}_{1,j}$. Therefore, the bond length observed in EXAFS corresponds to the distance between the centers of static and thermal displacements along the direction of the bond. This leads to the fact, that the EXAFS displacement parameter is not as sensitive to transverse phonon modes as the XRD displacement parameter, which averages displacements isotropically over longer distances.

(1) Anisotropic displacement distributions can be quantified in XRD by comparing the reduction of reflex intensities for different reflex families with different $\Delta\vec{k}/|\Delta\vec{k}|$. In EXAFS, however, only the mean square displacement in the direction of the interatomic distance $(\vec{u}_1 - \vec{u}_0)$ is taken into account. The resulting number σ_{EXAFS}^2 contains both, an average shift of the absorbing and of the scattering atom from the central position and static and thermal displacements are equally taken into account. For different atomic distances, i.e. for higher coordination shells, the direction of the interatomic distance will be different, and a different displacement parameter could occur. In the case of the meta-stable crystalline phase of GeTe-Sb₂Te₃ alloys, the EXAFS displacement parameter for the first coordination shell ({100}-directions) might underestimate the displacement amplitude in the {110}- and {111}-directions, which can be seen from the second and third coordination shells, respectively.

(2) Thermal vibrations of short, longitudinal wavelengths (i.e. $\lambda \approx a/2$) contribute equally to the XRD and EXAFS displacement parameters, but modes of long wavelengths and transversal modes in general contribute less to the EXAFS displacement parameter, because they leave the local atomic distances mostly unchanged. The different weighting can be immediately quantified from the equations given above by defining various snapshots of

vibrational modes and calculating σ^2 . However, this is very demanding and involves comparing the unknown coherence length of the employed x-rays (or neutrons) with the phonon wavelength.

In conclusion, displacement parameters of different samples should be compared between measurements with the same technique. If such data are not available, a larger displacement parameter is expected for XRD measurements, where also acoustic modes with longer wavelength are taken into account. In the case of this thesis, such displacement parameters will be compared for amorphous and crystalline PCMs in Sec. 4.2.3.

CHAPTER 3

Disorder in crystalline GeSb_2Te_4 : Modifications along the MIT

3.1 Disorder in solids

The fundamental switching mechanism in phase-change materials can be described as a transition between different levels of atomic disorder, with one state having translational symmetry (i.e. a crystalline state) and the other phase showing no sharp diffraction spots. The latter phase therefore does not comply with the definition of a crystal by the IUCr and translational periodicity must be absent. This section is included to provide a general framework for the description of these disordered materials, where long range order (LRO) is absent. In contrast to the extensive treatment of perfect crystals in courses on solid state physics, disordered matter is not so often discussed. This is partly due to the lack of a basic concept as fundamental as for example Bloch's theorem in the crystal. This section is therefore included to define the term disorder, which – by itself – is rather vague. In this sense, disorder refers not to mere chaos but rather to a specific deficiency of order [101]. Several types of disorder will be introduced and defined in the following, because they will simplify the description of disorder later.

Let us begin with the so-called *topological disorder* [30], p. 49. It is the type of disorder usually encountered in amorphous glasses and liquids. As introduced earlier, let us define disorder based on the deficiency of order. In a single crystal both, the coordination number and the chemical nature of the bonded atoms are well defined. In a topologically disordered network of bonds, these two conditions are replaced by statistical distributions. This also means that not every amorphous material is equally topologically disordered. Some compounds retain the well-defined bond length and the chemical nature of the bonds in the crystalline phase. This definition also implies that amorphous as well as crystalline PCMs contain topological disorder – the amorphous materials due to the existence of homopo-

lar bonds – the crystalline materials due to the local atomic displacements, which create a broad distribution of bond lengths. This shows that we need more precise terms to describe disorder.

There are three general types of continuous-random models: The continuous random network (CRN), which applies for covalent glasses, random close packing for metallic glasses and the random coil model for polymeric organic glasses. PCMs should fit most conveniently into the first category (CRN), since the bonding of the amorphous phase is mostly covalent due to the general applicability of the 8-N rule, cf. Sec. 4, for the coordination number and due to the rather well-defined bond lengths (as compared to the crystalline phase). However, Ge atoms in some PCMs are polyvalent with one contribution in a tetrahedral geometry being in good agreement with the covalent coordination numbers and the sum of covalent radii, while the other, distorted octahedral geometry, is less well-defined with a higher coordination number and larger bond lengths [102]. Therefore, the random close packing model can hold only approximately for amorphous PCMs.

In the crystalline phase of all PCMs, translational periodicity exists. In contrast to e.g. NaCl, some of the lattice sites are randomly filled with atoms of different chemical species. The meta-stable cubic phase of most GST compounds consists of Te atoms on one site and a random distribution of Ge and Sb atoms on the other site. This lack of order is the so-called *substitutional disorder* ([101], p. 6). We can equally say that the lattice sites form a regular lattice, whereas each element in the solid does not. It is worth mentioning that substitutional disorder does not include a chemical substitution with an arbitrary atomic species.

Quite frequently, this substitutional disorder induces static atomic displacements of various amplitudes. Here, the laterally random variable is the displacement (-amplitude and -direction) of each atom from its presumed site in a regular lattice. The same holds for a snapshot of the atomic positions in a single crystal at high temperature. The atomic displacements due to thermal vibrations or static disorder are therefore best described in the framework of displacement disorder. Although both types, thermal and static displacements lead to displacement disorder, they are quite different (cf. [78] p. 153): Thermal displacements fall in the category of imperfections of the first type, where distances fluctuate, but the mean position of the atom remains unchanged so that the long range order is preserved. Here, the fluctuation of distances to the first, second and n-th neighbor have the same amplitude, i.e. fluctuations are not additive. Imperfections of the second type reduce the long-range order. This occurs for example if the filling of lattice sites occurs in a random fashion so that the fluctuations of nearest neighbors is increased to the next nearest neighbor, and the distance fluctuations increase with distance and thereby destroy long-range order at large distances. This will become important later in the discussion of EXAFS data, which were obtained at 10 K, where thermal fluctuations are almost absent.

The degree of substitutional disorder should be put on a clear mathematical framework, which would allow comparing different atomic structures with each other. First, it is important to distinguish the different ranges of substitutional order: If only nearest neighbors are concerned, the majority of atoms on a perfect lattice might be ordered, but due to entropy

reasons, defects have to occur at finite temperatures. These rare fluctuations can cancel out the substitutional order on the long range. Therefore, short range order (SRO) and long range order (LRO) will be distinguished in the following.

SRO can be defined starting from a solid of N atoms of type A and B with $N_A + N_B = N$. Let N_{AB} define the number of nearest neighbors, i.e. bonds between type A and B. The coordination of every atom is z so that the probability for a randomly chosen bond to be of type A-B is given by

$$p_{AB} = \frac{N_{AB}}{0.5 \cdot zN}. \quad (3.1)$$

If each site would be occupied randomly, i.e. the lowest amount of order would exist, $p_{AB} = 2c_A c_B$. It is therefore straightforward to define an order parameter for short-range order as

$$\Gamma_{AB} = \frac{1}{2} p_{AB} - c_A c_B. \quad (3.2)$$

This concept can be easily extended to include LRO as well by taking $\Gamma_{AB}(r)$ and $p_{AB}(r)$ as a function of r . The existence of long range order is then given by

$$\Gamma_\infty = \lim_{r \rightarrow \infty} \Gamma_{AB}(r) \quad (3.3)$$

Experiments, however, are always limited to some maximum of length scale, up to which they can probe the distribution of atoms. This description of long range order is therefore not directly accessible in experiments. By investigating the radial dependence of $\Gamma(r)$, even the intermediate range order (IRO) can be defined. Usually, the radial dependence of this order parameter is given by the functional behavior

$$\Gamma(r) \propto r^{-n} \exp(-r/\zeta), \quad (3.4)$$

with n depending on the dimensionality of the solid (approx. 1 for 3D) and ζ is called the correlation length scale.

The next distinct type of disorder is the *topological disorder* ([101], p.36). Non-crystalline, amorphous, vitreous or glassy solids are categorized as topologically disordered: They appear homogeneous and isotropic on the macroscopic scale. The formalism to describe this disorder is the subject of research of statistical geometry, which is a field too large to present here. It should be noted, however, that the most common tools to investigate and to describe these systems theoretically are atomic radial distribution functions, bond angle distribution functions and ring statistics. For diatomic or more complex systems, these functions can be split into partial and total distributions functions. Most experimental techniques like total scattering and EXAFS are limited to the determination of atomic radial distribution functions.

3.2 Motivation

The atomic structure is the basis of all macroscopic properties of a solid – however, some properties like electronic and thermal conductivity are complex to predict even when the

atomic structure is known. In this sense, GeSb_2Te_4 is a very interesting material since it shows a continuous transition from insulating to metallic behavior (cf. Fig. 3.1) without a significant change in the local atomic configuration [21]: The transition takes place without a structural phase transition in the hexagonal phase. Therefore, it is interesting to study the subtle structural modifications, which lead to this change in conductivity. In the stable hexagonal phase, all Ge- and Sb-atoms are in a distorted octahedral 6-fold coordination with 3 shorter and 3 longer bonds, while Te atoms exist in two configurations: Some are octahedrally 6-fold coordinated with 3 short and 3 long bonds and some are located next to vacancy layers, leaving them 3-fold coordinated [49], [48]. This atomic arrangement was observed after long thermal treatment at high temperature. After thermal treatment at lower temperatures and/or shorter times, some substitutional disorder might remain even though the unit cell has already the hexagonal structure of the perfect crystal. Depending on these annealing conditions, either the insulating (lower annealing temperatures) or the metallic (higher annealing temperatures) phases are obtained. Thus, Sec. 3 will answer the question: **Which modifications of atomic disorder can be observed from the symmetry of the unit cell and from the interatomic distances to accompany the metal-insulator transition in GeSb_2Te_4 ?** This chapter is structured as follows: First, previous investigations from literature will be summarized for comparison. Experimental details of the XRD measurements performed for this thesis follow, and their results are finally discussed for annealing trends in the meta-stable cubic (Chpt. 3.5) and stable hexagonal phases (Chpt. 3.6). Finally, changes in the local atomic ordering are investigated based on EXAFS and neutron PDF analysis (Chpts. 3.11 and 3.12) and all results are concluded in Chpt. 3.13.

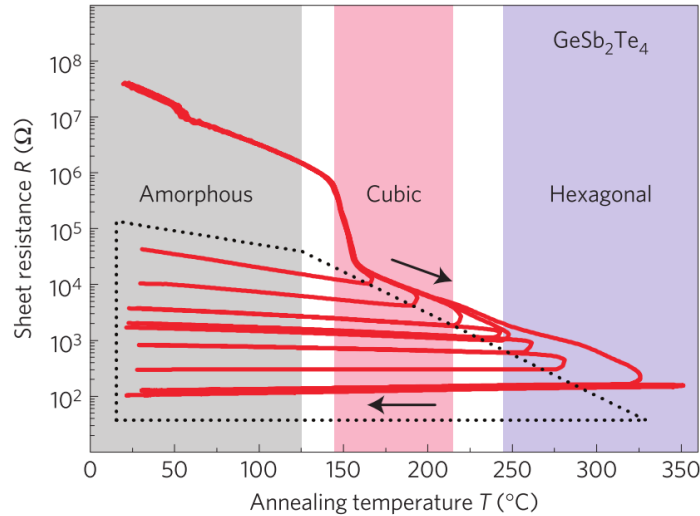


Figure 3.1: The sheet resistance of a 100 nm thin film of GeSb_2Te_4 is reduced irreversibly by increasing the annealing temperature, finally leading to a change from insulating behavior after annealing at about 450 K to metallic behavior after annealing at 550 K. Since also insulating samples with hexagonal lattice structure have been obtained, the electronic transition takes place within the hexagonal phase. Taken from [21].

3.3 Previous investigations

At 418 K, the as-deposited amorphous phase of GeSb_2Te_4 crystallizes in the meta-stable rock-salt phase (cf. Chpt. 7) with a significant amount of substitutional disorder. At even higher temperatures of about 548 K, the structure begins to transform to the hexagonal phase. In the following, previously published results on the atomic structure and its disorder will be discussed.

The atomic ordering in the rock-salt phase of GeSb_2Te_4 is reported to follow the space group $\text{Fm}\bar{3}\text{m}$ (No. 225) with a lattice constant of $a = 6.0430(9) \text{ \AA}$ [48]. The refinement of reflex intensities further revealed the occupation of the atomic basis, where two distinct lattice sites were necessary to refine the diffraction patterns. At room temperature, one site is fully occupied with Te ($B = 1.4 \text{ \AA}^2$), while the other is occupied to 25% with Ge and 50% with Sb ($B = 3.2 \text{ \AA}^2$), whereas the remaining 25% of the sites are vacant. This atomic structure can be considered a stacking of layers in $\text{abcabc} \dots$ sequence (cf. Fig. 3.2). In the typical fashion of a rock-salt lattice, the intensity of the 111 reflection I_{111} is proportional to the $|f_A - f_B|^2$, i.e. the difference of the average atomic form factors of the two sublattices A and B. The intensity of the 200 reflex on the other hand is proportional to the squared sum of these form factors $|f_A + f_B|^2$. Atomic form factors contain a real and an imaginary contribution, cf. Sec. 2.5.1. Since the real contribution of an atomic form factor dominates the imaginary contribution, the 111 reflex is usually much smaller than the 200 reflex and proves the existence of some ordering of the chemical species to particular lattice sites – because for a fully random sorting of atoms, the 111 reflex is absent.

The hexagonal phase of GeSb_2Te_4 was reported to comply with the space group $\text{R}\bar{3}$ with lattice parameters $a_h = 4.21 \text{ \AA}$ and $c_h = 40.6 \text{ \AA}$ [48], cf. Fig. 3.2. Now, in addition to the layers of Te, also "layers" of vacancies are formed, which induce a step in the stacking sequence, by which the cubic symmetry is destroyed. In total, 3 blocks of 7 layers each comprise a unit cell of GeSb_2Te_4 . In literature, also the phase-change material $\text{Ge}_2\text{Sb}_2\text{Te}_5$ was investigated and it behaves equally with regard to structural [49, 104] and electronic [21] properties, except that transition temperatures are slightly higher. Therefore, it seems reasonable to assume in the following that the atomic reordering processes in GeSb_2Te_4 and $\text{Ge}_2\text{Sb}_2\text{Te}_5$ are of the same nature. Due to the fact that the number of atoms in the formula unit of $\text{Ge}_2\text{Sb}_2\text{Te}_5$ is a multiple of three, the lattice parameters of $\text{Ge}_2\text{Sb}_2\text{Te}_5$ are $a_h = 4.22(1) \text{ \AA}$ and $c_h = 17.18(4) \text{ \AA}$ [105]. The lattice constant c is significantly smaller, because one block of 9 layers is sufficient to create a periodic stacking, including the step at the vacancy layer. As compared to these well known properties, there is no consensus on the occupation of lattice sites. This might be due to difficulties to distinguish Sb from Te, but also originate from the different states of substitutional ordering in the investigated samples. To describe the occupation of lattice sites, it suffices to consider only one block. In literature, there is still uncertainty whether the Ge and Sb atoms each occupy their own layers. The formation of single elemental layers is favored energetically, as obtained from DFT calculations on GeSb_2Te_4 and GeSb_4Te_7 [106]. On the other hand, the mixing of ele-

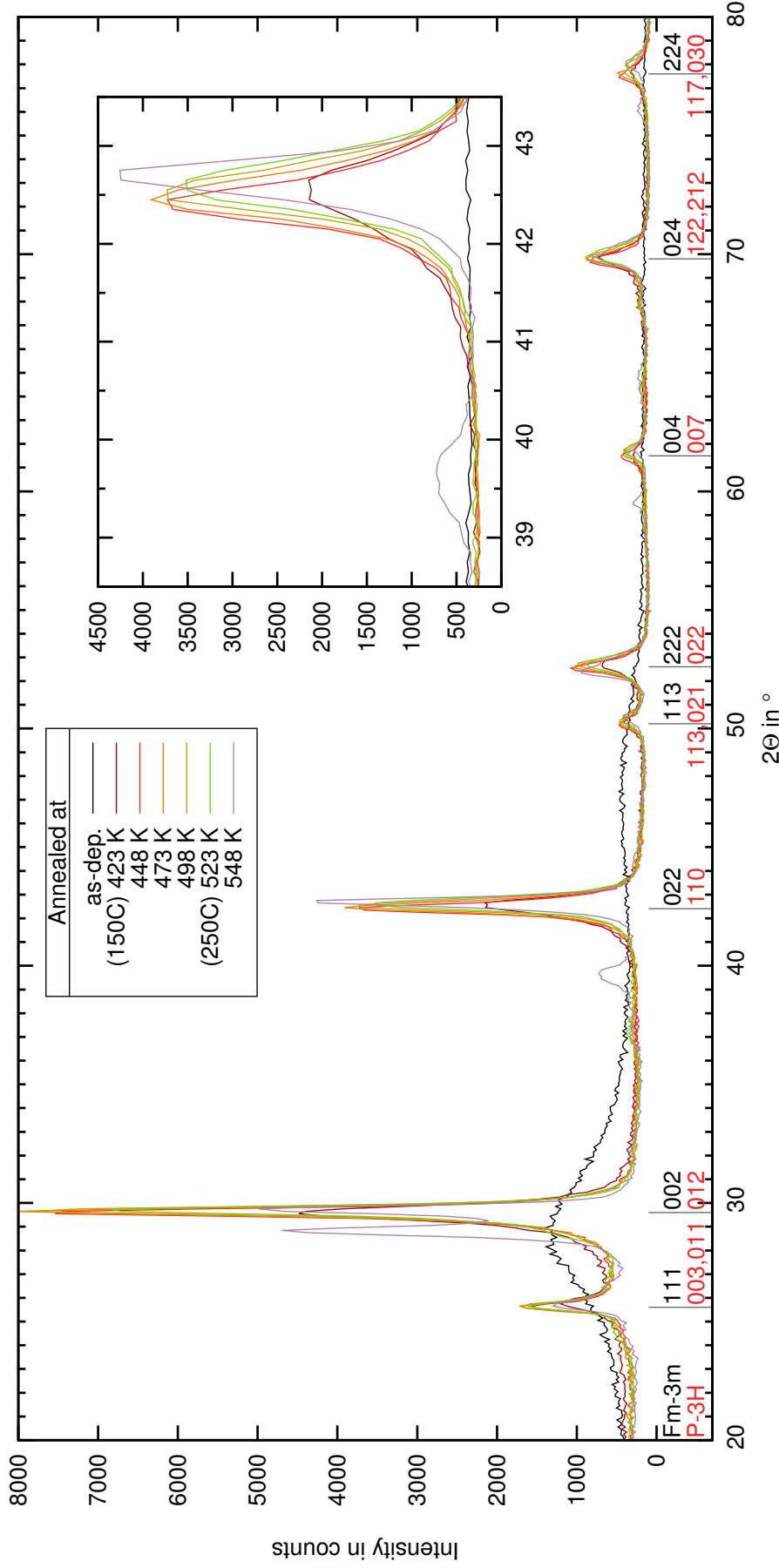


Figure 3.3: The XRD patterns of amorphous and meta-stable cubic GeSb₂Te₄ are shown for films of about 750 nm thickness measured in Grazing Incidence (GI) geometry. A rock-salt like phase (Fm $\bar{3}$ m, black miller indices, $R = 0.17$) is formed from the as-deposited amorphous films at 423 K. An angular shift can be seen from the reflections at large scattering angle, denoting a trend towards smaller lattice constants. All rock-salt like data sets can be refined by a rhombohedral (P $\bar{3}$ H, red indices, $R = 0.15$) as well. The lattice constant for the sample annealed at 448 K are $a = 4.26(1)$ Å and $c = 10.57(2)$ Å, where the smallest possible c value has been chosen. This corresponds to $a = 4.30(1)$ Å and $\alpha = 59.4(1)$ in rhombohedral notation. For comparison with the indices in Fig. 3.4, simply multiply the index l given here by 4.

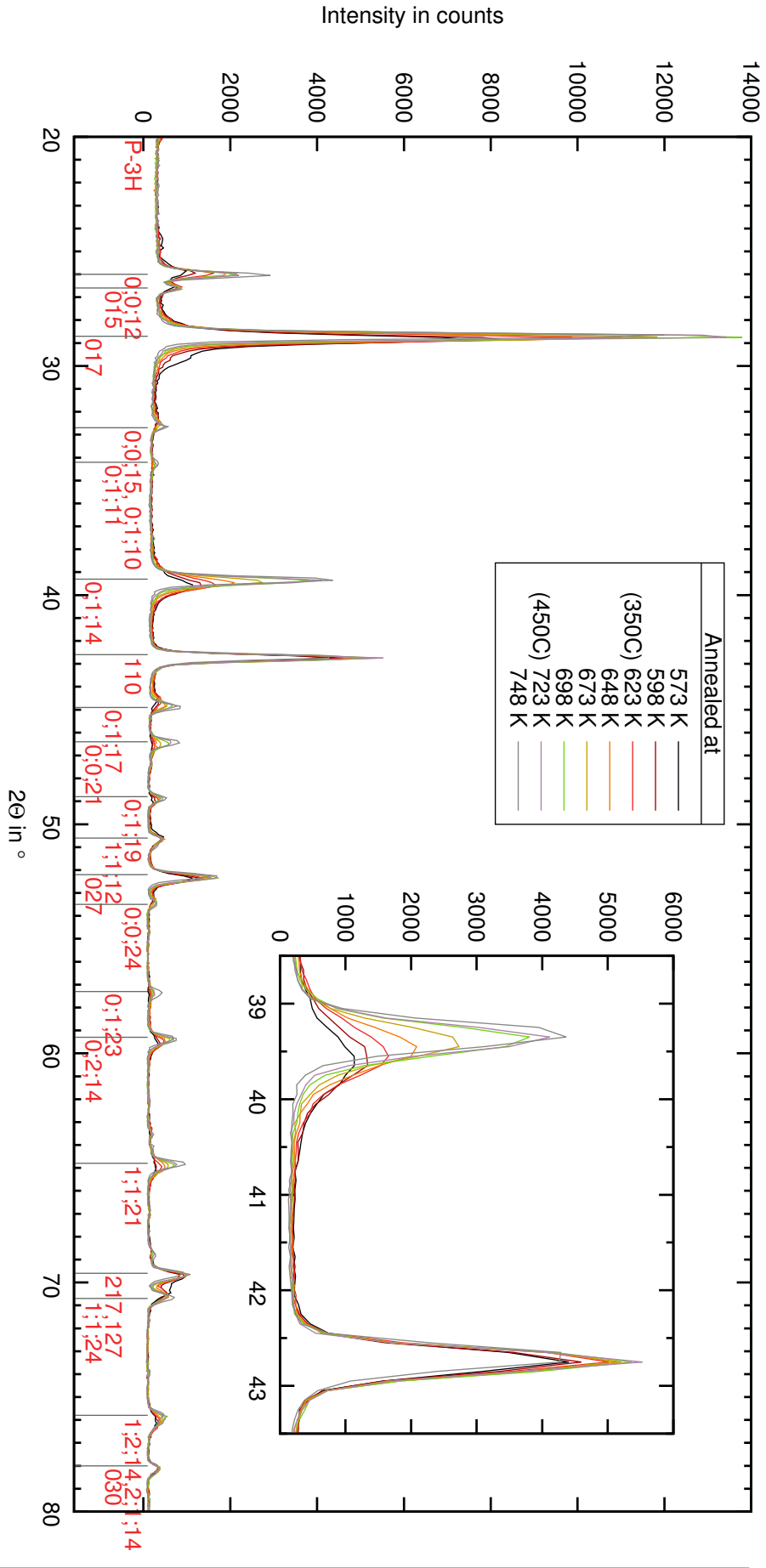


Figure 3.4: The XRD patterns of stable hexagonal GeSb_2Te_4 are shown for films of about 750 nm thickness measured in Grazing Incidence (GI) geometry. The stable hexagonal phase crystallizes above 548 K. Upon increasing the annealing temperature further, some reflections of the hexagonal phase become narrower (e.g. 39.3° , $\{0\ 1\ 14\}$), while some remain almost unchanged (e.g. 42.7° , $\{1\ 1\ 0\}$). This trend originates from a decreasing number of stacking faults (cf. text).

3.4 Experimental details for XRD

Figs. 3.3 and 3.4 show the trend in XRD patterns obtained for GeSb_2Te_4 after different annealing temperatures. 750(50) nm of GeSb_2Te_4 were deposited on borosilicate substrates and heated to the given temperatures with a heating rate of 5 K/min and a holding time of 30 min in a continuous flow of Ar. Each data set corresponds to a different sample so that the annealing effect is not accumulative and the samples were only heated from the as-deposited phase to the given temperature. The samples were not capped, but even after the treatment at 748 K, no segregation effects were observed in the subsequent XRD measurement at ambient conditions. Also, no significant evaporation residues were observed in the tube furnace. The XRD patterns were recorded in Grazing Incidence (GI) geometry at 1° angle of incidence, using Cu K- α X-rays.

3.5 Annealing dependence of the lattice constant in cubic GeSb_2Te_4

The scattering from the initially as-deposited amorphous structure shows a clear maximum just where the strongest crystalline reflexes occur and an additional shoulder at larger angles. At higher annealing temperatures, starting from 423 K, the meta-stable phase crystallizes. The atomic ordering in this phase is reported to follow the space group $\text{Fm}\bar{3}\text{m}$ with a lattice constant of 6.0430(9) Å [48], if the meta-stable phase is prepared by irradiating the as-deposited material with a laser. Fig. 3.3 shows that the reflex height increases when the annealing temperature is elevated from 423 to 448 K and remains almost constant thereafter. No broad features of the amorphous phase remain in both these diffraction patterns, so that both samples are fully crystalline. However, the width of the reflections and its θ -dependence changes according to an analysis of the peak parameters U and Y (cf. Eqs. 2.63 and 2.64). This shows that the grain size increases and that the strain decreases. Both parameters U and Y remain unchanged within the metastable cubic phase. To quantify the lattice parameters, the diffraction patterns have been fitted using the *Winprep* software, which fits peak functions to all reflections at the angles given by the space group and lattice constants. The intensity of each reflex is an additional free parameter in this model, i.e. no features of the atomic basis (like atomic numbers and positions) are refined. The results from this refinement are summarized in Tab. 3.1.

The data set of the sample annealed at 423 K is only partly crystallized as can be seen from the lower reflex intensity and the higher background signal between the reflections in Fig. 3.3. Starting from 448 K, the sample is completely in the meta-stable rocksalt phase. For higher annealing temperatures, a trend of increasing conductivity was found in literature [21] (and is confirmed here). If this trend originates from a reduction of disorder, then there should also be a trend in the structural properties. Indeed the lattice constant a shrinks with increasing annealing temperature. This is perfectly in line with the even larger lattice constant of the sample after very fast laser crystallization (6.043(1) Å [48]), which should

Table 3.1: Refinement of XRD patterns of meta-stable cubic GeSb₂Te₄ as a function of the annealing temperature, measured at room temperature. The lattice constant is observed to decrease, while simultaneously the sheet resistance measured in the van-der-Pauw four point geometry decreases as well.

Annealed at	Lattice constant a	2 Θ -offset	Reflex shape W	Residual	VdP Sh. Resist.
448 K	6.022(2) Å	0.07(1)°	0.44(2)	0.170	4708 Ω
473 K	6.015(1) Å	0.07(1)°	0.44(1)	0.169	1259 Ω
498 K	6.004(1) Å	0.10(1)°	0.45(1)	0.186	410 Ω
523 K	5.995(2) Å	0.13(1)°	0.48(2)	0.170	196 Ω

leave the sample in a more disordered state than those investigated here. Thus, the increase in conductivity in the meta-stable phase goes along with an increasing mass density of the specimen. The overall decrease in the lattice constant amounts to a density increase of 1.4% (2.4%, if the laser crystallized sample is used as reference), which is a rather low value as compared to the total volume of the vacancies, 12.5%, so that only a small fraction of vacancies might collapse.

3.6 Annealing dependence of the lattice constants in hexagonal GeSb₂Te₄

The annealing sequence has been continued for XRD measurements of the stable hexagonal phase, which is formed above 548 K. At this annealing temperature both, cubic and hexagonal phases coexist so that this dataset is not treated further. The hexagonal structure, which is the only solid phase that exists above 573 K, was reported to comply with the space group $R\bar{3}m$ with lattice parameters $a_h = 4.21$ Å and $c_h = 40.6$ Å [48]. The lattice constant c_h is quite large and the reason for this will be explained in the following. GeSb₂Te₄ has 7 atoms in the formula unit. In the meta-stable cubic structure, the atoms are stacked periodically . . . abcabca . . . but if a vacancy layer is introduced after every 7th layer and this block is declared a unit cell, then the stacking would begin from the same letter with which it started. It is energetically favorable to start with a different position so that 3 of these blocks are necessary to create a periodic sequence. The situation is different in Ge₂Sb₂Te₅, whose 9 layers can be perfectly stacked. The analysis of the obtained diffraction patterns was again performed with *Winprep* in the same way as described above for various annealing temperatures and the results are summarized in Tab. 3.2.

Does the trend of an increasing mass density from the meta-stable phase continue in the stable hexagonal phase? To answer this question, the volume of the unit cell was calculated by $V = a_h^2 c_h \sin(60)$. The results are presented in the table and show a reversed behavior: the volume increases for higher annealing temperatures, except in the last three measurements, where the density remains stable within the experimental error. This decreasing mass density can be traced back to an increasing lattice constant c_h . It goes along

Table 3.2: Refinement of XRD patterns of stable hexagonal GeSb₂Te₄ annealed at different temperatures. The lattice constant c_h is observed to increase with decreasing sheet resistance, obtained from four point measurements in the van-der-Pauw geometry.

Annealing	Lat. const. a_h	c_h	Volume	2 Θ -offset	W	Resid.	Sh. Resist.
573 K	4.240(1) Å	40.81(2) Å	635.4 Å ³	-0.11(1)°	0.18(1)	0.161	24.9 Ω
598 K	4.242(1) Å	40.85(2) Å	636.6 Å ³	-0.10(1)°	0.15(1)	0.154	20.8 Ω
623 K	4.238(1) Å	40.98(2) Å	637.4 Å ³	-0.08(1)°	0.13(1)	0.144	17.9 Ω
648 K	4.236(1) Å	41.11(1) Å	638.8 Å ³	-0.07(1)°	0.12(1)	0.136	15.0 Ω
673 K	4.237(1) Å	41.12(1) Å	639.3 Å ³	-0.04(1)°	0.10(1)	0.122	12.6 Ω
698 K	4.232(1) Å	41.15(1) Å	638.3 Å ³	-0.02(1)°	0.09(1)	0.110	11.1 Ω
723 K	4.233(1) Å	41.14(1) Å	638.4 Å ³	0.00(1)°	0.08(1)	0.097	10.4 Ω

with the transition from insulating to metallic behavior in Fig. 3.1. In the following, the question will be answered, **which atomic reordering mechanism is responsible for the increasing lattice constant during the metal-insulator transition?** The increase of a lattice constant with higher annealing temperature is a rather rare feature, since most materials shrink upon annealing. Changes in lattice constants are usually observed during the reduction of imperfections of the second kind (cf. Sec. 3.1), i.e. due to an increasing SRO. This material contains a significant amount of substitutional disorder on the Ge/Sb sublattice, which might decrease during annealing, leading to the observed change in c_h . This hypothesis will be discussed further in the remaining and in the following section. Several mechanisms could explain such behavior, but whereas strong covalent bonds connect the layers within the blocks, the spacing between the blocks is determined by a complex mixture of interactions: Van-der-Waals forces contribute to the bonding and counteract the ionic repulsion. It seems reasonable to investigate this repulsion mechanism further. It originates from the negative charge of Te atoms on the outer layers of each block. This negative charge originates from the slight ionicity of the bonding with Ge and Sb. It was reported that Sb atoms form a more ionic bond with Te [109] in hexagonal Ge₂Sb₂Te₅ compounds than Ge atoms. Therefore, a mechanism exists, which links the occupation of the layers next to the outer layers with the lattice constant c_h . If the increase in c_h originates from a change in the spacing between adjacent blocks, then an increasing concentration of Sb at the connection between blocks could explain this trend. Therefore, it remains to be shown that indeed the distance between neighboring blocks changes (cf. Sec. 3.7). First, let us recall that the stacking sequence is sometimes reported as Te-Sb/Ge-Te-Sb/Ge-Te-Sb/Ge-Te and sometimes as Te-Sb-Te-Ge-Te-Sb-Te (cf. introduction). This controversy could be explained by the slow diffusive occupation of layers at elevated temperatures. In addition, it was shown by DFT calculations that the driving force for the sorting of atoms is very low (3 meV/atom in GeSb₂Te₄ [106]) and can be easily compensated for by the gain in entropy (cf. Sec. 7). It is therefore reasonable to assume that both stacking sequences occur depending on the annealing conditions.

Therefore, continuous structural rearrangements might take place within the compound even in the stable hexagonal phase. The opposing trends of increasing and decreasing mass density in the meta-stable and stable phases, respectively, suggest that indeed two different mechanisms could exist. The next section will be devoted to analyzing a possible mechanism by which this sorting of atoms could be detected experimentally.

3.7 The layer distances in hexagonal GeSb_2Te_4

In the preceding paragraph, it was assumed that the block distance changes as a consequence of the ordering of Ge and Sb on the layers. A possible mechanism in support of this assumption will be presented in the following. It will be based on the observation that the $\{0\ 0\ 12\}$ reflection at 26° in the stable hexagonal phase changes its intensity continuously with the annealing temperature (cf. Fig. 3.4). It corresponds to the $\{111\}$ reflections in the meta-stable cubic structure. They originate from the diffraction of x-rays from next nearest layers at a distance of about $2\Delta c = 3.42\text{ \AA}$. To obtain insight in the origin of the different reflex intensities, the structure factor (cf. Eq. 2.45) can be calculated. For simplicity, $\text{Ge}_2\text{Sb}_2\text{Te}_5$ is calculated here, because its stable hexagonal phase consists of only 9 layers as compared to the 21 layers in GeSb_2Te_4 . It turns out that only the layer positions c_i enter the formula, which are referenced to the centered Te*-layer at the origin $c_0 = 0$: The stacking sequence in $\text{Ge}_2\text{Sb}_2\text{Te}_5$ is assumed as Te-Sb-Te-Ge-Te*-Ge-Te-Sb-Te [107]. In a high-symmetry configuration, the c_i are given by $i \cdot \langle \Delta c \rangle$, with $\langle \Delta c \rangle = c/9$, the average distance of layers. If, however, atoms are more distant at the vacancy layer due to the weaker van-der-Waals bonds, then the average distance of layers can decrease down to $\langle \Delta c \rangle = c/10$, which would imply that the atoms at the vacancy layer are $2 \langle \Delta c \rangle$ apart. The interlayer spacing was calculated by DFT to be between 3.0 and 3.2 \AA [106]. The structure factor for this model structure reads

$$\begin{aligned} S &= \sum_j f_j(q) \cdot \exp(i\vec{q}\vec{r}_j) \\ &= f_{\text{Te}} \cdot \left(1 + 2 \cos\left(10\pi \frac{c_2}{c}\right) + 2 \cos\left(10\pi \frac{c_4}{c}\right)\right) + 2f_{\text{Ge}} \cos\left(10\pi \frac{c_1}{c}\right) + 2f_{\text{Sb}} \cos\left(1\pi \frac{c_3}{c}\right) \end{aligned}$$

This structure factor depends on four parameters (c_i), which all influence the resulting intensity of the reflex $|S|^2$. Since the spacing of layers is roughly equidistant [49], the contributions to the structure factor are positive for Te and negative for Ge and Sb. If the vacancy spacing equals $\langle \Delta c \rangle$ (i.e. $c_i = i \cdot c/9$), the structure factor has a value of 40, but if the spacing increases to $2 \langle \Delta c \rangle$ (i.e. $c_i = i \cdot c/10$), the value increases to 95. This shows that the intensity ($|S|^2$) of the $\{005\}$ reflections of $\text{Ge}_2\text{Sb}_2\text{Te}_5$ (which correspond to the $\{0\ 0\ 12\}$ reflections of GeSb_2Te_4) increases with an increasing block spacing. This trend is also observed in Fig. 3.4 at 26° so that we conclude that the argument of the increasing ionic repulsion at the block distance is indeed consistent with the experimental observation. It is however not possible to proof that this is the only change of atomic disorder, which

accompanies the metal-insulator transition. To conclude, **the metal-insulator transition is accompanied by an ordering of Ge and Sb atoms to separate layers of the hexagonal phase of GeSb₂Te₄. Other mechanisms, like the imperfect ordering of some remaining vacancies and some remaining atoms in the vacancy layer might as well explain the metal-insulator transition and cannot be excluded after this analysis.**

3.8 Reflex broadening in XRD patterns of hexagonal GeSb₂Te₄

Another trend can be seen in the diffraction patterns in Fig. 3.4 (inset): The two reflections of the hexagonal phase at 39.6° and 42.7° have different peak heights and widths when the hexagonal phase is formed. This is rather surprising, since in most cases the reflex width is given by the grain size and thus depends only weakly on the momentum transfer. Increasing the annealing temperature increases the height of the first reflex, while it simultaneously reduces its width and shifts its position to lower angles of diffraction. The latter angular shift is simply a consequence of the change in lattice constants, but the change of reflex width could have two explanations: Grain growth and stacking faults. **Which atomic rearrangement is responsible for the narrowing reflection at 39.6°?**

Thermal vibrations about well-defined mean positions do not contribute to the broadening. ([78], p. 189) and therefore are not taken into account. The two remaining effects will be discussed in the following in order to see whether they can influence the disorder induced localization, which was reported recently [21]. Grain growth does not influence the localization phenomenon, since the electron mean free path is below 22 Å – even after annealing at 598 K, whereas the grain size is at least 84 Å. The stacking faults, however, could still influence the conductivity. The crucial way to distinguish grain size effects from stacking faults is the different dependence of the reflex broadening on the miller indices h , k and l : "The essential difference between size and distortion effects is that, in the first case, the apparent size is independent of the order of the reflection, while in the second case it is not independent." [78], p. 161. This dependence on miller indices will be discussed and compared to the data in the following. The experimental data were obtained by fitting Gaussian peak functions to the most significant reflections. However, the l -value of the reflections needs to be determined as well. They can be extracted from the angle of diffraction after the model of the unit cell was refined. The reflections listed in Fig. 3.3 were used to determine the Cagliotti- W 's (reflex widths) for the different annealing conditions (here, an example for 573 K is shown).

This table already shows that there is no trend of reflex broadening W with scattering angle, but that there is indeed a large difference in W 's for different reflections. This difference scales with the Miller index l . The resulting data for several annealing conditions are summarized in Fig. 3.5 and prove the l -dependence of W for those samples, which have just reached the fully hexagonal phase at the lowest possible temperature (573 K, black curve, which is a linear fit to the black data points). Upon increasing the annealing temperature, the slope decreases continuously. In the following, the different mechanisms, which could

Table 3.3: The broadening of various reflections in hexagonal GeSb₂Te₄ does not scale with the scattering angle 2θ , but quite well with the Miller index l .

Angle 2θ in $^\circ$	Broadening W	h	k	l
28.8	0.391	0	1	7
39.6	0.744	0	1	14
42.7	0.279	1	1	0
52.4	0.374	0	2	7
65.0	0.900	0	1	21

explain the reflex broadening will be discussed.

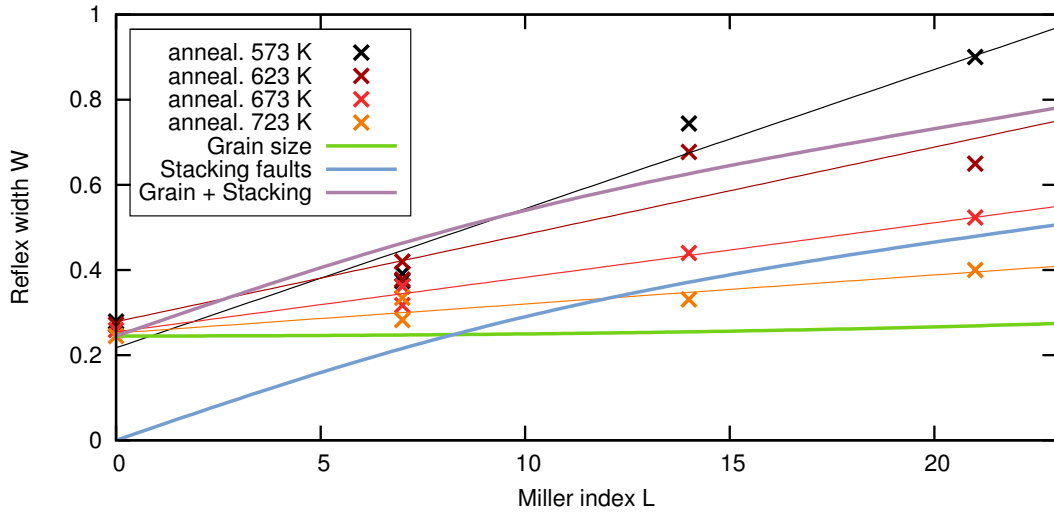


Figure 3.5: The Reflex width is plotted vs. the momentum transfer associated with the Miller index L in the stable hexagonal phase of GeSb₂Te₄. It can be seen that at lowest annealing conditions, the reflex width is dominated by the influence of stacking faults because it has a significant non-zero slope. At higher annealing temperatures, the slope is reduced so that the grain size broadening dominates. Therefore, stacking faults are removed upon increasing the annealing temperature.

Grain growth is approximately described by the Scherrer equation ([78], p. 124)

$$W = \sigma^2 = \frac{\lambda}{g \cos \Theta}, \quad (3.5)$$

where Θ is the angle of diffraction and g is the average thickness of the crystallites. Combining this equation with the general formula for the distance of lattice planes d_{hkl} for given h , k and l (cf. [110], p. 125),

$$\frac{1}{d_{hkl}^2} = \frac{4}{3} \left(\frac{h^2 + hk + k^2}{a_h^2} \right) + \frac{l^2}{c_h^2}, \quad (3.6)$$

and together with Bragg's law (Eq. 2.58), it follows that

$$\sin \Theta = \frac{\lambda}{2} \sqrt{\frac{4}{3} \left(\frac{h^2 + hk + k^2}{a_h^2} + \frac{l^2}{c_h^2} \right)}. \quad (3.7)$$

Therefore, by combining Eqs. 3.5 and 3.7, we obtain a general relationship of the reflex broadening σ^2 on the Miller indices, which should apply for every reflex. Only the dependence of θ on l will be considered in the following, i.e. h and k are left unchanged. A plot of this function is shown for the case that only grain size ($g = 482.5 \text{ \AA}$) leads to an increased width of the reflections in Fig. 3.5 (green curve). It is easily seen that the influence of grain sizes is rather constant with l and therefore also with θ . A comparison with the data at the lowest annealing temperature for the hexagonal phase (black curve) shows that grain sizes alone cannot account for the broadening.

Reflex broadening by stacking faults on the other hand shows a different angular dependence, as given by (cf. [78], p. 223)

$$W = \sigma^2 = \frac{\lambda^2}{c^2} l \frac{\Delta l}{\sin 2\Theta}. \quad (3.8)$$

It will be assumed in the following that the atoms on each layer are arranged in a perfect hexagonal grid, i.e. perfect 2-dimensional translational symmetry exists within each layer. The stacking faults are then described as an irregularity in the stacking sequence of these layers. In the case of hexagonal samples, the l direction is perpendicular to the layers. The resulting reflex broadening σ^2 is then a function of l and of the parameter Δl , which equals half the probability to find a stacking fault at a randomly chosen layer. It is obvious from this equation and from the sine in the denominator, that there will be a strong dependence of σ^2 on l . This dependence is indeed visible from a plot of this function with $\Delta l = 0.25$ in Fig. 3.5 (blue curve). It can very well reproduce the l -dependence of the broadening parameter σ^2 in the sample annealed at 573 K. It also reproduces the absolute numbers for the broadening, if the additional broadening from two sources is added: One originates from the grain sizes and another from the non-zero h and k terms, which contribute an additional broadening (cf. Eqs. 3.7 and 3.8). **The strong l -dependence of the reflection width shows that stacking faults of the layers are present in the hexagonal phase at lowest annealing temperatures. The decrease of this l -dependence upon annealing further shows that the stacking faults are reduced upon increasing the annealing temperature.**

In the following, the validity of the Williamson-Hall method is discussed. The dependence of reflex widths on l for lower annealing temperatures causes problems with the determination of grain sizes with the Williamson-Hall method, because it assumes that the broadening originates from the grain size alone and therefore averages the width of all reflections. The analysis presented above shows that the Williamson-Hall treatment does not deliver correct grain sizes in the presence of stacking faults. However, the Scherrer formula can be employed to approximate the grain size from those reflections, which are not broadened by the stacking faults – i.e. from the reflections with $l = 0$. The resulting grain size is rather constant as a function of annealing (cf. Fig. 3.5 at $l = 0$) and amounts to approximately 450 \AA .

3.9 Conclusions from Annealing trends in GeSb_2Te_4 from reciprocal space

Structural changes with increasing annealing temperature have been investigated. In the meta-stable cubic phase of GeSb_2Te_4 , the mass density increases with increasing annealing temperature. At even higher annealing temperatures, the structure transforms to a hexagonal phase, in which an metal-insulator transition is observed upon increasing the annealing temperature. Throughout this transition, the mass density of the sample is found to decrease. Thus, two different continuous structural transformations have been observed. The first could be related to the ordering of vacancies in the meta-stable cubic phase, leading to the formation of some vacancy layers, which still retain the cubic symmetry. This "collapse" would lead to the observed increase in mass density. The transformation in the stable hexagonal phase is probably related to the ordering of Ge and Sb atoms on separate layers. These diffusion processes are also suggested for a similar compound, SnSb_2Te_4 , in which the Ge atoms are isoelectronically replaced by Sn. Oeckler et al. show by resonant x-ray scattering (RXS) that the Sn and Sb atoms are neither fully ordered nor randomly distributed, but rather that Sn agglomerates on the center layer of the unit cell [108]. In the case of Ge atoms, this ordering increases the repulsive, ionic interaction across the blocks and thereby decreases the mass density. This opening of the block spacing takes place continuously during the metal-insulator transition. The grain sizes evaluated at $l = 0$ are found to be rather independent of the annealing temperature in both phases and can therefore not account for the MIT: They are 14 nm and 45 nm in the cubic and hexagonal phases, respectively. The observed structural transformations reveal that several ordering mechanisms can be responsible for the MIT:

1. some vacancies could continuously arrange to layers during annealing in the meta-stable cubic phase (however, due to the absence of scattering from vacancies, this mechanism cannot be discussed exactly)
2. the number of stacking faults in the hexagonal phase is reduced continuously upon annealing
3. the Ge and Sb atoms diffuse to separate layers in the stable hexagonal phase at elevated annealing temperatures, thereby increasing the spacing between the blocks

Unfortunately, it is not possible to determine a unique modification of the atomic order, which can be claimed responsible for the metal-insulator transition. The main problem is that experimentally, these different mechanisms cannot be decoupled because they take place simultaneously during the annealing process. An alternative approach might be the calculation of electronic conductivities by first principles. These calculations have been performed on systems containing about 200 atoms [111], but this number might be too small to sample the full substitutional disorder in these phase-change materials. It is still possible to investigate the localization-delocalization transition by calculating the so-called

inverse participation ratio of the electronic states to the transport. It was indeed found that fluctuations of the local density of vacancies have a pronounced influence on the localization of electronic states. If a Te atom is surrounded by 4 vacancies (i.e. by 2 atoms of either Ge or Sb), electronic states are localized [103]. These fluctuations in the local concentration of vacancies are reduced when the sample is annealed, since the formation of vacancy layers allows only three or zero vacancies in the direct neighborhood of Te atoms. Thus, a PCM in the stable hexagonal phase at highest annealing conditions cannot contain those Te sites with 4 vacancies, which were found to be responsible for the localization of charge carriers. In conclusion, the hexagonal phase turns out to be metallic at highest annealing conditions.

3.10 EXAFS analysis of meta-stable cubic GeSb_2Te_4

In the preceding sections, it was concluded that the SRO in crystalline GeSb_2Te_4 depends on the annealing conditions. Although a change in the diffraction patterns was observed, it was not possible to determine the exact modifications of the local atomic environment. In a crystalline material with large atomic displacements, a local probe can deliver complementary information. EXAFS is such a local probe and was applied to GeSb_2Te_4 at different annealing conditions. Up to now, EXAFS measurements on meta-stable crystalline $\text{GeTe-Sb}_2\text{Te}_3$ compounds have been reported in literature only once [31] and they were performed at room temperature. There, bond lengths of 2.83 Å and 2.91 Å were obtained for Ge-Te and Sb-Te bonds, respectively. No additional longer atomic distances were reported. Comparing the average atomic distance from this result, 2.87 Å, with the atomic distance obtained from XRD, 3.01 Å, one notices that a strong deviation exists in published structural information on meta-stable crystalline GeSb_2Te_4 . The fundamental goal of this section 3.10 is therefore to find out, **which properties of the local atomic arrangement of each individual atom can be obtained from an EXAFS analysis of GeSb_2Te_4 and to explain the discrepancy between published structural information of meta-stable crystalline GeSb_2Te_4 based on EXAFS and XRD.** The exact trends upon annealing will be discussed in the following section 3.11.

In a crystalline material, there are several coordination shells, whose backscattered electrons interfere and reduce the overall amplitude of the EXAFS oscillations. Therefore, it is even more important to have an accurate baseline than for amorphous materials with larger amplitudes. It is reported in literature, that several excitation channels exist at the Ge K-edge EXAFS at 11140 eV (1s-3d), corresponding to $k = 3.1 \text{ Å}^{-1}$, and more weakly at 11240 eV (1s-3p), corresponding to $k = 6.0 \text{ Å}^{-1}$, [112]. These energies correspond to electronic states of Ge with a core hole present, which are similar to the electronic transition energies in As. Because the first excitation is only closely above the edge, the corresponding data below 5 Å were not taken into account during the fitting process, because the remaining k-range from 5 Å to 16 Å is still sufficiently large. The second transition, however, is of low amplitude and was therefore neglected in the fit. However, increasing the fitting range above the first feature improved the data quality in real space significantly, as can be seen in Fig. 3.6

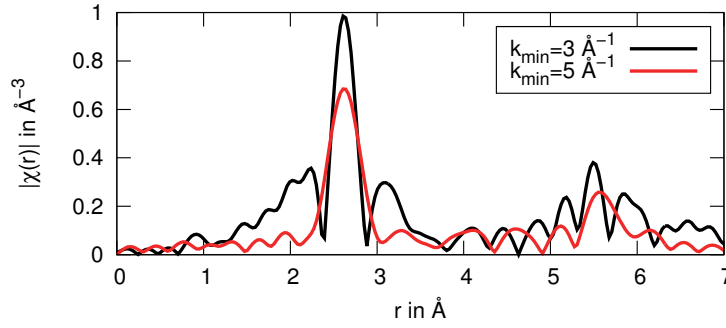


Figure 3.6: Fourier Transforms of EXAFS from crystallized GeSb_2Te_4 with different window functions for the Fourier transform. A higher k_{\min} (red curve) significantly reduces the noise in the data around the main peak, because features at $k \approx 3.1 \text{ \AA}^{-1}$ distort the absorption baseline.

EXAFS data of GeSb_2Te_4 were measured at 10 K sample temperature. These data have a significantly higher information content, as will be discussed later (cf. Sec. 4.2.3). Quantitative results can be obtained from an EXAFS analysis by performing least squares fits. The general fitting procedure was already described in Sec. 2.7.4 and was applied here as well. In the case of GeSb_2Te_4 , the structural model for each edge must be based on a rock-salt structure of one sublattice of Te atoms and displaced Ge and Sb atoms with vacancies on the second sublattice. Atomic displacements on the Ge/Sb sublattice could not be fitted by large Debye Waller factors (DWFs), because the distribution of distances is not of Gaussian shape, but consists rather of two or more individual contributions, which are at least 0.2 \AA apart. It follows that the large displacements are not of thermal, but rather of static nature. The atomic displacements could be refined, by including a short and a long nearest neighbor distance around Ge and Sb, as described elsewhere [113]. These short and long interatomic distances show individual distribution width, which are described by two independent DWFs, which include thermal and possible static variations from the average short and the average long distance. The resulting fit reproduces all features in the fitting range (gray shaded area), cf. Fig. 3.7. The fit has remaining residuals of 0.011, 0.016 and 0.040 at the Ge, Sb and Te edges, respectively and can be considered reliable. The energy shift ΔE between experiment and calculations amounts to 6(1), 11(1) and 8(1) eV for the three edges, which is in the usual range of energy deviations of 5 to 10 eV. Since the fitting model was based on a rock-salt model, the coordination numbers N were known in advance to be 6, 6 and 4.5 for Ge, Sb and Te, respectively¹. These numbers are valuable for the determination of the amplitude reduction factors S_0^2 , which are obtained from the fit via $N \cdot S_0^2$. They turned out as: 0.79(12), 0.97(14) and 0.84(14), for Ge, Sb and Te, respectively. These factors are in agreement with the common range of 0.7 to 0.9, but the errors are quite large due to the splitting of bond lengths and the large displacement parameters.

All parameters involved in the data refinement are summarized in Tab. 3.4. Taking the

¹These coordination numbers N were used for the sum of short and long nearest neighbor coordination numbers $N_1 + N_2$.

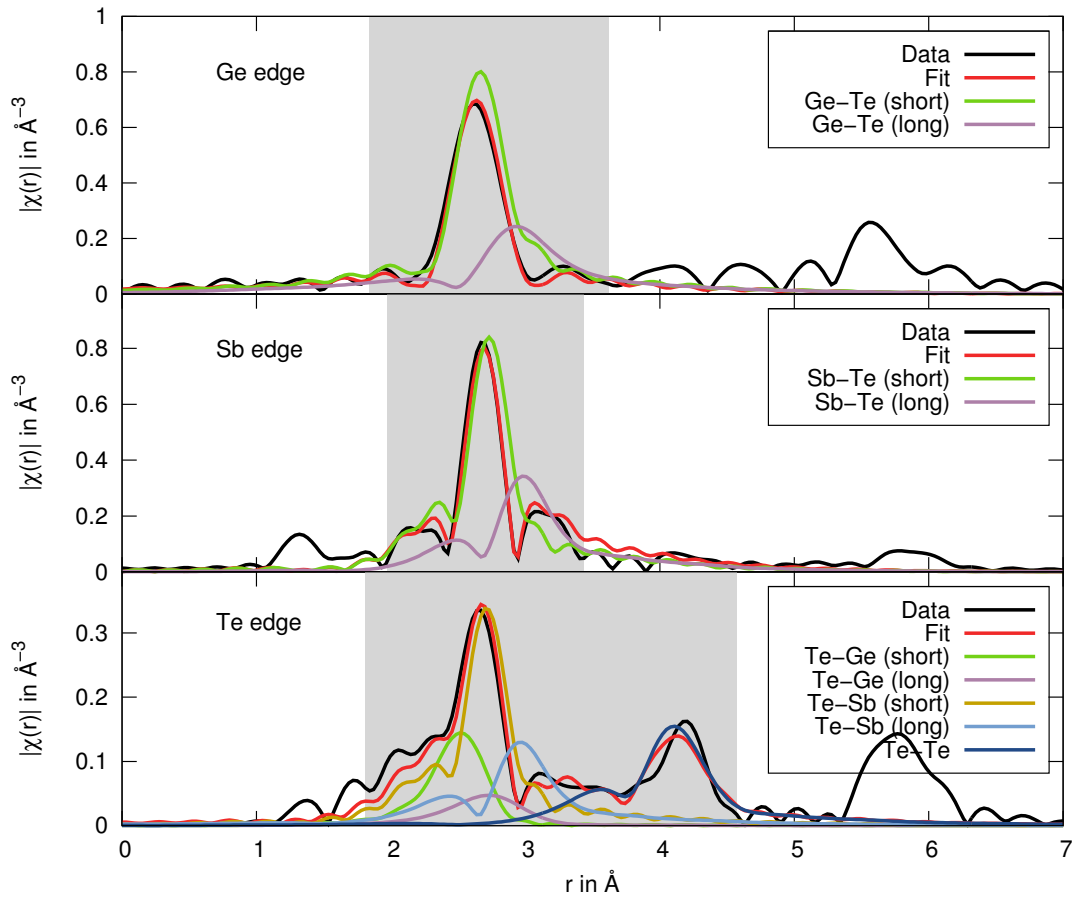


Figure 3.7: Fourier Transforms of EXAFS from meta-stable cubic GeSb_2Te_4 together with fits based on a rock-salt structure. The data are based on the treatment by Julia van Eijk [113], [114].

average of the short and long distance around Ge, one obtains $2.97(1) \text{ \AA}$ and around Sb $3.05(1) \text{ \AA}$. To determine the average atomic spacing in meta-stable cubic GeSb_2Te_4 , these numbers have to be weighted by the atomic occurrence in the ratio 1:2, which results in $3.02(1) \text{ \AA}$, which is only slightly larger than the result from XRD of $2.998(1) \text{ \AA}$ (extrapolated to 10 K [73]). The remaining deviation will be discussed later in this section. **The average atomic distance obtained from XRD and EXAFS is well in line, when the short and long nearest neighbor distances are taken into account.** It should be added, that the longer distances became visible by the low measurement temperature, where the amplitude of thermal vibrations is significantly reduced. Especially for the long bonds, the MSRD parameters are so large that their amplitude is low and very accurate measurements are necessary to detect them. This can be easily seen from Fig. 3.7 by comparing the signal from the long atomic distance to the overall signal. Already the MSRD parameters for the short atomic distances are exceptionally large, which shows that the displaced atomic position itself is not well defined.

Now, that separate short and long distances were determined, it might be tempting to

Table 3.4: Fit results from meta-stable cubic GeSb_2Te_4 , annealed at 378 K for 60 h and measured at 10 K. Around both, Ge and Sb, short and long distances to the nearest neighboring Te atom are found. This shows that the atomic displacements in GeSb_2Te_4 are of static and not of thermal nature.

Scattering Path	N	Distance	Displacement Parameter
Ge-Te (short)	2.5(5)	2.854(4) Å (a)	0.0056(6) Å ² (a)
Ge-Te (long)	3.5(5)	3.084(5) Å (b)	0.014(3) Å ² (b)
Sb-Te (short)	2.7(6)	2.933(5) Å (c)	0.0052(8) Å ² (c)
Sb-Te (long)	3.3(6)	3.16(1) Å (d)	0.012(8) Å ² (d)
Te-Ge (short)	0.6(1)	2.854(4) Å (a)	0.0056(6) Å ² (a)
Te-Ge (long)	0.9(1)	3.084(5) Å (b)	0.014(3) Å ² (b)
Te-Sb (short)	1.4(3)	2.933(5) Å (c)	0.0052(8) Å ² (c)
Te-Sb (long)	1.7(3)	3.16(1) Å (d)	0.012(8) Å ² (d)
Te-Te	9(2)	4.29(2) Å (d)	0.017(3) Å ² (d)

conclude that the atoms are displaced along the cubic $\{111\}$ directions. This seems to be a good approximation, indeed, but is not necessarily true. The short and long distances were obtained because it was assumed in the fitting model that exactly two different distances exist. Whereas it was obvious that a single distance is insufficient, also three distances can be refined and the resulting residual is even slightly lower (cf. [113] for details). The third distance obtains an intermediate value, which resembles half the lattice constant quite well. This three-fold splitting is the fingerprint of atomic displacements along the $\{100\}$ and $\{110\}$ directions. Therefore, even a random displacement direction with four or more distances is compatible with these EXAFS data as well.

The intrinsic vacancies of GeSb_2Te_4 were found to influence the electronic properties of these materials significantly: They shift the Fermi level from a mid-band state to the band edge [50]. It is also observed, that the electronic resistivity of GeSb_2Te_4 changes irreversibly with increasing annealing temperature. This suggests that atomic rearrangements take place. To understand how these rearrangements take place, it is necessary to understand the local atomic structure around the vacancy. To answer this question, several DFT calculations have been performed, which showed that charge is localized in the vacancy region [103]. They are based on the result that the Te atoms, which are direct neighbors to vacancies are displaced into the free space of the vacancy. This fundamental result seems counterintuitive at first sight, because it is well known that atoms at the surface of crystals tend to form short bonds into the bulk material. If the vacancy is considered a tiny surface area, the Te atoms are expected to be dragged away from the vacancy. The remaining deviation of average bond lengths at 10 K, 3.02 Å in EXAFS and 2.998 Å in XRD can be explained based on fundamental differences in the methods. As discussed in Sec. 2.8.2, EXAFS is

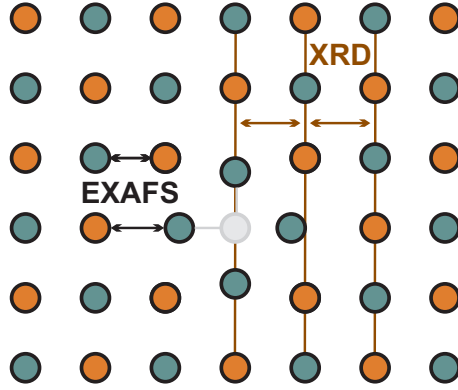


Figure 3.8: The effect of vacancies in meta-stable cubic GeSb_2Te_4 on the resulting EXAFS and XRD data is schematically depicted. The central vacancy (grey) elongates the bonds of the neighboring atoms. These elongated distances (black lines) are taken into account in EXAFS, but the corresponding shorter distances (grey lines) do not exist. In XRD, however, when only the Bragg reflections are refined (e.g. in the Rietveld method), the distortions cancel out and on average the lattice constant remains unchanged.

only sensitive to the displacements along the direction between two atoms, whereas Bragg reflections occur due to reflections at layers of atoms. A 2-dimensional lattice of a rock-salt lattice with a vacancy (in grey) is depicted in Fig. 3.8. If the atoms are displaced into the empty space of the vacancy, the nearest neighbor distances are on average longer, because there is no shorter nearest neighbor distance to compensate for this elongation. In XRD, however, the Bragg reflections are not shifted, because the average distance between planes is unaffected and averages out, when the whole structure is taken into account, since the average atomic position is not changed: If all displacement vectors are added, the result is zero. Therefore, the longer distance obtained from EXAFS is direct evidence for the displacement of Te atoms into the empty space of a vacancy. This leads to a decrease of the Te-Te distance across a vacancy, a_{Vac} . In the following, this distance will be calculated in order to compare it to published results from DFT calculations: In GeSb_2Te_4 , one sublattice is occupied by $n_{\text{Ge}} = 25\%$, $n_{\text{Sb}} = 50\%$ and $n_{\text{Vac}} = 25\%$. Let a_{Sb} be the average Te-Te distance along the $\{111\}$ -directions with a central atom of Sb. It then must hold that

$$a_{\text{XRD}} = n_{\text{Ge}} \cdot a_{\text{Ge}} + n_{\text{Sb}} \cdot a_{\text{Sb}} + n_{\text{Vac}} \cdot a_{\text{Vac}} \quad (3.9)$$

From this equation it follows that $a_{\text{Vac}} = 5.86(5) \text{ \AA}$, which is in line with the general observation from DFT [109]. This result is rather counterintuitive, because one would expect that there is lack of attractive force towards the vacancy – just as for the surface layer of a single crystal. In this surface layer, the distance between atoms in the first and second layers is reduced as compared to that inside the crystal [115]. One could expect a similar effect in the meta-stable phase of GeSb_2Te_4 due to the absence of attractive force from the vacancy, but on the contrary, the atomic positions relax into the vacancies, i.e. towards a more uniform filling of the space. **To conclude, an EXAFS analysis of the Ge and Sb edges**

provides precise interatomic distances and the respective MSD parameters, when the measurements are performed at low temperature. From these interatomic distances, the average atomic displacements could be determined. Their displacement pattern is in good agreement with the result of a Peierls distortion mechanism. It was further shown that Te atoms next to the vacancies are displaced towards the vacancy.

3.11 Annealing dependence of the crystalline phase from EXAFS analysis

It is now evident that the local atomic nearest neighbor distances can be obtained from EXAFS data for the local environment of all atoms and also for the vacancies. It was further shown from XRD experiments that the SRO changes upon increasing the annealing temperature. Therefore, EXAFS measurements have been performed on samples of GeSb_2Te_4 , which were annealed at different temperatures. The results from this analysis will be presented in the following in order to find out **which atomic features of the SRO in GeSb_2Te_4 change upon increasing the annealing temperature.**

As-deposited samples were annealed in a tube furnace under a constant flow of Ar at various temperatures. The heating rate was kept constant at 5 K/min and holding time 30 min were kept constant so that the observed trends are meaningful. The resulting data of all edges are compiled in Fig. 3.9 and will be analyzed in the following. It is worth repeating, that the samples annealed at 423, 448 and 473 K show reflections in line with space group $\text{Fm}\bar{3}\text{m}$ (rock-salt), while the samples annealed at 523 and 573 K show reflections at angles corresponding to space group $\text{R}\bar{3}\text{m}$ (hexagonal). The intermediate sample annealed at 498 K shows reflections of both types and therefore needs to be interpreted with caution.

Upon increasing the annealing temperature of GeSb_2Te_4 , a continuous change of the K-edge EXAFS of Sb is observed in Fig. 3.9. The Ge and Te K-edge EXAFS on the other hand change quite suddenly at the phase transition between 473 K and 498 K. This finding suggests that there is a continuous rearrangement of Sb atoms, whereas the Ge and Te atoms change their local order rather suddenly.

The most significant change around Ge is marked by #1 in Fig. 3.9. It is surprising to find it located at such large atomic distances, because this behavior is usually observed upon crystallization: In amorphous materials like pure Ge, the nearest neighbor spacing in the amorphous and in the crystalline phase is equivalent. Nevertheless, a change in the EXAFS spectra is observed upon crystallization in pure Ge, where an additional peak is formed at larger atomic distances [116]. This additional peak is due to the reduction of the variance of bond angles. It is therefore reasonable to conclude the same behavior for the annealing dependence of crystalline GeSb_2Te_4 : The large atomic displacements at lowest annealing temperature lead to a variance of bond angles as well and this variance is reduced when the stable hexagonal phase is obtained. It is worth mentioning that in the hexagonal phase, the displacement direction of Ge and Sb atoms is aligned with the c-axis, so that the distortion angle around Te is reduced.

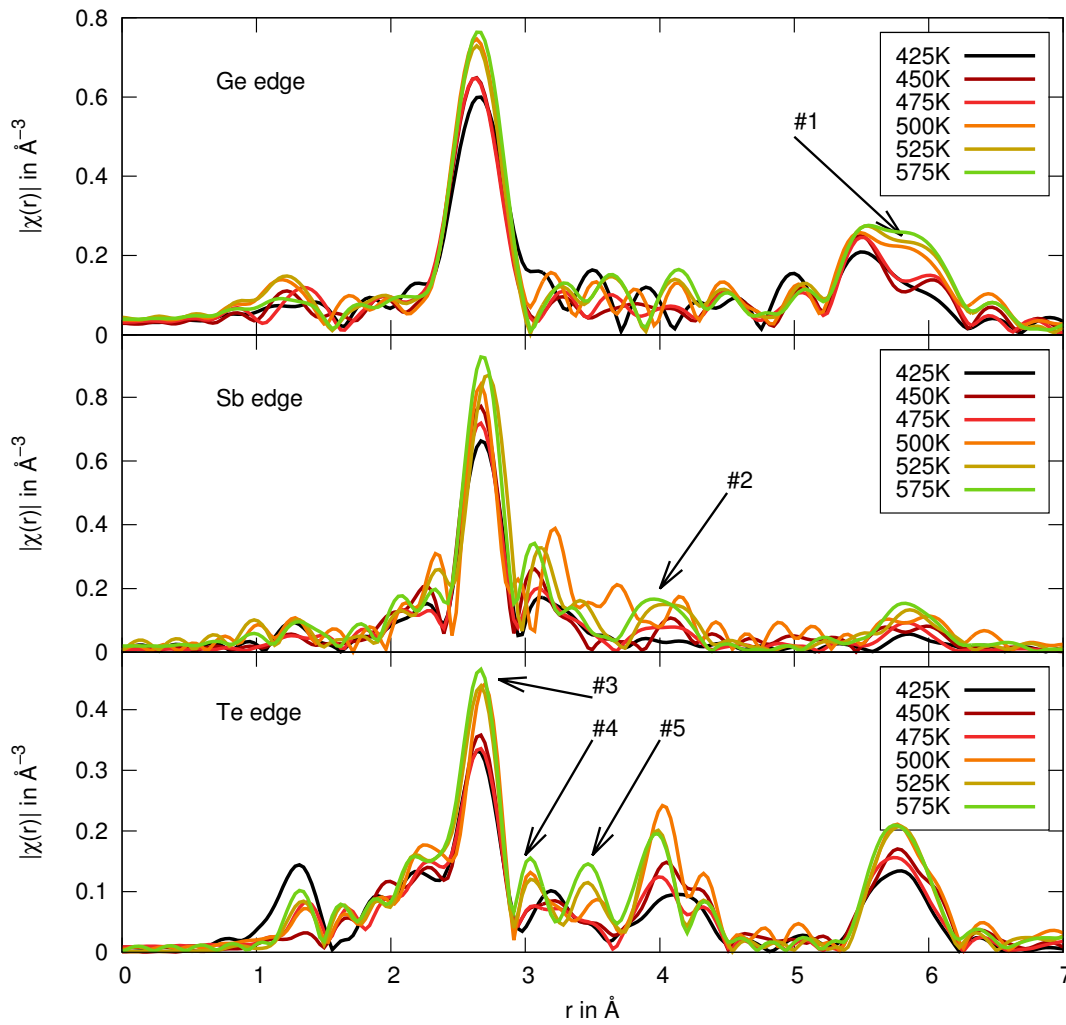


Figure 3.9: Fourier Transformed EXAFS spectra of crystalline GeSb_2Te_4 after different annealing temperatures. The changes in short-range order are quite subtle, but the fingerprint of the hexagonal ordering at 500 K and above is the Te-Te distance across the vacancy layer, which is 3.75 Å and is denoted by '5'.

At the Sb edge, the first peak grows continuously upon annealing. The exact mechanism behind this change has to be determined by fitting the peak, because two nearest neighbor distances exist and at least three parameters influence the height: The relative distance of short and long bonds and their MSD parameters. In addition to this effect, the peak at 4 Å (feature '2') increase with annealing conditions above 498 K. These changes correspond to Ge-Ge and Ge-Sb distances, which are getting more well defined, i.e. their MSD parameter is decreasing.

The most significant modifications can be observed at the Te edge. In order to find out, which peaks are significant, the lowest noise level has to be identified. This level represents the background noise over the full spectrum and is a good measure for the quality of the data and for the data extraction process. The lowest level is observed at 5 Å and 7 Å and

can be compared to the peak heights. This shows that also the features denoted as '#4' and '#5' are important. The first peak changes rather suddenly and at the same time an additional peak '#4' at 3 Å is created. It corresponds to the long Sb-Te bonds, which are getting more well defined. The feature at '#5' originates from the unique atomic distance across the vacancy layers, i.e. the interblock distance. These are Te-Te distances of 3.75 Å [49] and it can be clearly seen that this peak grows continuously upon heating above 475 K. This increase could either originate from the ordering of these distances or from the creation of vacancy layers. At the same time, Te-Te distances at 5.8 Å do not change with annealing in the hexagonal phase.

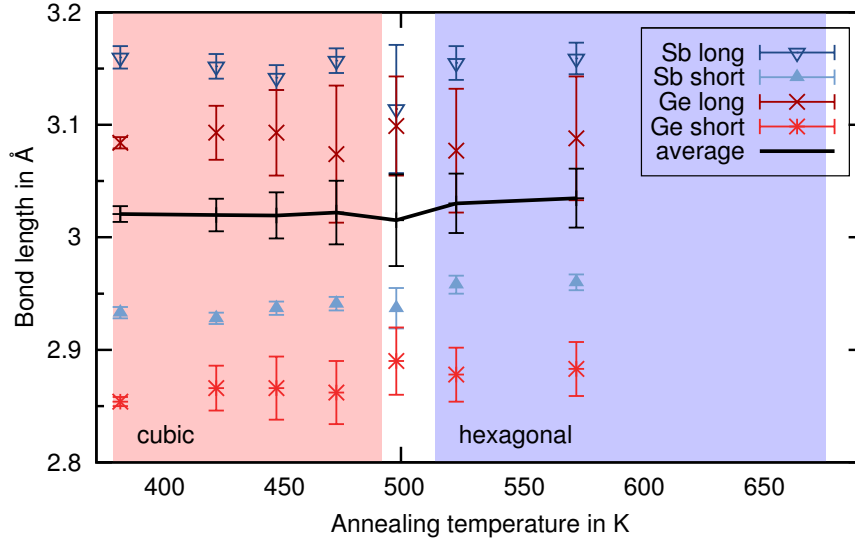


Figure 3.10: SRO in crystalline GeSb_2Te_4 : The resulting nearest neighbor distances obtained from fitting EXAFS data are plotted as a function of the annealing temperature. It is observed that within the meta-stable cubic phase, the average bond length (black line) remains rather unaffected, but the average atomic displacement (i.e. the difference between long and short bond) decreases (cf. Fig. 3.11).

All EXAFS data of crystalline GeSb_2Te_4 can be fitted using the model presented earlier, since the residuals for all annealing temperatures between 425 K and 575 K are each below 0.025. The resulting parameters are plotted as a function of temperature in Fig. 3.10. The average interatomic distance, $\langle d \rangle$ can be calculated from the individual atomic distances by

$$\langle d \rangle = 0.5 \cdot (x_{\text{Ge-Te}} (d_1 + d_2) + x_{\text{Sb-Te}} (d_3 + d_4)). \quad (3.10)$$

Here, the parameters x denote the fraction of a particular bond and d_1 and d_2 are the short and long bond around Ge, respectively. The plotted data show that this average bond length is very constant over the whole range of annealing temperatures. The data also show that a clear tendency exists for the short bond lengths to increase with increasing annealing temperature. This increase is mostly compensated by a shortening of the longer atomic distances, so that the average bond length remains almost unchanged. This means, in con-

clusion, that the amplitude of atomic displacements is reduced upon annealing. This reduced splitting between short and long bonds is considered to be responsible for the increase in EXAFS first peak height upon annealing the crystalline phase.

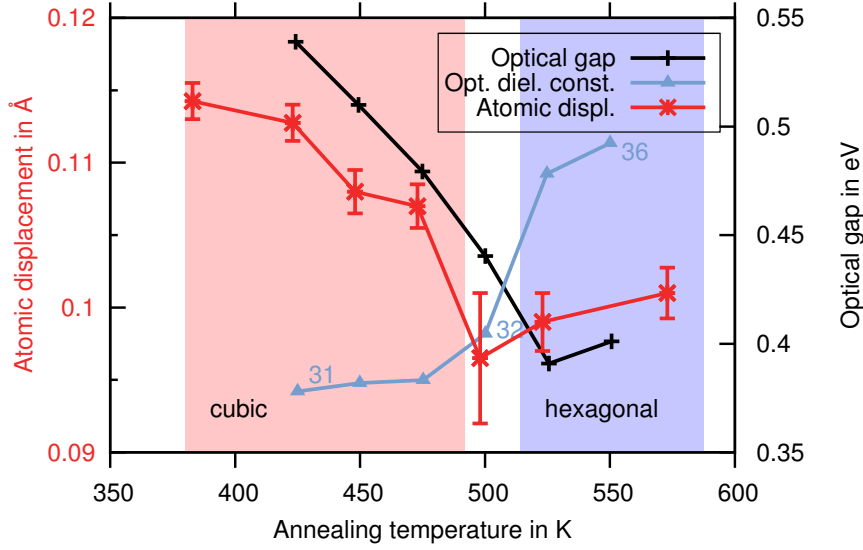


Figure 3.11: The average atomic displacements in GeSb_2Te_4 and the optical band gap [117] correlate for different annealing conditions. This correlation between both parameters is likely due to the Peierls distortion mechanism, which opens the band gap. The optical dielectric constant is also plotted for comparison (blue line and numbers). The latter number increases rather suddenly at the cubic-hexagonal phase transition and is therefore more likely controlled by the length of atomic chains along the cubic 111-direction. The transition temperatures for the cubic-to-hexagonal transition are taken from the study by Siegrist et al. [21].

The difference between the shorter and the longer nearest neighbor distance equals twice the displacement length of an atom from its ideal lattice site. This displacement length δd is defined by

$$\delta d = 0.5 \cdot (x_{\text{Ge-Te}} (d_2 - d_1) + x_{\text{Sb-Te}} (d_4 - d_3)). \quad (3.11)$$

and is plotted in Fig. 3.11 as a function of annealing temperature. A clear trend of decreasing local disorder can be seen in the meta-stable cubic phase. The hexagonal phase, however, shows the reverse trend. The figure also contains the optical band gap, as measured by FTIR (cf. [117], p. 126), which clearly follows the magnitude of the local atomic disorder, with a slightly shifted temperature scale. This shift might be due to the different sample preparation techniques and the different film thicknesses in particular. The correspondence of the two curves could have been expected from the Peierls distortion model. The Peierls mechanism opens an electronic gap by decreasing the energy of the occupied states and increasing the energy of unoccupied states, which actually does not cost energy. This usually occurs during the displacement of an atom from an octahedral coordination along the 111-direction. The theory of atomic displacements in IV-VI narrow-gap semiconductors has been worked out

by Enders in an interesting series of papers (cf. [41] and Ref. therein) based on an LCAO approach. He found that the band gap E_g is described by

$$E_g = 2|\Delta + i2\xi\omega| + \delta E_g, \quad (3.12)$$

where Δ denotes the ionic gap opening, ξ is the resonance integral, ω is the displacement amplitude $\omega = 2\frac{\delta d}{\sqrt{3}\langle d \rangle}$. δE_g is an additional term due to spin-orbit interaction and chain hybridization. It is reasonable to assume that both, Δ and δE_g remain unchanged, so that a direct relation is obtained between the optical band gap and the displacement amplitude. The resonance integral ξ of the pp σ -chains is in good approximation constant during the annealing series, since the average atomic distance $\langle d \rangle$ is unchanged (cf. Fig. 3.10). The formula can reproduce the relationship between ω and E_g very well with the parameters $\Delta = 0$ due to the low ionicity of GST. The resonance integral $\xi = 5$ eV, which is a value larger than that of GeTe ($\xi = 4$ eV) and Sb ($\xi = 3.7$ eV). Due to spin orbit coupling, $\delta E_g = -0.35$ eV.

To conclude, it was shown that the local atomic distortions are decreased during annealing the meta-stable crystalline phase. The strong scaling effect with the optical band gap can be described as a variable Peierls distortion and originates from the large resonance integral ξ . The Peierls distortion is due to an instability of the lattice against an atomic displacement. Since the amplitude of this distortion, ω is controlled by an elastic and an electronic part, we can further analyse the origin of the annealing dependence. Enders reported the distortion to have the magnitude

$$\omega^2 = \underbrace{4 \exp\left(-\frac{\pi\kappa_0}{8\xi}\right)}_{\text{elastic}} - \underbrace{\frac{\Delta^2}{4\xi^2}}_{\text{electronic}}. \quad (3.13)$$

Since all quantities of the electronic part are unaffected by changing the annealing temperature, it must essentially be the lattice rigidity κ_0 , which changes upon annealing. In conclusion, the lattice becomes harder upon increasing the annealing temperature.

Once the hexagonal phase is reached, however, the displacements start to increase again. Although it is tempting to correlate it with the opening of the band gap, the Fermi energy is shifted into the valence band, once the hexagonal phase is formed. Therefore, the Peierls mechanism can no longer be easily applied. However, there is no obvious reason why the Peierls mechanism should work only for exactly half filled bands. It is left for further theoretical investigations if the Peierls mechanism could be involved here as well. It might be tempting to relate the changes in the band gap also with the changes in electronic resistivity, but it is well known that the carrier densities reported in literature do not depend much on annealing temperature [21]. Therefore, only a negligible fraction of the charge carriers can be thermally excited.

3.12 Annealing dependence of the PDF of crystalline GeSb₂Te₄

In the previous sections, several trends of the structural rearrangement upon annealing were already found: Local atomic displacements in the meta-stable cubic phase of GeSb₂Te₄

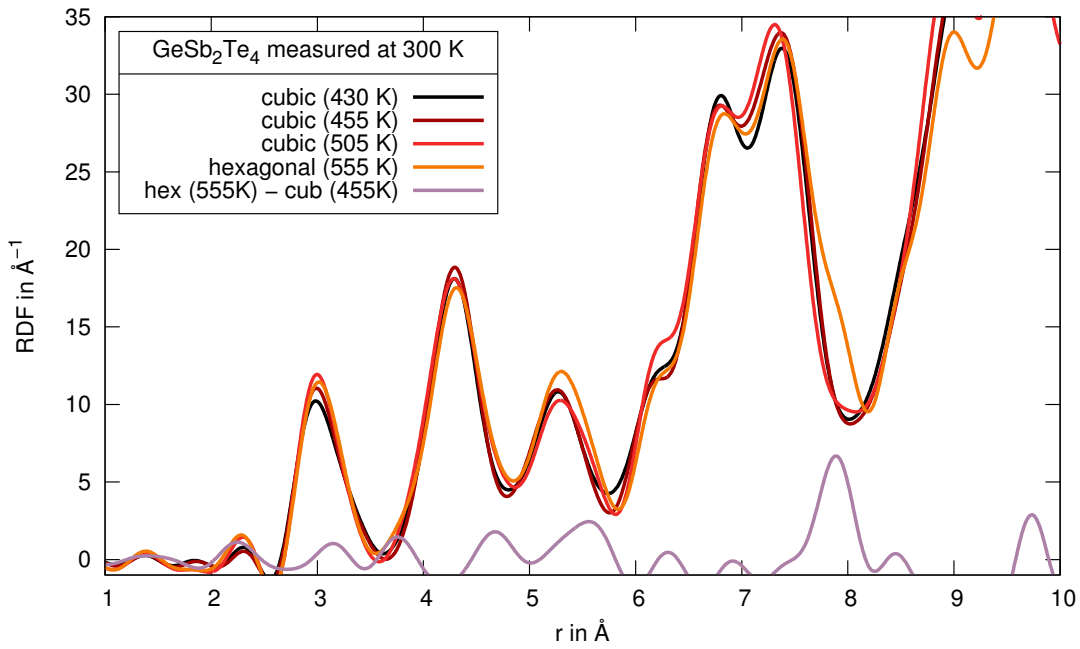


Figure 3.12: Radial Distribution Functions of crystallized GeSb₂Te₄ measured at 300 K for different annealing temperatures.

were shown to decrease based on an EXAFS analysis and atomic rearrangements of Ge and Sb atoms within the stable hexagonal phase were found by investigating the Bragg reflections from XRD. These analysis were based on an exact evaluation of individual nearest neighbor distances – the strength of EXAFS – and from the change of lattice parameters – the strength of XRD. In order to investigate trends in coordination numbers, the method of choice is the pair-distribution function (PDF) analysis. It also delivers information on atomic medium range distances between 3 Å and 12 Å, which is beyond the scope of EXAFS. At these distances, the unique fingerprint of the block structure of the hexagonal phase can be expected, so that an annealing series based on PDF analysis should allow following the formation of the hexagonal block structure. The essential questions of this section are therefore: **How does the coordination number change during the transformation to the hexagonal phase and when is the block-structure of the hexagonal phase formed?**

The PDF analysis is based on the knowledge of the structure factor $S(Q)$ over a large Q -range. This data set can be Fourier transformed in order to obtain its radial distribution function (RDF). These RDFs have been obtained from neutron scattering on phase-change materials at ambient conditions [118]. The neutron scattering experiments have been performed by P. Merkelbach, G. Bruns and H. Fischer at D4, ILL, Grenoble. The RDF of GeSb₂Te₄ has been measured at 300 K for the as-deposited amorphous and crystalline phases. They are shown in Fig. 3.12 for different annealing conditions of the material. Trends in the data of the crystalline phase have been related to a pronounced disorder on the local scale, which might be related to the metal-insulator transition [21].

The coordination number has been obtained by integrating the RDF to its first minimum

Table 3.5: The RDF of crystalline GeSb_2Te_4 was measured by neutron scattering at ambient conditions. This table shows the results of an integration up to 3.75 \AA (coordination numbers) and from fitting a Gaussian peak function (peak width FWHM and average nearest neighbor distance).

Annealing temperature	Avg. bond length	Peak width	Coord. No. (Integration)
cubic 430 K	$3.02(1) \text{ \AA}$	0.36 \AA	4.85
cubic 455 K	$3.02(1) \text{ \AA}$	0.34 \AA	4.85
cubic 505 K	$3.02(1) \text{ \AA}$	0.33 \AA	4.84
hexagonal 555 K	$3.04(1) \text{ \AA}$	0.34 \AA	4.99

at 3.63 \AA . The resulting numbers are presented in Tab. 3.5 and remain rather unchanged for different annealing temperatures, so that the increase in peak height observed in Fig. 3.12 has to be attributed to the reduction of the distribution width, which is also shown in Tab. 3.5 and is in line with the observation from EXAFS, that the amplitude of local distortions decreases. A similar comparison for the amorphous phase and in particular a comparison of both phases will be presented in Chtp. 4.2. Coming back to the coordination numbers, a slight increase is observed upon transformation to the hexagonal phase. This effect will be briefly discussed in the following. In a perfect cubic structure, it should equal six, but it is well known that the vacancies on the Ge/Sb sublattice reduce the coordination number because it contains 25% vacancies. This leads to an average coordination number of 5.25. The experimental value after annealing at 430 K is 4.85. The origin of this difference cannot be determined from this analysis.

In the stable hexagonal phase, the average coordination number of nearest neighbor distances remains unchanged. This can be seen from the data in Fig. 3.13 and it is further confirmed by the integration over the first peak. Looking for differences upon annealing, the most striking change occurs at about 8 \AA , whose origin shall be discussed in the following. When the hexagonal phase is formed, the vacancies arrange in a planar geometry so that layers of larger spacing exist. The spacing of atoms (Te-Te distances) across this layer is 3.75 \AA [49]. Their partial coordination number is only 0.75 and its fingerprint can be observed in the measured RDF from the difference curve of the cubic and hexagonal phases (cf. purple line). Since it cannot be discriminated easily from the first peak, this was a strong motivation to perform measurements at lower temperature. Nevertheless, it is worth highlighting the results that **it was experimentally shown that the coordination number remains unchanged during the cubic to hexagonal phase transition in the GST compounds.**

So far, the large difference at 8 \AA has not been explained, but we will see that it is of the same origin as the peak at 3.75 \AA , which was discussed before. A purely geometrical investigation of the distances across the vacancy layers is visualized in Fig. 3.13 and reveals that additional distances are formed at 5.72 \AA and 7.97 \AA . Their total contribution to the coordination number is 1.7 and 8.6, respectively. An integration over the difference between

the RDFs (cf. purple curve in Fig. 3.13) gives 7.9 for the peak around 8 Å. Since the expected value of 8.6(1.0) is obtained rather well, we can conclude that **the formation of vacancy layers can be observed from the height of the RDF at 7.97 Å, which shows that most of the vacancy layers ($\geq 90\%$) are formed during the transition from the cubic to the hexagonal phase.** A combined measurement of the RDF and the electronic resistivity could provide valuable insight on the changes in resistivity, which are accompanied by the formation of vacancy layers.

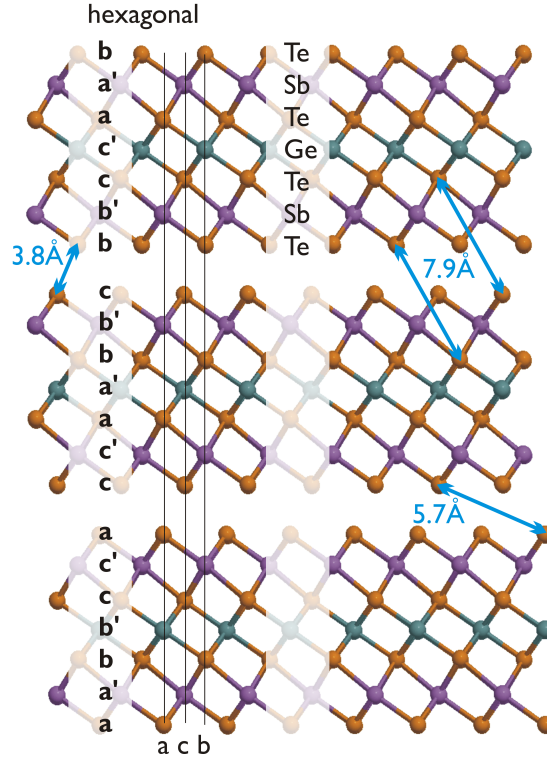


Figure 3.13: Atomic distances in GeSb_2Te_4 across the layer, to which the vacancies have diffused. The distances shown here can be seen as extra peaks in the RDF of the hexagonal phase and are particularly easy to observe in the purple difference curve in Fig. 3.12.

The trend of an increasing average bond length, which was predicted from the EXAFS data in Sec. 3.11 is consistently found in the analysis of the RDF as well. In particular, its increase upon the transition to the hexagonal phase is reproduced, cf. Tab. 3.5.

It was suggested earlier, that measurements at lower temperatures reduce the width of peaks in the RDF and thereby reveal more features of the local atomic structure. The data shown in Fig. 3.14 were therefore measured for different annealing conditions at low temperatures of 10 K. This time, $\text{Ge}_2\text{Sb}_2\text{Te}_5$ was measured in order to investigate a material with similar contributions from Ge and Sb. The samples were prepared in the meta-stable cubic phase by annealing at 450 K. The higher temperature annealing steps were performed in an external furnace under vacuum conditions at the ILL in steps of approx. 50 K, but without a clear reference temperature so that no precise temperature values can be given

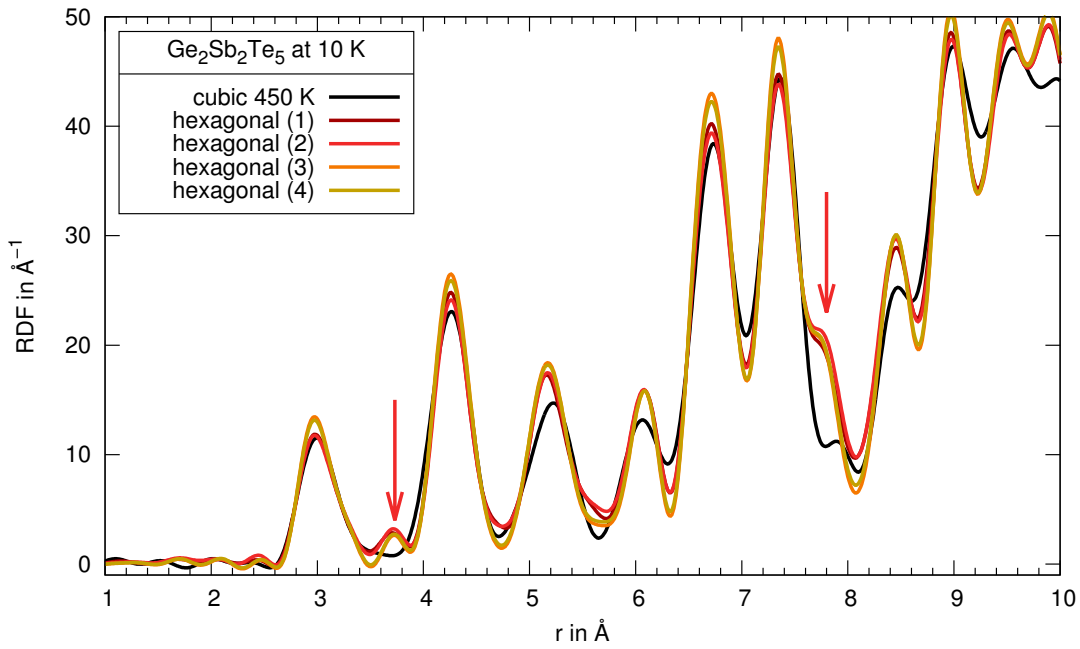


Figure 3.14: Radial Distribution Functions of crystallized $\text{Ge}_2\text{Sb}_2\text{Te}_5$ were measured at 10 K. New interatomic distances are formed in the hexagonal phase (red arrows) and originate from the different atomic spacing across the vacancy layer. The curves hexagonal (1) to hexagonal (4) originate from an annealing series, but the annealing temperature during this measurement was not sufficiently reliable to report it here. The temperature spacing between the different annealing temperatures is approx. 50 K.

here.

The resulting data are depicted in Fig. 3.14 and indeed, the overall information content has increased as compared to the measurements at ambient conditions (compare Fig. 3.12). An analysis of the annealing effect will be performed for $\text{Ge}_2\text{Sb}_2\text{Te}_5$ as well, but the temperature scale of the furnace, which was used to anneal the samples was for some reason rather poorly defined so that the samples were already in the hexagonal phase after annealing them significantly below the transition temperature of 599 K. The most striking additional feature at 10 K is the peak at 3.75 Å in the hexagonal phase, which is highlighted with a red arrow and originates from the formation of vacancy layers. The additional difference at 7.97 Å is observed very clearly as well. Since no continuous annealing was performed, it is not possible to determine a temperature window for the transition from the cubic to the hexagonal phase.

An increase in the average atomic coordination number is observed again, which has to be compared to the ideal coordination number in $\text{Ge}_2\text{Sb}_2\text{Te}_5$, 5.4. This coordination number is only reached in the hexagonal phase and the deviation in the cubic might be due to the remaining atomic density between the first and second peaks, which most likely results from some particularly long Sb-Te bonds, which were not included in the counting

Table 3.6: The results from a RDF analysis for different annealing conditions of $\text{Ge}_2\text{Sb}_2\text{Te}_5$ are summarized and a trend of slightly decreasing bond lengths and peak width is observed, which suggests that the substitutional disorder is reduced upon annealing. The coordination number increases only slightly during the cubic to hexagonal transition. Due to the slightly asymmetric distribution function of nearest neighbors, the average bond length was extracted by integrating the RDF to half the total coordination number reported.

Annealing temperature	Avg. bond length	Peak width	Coord. No. (Integrated)
cubic 450 K	3.015(3) Å	0.420(3) Å	5.2(1)
hexagonal (1)	2.995(3) Å	0.400(3) Å	5.4(1)
hexagonal (2)	2.995(3) Å	0.405(3) Å	5.5(1)
hexagonal (3)	3.000(3) Å	0.375(3) Å	5.4(1)
hexagonal (4)	3.000(3) Å	0.380(3) Å	5.4(1)

of nearest neighbors.

3.13 Conclusions from Annealing trends in GeSb_2Te_4 from real space

The atomic microstructures of crystalline GeSb_2Te_4 and $\text{Ge}_2\text{Sb}_2\text{Te}_5$ have been reported in literature and have been compared based on the difference between the well-defined meta-stable cubic and the stable hexagonal phase. The analysis in the preceding sections has revealed that subtle, but significant structural differences exist within the meta-stable phase after different annealing conditions (and timescales). Similar dependencies were observed in the stable phase as well. This section is included to summarize these findings and to interpret them based on their relevance for the disorder induced metal-insulator transition.

A precise description of a disordered system must be based on a clear definition of the order, from which it falls short. For the phase-change material GeSb_2Te_4 , this definition must be based on the perfectly ordered hexagonal state, cf. Fig. 3.2. Let us now summarize the various sources of disorder one by one. The smallest increase in total energy occurs, if the Ge and Sb atoms are chemically mixed on the layers (about 3 meV/atom [106], [103]). Experimentally, this mixing is observed indirectly in XRD and in EXAFS: The lattice constant c_h increases with annealing temperature, which is compatible with the increasing ionic repulsion of the building blocks. The most direct evidence of the remaining atomic mixing of Ge and Sb atoms on the layers even in the hexagonal phase comes from a comparison of EXAFS spectra and DFT-based atomic relaxations. The DFT calculations are based on an atomic model with 1008 atoms and was relaxed using CP2K [103] [119]. The EXAFS spectra of these models was calculated using a custom made code including a Debye model

to include atomic displacements. These data are shown in Fig. 3.15 for two different atomic models: In the first (ordered Ge/Sb), the layers are sorted and contain only one specific element. In the second (mixed Ge/Sb), the layers contain both, Ge and Sb atoms. It is easy to see that the structure with mixed layers is in much better agreement with the experimental data than the ordered one. This suggests that mixed layers of Ge and Sb are observed after annealing sputter deposited GeSb_2Te_4 at 575 K. At even higher temperatures, the layers might obtain higher degree of ordering.

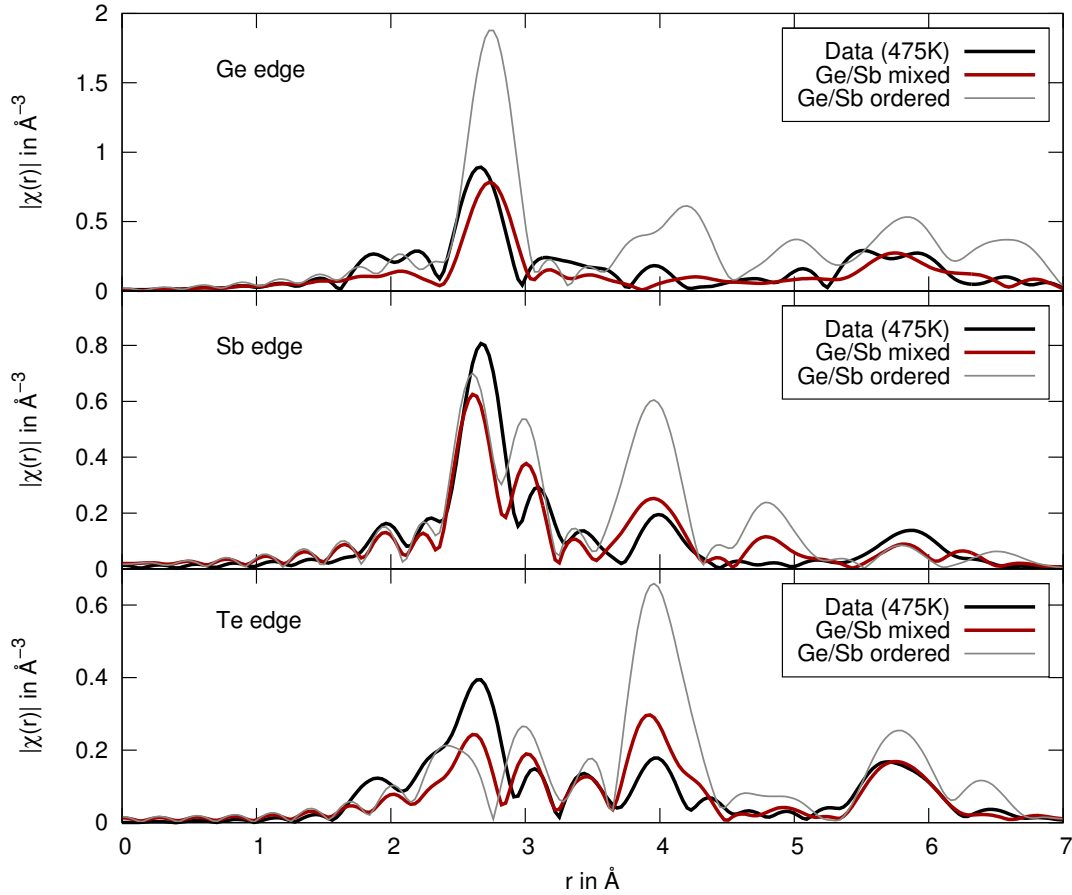


Figure 3.15: A comparison of calculated and measured EXAFS data of hex. GeSb_2Te_4 . The calculated data originate from a model after DFT-based atomic relaxation for ordered and mixed layers of Ge/Sb. A comparison to the experimental data after annealing at 575 K shows that they are incompatible with the spectra of perfectly ordered GeSb_2Te_4 .

At lower annealing temperatures around 570 K, the XRD pattern of the stable hexagonal phase shows some broadened reflections, which originate from irregularities in the stacking sequence of layers. These stacking faults are removed upon heating the samples to higher temperatures, because the reflex width decreases. The nature of these stacking faults cannot be resolved from the present data, but it is worth mentioning that a modification of the stacking sequence is responsible for the significant change of the diffraction pattern from

the cubic to the hexagonal phase (cf. Fig. 3.2).

In the hexagonal phase even after lowest annealing conditions, the majority of vacancies are ordered on layers. This was observed from total neutron scattering data, where an additional shoulder at 7.97 Å was uniquely attributed to atomic distances between the building blocks. It was shown by DFT-based calculations, however, that already a filling of the vacancy layers by 10% atoms leads to the formation of localized states, which are expected to turn the system insulating. It would therefore be very important to observe the ordering of vacancies with high accuracy, but the absence of scattering from the vacancies makes it experimentally almost impossible to reveal their ordering.

An analysis of EXAFS data for different annealing conditions revealed that a large amplitude of local atomic distortions is maintained during the entire annealing series. This distortion was derived from the difference between shortest and longest nearest neighbor spacings for the Ge-Te and Sb-Te distances. An initial reduction of this displacement amplitude by annealing the meta-stable cubic phase does not continue in the stable hexagonal phase. In conclusion, a change in the amplitude of atomic displacements cannot be responsible for the metal-insulator transition. However, the direction of these displacements might still change from random displacements in the meta-stable cubic phase to aligned displacements along the hexagonal c -axis. Therefore, no unique mechanism for the reduction of disorder along the metal-insulator transition could be revealed – however, several experimental observations reveal the nature of the disorder in crystalline GeSb_2Te_4 and proof that the configurational entropy due to the substitutional disorder continuously decreases upon increasing the annealing temperature – even within the hexagonal phase.

CHAPTER 4

Structure contrast between amorphous and crystalline phase-change materials

4.1 Motivation

Data storage in phase-change memory devices is based upon cycling between the amorphous and the crystalline phase, where the time-limiting process is the crystallization. This does not deviate in its fundamental principle from the crystallization of SiO_2 or Si, but whereas SiO_2 and Si crystallize very slowly even at elevated temperatures, the transition is several orders of magnitude faster in phase-change materials. To point this out even more clearly, the maximum growth velocities of these materials can be compared. It turns out that crystals in Si grow with a maximum velocity of 10^{-2} m/s [120], 10^{-9} m/s in SiO_2 [121] and more than 1 m/s in the phase-change material $\text{Ge}_2\text{Sb}_2\text{Te}_5$ [122]. There are also several chalcogenide glasses, which are good glass formers, so that the question is naturally derived, why phase-change materials crystallize so rapidly. A first step in the analysis of the crystallization process follows the suggestion "If you want to understand function, study structure!", by the Nobel price winner Francis Crick, who has revealed the structure of the DNA. In phase-change materials, this study is based upon the initial amorphous and the final crystalline atomic structures. It will be very difficult, however, to derive the crystallization mechanism from the atomic ordering, but some hints from the analysis of atomic structure on thermodynamic properties exist and will be discussed later.

In good glass forming materials, the local order is usually preserved upon crystallization and the contrast originates mostly from the absence of long-range order. It is natural to wonder, whether this also applies to phase-change materials. It is already known from

literature, that the atomic configuration of both phases is different: The average bond length in amorphous $\text{Ge}_2\text{Sb}_2\text{Te}_5$ (GST) prepared by quenching from the melt was reported to be 2.73 \AA , whereas in the same study, the meta-stable crystalline phase was reported to possess an average bond length of 2.87 \AA [31]. This corresponds to an increase of 5% upon crystallization, but the average bond length of the crystalline phase is not compatible with the lattice constant obtained from XRD, which is between 3.00 \AA and 3.02 \AA , cf. Tab. 3.1. After this initial result, no comprehensive study of the local atomic environment in both phases, amorphous and crystalline, was reported in literature. This lack of consistent data was the motivation to study the local atomic arrangement in different phase change materials in the amorphous and in the crystalline phase. Some of these results were subsequently published [73] and will be discussed in more detail in the following for many phase-change materials. The fundamental task is to find out, **whether a motif exists, that distinguishes the structural contrast between amorphous and crystalline PCMs from that of common glass forming materials.**

In addition to this fundamental question, it is often written that some PCMs like GeTe and $\text{Ge}_2\text{Sb}_2\text{Te}_5$ crystallize in a nucleation dominated way, whereas Sb-based materials like $\text{Ag}_4\text{In}_3\text{Sb}_{67}\text{Te}_{26}$ crystallize growth dominated. This difference is indeed suggested by TEM images, which are depicted in Fig. 1.3. They were obtained after recrystallizing areas of the respective material by short (ns) laser pulses. On these length scales, however, the dominant mechanism can be observed from the many tiny crystallites in $\text{Ge}_2\text{Sb}_2\text{Te}_5$, which imply that the crystal growth velocity is actually low. In $\text{Ag}_4\text{In}_3\text{Sb}_{67}\text{Te}_{26}$ (AIST), on the other hand, larger crystallites are observed – indicating that only few nucleation events were necessary for the nuclei to grow all over the heated volume. Therefore, a distinction is commonly made between nucleation- and growth dominated materials. It has to be kept in mind, however, that the dominating mechanism inside a phase-change memory cell depends on the geometry of the cell – most significantly on the ratio of interfaces to volume. In this way, even in the nucleation dominated material GeTe, features of growth dominated crystallization were observed [8]. This observation, however, does not affect the basic crystallization mechanism with nucleation and growth processes, which can be clearly distinguished from optical switching experiments as shown in Fig. 1.3. The models for nucleation and growth are briefly described in Chpt. 6.1.1 to be controlled by a specific activation energy ΔG . This theory relies on a macroscopic model of the crystalline nuclei and microscopic properties of the atomic bonds are not taken into account. Unfortunately, no established model exists so far, which links the observed activation energy ΔG to microscopic potential barriers. Since the crystallization process is a rearrangement of atoms, a full understanding of crystallization is only possible once microscopic models exist. There has been quite some advance in this respect recently, when it became possible to simulate the crystallization of a PCM based on AIMD. These simulations have to be checked against experiments and therefore, it is of particular importance to know the microscopic structure of PCMs with great accuracy. Furthermore, a knowledge of the atomic structure allows calculating the potential barriers for atomic rearrangements (nudged elastic band calculations). In this respect, different

atomic structures in the amorphous phase will have different potential barriers for atomic rearrangements. Due to the absence of a microscopic model for crystallization, there is a lack of design-rules for fast crystallization. In order to derive such design rules, kinetic, thermodynamic and structural data should be available to model the microscopic transition process. In this respect, a knowledge of the amorphous – crystalline contrast of GST and AIST systems will be of particular interest, since it is already known from macroscopic properties that those materials crystallize differently. Therefore, this chapter will answer the questions, **how are the atoms in amorphous GST (or GeTe) and AIST (or Sb_2Te) arranged and how does this local structure compare to the respective local configurations of the crystalline phase?** To answer these questions, EXAFS and PDF analysis will be employed.

4.2 Amorphous and Crystalline GeSb_2Te_4 and $\text{Ge}_2\text{Sb}_2\text{Te}_5$

The atomic structure of crystalline GeSb_2Te_4 was already discussed in the preceding chapter. In the following, a detailed analysis of the amorphous phase will follow so that both phases can be compared at the end of this section. The amorphous phase has been measured by EXAFS at 10 K sample temperature and by neutron total scattering.

4.2.1 Amorphous GeSb_2Te_4 and $\text{Ge}_2\text{Sb}_2\text{Te}_5$

EXAFS analysis of amorphous GeSb_2Te_4

A significant number of publications have focussed on the atomic structure of amorphous GeSb_2Te_4 or $\text{Ge}_2\text{Sb}_2\text{Te}_5$. The results of these studies are summarized in Tab. B.2 and will be discussed in the following. Both compounds are reported to show the same structural features with only small variations in magnitude. The different preparation techniques should be distinguished: The melt-quench (MQ) phase is usually obtained in AIMD studies and can be prepared experimentally by rapidly quenching the liquid phase, e.g. applying short laser pulses to thin films of the material on a substrate with reasonable thermal conductivity. The as-deposited (AD) structures are usually investigated in experiments, since the sputtered films are amorphous but they might be more disordered than the melt-quenched samples. Tab. B.2 shows, however, that there is no significant difference between the MQ and AD amorphous phases, since the average bond lengths of Kolobov et al. (entry no. 12) and Baker et al. (entry no. 13) are equal. Furthermore, no significant differences were found at the Ge K-edge for AD and MQ samples [123].

The collection of results in Tab. B.2 further shows that most AIMD simulations (1-7) agree very well in the fact, that the coordination numbers of Sb and Te are larger than those from experiments (9-13). All experimental studies derive coordination numbers, which are consistent with the 8-N rule. A particularly interesting case is the calculation (8), which was performed on $\text{Si}_2\text{As}_2\text{Se}_5$. After the simulated quench, the atoms were replaced by $\text{Ge}_2\text{Sb}_2\text{Te}_5$ and the resulting atomic positions and the geometry of the cell were relaxed.

Tab. B.2 shows that this is the only AIMD simulation, where the resulting coordination number of Te (2.1) is in good agreement with experiment (2.0). All other AIMD simulations lead to an average coordination of the Te atoms of 3.0(1), which is far outside the experimental error bars. Similar arguments can be made for Sb, but not for Ge.

After this summary of controversies from literature, we can turn to a discussion of the additional data, which were obtained by EXAFS experiment with a sample temperature of 10 K. This low measurement temperature reduces the MSRD parameters for the coordination shells and might reveal additional atomic distances in the samples. In particular the large atomic distances of $\approx 3.15 \text{ \AA}$, which are related to the distorted octahedral coordination of Ge-Te bonds, might be revealed and might explain the deviation of bond lengths between AIMD simulations and experiments.

The resulting EXAFS data are shown together with a fit in Fig. 4.1. The fit was performed as described in 2.7.4 and is based on the constrained scattering paths shown in Tab. 4.1. This refinement is based on a dominating contribution of Ge-Te and Sb-Te bonds and few additional bonds of Ge-Ge and Ge-Sb type. It is worth mentioning that a single distance with even a small variance was sufficient to describe the dominating Ge-Te and Sb-Te interatomic distances. This means in particular, that no evidence of distorted octahedral configurations with short and long bonds could be evidenced in amorphous GeSb_2Te_4 for both, Ge and Sb atoms. This configuration is frequently reported for Ge atoms in amorphous GeSb_2Te_4 based on AIMD calculations [124], but no experimental evidence for octahedrally distorted coordinations was shown so far. On the other hand, a tetrahedral arrangement of Ge atoms was proposed to explain the local geometry of the amorphous phase, since the measured interatomic distances around Ge are well in line with the tabulated values for the covalent radii of Ge and Te – which is not the case for the results of AIMD calculations, where the Ge-Te distances turn out to be about 5% longer than the experimental value. After all, no experimental evidence exists in literature for any of both local configurations. Even at 10 K no longer atomic distances were revealed by the measurements. Although this could be a problem with the EXAFS technique, the good agreement of the averaged bond lengths from EXAFS and the result from neutron total scattering (where the peak area is directly proportional to the number of atoms at that distance), cf. Figs. 4.2 or 4.3, shows that there is a real deviation between experiments and computer simulations based on AIMD. With an averaged resulting residual of 0.008 (clearly below 0.02), the refinement can be considered reliable and the resulting parameters can be compared with the data from literature¹.

In order to compare the coordination numbers from Tab. 4.1 with those from literature, the given numbers have to be divided by the amplitude reduction factors S_0^2 of the crystalline phase. These numbers can be transferred from measurements of the same element in a crystal with similar bonding conditions, but well known coordination numbers. Due to the complex distortion pattern in crystalline GeSb_2Te_4 , those amplitude reduction factors have significant uncertainties and should not be employed here. In this discussion, the

¹The edge energy corrections between theory and experiment turned out as $\Delta E = 4.1(2) \text{ eV}$, $9.6(4) \text{ eV}$ and $7.7(6) \text{ eV}$ for Ge, Sb and Te, respectively

Table 4.1: Interatomic distances in amorphous GeSb_2Te_4 at 10 K. It can be seen that Ge-Te and Sb-Te strongly dominate over other 'wrong' bonds.

Scattering Path	$N \cdot S_0^2$	Distance	Displacement Parameter
Ge-Ge	0.2(1)	2.49(2) Å	0.000(4) Å ²
Ge-Sb	0.4(2)	2.67(1) Å (c)	0.001(2) Å ²
Ge-Te	1.9(3)	2.60(1) Å (a)	0.004(1) Å ² (a)
Sb-Ge	0.2(1)	2.67(1) Å (c)	0.001(2) Å ²
Sb-Te	2.0(1)	2.839(3) Å (b)	0.0033(3) Å ² (b)
Te-Ge	0.6(1)	2.60(1) Å (a)	0.004(1) Å ² (a)
Te-Sb	1.0(1)	2.839(3) Å (b)	0.0033(3) Å ² (b)

amplitude reduction factors of the binary systems will be used. In this way, S_0^2 of Ge and Te is obtained from crystalline GeTe as 0.67(6) and 0.86(8) [113]. The corresponding value for Sb is obtained from crystalline Sb_2Te_3 as 0.68(6), where all Sb atoms are in a distorted octahedral coordination with three short and three long bonds [125]. The resulting elemental coordination numbers N are 3.7(3), 3.2(3) and 1.9(1). These values are given as entry no. 17 in Tab. B.2 and agree well with the average coordination numbers from other experimental techniques. If all atomic nearest neighbor distances are observed in this EXAFS analysis, the resulting average bond lengths should correspond to the result of a PDF analysis. Such an analysis was performed based on total neutron scattering data and is presented in the following.

PDF analysis of amorphous GeSb_2Te_4

The RDF(r) of amorphous GeSb_2Te_4 has been measured at ambient conditions and is depicted in Fig. 4.2, black curve. A clear peak can be observed at approx. 2.8 Å and is related to the average nearest neighbor in the compound. Since it has an almost Gaussian shape, it can be reproduced by refining all parameters of the following function,

$$y = \frac{A}{w \sqrt{\pi/2}} \exp\left(-2\left(\frac{r - r_0}{w}\right)^2\right). \quad (4.1)$$

Here, r_0 is the bond length, w is related to the mean-square relative displacement (MSRD) parameter used in EXAFS analysis (cf. 2.97) via $\sigma^2 = 0.25 \cdot w^2$. The area parameter A directly gives the partial coordination number of the respective contribution. The first peak in this RDF is rather broad ($\sigma^2 = 0.036(1) \text{ Å}^2$ ($w = 0.381(2) \text{ Å}$)) and has a slightly asymmetric Gaussian shape with an area of 2.85(1) atoms – slightly more than what is expected from the 8-N rule: 2.80 atoms². The aim of this measurement was to find out if the average bond lengths obtained from PDF analysis is in line with the result from the

²Please mind that this value is larger than the average coordination number of GeSb_2Te_4 with 8-N coordination (2.57 atoms) due the larger neutron scattering length of Ge

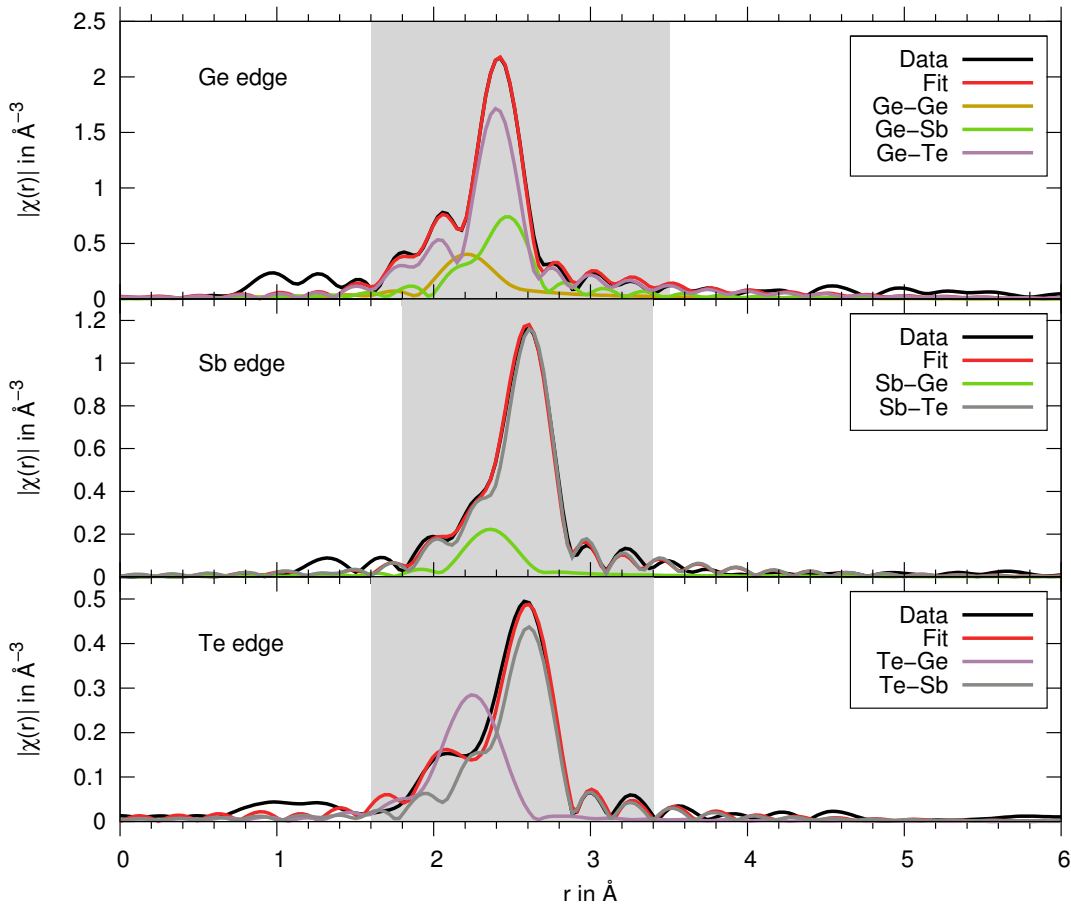


Figure 4.1: Fourier Transforms of EXAFS data (black) of as-deposited amorphous GeSb_2Te_4 at 10 K. The fit (red) consists of several scattering paths from atoms on the first neighboring shell. No peaks from higher shells are visible in the data. Bond lengths and Displacement parameters of all equal scattering paths have been constrained. The resulting R-factor is 0.008. Homopolar bonds between Sb and Te cannot be distinguished from heteropolar Sb-Te bonds, so that Sb-Sb and Te-Te scattering paths were not taken into account because their error would be large.

previous EXAFS analysis (2.75 Å). Therefore, the average nearest neighbor distance was obtained from the RDF by integrating it over the distance until half the coordination number is reached. The resulting distance is 2.78(1) Å, a value which has to be compared against the partial atomic distances from EXAFS weighted by the neutron scattering lengths. The resulting value for the EXAFS data is: 2.74(1) Å. This deviation is of the order of the commonly observed thermal expansions for the EXAFS data taken at 10 K and the PDF analysis performed at 300 K: A linear coefficient of thermal expansion of $5 \cdot 10^{-5} \text{ K}^{-1}$ applied to the result from EXAFS would predict an average bond lengths of 2.78 Å at ambient conditions, which is well in line with the observed result.

Due to the smooth and featureless Gaussian shape, no partial contributions can be de-

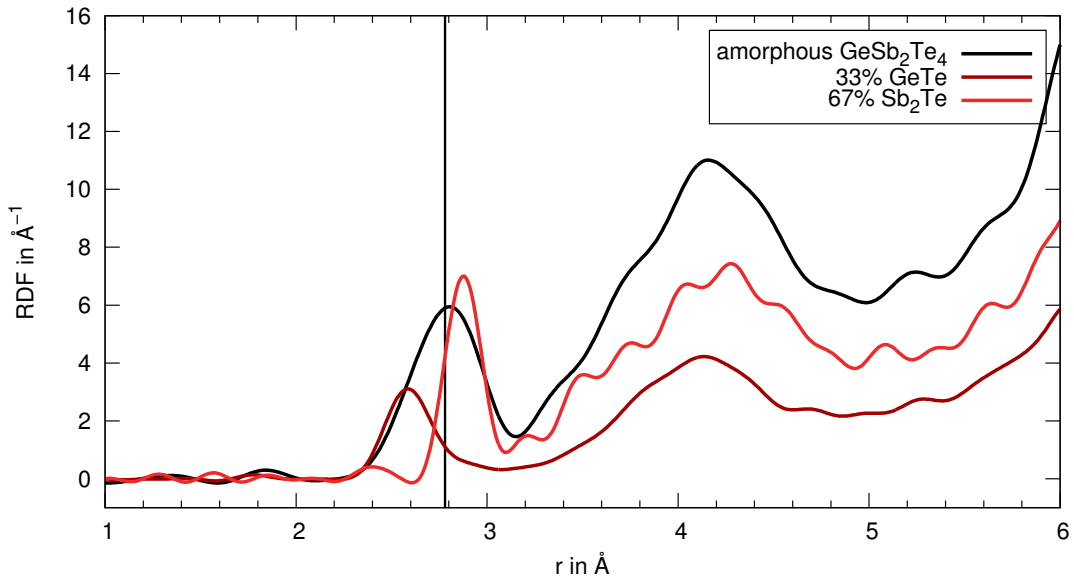


Figure 4.2: Radial Distribution Functions of as-deposited amorphous GeSb_2Te_4 measured at ambient temperature. The plot also contains the RDFs of as-deposited amorphous GeTe and Sb_2Te for comparison of the bond lengths. Those data are rescaled to reproduce approximately the number Ge-Te and Sb-Te distances in GeSb_2Te_4 . It is clearly visible that the range of bond lengths in GeSb_2Te_4 extends over both partial contributions. The black vertical lines denotes the averaged bond lengths derived from the EXAFS analysis of samples at 10 K.

rived from the RDF. It is, however, instructive to compare the RDF of amorphous GeSb_2Te_4 to those of amorphous GeTe and Sb_2Te^3 – also measured at ambient conditions and presented for comparison with a weighting factor in Fig. 4.2. It becomes clear that their average bond lengths could be well contained within the first coordination shell of amorphous GeSb_2Te_4 . Since it was observed during EXAFS measurements, that a lot more information can be obtained by cooling the sample to 10 K, the same approach has been applied in Neutron PDF analysis as well.

Amorphous $\text{Ge}_2\text{Sb}_2\text{Te}_5$

Total neutron scattering experiments were also performed on amorphous $\text{Ge}_2\text{Sb}_2\text{Te}_5$ at low temperatures of 10 K. $\text{Ge}_2\text{Sb}_2\text{Te}_5$ was used in this measurement due to its equal atomic fraction of Ge and Sb atoms. The resulting $\text{RDF}(r)$ of $\text{Ge}_2\text{Sb}_2\text{Te}_5$ is depicted in Fig. 4.3, black curve and will be discussed in the following. A visual analysis of the first peak alone suggests the higher information content of these data. It can be seen well, that the first peak is composed of two contributions and it was decomposed into two Gaussian distributions, Eq. 4.1. The bond lengths corresponding to the two nearest neighbor distances (blue curve

³The comparison should be based on a dataset of Sb_2Te_3 , but the latter compound cannot be prepared in an amorphous phase by means of sputter deposition, because its crystallization temperature is too closely above ambient temperature.

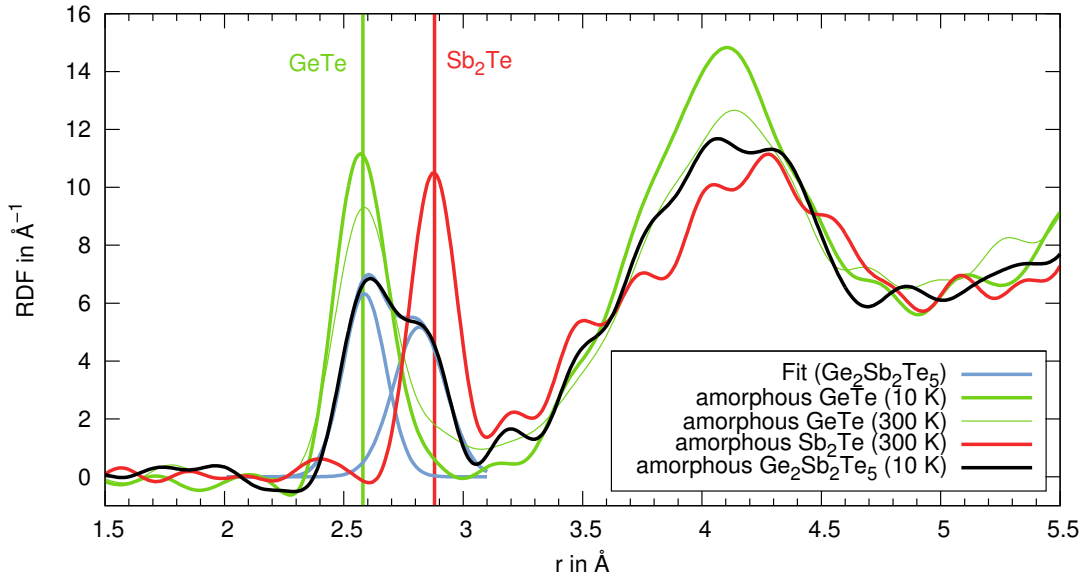


Figure 4.3: Radial Distribution Functions of as-deposited amorphous $\text{Ge}_2\text{Sb}_2\text{Te}_5$ and GeTe measured at 10 K together with as-deposited amorphous Sb_2Te , measured at 300 K. The data of $\text{Ge}_2\text{Sb}_2\text{Te}_5$ are decomposed to two Gaussian peaks (blue). Of these two Gaussians, the first compares very well to the average first neighbor distance in as-deposited amorphous GeTe at 2.58 Å, while the second corresponds well to the average distance in Sb_2Te at 2.88 Å. These values are further indicated by vertical lines and are in good agreement with those obtained from an EXAFS analysis for Ge-Te and Sb-Te distances in amorphous GeSb_2Te_4 at 10 K (2.60 Å and 2.84 Å).

in Fig. 4.3) are 2.586(6) Å and 2.816(8) Å. They contribute partial coordination numbers of $A_1 = A_2 = 1.4(1)$ for both. This is well in line with the result of a numeric integration of the RDF up to the first minimum at 3.05 Å, which results in an average coordination number of $A = 2.78$. The widths w of the two fitted Gaussian are 0.180(6) Å and 0.22(1) Å, respectively. Since it is well known from EXAFS analysis, that Ge-Te distances are shorter than Sb-Te bond lengths in GeSb_2Te_4 (cf. Sec. 4.2.1), the two partial contributions can be related to Ge-Te and Sb-Te nearest neighbor distances. This is further supported by the good agreement with the RDFs of amorphous GeTe at 10 K and of amorphous Sb_2Te at ambient conditions. Let us assume in the following, that this assignment of nearest neighbor distances is indeed correct. Then, the areas under the peaks can be related to actual partial coordination numbers $A_{i,j}$ by taking into account the neutron scattering lengths b_i . It holds that the partial coordination numbers are weighted by

$$A = \sum_{i,j} c_i c_j b_i b_j A_{i,j}. \quad (4.2)$$

If only Ge-Te and Sb-Te distances are taken into account, the ratio of scattering from Ge-Te to Sb-Te is simply

$$\frac{c_{\text{Ge}} c_{\text{Te}} b_{\text{Ge}} b_{\text{Te}} N_{\text{Ge,Te}}}{c_{\text{Sb}} c_{\text{Te}} b_{\text{Sb}} b_{\text{Te}} N_{\text{Sb,Te}}} = 1.45 \quad (4.3)$$

Table 4.2: Local atomic arrangement in amorphous and crystalline Ge₂Sb₂Te₅

	$\langle r \rangle$	σ^2	N
Amorphous phase	2.72(1) Å	0.008 Å ² and 0.012 Å ²	2.78(3)
Crystalline phase	3.02(1) Å	0.044 Å ²	5.23(5)
Change	+11%	+340%	+88%

This ratio does not agree with the equal number of scattering events observed experimentally for both contributions so that we have to conclude that the two Gaussian peaks do not distinguish Ge-Te from Sb-Te distances. Therefore, this splitting must have a different origin. We know from the EXAFS analysis, that no atomic nearest neighbor distances exist around Sb, which are short enough in order to contribute to the first peak. Therefore, we can ask how many Ge-Te distances have to contribute to the second peak in order to obtain the observed ratio of scattering events in those peaks. We can do this by including an extra Ge-Te contribution to the previous equation, contributing for a fraction x of the atoms:

$$\frac{c_{\text{Ge}}c_{\text{Te}}b_{\text{Ge}}b_{\text{Te}}N_{\text{Ge,Te}}(1-x)}{c_{\text{Sb}}c_{\text{Te}}b_{\text{Sb}}b_{\text{Te}}N_{\text{Sb,Te}} + xc_{\text{Ge}}c_{\text{Te}}b_{\text{Ge}}b_{\text{Te}}N_{\text{Ge,Te}}} \stackrel{!}{=} 1. \quad (4.4)$$

It follows that a fraction of $x = 0.15(3)$ of the Ge-Te distances contribute to the second peak.

4.2.2 Comparison of amorphous and crystalline GST-compounds

The experimental EXAFS and PDF data for amorphous and crystalline GST compounds are compiled in Fig. 4.4. This figure shows that an unexpectedly large change of the local atomic arrangement occurs upon crystallization. The change regards all parameters of the local atomic coordination: Nearest neighbor distances $\langle r \rangle$, their variance σ^2 and the coordination numbers N . These parameters are summarized in Tab. 4.2.

Also a common semiconductor glass crystallizes at elevated temperature – usually with a lower growth velocity, but the fundamental thermodynamic principles are the same. This also applies to pure amorphous Ge, which has been studied in detail. There, the coordination number in the amorphous phase is found to be 4.0(2) and remains 4.0 upon crystallization. At the same time, the average bond length slightly decreases from 2.47 Å to 2.45 Å and its variance disappears almost totally. This behavior is also found in heavier elements, like e.g. GaSb [126] and reflects the common atomic rearrangement upon crystallization in common semiconductors with $\langle n_{\text{sp}} \rangle = 4$.

In PCMs, all of these differences are reversed: The average bond length increases by as much as 11%, while simultaneously the atomic displacement parameter increases. Furthermore, the average coordination number increases almost by a factor of two. It is natural to wonder, if this trend holds for all PCMs and therefore, several more materials will be discussed in the following. However, before continuing with this task, let us investigate the surprising increase in local disorder in more detail. This investigation is essentially based on the displacement parameter from EXAFS, which measures the variance of interatomic

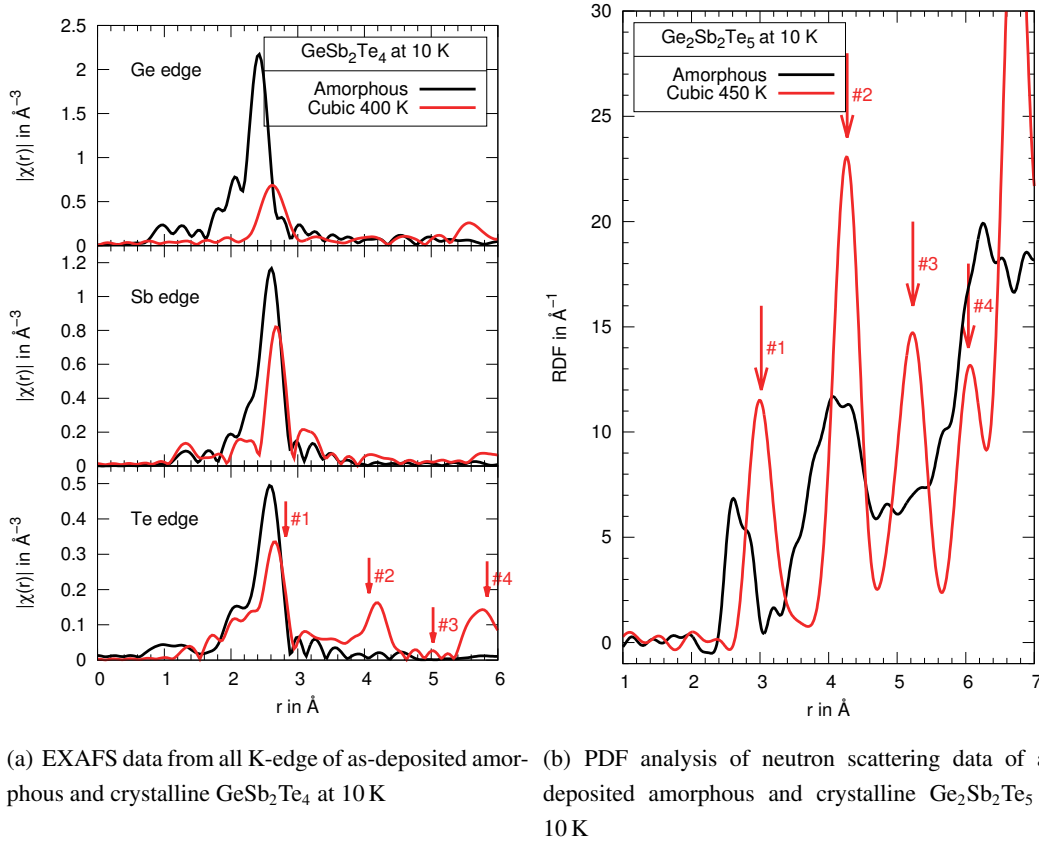


Figure 4.4: The local order in amorphous and crystalline GST-compounds shows several significant differences: In EXAFS, the height of the first peak shows a rarely observed decrease upon crystallization, which is due to the larger variance of nearest neighbor distances in the crystalline phase. This shows that the crystalline phase shows a less well defined local atomic coordination than the amorphous phase. Both techniques consistently show that the average nearest neighbor spacing – in particular that around Ge – increases upon crystallization. The PDF analysis further shows that the average coordination number increases significantly upon crystallization. The Te-EXAFS data of the crystalline phase show a lower height of the odd numbered peaks, which is related to the lower amplitude of atomic displacements on the Te sublattice, as compared to the Ge/Sb/Vac-sublattice.

distances. The variance most surprisingly increases upon crystallization – even for samples measured at 10 K, where thermal vibrations are almost absent. This effect implies that the local atomic configuration of the amorphous phase contains more well defined next nearest neighbor distances than the corresponding crystalline phase, although the amorphous phase is disordered, whereas the crystalline phase shows a well defined cubic lattice. Therefore, crystalline GeSb_2Te_4 and $\text{Ge}_2\text{Sb}_2\text{Te}_5$ show a record-large amplitude of static atomic displacements. These displacements are most likely induced by substitutional disorder on the Ge/Sb/Vacancy sublattice. The total amount of disorder in this materials is sufficient even to

induce insulating behavior by localizing the charge carriers [21]. So far, the measurement of atomic displacements was conducted at low temperature, so that mostly static displacements were observed. Under real conditions, additional thermal disorder occurs due to atomic vibrations. It will be interesting to compare the amorphous and crystalline phases at ambient temperature in order to see whether still the crystalline phase has a larger variance of interatomic nearest neighbor distances. Therefore, EXAFS measurements of both phases were performed at various temperatures.

4.2.3 Temperature dependence of EXAFS spectra of GeSb₂Te₄

The variance of the average nearest neighbor distance, i.e. the MSRD parameter σ^2 , was observed to be larger in the crystalline phase and since the data were obtained at only 10 K, the fundamental atomic displacements must be of static nature. With increasing temperature, the amplitude of average atomic displacements increases and its slope can be used to derive an approximate value for the Debye temperature, cf. Eq. 2.56, to which an additional offset σ_0^2 has to be added, which takes into account the static displacements. The Debye temperature θ_D is a valuable quantity, since it is directly related to the thermal conductivity,

$$\kappa = \frac{1}{3} C_p v_l l, \quad (4.5)$$

where C_p is the specific heat at constant pressure, v_l the longitudinal speed of sound and l the phonon mean free path. The Debye temperature enters via the temperature dependence of the specific heat, which dominates the thermal conductivity at low temperatures. Even at elevated temperatures, thermal conductivity is observed to roughly follow [127]

$$\kappa \propto \langle m \rangle \Omega^{1/3} \Theta_D^3, \quad (4.6)$$

where Ω is the volume of the unit cell and $\langle m \rangle$ is the average mass of the atoms.

Therefore, temperature dependent EXAFS measurements have been performed and the resulting data are shown in Fig. 4.5 for the Te edge of GeSb₂Te₄. Upon reducing the temperature, there are two most significant changes in the data. The height of the first peak increases and finally at 10 K, new features become visible in the crystalline phase. These additional features have already been taken into account during the least squares fitting and this result motivated us to continue measuring phase-change materials only at this low temperature in the following. The change in peak height is surprisingly larger in the crystalline phase. This is remarkable, since according to Eq. 2.85, the peak height is mostly dominated by the displacement parameter σ^2 , which usually changes linearly with temperature and the slope of this linear dependence indicates the softness of the interatomic potentials. And since the crystalline phase shows a higher slope of MSRD vs. temperature, we have to conclude that the interaction potential is weaker in the crystalline phase. This point will be discussed further in Sec. 5.

A quantitative evaluation of such EXAFS data for the amorphous phase shows that its displacement parameter indeed depends only weakly on temperature, cf. Fig. 4.6. The

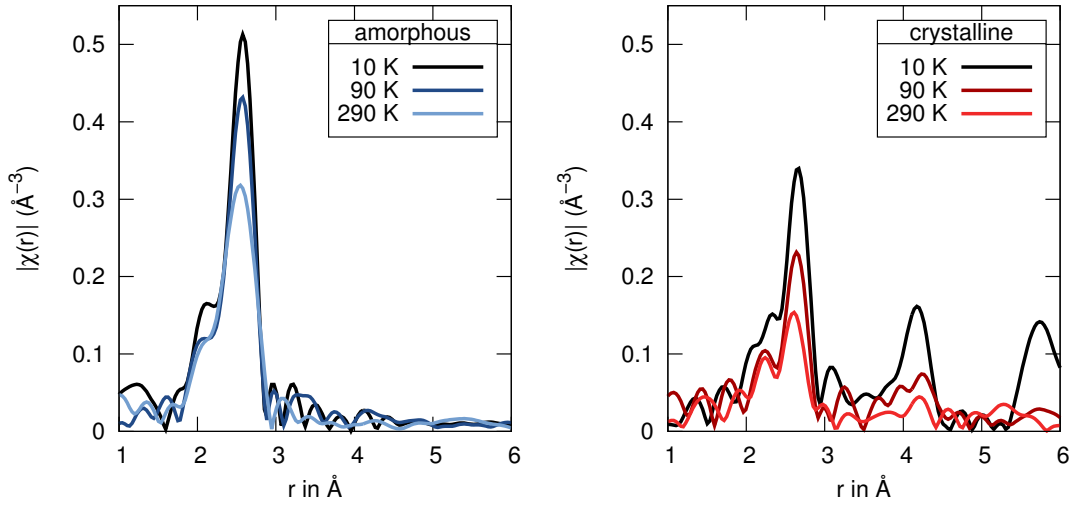


Figure 4.5: EXAFS spectra of the Te K-edge of GeSb_2Te_4 measured at different temperatures. A higher data content is obtained upon reducing the measurement temperature of the crystalline phase to 10 K, where larger interatomic distances are revealed. A more pronounced temperature dependence of the peak heights is observed in the crystalline phase [114]. This indicates that the atomic interaction potentials soften upon crystallization.

displacement parameter of the crystalline phase can be better obtained from XRD measurements, since no ambiguity of the treatment of short and long bonds exists: The difference between short and long bonds is observed in XRD as an additional static contribution to the displacement parameter, whereas in EXAFS, separate displacement parameters are defined for the short and long bonds. Although this splitting in EXAFS does not influence the temperature dependence of the displacement parameters, the determination of exact values is hampered by the overlap of both atomic distances.

The displacement parameter of $\text{Ge}_2\text{Sb}_2\text{Te}_5$ is depicted in Fig. 4.6, where indeed a stronger temperature dependence is observed for the crystalline phase. This strongly indicates that the atomic interaction potential softens upon crystallization. Fitting the Debye model to these data results in a Debye temperature of 155(5) K for both, Ge/Sb and Te data. The static displacement parameter σ_0^2 , however differs from $0.07(1) \text{ \AA}^2$ for Te to $0.17(1) \text{ \AA}^2$ for Ge/Sb. In the amorphous phase, the lower slope leads to a significantly higher Debye temperature of 300(30) K. This result is rather surprising, because it is commonly expected that the Debye temperature increases upon crystallization - even in chalcogenide materials [128]. As discussed in Sec. 2.8, acoustic modes with long wavelengths do not contribute as significantly to EXAFS data as to XRD data. This might also decrease the slope of the displacement parameter of the amorphous phase, which was measured by EXAFS. It is therefore necessary to measure the density of phonon states of phase-change materials. These measurements will be presented in Chpt. 5.

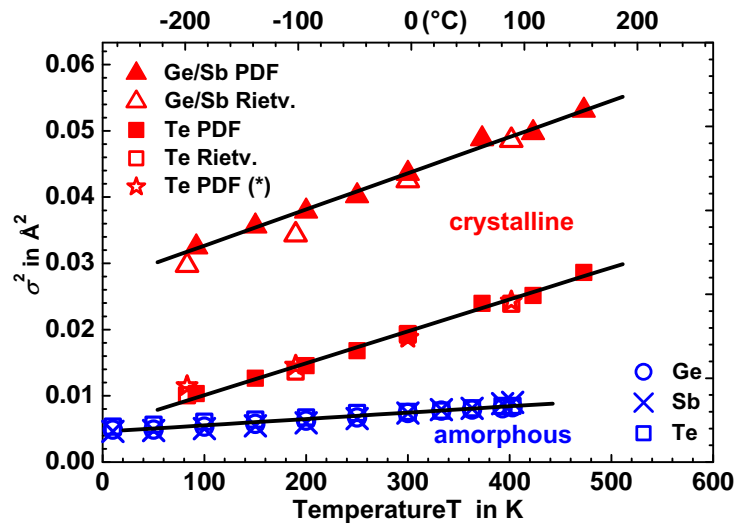


Figure 4.6: Displacement parameter σ^2 of $\text{Ge}_2\text{Sb}_2\text{Te}_5$ as a function of temperature. Indeed, a larger temperature dependence is observed in the crystalline phase, based on both Rietveld and PDF analysis. EXAFS data were analysed to determine the atomic displacements in the amorphous phase.

4.3 Amorphous and Crystalline GeTe

Let us return to the initial question, if the structural contrast differs among the phase-change materials. The compound GeTe was reported to crystallize on the time-scale of only nanoseconds [8] and due its binary composition, it should be a preferred material for investigations of its local atomic arrangement. The composition of the material investigated here is $\text{Ge}_{53}\text{Te}_{47}$, as obtained from Rutherford backscattering spectroscopy (RBS) [129]. The crystalline phase of this material at 10 K has been investigated in detail by J. van Eijk [113] and was found to follow the $R\bar{3}m$ space group, with lattice parameters $a = 4.27(1)$ Å, $\alpha = 58.4(1)$ and $u = 0.528(1)$. In addition, 7(4)% of the Ge-atoms were found to phase separate upon crystallization of GeTe. This result is well in line with the 6% excess Ge obtained from the stoichiometry of the investigated materials, leaving the GeTe-phase without a significant contribution from additional vacancies. It was found that the minimum pulse duration for crystallization depends more critically on excess Te than on excess Ge [130], so that the essential fast crystallization mechanism is not affected by this off-stoichiometric composition. Given these information, the amorphous structure can be investigated to compare the start- and end-point of the crystallization transition.

4.3.1 Amorphous GeTe

The following analysis is partly based on the previous analysis by Julia van Eijk [113], but an additional scattering path is included, which turns out to be consistent with crystalline GeTe and a slightly lower residual is obtained. The EXAFS data of amorphous GeTe and the respective fits are shown in Fig. 4.7 together with the individual scattering paths. The

residuals for the Ge and Te edges are 0.002 and 0.009, respectively, which is clearly below the upper limit for a reliable fit of 0.02 so that the fitting model can be considered reliable. The technically caused edge energy corrections were obtained from the fit to be 3(1) eV and 7(1) eV at the Ge and Te edges, respectively. As will be discussed later, the model is based on Ge-Ge and several Ge-Te distances (i.e. scattering paths). In addition, some Te-Te bonds can be included to improve the quality of the fit at the Te edge. This improvement, however, is rather low and therefore, Te-Te bonds were not taken into account here (cf. [113] for a more detailed discussion). The amplitude reduction factors S_0^2 , which allow the determination of absolute coordination numbers, were taken from the crystalline phase of GeTe, where 0.67 and 0.86 are obtained for the Ge and Te edges, respectively (cf. Sec. A.3.1).

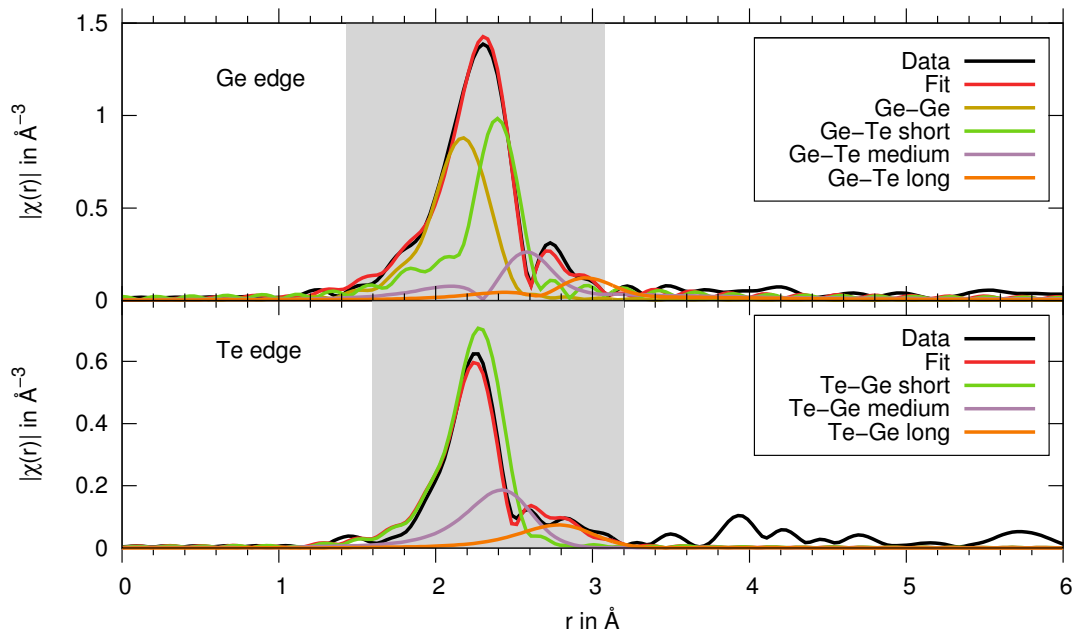


Figure 4.7: Amorphous GeTe at 10 K: The Fourier transformed EXAFS data (black curves) are shown for the Ge (upper figure) and Te (lower figure) K edges together with the refinement (red curve). The refinement consists of several scattering paths, which are included as well. The curves show nicely that the short Ge-Ge bonds are responsible for the broad first peak at the Ge edge and that the dominant contribution originates from bond lengths, which correspond to particularly short Ge-Te distances.

The results from the fitting of scattering paths is summarized in Tab. 4.3 and will be discussed in the following. While several binary amorphous materials contain only a single atomic nearest neighbor distance (cf. e.g. the analysis of amorphous SnSe_2 [59]), as many as four different scattering paths were necessary to reproduce the experimental data of amorphous GeTe. This can be expected already from the large width of the first peak especially at the Ge edge. This shows that Ge can exist in several different chemical environments. Most of the observed chemical environments of Ge involve bonds to Te. Indeed, these atomic distances are in good agreement with those obtained at the Te edge, so that both data sets

Table 4.3: EXAFS fitting parameters of amorphous GeTe at 10 K. These data show that Ge atoms are in various chemical environments. Parameters with the same letter in brackets were constrained.

Scattering Path	N	Atomic distance r	Displacement Parameter σ^2
Ge-Ge	1.7(2)	2.470(5) Å	0.0034(6) Å ²
Ge-Te (short)	1.4(3) (a)	2.604(6) Å (a)	0.0027(5) Å ² (a)
Ge-Te (medium)	1.0(0.5) (b)	2.77(3) Å (b)	0.008(6) Å ² (b)
Ge-Te (long)	1.0(0.5) (b)	3.15(2) Å (c)	0.011(7) Å ² (c)
Te-Ge (short)	1.4(3) (a)	2.604(6) Å (a)	0.0027(5) Å ² (a)
Te-Ge (medium)	1.0(0.5) (b)	2.77(3) Å (b)	0.008(6) Å ² (b)
Te-Ge (long)	1.0(0.5) (b)	3.15(2) Å (c)	0.011(7) Å ² (c)

were refined simultaneously by a model that constrained parameters as indicated in Tab. 4.3.

The amorphous phase of GeTe in this specific stoichiometry contains a significant quantity of short bonds (2.470(5) Å) around Ge. These can be identified as Ge-Ge bonds for three reasons: (i) No bonds exist at this short distance at the Te edge; (ii) the phase-shift during backscattering corresponds to backscattering from a lighter element (Ge, but not Te); (iii) the resulting bond length of 2.470(5) Å agrees with the Ge-Ge distance observed in pure amorphous Ge (2.468(5) Å [116]). In order to quantify the relative amount of Ge-Ge bonds, all scattering paths around Ge have to be analyzed first.

The next longer bond length is denoted "Ge-Te (short)" in Tab. 4.3. The EXAFS data analysis shows that the backscattering atoms at this distance are Te atoms. Their atomic distance of 2.604(6) Å agrees perfectly to those observed in amorphous GeSb₂Te₄ (2.60(1) Å cf. Tab. 4.1).

Furthermore, two longer bonds are obtained, which are denoted "Ge-Te (medium)" and "Ge-Te (long)". Their distances correspond rather well to the distorted octahedral environment observed in crystalline GeTe, where 2.863 Å and 3.127 Å are obtained for the short and for the long bond, respectively (cf. Sec. A.3.1). Their average, 2.96 Å, is in good agreement with the average of the crystalline phase of GeTe (2.99 Å). However, the difference between both is larger in the amorphous phase. This shows that octahedral sites can be even more strongly distorted in amorphous GeTe. This additional distortion corresponds to a static displacement of atoms, which can be described as a freezing of the atomic displacements induced by the thermal vibrations of the A₁ phonon mode in the crystalline phase of GeTe [131]. This A₁ phonon mode softens upon heating, and at the same time, the static distortion decreases. Finally, the energy of the phonon mode goes to zero at the $\alpha \mapsto \beta$ phase transition from a rhombohedral to a cubic phase. This shows that the magnitude of the distortion strongly depends on temperature (and pressure), which could explain the stronger distortion amplitude of defective octahedral Ge sites in amorphous GeTe.

All atomic distances, which were discussed so far based on the EXAFS data of the Ge edge were transformed to the Te edge and nicely reproduce those data as well, as can be seen in Fig. 4.7.

Let us continue with a quantitative discussion of the different chemical environments. According to the 8-N rule [132], the coordination numbers of Ge and Te are 4 and 2, respectively. Following this rule and assuming that heteropolar bonds are favorable over homopolar bonds, 50% of the Ge atoms should remain without bonds. It is therefore expected, that a large number of Ge-Ge bonds should occur in amorphous GeTe, but the situation is more complex, since the 8-N rule is broken in the amorphous phase of GeTe as well as in its crystalline phase. The total coordination numbers of amorphous GeTe are 5.1(8) and 3.4(8) for Ge and Te, respectively. They are in fact larger as expected from the 8-N rule due to the influence of distorted octahedral environments.

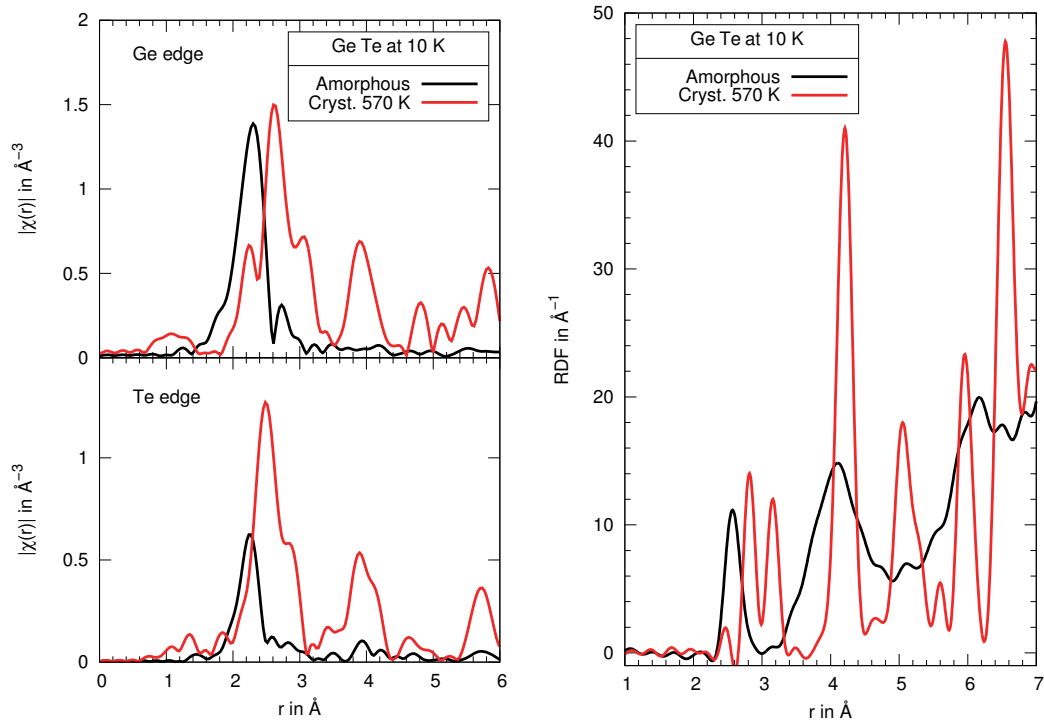
We can conclude that it is possible using EXAFS analysis to distinguish several distinct bond lengths, which are only 0.2 Å apart. This is a remarkable resolution and would not be possible by diffraction techniques, since the available Q -range of the signal is usually too short ⁴. Using EXAFS analysis and the connection between bond lengths and -angles, different coordination environments could be quantified.

4.3.2 Structural change upon crystallization in GeTe

A comparison of the local atomic ordering in amorphous and crystalline GeTe can be found in Fig. 4.8, containing EXAFS and PDF data. The EXAFS data show a different transition than in the GeTe-Sb₂Te₃ compounds: Upon crystallization, the height of the first peak increases – just as expected for more well defined nearest neighbor spacings in crystalline materials. Therefore, the crystalline phase of GeTe contains significantly less substitutional disorder than the related GST compounds. This is most likely related to the fact that the local atomic displacements in GeTe, which can be well observed in the RDF, are aligned in the same crystallographic direction. This alignment breaks the cubic symmetry and explains why the space group is $R\bar{3}m$ – just the same as the stable hexagonal phase of several GeTe-Sb₂Te₃ compounds. To conclude, GeTe directly crystallizes to the stable rhombohedral phase, without an intermediate meta-stable phase. The reason for the existence of this meta-stable phase will be discussed further in Chpt. 7.

It is worth mentioning that the atomic nearest neighbor distances of amorphous and crystalline GeTe hardly overlap, which underlines the magnitude of the change in average bond lengths. All related parameters are summarized in Tab. 4.4.

⁴More than $Q = 32 \text{ Å}^{-1}$ would be necessary to indeed resolve these contributions, but already above $Q = 12 \text{ Å}^{-1}$ hardly any features was observed in the neutron scattering experiments.



(a) EXAFS data from all K-edge of as-deposited amorphous and crystalline GeTe at 10 K (b) PDF analysis of neutron scattering data of as-deposited amorphous and crystalline GeTe at 10 K

Figure 4.8: Amorphous and crystalline GeTe at 10 K: A comparison of EXAFS and RDF data show that a significant increase of the nearest neighbor distance occur upon crystallization. There is hardly any overlap between the nearest neighbor peaks in the RDFs of both phases.

4.4 Amorphous and Crystalline AIST and Sb_2Te

All materials, which were discussed so far contained Ge. Another class of phase-change materials is based on Sb and well-known from its application in rewriteable DVDs. This compound is commonly referred to as AIST (in our case $\text{Ag}_4\text{In}_3\text{Sb}_{67}\text{Te}_{26}$, but slightly different compositions are used as well). It is essentially based on Sb_2Te , which has a rather low crystallization temperature of only 376 K ([133], p. 94; [51]). This temperature is too low for application and therefore, Ag and In have been added in order to increase the crystallization temperature to 451 K (cf. Fig. 7.5).

The crystallization in these Sb_2Te -based materials is usually considered growth-dominated. Indeed, the TEM images of a crystallized region show significantly larger grains than those of GST (cf. Fig. 1.3). In the absence of a microscopic theory for crystallization, it is helpful to find differences in the amorphous atomic arrangement of nucleation dominated and growth dominated materials. Since the activation barriers for local atomic rearrangements are given by the atomic coordinates, a knowledge of the latter would help to propose microscopic models of crystallization – in particular during the early formation of critical nuclei,

Table 4.4: Local atomic arrangement in amorphous and crystalline GeTe at 10 K

	$\langle r \rangle$ (PDF)	σ^2 (EXAFS)	N (PDF)
Amorphous phase	2.59(1) Å	0.0027(5) Å ² (short) 0.008(6) Å ² (medium) 0.0011(7) Å ² (long)	2.8(2)
Crystalline phase	2.99(1) Å	0.0031(3) Å ² (medium) 0.0049(4) Å ² (long)	5.4(4)
Change	+15(1)%	-60(10)%	+90(13)%

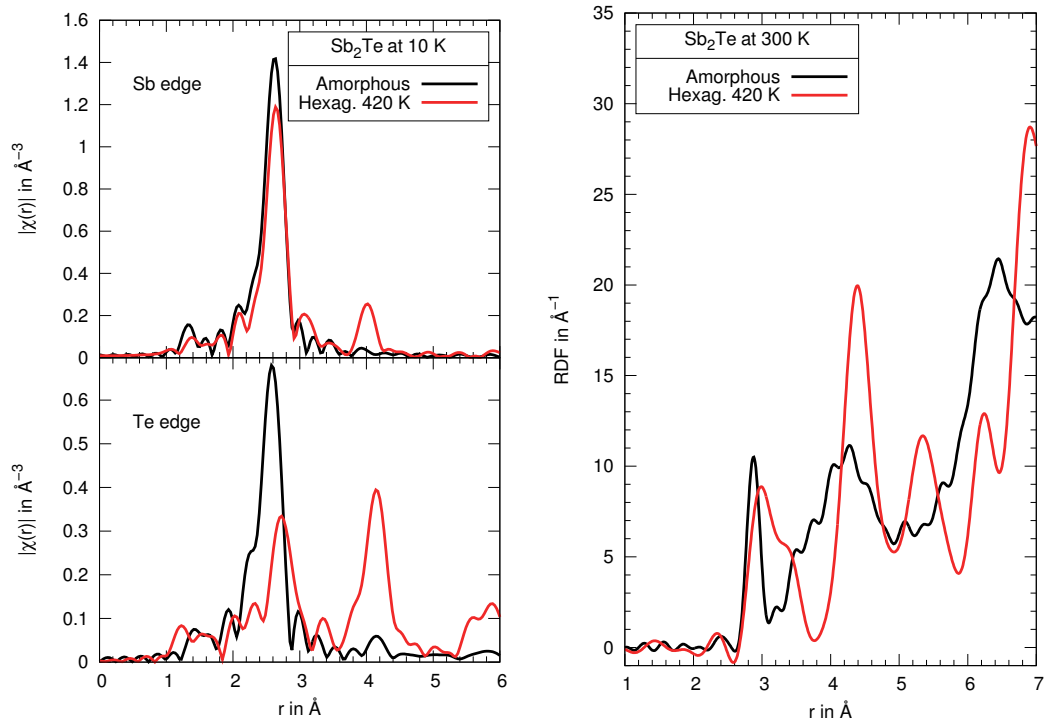
where the continuum approach of driving force of crystallization ΔG and the surface tension can only be crude approximations. Therefore, and because the property contrast between the amorphous and crystalline phases shall be investigated, EXAFS and total neutron scattering experiments have been performed on these Ge-free compounds. The resulting data for Sb_2Te are depicted in Fig. 4.9.

The amorphous phase of Sb_2Te has an average atomic nearest neighbor distance of 2.87(1) Å, which is larger than the sum of averaged covalent radii for Sb and Te, which is 2.77 Å [134]. Nevertheless, the coordination number of 2.6(2) is well in line with the 8-N rule, which predicts 2.7 nearest neighboring atoms. The crystalline phase has even longer average interatomic distances. Fig. 4.9 shows that an additional long bond forms upon crystallization, which significantly increases the coordination number.

The EXAFS data again show a decrease in the peak height upon crystallization, which – in the case of Sb_2Te – is related to an overlap of short and long atomic nearest neighbor distances in the crystalline phase. The displacement parameter σ^2 of the short distances remains almost identical upon crystallization (cf. Tab. 4.5). However, an additional longer nearest neighbor distance is established upon crystallization. This effect is hard to observe from the EXAFS data, since the large displacement parameter, 0.014(3) Å² significantly dampens the EXAFS oscillations. In the PDF data, however, these longer distances can be clearly observed. This transition shows, that the crystallization in Sb_2Te is accompanied by the formation of an additional, longer interatomic distance. This leads to an increase of the average nearest neighbor distance by 8%. It is worth mentioning that in Sb_2Te , there is a strong overlap of atomic distances in the amorphous and crystalline phases – in striking contrast to the behavior of GeTe, where no such overlap was observed.

4.5 Amorphous and Crystalline In_3SbTe_2

In_3SbTe_2 is another candidate for future phase-change memory devices. The ternary compound crystallizes at around 500 K, depending on the film thickness [54]. The crystalline phase is reported to show a rock-salt like structure with a lattice constant of 6.126(1) Å at 293 K, which results in a density of 6.95 g cm⁻³ [56]. It is well known that In atoms occupy



(a) EXAFS data from all K-edges of as-deposited amorphous and crystalline Sb_2Te at 10 K (b) PDF analysis of neutron scattering data of as-deposited amorphous and crystalline Sb_2Te at 300 K

Figure 4.9: Amorphous and crystalline Sb_2Te : A comparison of EXAFS data shows that the structural contrast between both phases is less based on a change of the nearest neighbor distances. Instead, the RDF's show that an additional longer bond forms in the crystalline phase, which was absent (not disordered) in the amorphous phase. This comparison nicely shows the complimentary use of EXAFS and PDF analysis, since the long nearest neighbor distances in the crystalline phase are too disordered to give a clear signal in the EXAFS data.

the first, and Sb and Te atoms the second sublattice. No information were found in literature on the ordering of the Sb and Te atoms on their sublattice. The crystalline phase is of rocksalt-structure and was prepared by sputter depositing thick films of 1400 to 1700 nm on microscope slide and scratching the film to powder. Subsequently, the powder was annealed under a constant flow of Ar gas at 533 K. The films of this thickness were found to be relatively unstable against crystallization and at several occasions, the sample preparation for EXAFS measurements crystallized the samples. Therefore, the EXAFS data of the as-deposited phase were obtained from thinner samples, whose preparation was described earlier (cf. Sec. 2.7.2).

4.5.1 Atomic structure of crystalline In_3SbTe_2

The refinement of EXAFS data for crystalline In_3SbTe_2 (IST) will be summarized in the following. The rocksalt-like structure consists only of In-Sb and In-Te bonds, so that only

Table 4.5: Local atomic arrangement in amorphous and crystalline Sb_2Te . Values denoted by * from ND, and ° from EXAFS. $S_0^2 = 0.7(1)$ was assumed to determine the coordination numbers from EXAFS data.

	$\langle r \rangle$	σ^2	N
Amorphous phase	2.87(1) Å*	0.0026(2) Å ² °	2.6(2)*
	2.870(2) Å °		2.3(3)
Crystalline phase	3.10(1) Å*		5.4(4)*
	2.909(4) Å(short) °	0.0028(4) Å ² (short) °	7(1) (of Sb)
	3.39(2) Å(long) °	0.014(3) Å ² (long) °	3.1(4) (of Te)
			5.7(6) (avg.) °
Change	+8%	±0% + longer distance	+108(15)%

these were taken into account during the fitting process. Indeed, single scattering paths were sufficient to refine the structure of this compound as can be seen from the comparison of experimental EXAFS data and the refinement in Fig. 4.10. According to the rock-salt structure, also larger atomic distances were taken into account during the fitting process in order to refine the higher order coordination shells as well.

An important observation in the meta-stable phase of GST was the large amplitude of local atomic displacements. These displacements are related to the substitutional disorder of both, vacancies and Ge/Sb atoms. This disorder was shown to be responsible for the insulating behavior of this compound, because it led to a localization of charge. We can now wonder if the same holds for IST, since Sb and Te atoms might be disordered as well. The resulting information from the EXAFS analysis are sufficient to reveal the nature of atomic displacements in IST, which will be discussed in the following. The In-Sb distances are shorter than the In-Te distances (which can be evidenced from the different nearest neighbor distances at the Sb and Te edges, respectively). This is well in line with the observations in GST, where shorter Ge-Te than Sb-Te distances are observed. However, in GST, a splitting to short and long Ge-Te and Sb-Te distances was observed, whereas no such splitting exists in IST. The absence of this splitting shows that in IST, the atoms on the In sublattice are displaced from their lattice sites with the Sb-In₆ octahedra (A) being smaller than the Te-In₆ octahedra (B). This size difference suggests that an approximately alternating sequence ABAB of these octahedra should prevail, because otherwise a large sequence of one type of octahedra AAAA would accumulate a too large lattice mismatch. Since no tetragonal lattice parameters are found by XRD, we can conclude that substitutional disorder exists for Sb and Te atoms on the anion sublattice. The displacement amplitude for atoms in IST is by far lower than that of GST and therefore, it resembles much closer the rock-salt structure, which is rather surprising when the charge carrier concentration $n = 1.2 \cdot 10^{22} \text{ cm}^{-3}$ [135], [54] is considered. This charge carrier density corresponds to as much as 0.34 electrons/atom.

The lattice constant resulting from the EXAFS analysis for IST at 10 K is 6.095(8) Å.

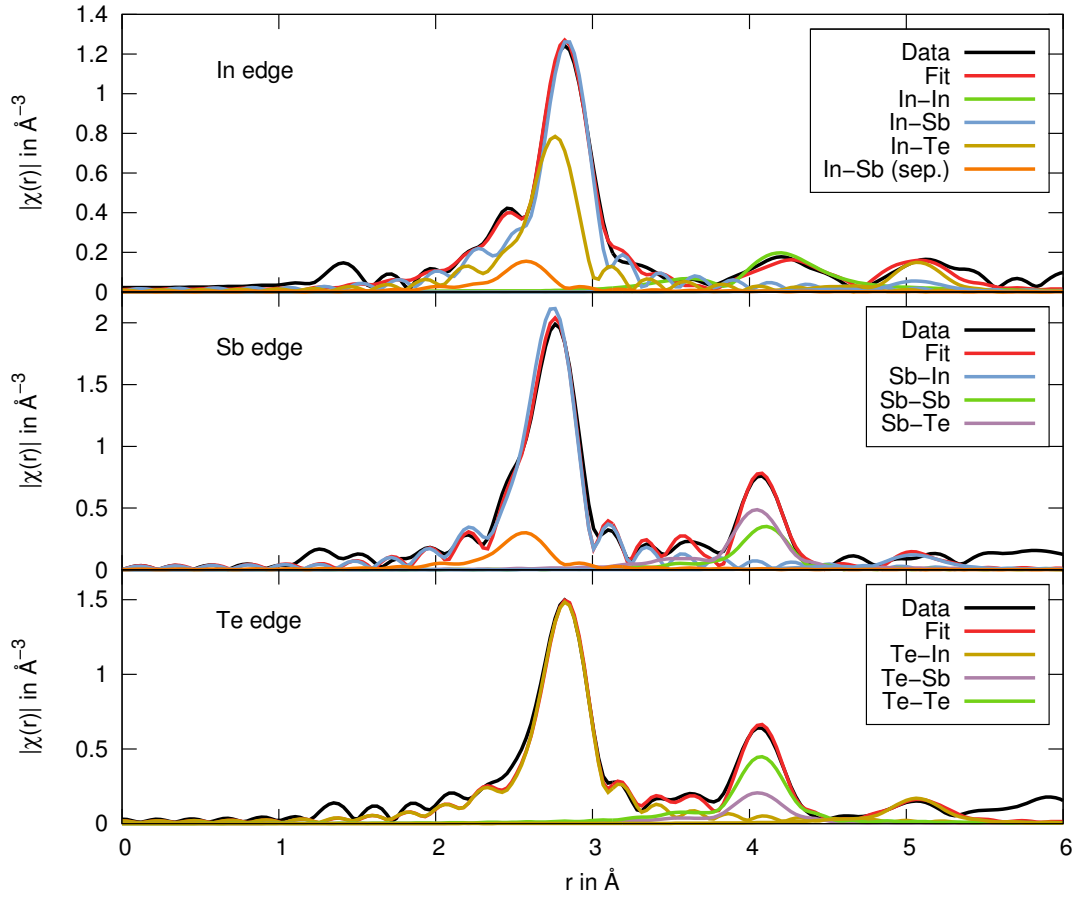


Figure 4.10: Fourier Transforms of EXAFS data (black) of crystallized In_3SbTe_2 at 10 K. The sample was annealed at 533 K. The fits (red) consist of several scattering paths at all edges and the crystal structure resembles rocksalt. Bond lengths and displacement parameters of all equal scattering paths (i.e. In-Sb and In-Te) have been constrained. The resulting total residual is 0.012. Some additional In-Sb bonds (orange) are related to segregated InSb. They improve the quality of the fit by 0.002 on the total residual and were observed by XRD at higher annealing temperature [135].

This result can be used to determine the coefficient of linear thermal expansion (CLTE) using the reference value by Deneke et al. [56] of $6.126(1) \text{ \AA}$ at 293 K. It turns out that the CLTE is $2.1(4) \times 10^{-5} \text{ K}^{-1}$. This number agrees well with the CLTE published in literature: $2.4 \times 10^{-5} \text{ K}^{-1}$ [136] and $2 \times 10^{-5} \text{ K}^{-1}$ (cf. [137]). The thermal expansion of In_3SbTe_2 is significantly smaller than the value reported for $\text{Ge}_2\text{Sb}_2\text{Te}_5$ ($5.05 \times 10^{-5} \text{ K}^{-1}$ [73]). The lattice constant of similar samples obtained by the same sputtering technique were measured by Rausch [135], who obtained $a = 6.11(1) \text{ \AA}$. Even using this value, the CLTE of $0.9(4) \times 10^{-5} \text{ K}^{-1}$ remains smaller than that of $\text{Ge}_2\text{Sb}_2\text{Te}_5$.

Table 4.6: Interatomic distances in crystalline (rock-salt-like) In_3SbTe_2 at 10 K. The edge energy corrections ΔE are 6.9(2), 5.6(4) and 7.2(3) eV for IST, respectively. The fit values of $N \cdot S_0^2$ are readily divided by the coordination numbers N of a rock-salt lattice, so that the remaining parameter S_0^2 can be determined.

Scattering Paths	S_0^2	Distance	MSD
In-Sb (1st shell)	0.66(2)	2.992(3) Å	0.0014(3) Å ²
In-Te (1st shell)	0.66(2)	3.071(2) Å	0.0031(2) Å ²
Sb-Te (2nd shell)	0.64(3)	4.28(2) Å	0.006(2) Å ²
Te-Te (2nd shell)	0.59(2)	4.30(1) Å	0.056(1) Å ²
In-In (2nd shell)	0.66(2)	4.34(1) Å	0.015(1) Å ²
Sb-Sb (2nd shell)	0.64(3)	4.34(2) Å	0.004(2) Å ²
In-Sb (3rd shell)	0.66(2)	5.25(3) Å	0.009(3) Å ²
In-Te (3rd shell)	0.66(2)	5.28(1) Å	0.007(1) Å ²
In-Sb (segregated)	$N = 0.36(6)$	2.80(1) Å	0.007(1) Å ²

4.5.2 Amorphous In_3SbTe_2

The K-edge EXAFS spectra have been recorded for all three K absorption edges of as-deposited amorphous In_3SbTe_2 . The resulting data are depicted in Fig. 4.11 together with a least squares refinement. Since IST consists of three elements with very similar atomic charges (49, 51 and 52), large uncertainties are expected for the partial coordination numbers N_{ij} (e.g. $N_{1,2}$ corresponds to the number of In-Sb bonds per In atom). These nine parameters are constrained in a homogeneous sample by the stoichiometry, which is given by the atomic fractions x_i with $\sum_i^3 x_i = 1$. The partial coordination numbers are then constrained by $N_{ij} = (x_j/x_i) \cdot N_{ji}$. For the case, that no homopolar bonds exist, i.e. $N_{ii} = 0 \forall i$, the fit has only three remaining coordination numbers and the total residual R for all edges is 0.017. This residual is below 0.02 and shows that the inclusion of homopolar bonds to the fitting model is not necessary to obtain a reliable model. If e.g. homopolar bonds of In are included in the fit, like they are observed in MD-DFT calculations [135], the residual reduces significantly to 0.011 and the reduced chi-square is reduced as well from 28.0 to 22.1. All other bond types reduce the residual less significantly. E.g. Sb-Sb bonds only improve the residual from 0.017 to 0.016. All further scattering paths only increase the reduced chi-square due to the larger number of fit parameters. All resulting values of the scattering paths in amorphous In_3SbTe_2 are summarized in Tab. 4.7, where constrained parameters are denoted by the same letter in parenthesis. Partial coordination numbers N_{ij} have been obtained by dividing by the amplitude reduction factors S_0^2 of the crystalline phase.

The resulting coordination numbers of amorphous In_3SbTe_2 are 5.7(6), 5.2(4) and 3.8(3), respectively. These numbers are significantly larger than those predicted by the 8-N rule [132], i.e. 5, 3 and 2 for In, Sb and Te. Therefore, the amorphous phase of In_3SbTe_2 differs

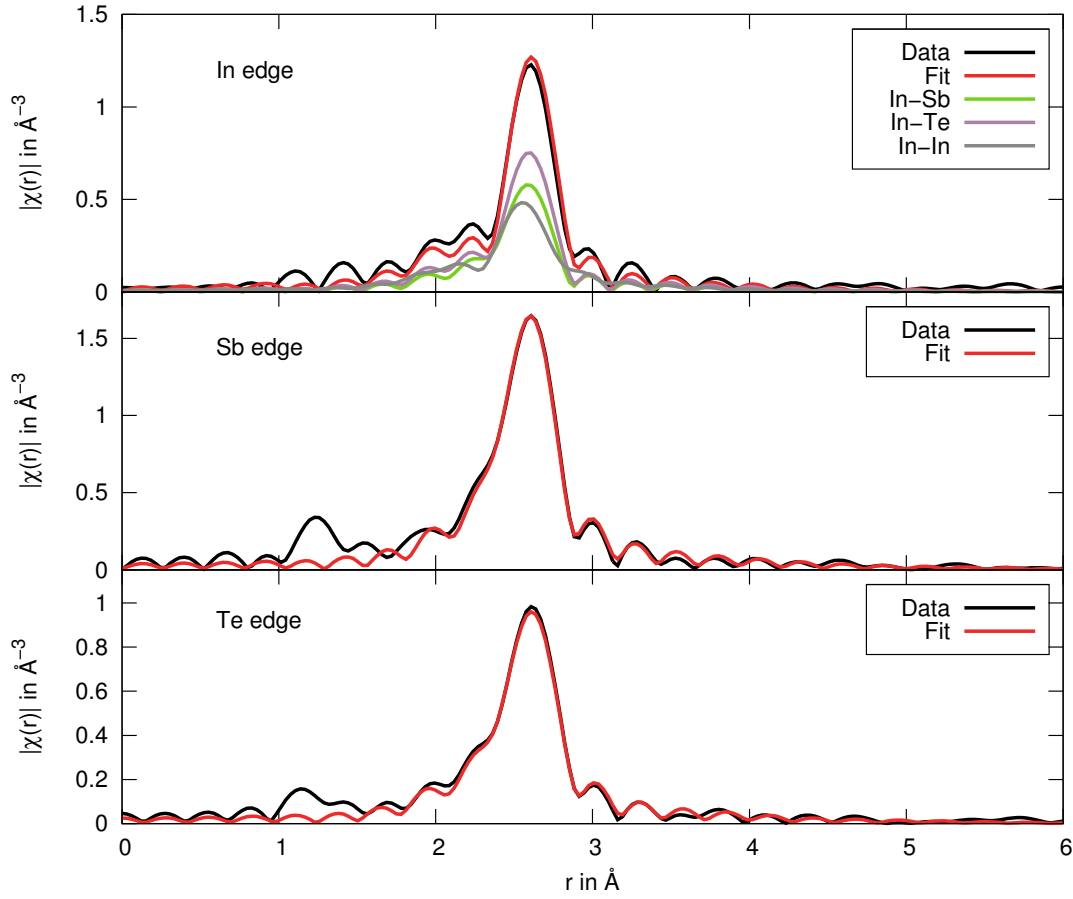


Figure 4.11: Fourier Transforms of EXAFS data (black) of as-deposited amorphous In_3SbTe_2 at 10 K. The fits (red) consist of three scattering paths at the In edge and of only single heteropolar scattering path at the Sb and Te edges. Only atoms on the first neighboring shell can be detected. Bond lengths and Displacement parameters of all equal scattering paths (i.e. In-Sb and In-Te) have been constrained. The resulting R-factor is 0.011.

from that of all phase-change materials investigated in this thesis. This deviation is partly confirmed by AIMD simulations performed by Rausch [135], who obtained coordination numbers of 5.0(5), 4.8(5) and 4.7(4). Just like the AIMD simulations for GST compounds, the coordination number of Te in IST turns out larger than the experimental result.

Bond lengths in covalently bonded systems can be compared to the sums of tabulated covalent radii, which give the following results: In-In 2.84(1) Å, In-Te 2.80(1) Å and In-Sb 2.81(1) Å. The predictions for In-Sb and In-Te distances agree very well to the observed values, but a deviation exists for In-In bonds. A comparison to values from literature shows that this deviation is not a unique observation: Studies on the structure of other crystalline indium-chalcogenides revealed In-In bond lengths of 2.760(5) Å in In_6Se_7 [138] and 2.763(4) Å in $\text{In}_7\text{Te}_{10}$ (at room temperature) [139]. These values agree with those from amorphous In_3SbTe_2 , but the In-In distances in pure In (3.25 Å), however, are larger than

Table 4.7: Atomic nearest neighbor distances in as-deposited amorphous In_3SbTe_2 at 10 K. The edge energy corrections are 5(1) eV, 9(1) eV and 8(1) eV for IST, respectively.

Scattering Path i-j	N_{ij}	Distance	σ^2 in \AA^2
In-In	1.5(5)	2.77(1) \AA	0.006(2)
In-Sb	2.5(2) (a)	2.829(4) \AA (a)	0.0033(5) (a)
In-Te	1.7(2) (b)	2.839(5) \AA (b)	0.0039(5) (b)
Sb-In	5.2(4) (a)	2.829(4) \AA (a)	0.0033(5) (a)
Te-In	3.8(3) (b)	2.839(5) \AA (b)	0.0039(5) (b)

these and explain why the tabulated numbers for covalent radii of In are larger.

4.5.3 Comparison of amorphous and crystalline IST

Significant changes in the local atomic ordering occur in IST as well. These changes are described by the numbers in Tab. 4.8, which show that although a large increase of the average interatomic distances occurs, the coordination number increases only slightly. In this respect, the structural contrast in IST differs from all other phase-change materials – because the atomic coordination in the amorphous phase exceeds the prediction of the 8-N rule. Therefore, the bonds in amorphous IST are not ordinary covalent – just as those of the crystalline phase. It is not yet clear, if resonance bonding occurs in crystalline IST – although the atomic geometry seems to be strongly in favor of resonance bonding due its cubic rocksalt structure and the p-bonding. This is because measurements of ϵ_∞ have not been possible due to the large carrier concentration, which results from the lower number of electrons per atom ($\langle n_p \rangle = 2.33$) and the position of the Fermi level inside the p-band. Local atomic distortions are very small and do not open a gap at the Fermi level. The ionicity of IST is comparable to that of SnTe , which is no phase-change material any longer, but still has resonance bonding. It is therefore rather likely that resonant bonds exist in IST as well, which are screened by the large susceptibility of the many free charge carriers.

As expected for a glass forming material, the displacement parameter reduces upon crystallization. The parameter of the crystalline phase of IST is rather low, although local atomic displacements and substitutional disorder prevails. In contrast to GST, the radii of the different atoms are rather similar and no vacancies have yet been reported for IST so that there is by far less displacement disorder in the crystalline phase. In conclusion, the structural contrast resembles more closely the features found in Sb_2Te_3 , than those of GST.

4.6 Conclusions from the study of atomic order

The local atomic ordering in the amorphous and crystalline phases of at least four different phase-change materials has been investigated. This comprehensive analysis has shown that

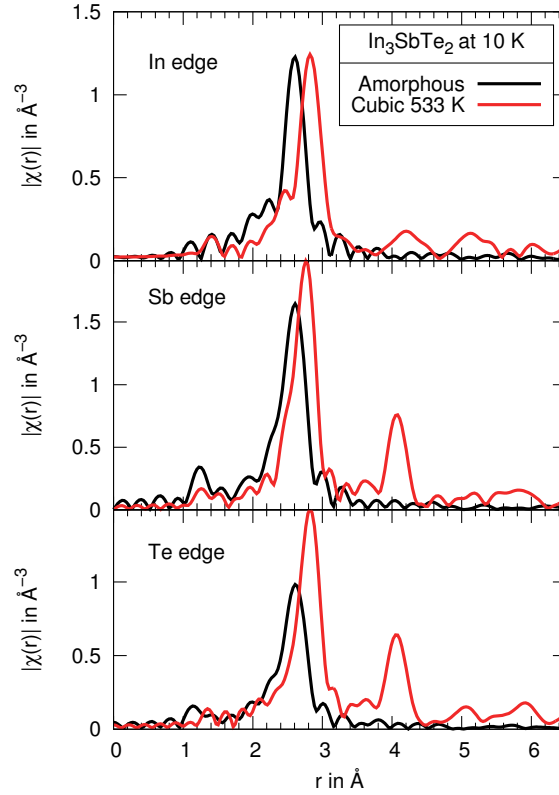


Figure 4.12: Fourier transformed EXAFS data reveal the contrast of the local atomic environment between amorphous and crystalline In_3SbTe_2 . An increase in bond lengths and a decrease of the atomic displacement parameters is observed upon crystallization. The data were measured at 10 K.

the average interatomic distance increases in all these materials upon crystallization. Since this list of materials contains compounds of all so-called families of phase-change materials, it can be concluded that the increase in bond length is a general structural motif of phase-change materials. It was observed in $\text{Ge}_2\text{Sb}_2\text{Te}_5$, GeTe , AlST , Sb_2Te and In_3SbTe_2 . The largest increase of nearest neighbor spacing was observed in GeTe (+15%), in $\text{Ge}_2\text{Sb}_2\text{Te}_5$ (+11%), in In_3SbTe_2 (+8%) and in Sb_2Te (+8%). This modification of the local atomic arrangement is related to a change in bonding mechanism, which supports the property contrast desired for phase-change applications. This structure-property relationship is important for the design of phase-change materials for optical data storage. However, the

Table 4.8: Local atomic arrangement in amorphous and crystalline In_3SbTe_2

	$\langle r \rangle$	σ^2	N
Amorphous phase	2.82(1) Å	0.0035(5) Å ²	5.0(4)
Crystalline phase	3.05(1) Å	0.0025(2) Å ²	6.0
Change	+8%	-29%	+20%

investigation of static atomic structures cannot explain the exact route of the fast crystallization mechanism. Therefore, further investigations are necessary, which can be based on thermodynamic and kinetic properties. These measurements will be presented in the following and it will become clear, why thermodynamic measurements should be based on the previous knowledge of the atomic structures.

CHAPTER 5

Vibrational properties of phase-change materials

The structural analysis by EXAFS and XRD analysis revealed that the crystalline phase of GST shows a stronger variance of nearest neighbor distances than the amorphous phase (cf. Sec. 4.2.3). This result was based on the comparison of the temperature dependence of displacement parameters from EXAFS and XRD data. Since these displacements are based on a different weighting of short- and long-wavelengths modes, it was only possible to speculate that the atomic interaction potential softens upon crystallization. **Are the interaction potentials of the crystalline phase softer than those of the amorphous phase and could this behavior be linked to the prevalence of resonance bonding in the crystalline phase.**

It was shown in Sec. 2.3.5, that these force constants can be obtained from an analysis of the densities of phonon states. Therefore, such measurements are desirable to further investigate the surprising observation, that the displacement parameter increases upon crystallization (softening of the atomic potentials), whereas the bulk modulus increases from 28(5) GPa to 45(9) GPa as well [25] and the compound hardens macroscopically (or 30(2) to 37(2) GPa in a different study [140]).

Nuclear Inelastic Scattering (NIS) is a technique, whose fundamentals were pioneered in 1995 (cf. [141] and references therein), when highly brilliant pulsed synchrotron radiation from undulator sources became available at the European Synchrotron Radiation Facility (ESRF). It can be employed to measure the partial density of phonon states (pDOPS) of specific Mößbauer atoms in samples in every phase. The low spot size of the synchrotron beam further enables the measurement of small samples and in particular of thin film samples. Therefore, this method does not face the challenges of INS, where large sample quantities are necessary and of Raman scattering, where a profound structural model is necessary to interpret the results. The limited availability of Mößbauer active atoms on the other hand is a challenge to NIS. However, recently, the method became available for ^{121}Sb [142] and

^{125}Te [143]. ^{121}Sb has a natural abundance of 57% and is sufficient for NIS in most samples, whereas the natural abundance of ^{125}Te is only 7% and therefore, samples need to be enriched in ^{125}Te . With these two elements, the largest fraction of atoms in most common phase-change materials is accessible and measurements have been performed at the ESRF to obtain the pDOPS of as-deposited amorphous, meta-stable crystalline GeSb_2Te_4 [73]. The beauty of this method lies within its simplicity, once the very high technical requirements concerning both, beamline and sample, are realized. The physical principle will be explained, followed by a discussion of the results.

5.1 Mössbauer Effect

The Mössbauer effect is sometimes referred to as the recoil-free absorption of gamma (or X-) rays by a nucleus. The energy is then entirely transferred to an excitation of the nuclear spin. This recoil-free process seemed puzzling at first, because the momentum of the gamma photon has to be retained – just as in the Compton effect, where a photon scatters inelastically ¹ with a free electron. The essential difference is, that the Mössbauer effect is only observed on atoms, which are bonded in a solid. Then, just as for the reflection of a ball from a hard wall, the solid does not obtain a significant amount of kinetic energy and the absorption occurs without recoil so that the total energy retained in the excited nucleus and can be passed, thereby leading to resonant absorption.

5.2 Nuclear Inelastic Scattering

First, the incident x-rays are monochromatized by Si 111 double crystals for pre-selection and in particular to reduce their intensity. The resulting beam is further monochromatized by a highly specialized monochromator (sapphire, Al_2O_3) to adapt the nuclear transition [141] in the investigated ^{121}Sb (37.13 keV) and ^{125}Te (35.492 keV) isotopes with an energy resolution of 6.6 meV (corresponding to $1.8 \cdot 10^{-7}$). The incident flux of x-rays is measured using an ionization chamber.

Hitting the sample, some x-ray photons are scattered by the electrons and some are scattered by the nuclei. One of the key challenges is to resolve the nuclear scattering, which is generally a factor of 10^{-9} lower than the electronic scattering [144]. This filtering is possible due to the different time structure of the scattering with the electronic scattering being prompt (<1 ns) and the nuclear scattering being delayed by some ns. Two avalanche photodiode (APD) detectors are placed at different scattering angles and at different distances to the sample so that they are able to resolve both different scattering processes, if the delay is some nanoseconds. The nuclear scattering has an inelastic contribution from photons, which have been ejected after the creation or annihilation of a vibrational state. These inelastic scattering events occur spatially incoherent within the sample and therefore only lead to constructive interference in the forward direction, where the distance to the

¹except for forward scattering

sample is constant for all scattering paths. This coherent scattering is measured by detector #2 in Fig. 5.1, which is located far from the sample. The first detector measures the incoherent nuclear scattering over the largest possible solid angle so that it is placed as closely to the sample as the sample environment (temperature, pressure and atmosphere) allows.

The temporal delay of nuclear scattering allows filtering out the electronic scattering and the directly transmitted beam from both detectors. The half-life time of excited ^{121}Sb , is only 3.5(4) ns [145], making a distinction of the different scattering mechanisms more difficult than in ^{57}Fe , where it amounts to 99.3 ns [145]. ^{125}Te is even more complicated to measure, since the half-life time of the excited state with $I_c = 3/2+$ (as compared to the ground state with $I_g = 1/2+$) is only 2.14(1) ns [143].

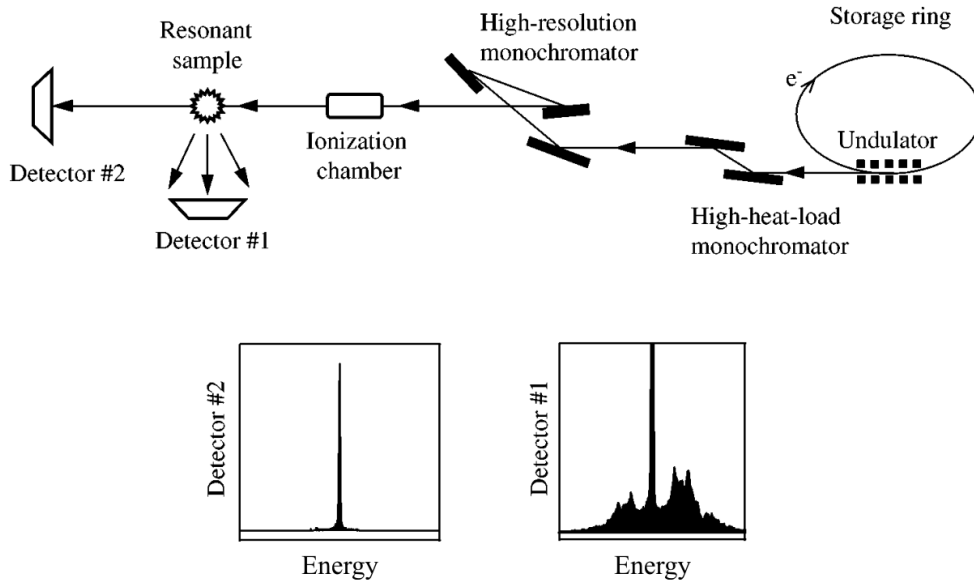


Figure 5.1: The experimental setup for Nuclear Inelastic Scattering experiments is based upon a set of monochromator crystals, which are placed at an undulator source. This is the only energy discrimination, which is necessary for NIS. By tuning the energy, the detectors #2 and #1 record the coherent elastic and the nuclear inelastic absorption spectra, which allow extracting the density of phonon states (cf. text). Adapted from [141].

The name nuclear inelastic scattering is not precise, since there are two methods, by which the excited nucleus can decay: (a) Internal conversion and (b) radiative decay. The internal conversion coefficient α describes the probability $\alpha/(1 + \alpha)$, with which internal conversion is the decay mechanism of the nucleus.

(a) Internal conversion (also called nuclear inelastic absorption) refers to the transfer of the excitation energy to an electron of the atomic shell, which is emitted from the atom and a γ or Auger electron is released when another electron fills the hole. This channel was measured for phase-change materials.

(b) For radiative decay, the probability is $1/(1 + \alpha)$ and refers to the emission of γ fluorescence radiation, which can have the energy of the nuclear transition (elastic) or that

plus/minus the energy of a vibrational state.

For several reasons (the most significant one being the fact that $\alpha \gg 1$), the internal conversion mechanism leads to the strongest signal in emitted x-rays. This is a huge benefit, since the internal nature of the mechanism leads to the fact that the emission is isotropic and therefore does not depend on the exact geometry of the setup. Therefore, always the whole k -space within the dispersion of the X-rays is integrated automatically.

The energy scale in NIS can be easily aligned by setting $E = 0$ to the highest peak in the nuclear inelastic absorption spectrum, which is measured by detector #1 in Fig. 5.1. Its spectrum is given by

$$W(E) = f_{\text{LM}} \left(\delta(E) + \sum_{n=1}^{\infty} S_n(E) \right), \quad (5.1)$$

where f_{LM} is the Lamb-Mössbauer factor, $\delta(E)$ denotes the elastic scattering (i.e. the zero-phonon term) and the following sum is an expansion of n -phonon terms $S_n(E)$, which will be discussed in the following. The density of phonon states $g(E)$ can be extracted from the experimental data in Eq. 5.1 by the recursive definition of the n -phonon terms,

$$S_1(E) = \frac{E_r g(E)}{E(1 - e^{-\beta E})} \quad (5.2)$$

$$S_n(E) = \frac{1}{n} \int_{-\infty}^{\infty} S_1(E') S_{n-1}(E - E') dE', \quad (5.3)$$

where $E_r = \hbar^2 k^2 / 2M$ is the recoil energy of a free nucleus of mass M after absorbing the X-ray photon with wave vector k . Furthermore, $\beta = (k_B T)^{-1}$, as usual. The series expansion for n -phonon terms converges particularly fast, if the Lamb-Mössbauer factor f_{LM} is close to unity, which is the case at lower temperature, since

$$\sigma^2 = -\frac{\ln(f_{\text{LM}})}{k^2}, \quad (5.4)$$

where σ^2 is the well-known atomic displacement parameter. Therefore, NIS experiments were performed at very low temperature.

5.3 Results and Conclusion

Measurements of this kind were performed at the ESRF, Grenoble, France around the ^{121}Sb and ^{125}Te nuclear excitations at about 36 keV, where the momentum transfer is about 20 \AA^{-1} . The samples of GeSb_2Te_4 were prepared by evaporating from 3 different cells simultaneously: GeTe and Sb in natural abundance and from ^{125}Te . In the case of GeSb_2Te_4 , this led to an isotopic concentration of 77% ^{125}Te , sufficient for the NIS experiments.

The resulting densities of phonon states are depicted in Fig. 5.2 for the amorphous (black curve) and meta-stable crystalline (red curve) phases of GeSb_2Te_4 . It is clearly observed for modes involving Sb and Te, that the low energy acoustic modes increase in energy, i.e. harden upon crystallization. This hardening is commonly observed in glass forming materials and is related to the macroscopic hardening of the material, which goes along with an

Table 5.1: Parameters of the vibrational properties of phase-change materials. The elastic hardening is reflected by the increase of the Debye temperature, although the exact numbers have to be taken with care (cf. text). The surprising result of a vibrational softening upon crystallization can be evidenced by the decrease of interatomic force constants. [73]

Phase	Sb		Te	
	θ_D in K	F in Nm^{-1}	θ_D in K	F in Nm^{-1}
As deposited amorphous	131	97(4)	120	84(4)
Meta-stable crystalline	153	72(4)	151	68(4)

increase in the sound velocity (cf. formulae in Sec. 2.3.4). This macroscopic hardening is best reflected by the Debye temperature, which is a good measure for the acoustic phonon modes. The low energy regime has been refined with a Debye model, resulting in the numbers given in Tab. 5.1. These numbers well reflect the elastic hardening upon crystallization. The exact values, however, have to be taken with care since the densities of phonon states are the average over a large k -range, where averaging effects can influence the resulting spectra especially in the amorphous phase. In the crystalline phase, the Debye temperature should be more accurate and is indeed found to be in good agreement with the value of 155(5) K, found from the temperature dependence of displacement parameters (cf. Sec. 4.2.3).

In addition, the interatomic force constants can be derived from the densities of phonon states. Therefore, measurements of vibrational properties allow the rare chance to investigate both, macroscopic and microscopic properties simultaneously. Most surprisingly, and in contrast to common glass forming semiconductors, the force constant decreases upon crystallization. This effect shows that there is a significant change of the bonding mechanism upon crystallization with purely covalent bonds in the amorphous and resonant covalent bonds in the crystalline phase. This observation is well in line with the larger temperature dependence of the displacement parameter in the meta-stable crystalline phase, cf. Fig. 4.6.

In conclusion, it was shown that optical modes of higher frequencies exist in the amorphous phase, so that a **vibrational softening occurs upon crystallization**. It can be wondered, whether these soft interaction potentials could be related to the high values of ϵ_∞ . Although this relation is likely, it is difficult to proof, since the frequencies of optical vibrational modes are lower in energy than the optical dielectric constant ϵ_∞ . The optical dielectric constant is based upon electronic properties, where the atoms can no longer follow the excitation frequency. On the other hand, the large dynamic charge of phase-change materials [42] shows that also the electrons can be significantly displaced by small atomic movements. **Consequently, a soft atomic interaction potential implies a large electronic polarizability in case of a large dynamic charge.**

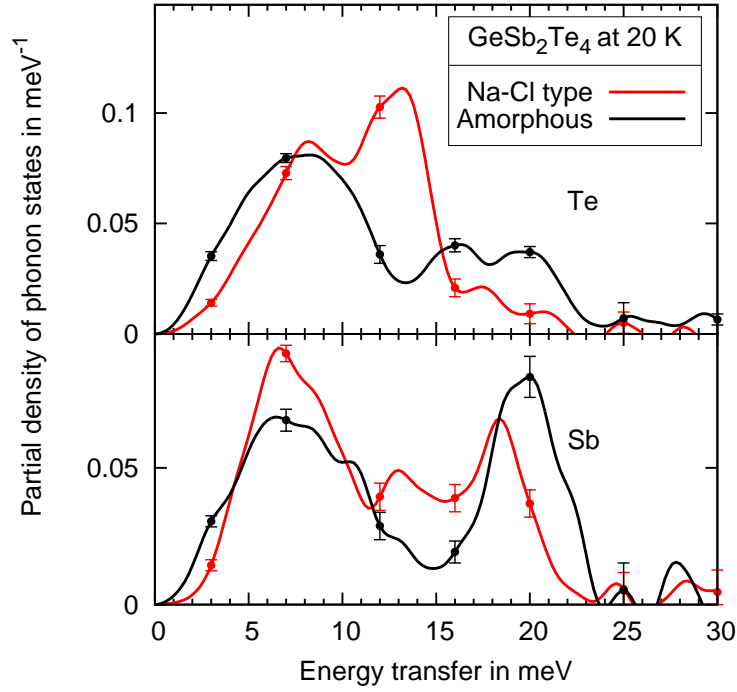


Figure 5.2: Partial density of phonon states in GeSb_2Te_4 . The low-energy acoustic modes harden upon crystallization, whereas surprisingly the optical modes soften. This shows that the atomic interaction potentials are softer in the crystalline phase [73].

CHAPTER 6

Thermodynamic properties of phase-change materials

So far, the static and dynamic structures of phase-change materials have been discussed. It was revealed, how the atoms are locally arranged in both phases involved in the phase-change. The essential switching mechanism, however, was not addressed by those studies. Therefore, the earlier results shall be brought in context with the thermodynamics and kinetics of the phase-transition. **This chapter is included to provide the theoretical foundation of thermodynamics and calorimetry for the thermal analysis presented in Chpt. 7.**

6.1 Crystallization / Motivation

Phase transitions are governed by both, kinetics and thermodynamics. Thermodynamically, any phase transition can occur spontaneously, if the free enthalpy G is reduced. However, the transition can be kinetically suppressed by a large activation barrier. Hence, both influences have to be investigated to describe and predict the crystallization process. In this section, the thermodynamic properties are discussed and it will be explained how the kinetics of crystallization can be assessed based on thermodynamic properties. The driving force of crystallization is the change in free enthalpy $\Delta G = G_a - G_c$. In case of $\Delta G > 0$, crystallization can take place thermodynamically any time. At the same time, the entropy changes by $\Delta S = S_a - S_c > 0$, because the entropy of an amorphous system is necessarily larger than that of a crystal. This follows directly from the fact that the crystal is the thermodynamically stable state (below the melting temperature). Therefore, the change in enthalpy is $\Delta H = \Delta G + T\Delta S$, and consequently, $\Delta H > \Delta G$. The driving force of crystallization is always smaller than the measured change in enthalpy ΔH and the difference is given by the entropy difference between the final and the initial states involved in the crystallization $T_c\Delta S$. It is the aim of this section to determine both quantities in order to understand in how

far phase-change materials differ from other glass-forming materials.

6.1.1 Kinetics

This section will show how the change in free enthalpy per atom $\Delta g_V = \Delta G/V$ (V is the volume of atoms that crystallize) enters the kinetic models of crystallization. These models are given also to motivate the measurement of thermodynamic properties – or more precisely the measurements of not only ΔH , but also ΔS .

Nucleation

The classic theory of *nucleation* dates back to Gibbs, Volmer, Becker and Döring (cited from [146], p. 183). The basic idea is that crystallites form with a given rate and that they have to exceed a specific critical radius – linked to an activation barrier – above which they gain free enthalpy by growing further. The rate, with which nuclei reach this critical radius per unit volume is termed nucleation rate J and follows an Arrhenius temperature dependence. It is given by

$$J = A \cdot \exp\left(\frac{\Delta g_{nuc}(r)}{k_B T}\right) \quad (6.1)$$

The activation barrier of nucleation has two contributions, $\Delta g_{nuc}(r) = \Delta \bar{g}_S(r) + \Delta \bar{g}_V(r)$. $\Delta \bar{g}_V = 4/3\pi r^3 \Delta g_V$ is the driving force due to Δg_V , the free enthalpy difference between amorphous and crystalline material per atom (which will be studied in detail in this and the following chapter). $\Delta \bar{g}_S = -4\pi r^2 \gamma$ contributes the activation barrier due to the interface energy γ . It is important to note that the volume effects favor crystallization, so that $\Delta \bar{g}_V > 0$, while the extra surface tension γ between the crystalline nucleus and the surrounding amorphous material disfavors crystallization and therefore $\Delta \bar{g}_S < 0$. At this point it is worth mentioning that the GST-based materials, i.e. at least GeSb_2Te_4 and $\text{Ge}_2\text{Sb}_2\text{Te}_5$ possess a high nucleation rate, which might be related either to a large gain in free enthalpy Δg_V or a low interface energy γ . In the absence of a comparative study of the interface energy for different PCMs, its influence will be discussed only briefly. As can be seen from the equation for $\Delta \bar{g}_S(r)$, a large interface energy increases the activation energy for nucleation and reduces the nucleation rate. The interface energy for different materials can be measured by the shape of crystals at the surface, since their contour allows deriving the wetting angle at the amorphous-crystal interface, if the densities of both phases are known. It was shown already that such contours can be recorded by means of atomic force microscopy [147] – however, no interface energies were calculated. This work will focus only on the influence of the volume term Δg_V to the nucleation rate. It will be discussed with respect to calorimetric measurements as well as the important influence of atomic disorder.

Growth

In case a stable nucleus has formed (i.e. if its size exceeds the critical radius), it will continue growing. The *growth* rate is either limited by atomic rearrangement processes at the

interface of the nucleus, or, in the case of a change of composition upon crystallization, the growth rate is limited by diffusion processes. Since all investigated phase-change materials, which do not phase-separate (this excludes $\text{Ge}_{15}\text{Sb}_{85}$ and $\text{Ge}_{15}\text{Te}_{85}$), retain their composition upon crystallization, only the first interface limited process is considered. Then the growth velocity of the nucleus' interface is limited by atomic rearrangement processes. This model is derived in the work by Christian [148], p. 436 (and references therein) and the resulting velocity with which the interface proceeds is given by

$$Y = \delta^B \nu \left(\frac{\Delta g_V}{k_B T} \right) \exp \left(- \frac{\Delta g_{\text{int}}}{k_B T} \right). \quad (6.2)$$

In this expression, ν is the attempt frequency of an atom trying to access the growing crystal. It is of the same order of magnitude as atomic vibrations [148], p. 499. δ^B is the distance across the amorphous-to-crystal interface and $\Delta g_{\text{int}} > 0$ is the activation barrier for the atom to cross this interface. $\Delta g_V > 0$ is the driving force for crystal growth, i.e. the difference in free enthalpy per atom in the amorphous and crystalline phases.

It was shown that both mechanisms, nucleation and growth, are driven by a reduction of the free enthalpy per crystalline volume, Δg_V . But whereas the nucleation rate depends exponentially on differences in the driving force, the growth velocity is only a linear function of this value. Therefore, this quantity offers new insight to the differences in the mechanism of nucleation and growth and will be discussed in more detail in the following.

6.2 Thermodynamics of glass forming systems

6.2.1 Free enthalpy

The driving force of crystallization is a reduction of the free enthalpy $G(T, p) = U - TS + pV$, which enters in both dominant mechanisms, i.e. in crystal nucleation and -growth rates. The pV term can usually be neglected in solids, and even during the density change of approx. 5%, the term $p \cdot \Delta V/V \approx 1 \mu\text{eV/atom}$ at ambient pressure ($p = 0.1 \text{ MPa}$). By comparison with the values given in Tab. 6.1 for the entropy and energy changes, it becomes obvious that the pV -term remains negligible even up to pressures of 10 MPa, where it is less than 1% of the entropy change. Hence, only the enthalpy difference ΔH_{ac} and the entropy difference ΔS_{ac} enter the expression for ΔG_{ac} , since $G = H - TS$ and

$$\Delta G_{ac}(T) = \Delta H_{ac}(T) - T \cdot \Delta S_{ac}(T). \quad (6.3)$$

It is instructive to compare the magnitude of both contributions upon crystallization, i.e. $\Delta H_{ac} > 0$ and $-T_c \cdot \Delta S_{ac} < 0$ for various compounds, for which they are known.

From Eq. 6.3, it is clear that three quantities are necessary for the calculation of $\Delta G_{ac}(T_c)$: T_c , ΔH_{ac} and ΔS_{ac} , which will be discussed in sequence. To gain insight on the order of magnitude of these quantities, the numbers for amorphous Si and Ge, prepared by ion bombardment are given in Tab. 6.1. Amorphous Si crystallizes at 960 K and amorphous Ge at 750 K. $\Delta G_{ac}(T_c)$ is about 25% smaller than $\Delta H_{ac}(T_c)$, which proves that, considering the

Table 6.1: Contributions to the change in free enthalpy upon crystallization of pure Si and Ge. The values reveal, that the entropy contribution must not be neglected [149].

Element	$\Delta H_{ac}(T_c)$	$-T \cdot \Delta S_{ac}(T)$	$\Delta G_{ac}(T_c)$
Si	124 meV atom ⁻¹	-31 meV atom ⁻¹	93 meV atom ⁻¹
Ge	119 meV atom ⁻¹	-26 meV atom ⁻¹	93 meV atom ⁻¹

exponential dependence in the nucleation rate, the entropy difference is a crucial parameter for the thermodynamic description and prediction of the crystallization rates.

Fig. 6.1 depicts the free enthalpy as a function of temperature for the amorphous and crystalline phases. Both phases are in equilibrium at the melting temperature T_m and the slope of G must be negative with temperature, since $\partial G/\partial T = -S$ and absolute values of entropy are always positive. Furthermore, the undercooled liquid must be unstable as compared to the crystalline phase so that the entropy of the (undercooled) liquid must be larger than that of the crystal. If the undercooled liquid is cooled below the glass transition temperature without crystallizing, it has fallen out of equilibrium at the glass transition temperature. Below, no longer are all microstates of the system sampled on the time-scale of the experiment. This state is referred to as a glass. At lower cooling rates, however, crystallization sets in before the glass transition temperature is reached (red arrow). The crystalline phase of many phase-change materials, e.g. on the GeTe-Sb₂Te₃ line, is not well defined because additional metastable crystalline phases exist. These phases are obtained depending on the applied temperature program.

6.2.2 Entropy

The entropy is usually referenced to its value at very low temperatures, which – according to the third law of thermodynamics – equals zero, i.e.

$$\lim_{T \rightarrow 0} S = 0. \quad (6.4)$$

However, this law only applies to system with a non-degenerate ground state. A quantum mechanical treatment for systems with a g_0 -fold degenerate ground state reveals the residual entropy at $T = 0$ ([150], p. 525f)

$$S(T = 0) = k_B \log(g_0) > 0. \quad (6.5)$$

This residual entropy also exists in glasses, although no commonly accepted strategy exists to predict the degeneracy of the amorphous state. It should be noted, however, that there is an ongoing discussion about the question, which states have to be taken into account, when the degeneracy g_0 is calculated: Only those, which are sampled at the actual temperature on the time scale of the experiment (favored by Gupta et al. [151]) or all those, which correspond to a state of the same energy (favored by Goldstein [152]). In the first model only the

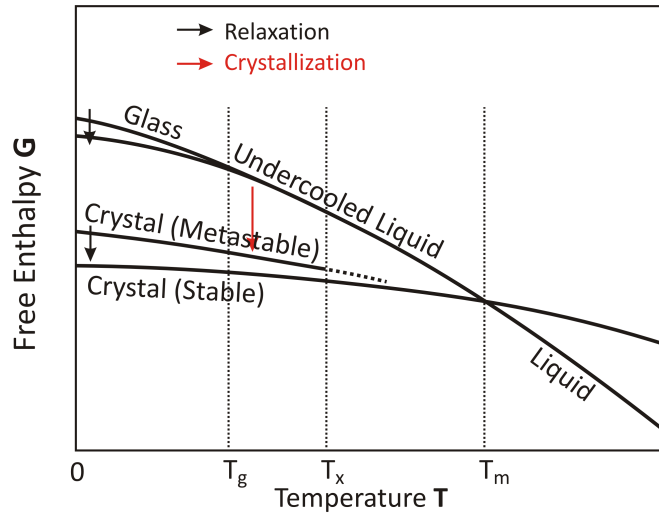


Figure 6.1: The free enthalpy G of glass forming materials is shown schematically for the amorphous and crystalline phases. At the melting temperature, the liquid and crystalline phases are in equilibrium, but below this temperature, the undercooled liquid and glassy phase are only meta-stable states. The difference in free enthalpy depends not only on the state of relaxation of the glass, but also on the crystalline phase. If a meta-stable crystalline phase exists, its free enthalpy must be larger than that of the stable phase over the full range where it exists. In contrast to glassy states, the meta-stable crystalline phase of GST-compounds has not yet been observed above its transition temperature to the stable phase, T_x .

states are counted, which are actually sampled, so that all other states have to be added when the glass transition temperature is passed. Then, the same residual entropy has to be added during T_g , which was assumed to exist at 0 K in the second model. This discussion implies that the absolute entropy of a substance out of internal equilibrium cannot be obtained by measuring the specific heat from 0 K. Therefore, the only reasonable reference state for such substances is the liquid state, where different cooling rates lead to the amorphous or the crystalline phase.

Fig. 6.2 shows the entropy of glass forming systems as a function of temperature. Starting from the liquid phase at high temperature, the material crystallizes upon cooling below the melting temperature, where the latent entropy is lost and depending on the cooling rate, several meta-stable crystalline modifications can occur. In this compound, only the entropy of the unique stable phase goes to zero upon cooling to 0 K. This means that the convention of Goldstein is followed, where all degenerate microstates are considered in the calculation of the entropy. Consequently, the residual entropy of the amorphous phase remains at 0 K. Upon heating the glass above the glass transition, a step in the specific heat occurs, which changes the slope of entropy vs. temperature. In phase-change materials, however, this undercooled liquid state above the glass transition temperature is almost not accessible due to

the fast onset of crystallization.

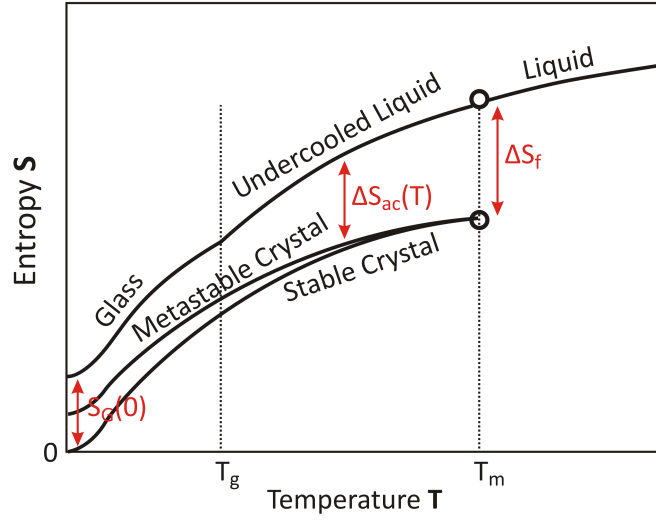


Figure 6.2: Temperature dependence of the entropy in glass forming systems. Starting from the liquid state, the entropy splits to a crystalline and an undercooled liquid phase – depending on the cooling rate, i.e. on kinetic aspects. Also a meta-stable crystalline state has residual configurational entropy at 0 K, which reduces the entropy difference to the glassy and undercooled liquid state.

With the liquid state as reference, the entropy difference ΔS_{ac} between the amorphous/undercooled liquid and crystalline phases is given by the following expressions:

$$\Delta S_{ac}(T) = S_a(T) - S_c(T) \quad (6.6)$$

$$= \Delta S_m + \int_{T_m}^T \frac{C_{p,a}}{T} dT - \int_{T_m}^T \frac{C_{p,c}}{T} dT \quad (6.7)$$

$$= \Delta S_m + \int_{T_m}^T \frac{\Delta C_p}{T} dT, \quad (6.8)$$

$$(6.9)$$

which shows that the entropy difference can be obtained experimentally from the specific heat difference. However, for an assessment of the entropy difference $\Delta S_{ac}(T) = S_a(T) - S_c(T)$, the specific heats of the undercooled liquid and crystalline phases have to be known. By using cooling rates of less than 10 K/s, the undercooled liquid phase is not accessible. It is therefore not possible to determine the entropy difference by commonly available calorimeters¹. Another strategy to follow is to extrapolate the entropy of the undercooled liquid by [25]

$$\Delta S_{ac}(T) = a \ln\left(\frac{T}{T_m}\right) + b(T - T_m), \quad (6.10)$$

¹The emerging technique of chip calorimetry might lead to significant improvements in this field [153]

where $\Delta S_{ac}(T) = 0$ at $T_K < T_g$ is the Kauzmann temperature. Both constants, a and b can be obtained by fitting a straight line to the specific heat of the undercooled liquid.

Therefore, absolute values for both, the amorphous and the crystalline phases can be obtained from a measurement of the specific heat of the liquid state and crystalline phase, when in addition the glass transition temperature is known. Therefore, the specific heat and all its contributions will be discussed in the following.

6.2.3 Specific heat

The specific heat is given by either $C_p = T \cdot \partial S / \partial T|_p$ or $C_V = T \cdot \partial S / \partial T|_V$, depending on the fixed property during the experiment p or V . In this study, the specific heat at constant pressure is used, since the experiments are performed in sample pans with a small opening. Furthermore, the well known stoichiometry of all samples enables the calculation of molar heat capacities $c_p = C_p(m_{\text{mol}})^{-1}$, which have the benefit of being easily comparable for different substance, since according to the law by Dulong-Petit, the molar specific heat at constant volume should always converge to $c_p = 258 \mu\text{eV} (\text{atom K})^{-1}$.

Configurational contribution

The configurational entropy is defined in general by

$$S_{\text{conf}} = -k_B \ln W, \quad (6.11)$$

where W is the number of possible configurations of the whole system for a given energy. Thus, single crystals have no configurational entropy. Amorphous systems, however, have a significant configurational entropy even at zero temperature. This is the largest contribution to the residual entropy observed in these systems ([154], p. 56). An efficient method to determine the configurational entropy of disordered network systems is found e.g. in the work by Vink et al. [155], [156]. Amorphous phase-change materials are distinct from these materials because they have variable coordination numbers and because they are diatomic. The extension of the model by Vink et al. is beyond the scope of this thesis and the configurational entropy is used here only to determine the configurational disorder of the different crystalline phases, where substitutional disorder occurs. The configurational entropy is usually temperature independent (except for relaxation effects at higher temperature) and therefore does not contribute to the specific heat.

Compounds from the GeTe-Sb₂Te₃ pseudobinary line possess a large configurational entropy in the metastable cubic phase due to substitutional disorder on the Ge/Sb/Vac sublattice. Its configurational entropy due to substitutional disorder can be quantified by

$$S_{\text{conf}} = k_B \cdot \ln \left(\frac{N!}{N_{\text{Ge}}! N_{\text{Sb}}! N_{\text{Vac}}!} \right) \quad (6.12)$$

using the Stirling formula

$$\ln(N!) \approx N \cdot \ln N - N \quad (6.13)$$

Table 6.2: Configurational entropy of GST phase-change materials in the meta-stable cubic phase, assuming fully random substitutional disorder on the Ge/Sb/Vac sublattice.

Compound	GeSb ₄ Te ₇	GeSb ₂ Te ₄	Ge ₂ Sb ₂ Te ₅	Ge ₃ Sb ₂ Te ₆
S_{conf} in $\mu\text{eV}(\text{atom K})^{-1}$	-41.1	-44.8	-45.4	-43.5
$-T_c \cdot S_{\text{conf}}$ in meV/atom	-17.0	-18.7	-19.4	-19.2

can be simplified to

$$S_{\text{conf}} = -k_B \cdot N [x_{\text{Ge}} \ln x_{\text{Ge}} + x_{\text{Sb}} \ln x_{\text{Sb}} + (1 - x_{\text{Ge}} - x_{\text{Sb}}) \ln (1 - x_{\text{Ge}} - x_{\text{Sb}})] . \quad (6.14)$$

Since only one sublattice is involved, $N = 0.5N_a$, with N_a Avogadro's constant, in order to obtain the specific entropy per mole. The resulting values of several phase-change materials is calculated in Tab. 6.2, which shows that the substitutional disorder increases the driving force of crystallization ΔG by approx. 21 meV/atom at the average crystallization temperature of 500 K.

It is of particular interest to note that the meta-stable phase of GST compounds is only observed, when its configurational entropy is larger than the entropy k_B from thermal fluctuations of energy $k_B T$, cf. Fig. 6.3.

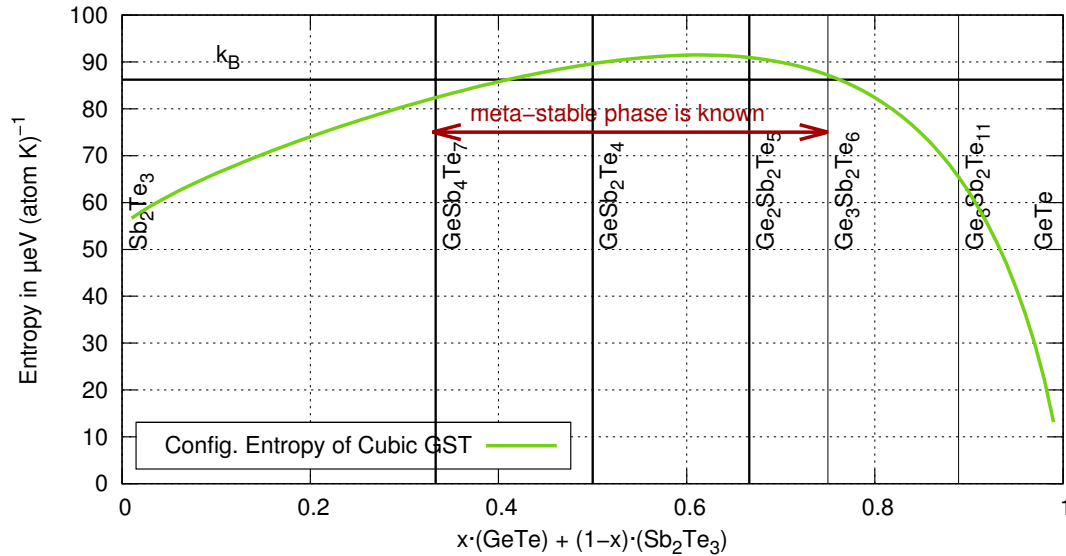


Figure 6.3: The configurational entropy due to substitutional disorder in the metastable phase of several GeTe-Sb₂Te₃-compounds is compared to the thermal energy of the atoms. It turns out that the meta-stable phase only crystallizes, when the disorder suffices to overcome the influence of thermal fluctuations.

Vibrational entropy

The vibrational entropy has already been discussed in Sec. 2.3.5, where also the respective formula was given to calculate the vibrational entropy from a density of phonon states. This calculation should be based on the full density of phonon states and since the NIS data only contain the partial density of states of the Sb and Te atoms, the entropy is not calculated here. However, in a fundamental article from 1964, Adam and Gibbs suggest that the vibrational entropy of a glass and the respective crystal do not deviate significantly [157].

Electronic contribution

In a band model, the electrons at the Fermi level can be thermally excited and therefore contribute to the specific heat as well. Their contribution to the specific heat is linear in temperature and determined by [115], p. 155,

$$C_{p,el} = \frac{\pi^2}{3} D(E_F) k_B^2 T \quad (6.15)$$

In phase-change materials, the density of states at the Fermi level can be roughly estimated from the carrier concentration n and the Fermi energy E_F . In order to obtain an upper limit for the electronic contribution in e.g. GeSb_2Te_4 , the values after annealing at 573 K are used, which are $n = 2.2 \cdot 10^{20} \text{ cm}^{-3}$ and $E_F = 0.14 \text{ eV}$. With $D(E_F) = 1.5N/E_F$, the resulting specific heat is $C_{p,el} \leq 0.081 \text{ J (mol K)}^{-1}$, which is negligible as compared to the Dulong-Petit limit, 24.942 J/(K mol).

In conclusion, the most significant contributions to the entropy originate from atomic thermal vibrations and from configurational disorder. This could allow determining the excess entropy of the undercooled liquid. However, the enthalpy difference $\Delta G_{ac} = G_a - G_c > 0$ consists of a change in enthalpy ΔH_{ac} and in entropy ΔS_{ac} . It is therefore the aim of the following section to explain calorimetry, from which both numbers can be obtained.

6.3 Calorimetry

How is the entropy of a system accessible by calorimetric measurements and what exactly does a calorimeter measure? These questions will be answered in the following. In a calorimeter, the power P is measured, which is necessary to compensate the temperature difference between the sample and an empty container. During the measurement, sample and empty container are at the same temperature, which can be modified linearly with time. To describe the situation quantitatively, let us start from the basic situation in a calorimeter: A sample with heat capacity $C_p(T)$ (under constant pressure, the specific heat is defined as $C_p = \partial H / \partial T|_p$) is heated by a heat flow rate Φ_{FS} from the furnace to the sample. The sample itself can be another source of heat flow, Φ_r . Both change the temperature of the

sample T_S . A similar equation holds for the empty container (reference) [158].

$$C_{p,S}(T) \cdot \frac{dT_S}{dt} = \Phi_{FS} - \Phi_r \quad (6.16)$$

$$C_{p,R}(T) \cdot \frac{dT_R}{dt} = \Phi_{FR} \quad (6.17)$$

As briefly denoted before, it is the difference in sample and reference temperature, $\Delta T = T_S - T_R$, which is compensated by the DSC. Therefore, we need to continue with the difference of Eqs. 6.16 and 6.17, which reads

$$\Phi_{FS} - \Phi_{RS} = (C_{p,S} - C_{p,R}) \cdot \frac{dT_R}{dt} + C_{p,S} \cdot \frac{d\Delta T}{dt} + \Phi_r \quad (6.18)$$

In a last step, the heat flows Φ are replaced by the respective temperature differences between furnace and sample/reference: $\Phi_{FS} = (T_F - T_S)/R$, where R is the universal thermal contact resistance between furnace and sample/reference. We find that

$$\Phi_r = -\frac{\Delta T}{R} - (C_{p,S} - C_{p,R}) \cdot \beta - C_{p,S} \cdot \frac{d\Delta T}{dt}. \quad (6.19)$$

This means, that the reaction flow rate equals the measured signal ΔT (which is in turn proportional to the compensating power P) divided by the thermal resistance R plus some additional terms. The second term on the right originates from the unequal heat capacities of sample and reference. Since heat capacities are smooth functions, it contributes a background signal behind the chemical reaction, which is proportional to the difference in specific heats and to the heating rate $\beta = dT_R/dt$. This also shows that it is difficult to distinguish chemical reactions which take place over a large temperature window from the heat capacity. The third term on the right includes a thermal delay due to the limited heat flow and can be simplified by introducing a time constant $\tau = C_{p,S} \cdot R$ to replace $C_{p,S}$. In this notation, it becomes obvious that a sufficient thermal contact (large R) with a sufficiently low heating rate makes this term negligible. In practice, this effect is taken care of by investigating the equilibration times of the calorimeter and making sure that they are shorter than the time scale of the investigated effects. It can become important, however, and needs to be compensated if the heating rate is increased to investigate the kinetics of a specific chemical reaction (e.g. during the so-called Kissinger analysis).

It is instructive to discuss the influence of the heat capacities a little further, since e.g. $C_{p,S} = C_p + C_{p,\text{pan},S}$ contains both, the contribution of the specimen C_p and that of the sample container/sample pan $C_{p,\text{pan},S}$, which is usually made of Al. In a similar way, $C_{p,R} = C_{p,\text{pan},R}$, so that the final equation reads

$$\Phi_r = -\frac{\Delta T}{R} - (C_p + (C_{p,\text{pan},S} - C_{p,\text{pan},R}))\beta - C_{p,S} \frac{d\Delta T}{dt}. \quad (6.20)$$

The calibration of the DSC works as follows: The measured signal ΔT is integrated over time during the melting process of In at low heating rates (without the specific heat of In). This number is then calibrated to the latent heat of the melting of In at about 430 K, which is a well-known property. After this calibration, the temperature difference ΔT can

be converted to a power P and the latter physical quantity will be used in the treatment of experimental data.

Integrating this power over time t results in the heat $\Delta Q = \int \Delta P \cdot dt$ (as for the latent heat of melting In). For any experiment, where the heat release due to the chemical reaction can be properly distinguished from changes in the specific heat (or sometimes even changes in the sample quantity), its total heat ΔQ can be measured. It equals the change in enthalpy ΔH , since the first law of thermodynamics, including internal changes in energy, is

$$dU = \delta Q + \delta W \quad (6.21)$$

and the enthalpy $H = U + pV$ is differentiated $dH = dU + pdV + Vdp$. It follows that $\delta Q = dH - Vdp$. Under constant pressure (as discussed above and it even holds for closed Al pans, which can hold a maximum additional pressure of about 1 bar), and without changes in the sample mass,

$$\delta H = \delta Q. \quad (6.22)$$

Therefore, **changes in enthalpy H upon a phase transition can be measured in a calorimeter.** For a reversible transition, this allows deriving the latent entropy as well, since the second law of thermodynamics,

$$dS \leq \frac{\delta Q}{T}, \quad (6.23)$$

holds exactly (i.e. the \leq is a $=$), when the phase transition is reversible. This trivial solution $\Delta S \cdot T = \Delta H$ is valid e.g. for the melting transition. The additional temperature dependence of the entropy in the absence of phase transition follows from a measurement of the specific heat. Therefore, relative values of the entropy can be measured calorimetrically as well. Crystallization, however, is a thermodynamically irreversible process and therefore, only an upper limit for the change in entropy can be given. **In the absence of phase-transitions, the entropy as a function of temperature can be exactly obtained via $S(T) - S(T_0) = \int_{T_0}^T C_p/T dT$.**

CHAPTER 7

Phase transitions and Entropy

In the preceding chapter, the fundamental thermodynamic properties of glass forming materials were discussed and it was motivated that both, entropy and enthalpy difference upon crystallization $\Delta S_{ac}(T_c)$ and $\Delta H_{ac}(T_c)$ influence the driving force of crystallization, $\Delta G_{ac}(T_c)$ and a strategy was presented, how these numbers could be obtained. **Therefore, this chapter is devoted to the results from measurements of the specific heat, the entropy and the latent heats involved in the phase transition. How much does the change in entropy $\Delta S_{ac}(T_c)$ influence the driving force of crystallization?**

This chapter is organized as follows: First, some details on the experimental method and data treatment procedure of thermal analysis are briefly introduced. Subsequently, the phase transitions of crystallization and melting are investigated for several compounds, like e.g. AIST and GST. From these investigations, $\Delta H_{ac}(T_c)$ and $\Delta H_{ac}(T_m)$ are obtained. Then, information on the specific heat C_p will be discussed, which should provide an estimate for the excess entropy upon crystallization, $\Delta S_{ac}(T_c)$. Finally, the results will be summarized and discussed.

7.1 Sample preparation

The experimental procedure begins with sputter-depositing layers of the specific material with 20 W sputtering power from stoichiometric targets. The substrates were continuously rotated (dynamic mode) in order to keep the temperature of the substrates low and in order to cover a larger surface. The substrates consisted of spring steel, from which the layers could be easily removed by bending the steel. The so obtained flakes were ground and filled into Al pans of 6 mm diameter and approx. 18 mg mass, which then contained about 30 to 50 mg phase-change material each. Finally, they were closed with a lid of about 10 mg Al, which was not sealed so that the pressure could equilibrate. All samples were weighted before and after thermal scans in order to make sure that no material evaporated. The scale used for

this purpose is a Mettler Toledo UMT 2 with a resolution of $1\text{ }\mu\text{g}$, which corresponds to a detection of mass changes of 25 ppm.

7.2 Differential Scanning Calorimetry

7.2.1 DSC Setup

A Diamond DSC by Perkin-Elmer was used to perform differential scanning calorimetry (DSC). It allows for heating rates between 1 and 500 K/min up to a maximum temperature of 1003 K, but since the sample containers are made of Al, the maximum temperature was limited by the melting of Al at 933.5 K [159] to a safe value of 863 K, which is unfortunately below the melting temperature of all GST compounds (cf. Tab. 7.1). In literature, a safe range of operation of 913 K is given [160], which is only 20 K below the melting temperature of Al, but also only slightly above the melting temperature of GST. Therefore, different sample containers would be necessary to measure the liquid state of GST. A method will be presented later in Sec. 7.3.1, where the material under investigation is admixed with powderous Boron-Nitride and pressed to a pellet. Steel pans might then be sufficient to prevent alloying of any of the materials involved.

The DSC is supplied with cooling water from the tap and Argon of purity 4N8 for purging the sample compartment. Due to the use of tap water, sufficient cooling rates can only be achieved at 323 K and above, thereby limiting the measurement range to 323 K to 863 K. The phase-change material with its sample pan is inserted to one furnace, while a similar empty reference pan is inserted to the neighboring furnace for power-compensation.

The temperature and heat-flux are calibrated to the melting temperature and latent heat of melting In, respectively. The reference values are well-known from literature as $T_{\text{m, In}} = 429.7\text{ K}$ and $34.0(3)\text{ meV atom}^{-1}$. The high temperature range is additionally calibrated to the melting temperature of pure Bi, which melts at 544.6 K. Due to the thermal lag discussed in Sec. 6.3, the detected melting temperature depends on the heating rate. This effect has been investigated based on the melting process of In at different heating rates between 1 and 500 K/min. The resulting calibration curve for heating rates between 1 and 40 K/min is obtained as $T_{\text{m, In, measured}} = T_{\text{m, In}} - 0.4\text{ K} + 0.041/\text{min} \cdot \beta$. At even higher heat rates, a different linear behavior is observed, which corresponds to $T_{\text{m, In, measured}} = T_{\text{m, In}} + 0.4\text{ K} + 0.021/\text{min} \cdot \beta$. To maintain a small thermal lag, temperature scans have usually been performed at 5 K/min, where the error in temperature is below 0.5 K. The additional calibration for specific heat measurements is described later, after the method of measuring specific heats is introduced.

7.2.2 Direct Scans

Measurements of the heat flow of a sample, Φ_r , as a function of temperature are referred to as direct scans, because the temperature is swepted continuously from the lowest to the highest value. The DSC maintains a steady state equilibrium to balance the temperatures

of sample and reference. The resulting data allow evaluating the latent heat of a phase transition and the transition temperature. These measurements were performed at heating and cooling rates of ± 5 K/min with an additional rescan to distinguish reversible from irreversible transitions.

7.2.3 3-step method

Specific heats can be measured in DSC's by employing the so-called three-step method, which will be discussed in the following. In principle, also a direct scan can be used, since according to Eq. 6.20, the measured signal is proportional to the specific heat, but in practice, the baseline in a calorimeter is not sufficiently stable. That means that the drift in the background signal is larger than the signal resulting from the specific heat. Therefore, it is not even sufficient to take the difference of two subsequent measurements with and without the sample, because the time between these measurements is too large. The three-step method, however, eliminates almost all effects caused by drift of the baseline. Essentially, it is based on a measurement of the heat ΔH to increase the temperature of the sample by ΔT . The specific heat is obtained, if only ΔT is chosen sufficiently small. In this case, ΔT has been chosen to be 10 K as a compromise between too much drift at larger steps and too large errors on the heat ΔH at smaller steps. This method has the advantage, that isothermal conditions are established before and after each temperature step. The isothermal heat flow does not depend on the sample quantity, but only on the temperature (and of course the geometry of the calorimeter). Therefore, these isothermal heat flow rates can be aligned, by adding the difference of the fitted lines of sample and reference over the full time of the scan. Two such scans are shown in Fig. 7.1 for $\text{Ge}_2\text{Sb}_2\text{Te}_5$ at 528 K, where the heating rate between the two isotherms was 10 K/min.

From this measurement over different temperature steps from T_1 to T_2 , the specific heat $C_p(T_0)$ can be obtained with $T_0 = 0.5 \cdot (T_2 + T_1)$, by calculating $C_p(T_0) = \Delta H / \Delta T$ for each step. Then, the specific heat originating from the mass difference between the sample pan and the reference pan is subtracted. Finally, the specific heat is divided by the molar mass to obtain c_p . Two such reference measurements are shown in Fig. 7.2. One measurement was performed on the reference material Al_2O_3 (a sapphire disc), whereas the second measurement was performed on a powderous specimen of sputter-deposited Sb. The measurements show that the literature data from Al_2O_3 are very well reproduced with small deviations at very low temperatures below 400 K and a slight additional slope above 750 K. The reference measurements of sputter deposited Sb show that the specific heat can be measured reproducibly upon heating or cooling the sample. Furthermore, the similarity of the heating and cooling curves on sputter deposited samples shows that no outgasing effects occur, which could change the specific heat irreversibly. The data on Sb also show that there is a deviation of approx. 2% from literature data on Sb, which might originate from various facts: When the measured specific heats were transformed to molar heat capacities, the molar mass of pure Sb was used. The real molar mass, however, might be influenced by some O, Ar or H contamination of the sample. It should be noted, that already a total

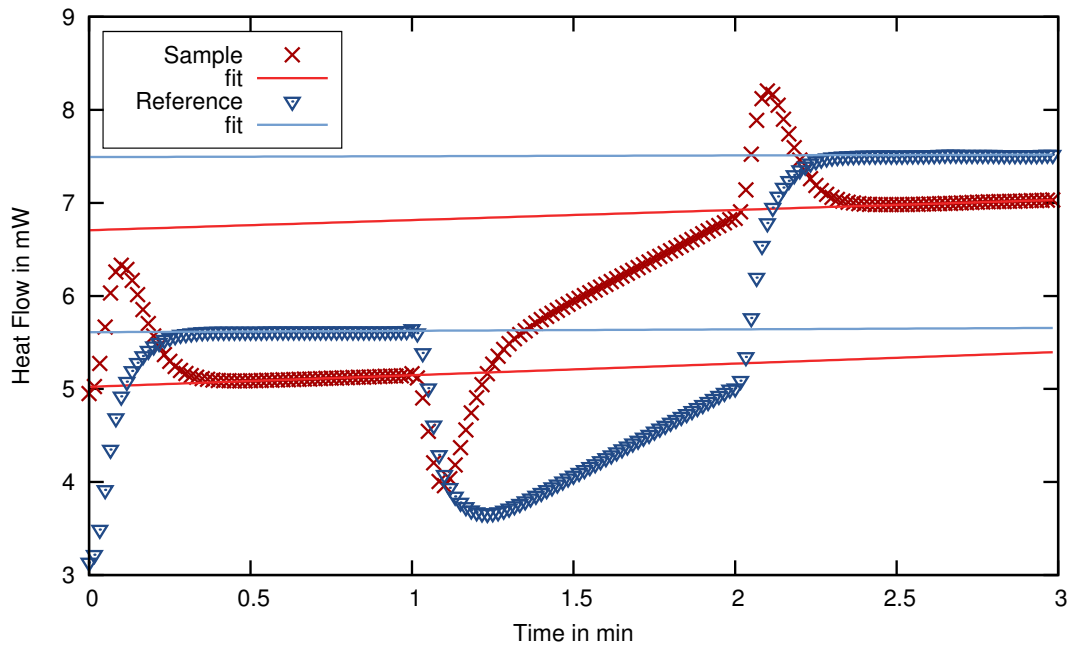


Figure 7.1: A calorimetric step-scan of $\text{Ge}_2\text{Sb}_2\text{Te}_5$ from 523 K at $t < 1$ min to 533 K at $t > 2$ min is shown for sample and reference scans. Straight lines are fitted to the isothermal data after an equilibration time of 0.5 min. Subsequently, the isotherms are aligned so that the integral over the difference between the two curves can be calculated. The specific heat is obtained after some final corrections are applied (cf. text for details).

atomic percentage of $<0.5\%$ of O, Ar or H could explain the increase in molar specific heat, since all these lighter atoms contribute significantly less to the mass, but contribute a similar molar specific heat c_p . If the isotherms show a remaining slope, an isothermal phase transition is taking place in the sample and the resulting data point cannot be used.

It can be concluded that a promising method has been established to measure the specific heat of sputter deposited materials in a wide temperature range of 350 K to 863 K. The calorimetric method of obtaining specific heats is well established for adiabatic calorimeters, but it is not commonly performed in power compensated DSCs, because the drift of the zeroline is significant. This prohibits the evaluation of specific heats from direct scans. However, if the drift of the zeroline is compensated for, precise measurements can be performed once sufficient amounts of sample quantity are available. The basic idea is that the isothermal heat flow is not affected, whether the sample or an empty container is measured. In fact, the heat flow does change in subsequent isothermals at the same temperature. By aligning these isothermal heat flows, the drift can be compensated. Fig. 7.1 shows two scans of sample and empty container, each starting with an isotherm at T_1 , followed by a temperature scan and then another isotherm at T_2 . The resulting difference in heat flow between the two curves can be integrated over time to determine the enthalpy ΔH that had to be supplied to the sample in order to increase its temperature by $\Delta T = T_2 - T_1$. Hence, the specific heat

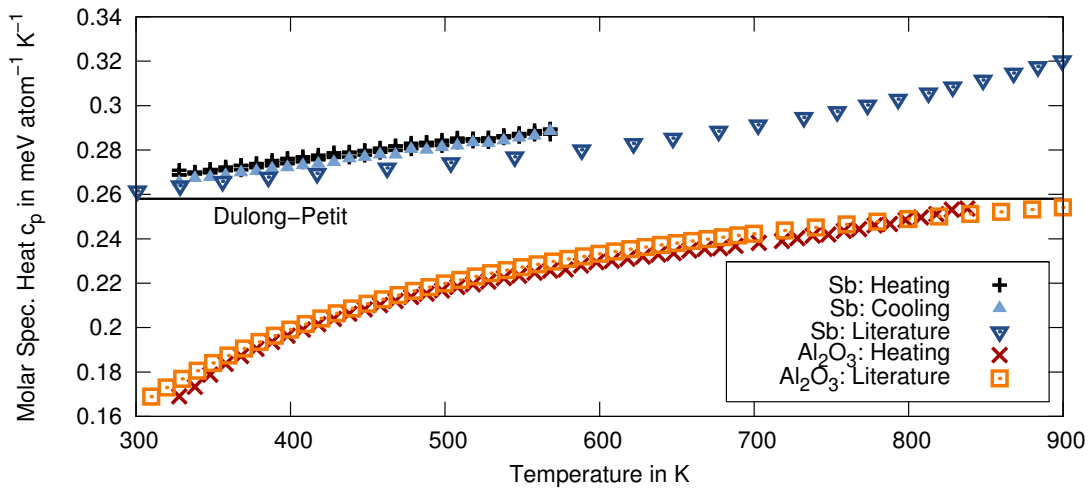


Figure 7.2: The molar specific heat has been measured for Al_2O_3 (a sapphire disc) and for sputter deposited Sb. While the data for Al_2O_3 are in good agreement, the molar specific heats of sputter deposited Sb are by approx. 2% larger, which might originate from contamination with light atoms.

is obtained.

7.3 Thermodynamics of the phase transitions

7.3.1 Phase separation in $\text{Ge}_{15}\text{Sb}_{85}$

A complete study of phase transitions in a phase-change material was performed for $\text{Ge}_{15}\text{Sb}_{85}$, where two techniques were combined to reveal the two-fold crystallization process based on structural and thermodynamic changes. It was already suspected from an annealing series, that amorphous Ge is segregated upon the first exothermal phase transition [161]. A combined DSC and in-situ EXAFS analysis was performed on the as-deposited amorphous phase of this compound in order to determine the local atomic structure after the first crystallization transition. The combination of these two instruments is a non-trivial task as will be explained in the following. To achieve a good detection of the heat flux during a DSC measurement, the sample needs to be in good thermal contact with the measuring system. For EXAFS measurements, however, the sample should be homogeneously distributed over all the incident X-rays and have a constant thickness. These requirements for sample preparation are contradictory. In addition, the absorption of X-rays by the sample could generate extra heat, which could affect the calorimetric signal. These challenges could be solved by modifying a Sensys, SETARAM calorimeter. The used setup is depicted in Fig. 7.3, which shows a cross section through this specific calorimeter, which was used for this study only. Due its larger size, the heating rates of this calorimeter are further limited than those of the other DSC of the Diamond DSC used for all other thermal analyses. The cross sectional drawing depicts the two tubes, which contain the sample and a reference. Both consist of

a pressed pellet of Boron-Nitride (BN), to which powderous amorphous $\text{Ge}_{15}\text{Sb}_{85}$ was admixed for the sample compartment. Due to the higher sensitivity of this calorimeter, already 15 mg of sample material were sufficient to detect the heat released by the sample. This DSC has the additional advantage, that X-rays can pass the sample compartment without significant further modifications. Only the supply of a purge and contact gas (He in this case) had to be rotated by 90° – and including a thin film of mylar for thermal radiation reflection, X-ray transmissivity and as a barrier for the He atoms.

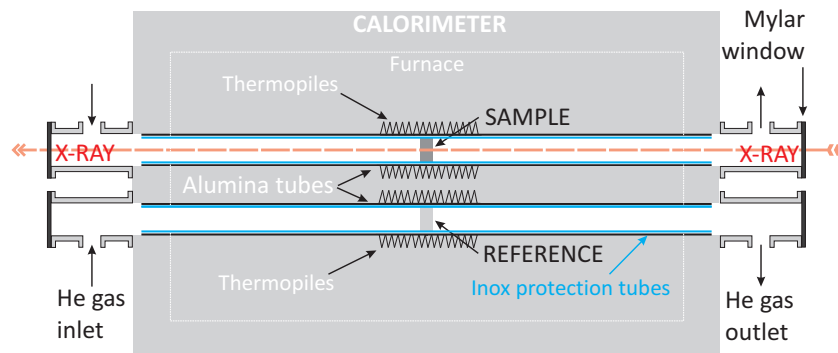


Figure 7.3: Technical drawing of the coupled DSC and EXAFS experiment.

The DSC was calibrated prior to the synchrotron experiment with exactly the same sample geometry and operating conditions. The calibration of temperature and energy was performed using the melting of high purity In, Sn, Pb, Sb samples prepared as ingots of 30 mg inside a 100 mg BN pellet. The heat flow dependence of the calibration factor was taken into account by performing the measurements of In, Pb, Sb and Sn references at 5 K/min and 10 K/min. The DSC was calibrated to the standard values as proposed by Stolen [159]. The resulting thermal scans are depicted in Fig. 7.4, center. The peaks in this figure correspond to exothermal phase transitions, whose onset temperatures are 514 K and 604 K with enthalpy changes of $45(4) \text{ meV atom}^{-1}$ and $6(1) \text{ meV atom}^{-1}$, respectively. These numbers are in good agreement with the results from literature [53].

During the heating ramp, the X-ray energy was scanned over the Ge K-edge at 11103 eV up to 11850 eV (15 \AA^{-1}) continuously every half minute, so that a full EXAFS pattern could be recorded. The same experiment was repeated for the Sb K-edge and the resulting EXAFS data sets were treated by refining a fixed set of parameters as published in literature [53]. Details in the data treatment are given in literature [161] and the resulting data are depicted in Fig. 7.4, left and right plots. The most dominant change is visible at the Ge edge, where a continuous reconfiguration of bonds can be observed: The number of Ge-Ge bonds (n_{Ge} in the left plot) increases as soon as the first exothermal transition sets in, whereas the number of Ge-Sb bonds (n_{Sb}) decreases. This reconfiguration is due to a phase separation, when an Sb-rich phase crystallizes upon the first transition. The second peak goes along with a shortening of the Ge-Ge atomic distances at 604 K. This decrease corresponds perfectly to the decrease in Ge-Ge bond lengths upon crystallization, which is reported to be 0.02 \AA in pure Ge [116].

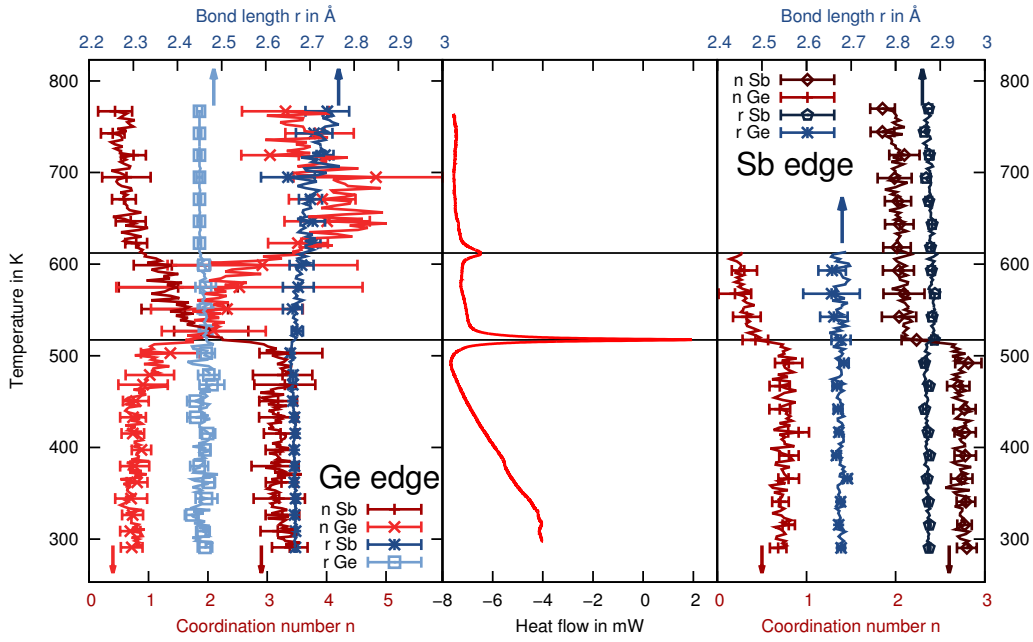


Figure 7.4: DSC and in-situ EXAFS scan of $\text{Ge}_{15}\text{Sb}_{85}$: Phase separation can be observed from the data on the Ge edge (left panel), where the ratio of Ge-Sb to Ge-Ge distances reverses during the crystallization. At the same time, also the number of Sb-Ge bonds reduces at the Sb edge.

It was shown that a calorimetric analysis allows determining the latent heats of a phase transition like crystallization. Even a small signal due to the crystallization of the segregated Ge atoms could be evidenced and evaluated. From this latent heat and from the number of Ge-Ge bonds, it can be concluded that 33(8)% of the Ge atoms segregate during the first crystallization. If the phase separation prevails after melt-quenching the material (as it occurs in a phase-change memory cell), the crystallization temperature is significantly reduced due to the higher concentration of Sb [162] and the stability of the stored information is no longer assured.

7.3.2 Phase transitions in AIST

$\text{Ag}_4\text{In}_3\text{Sb}_{67}\text{Te}_{26}$ (AIST) was measured because of its low melting temperature, which is accessible even in a DSC with aluminum containers. A calorimetric scan of 22.062 mg of powderous, as-deposited amorphous AIST is depicted in Fig. 7.5. The scan was performed up to the melting temperature so that a larger vapor pressure might exist. Therefore, the scan was performed more rapidly with a heating and cooling rate of 40 K/min. The mass of the sample did not change by more than 0.1 mg. The first crystallization from the amorphous phase took place at an onset temperature of 451 K and a latent heat of 47.2 meV/atom is released. The melting process begins at 805 K, peaks at 819 K and a latent heat of $\Delta H = -190$ meV/atom is necessary to complete the melting. The crystallization from liquid state begins at 809 K, peaks at 804 K and releases a total heat of $\Delta H = -182$ meV/atom. Upon

the second heating, no more phase transitions occur and the melting transition set in very reproducibly at 805 K, peaks at 819 K and costs a latent heat of $\Delta H = -186$ meV/atom.

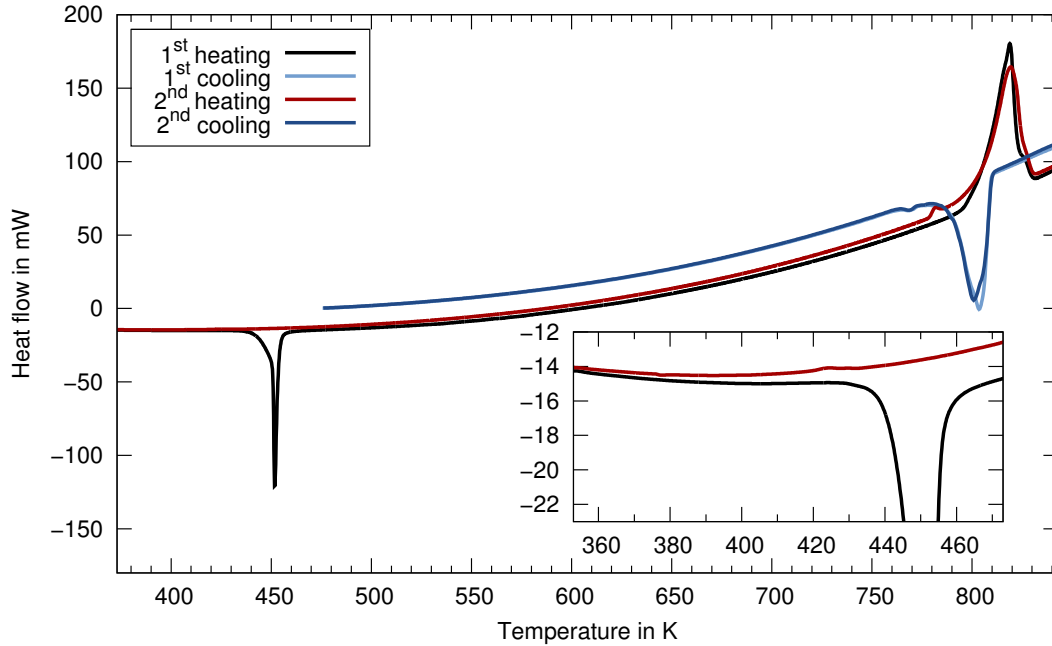


Figure 7.5: A direct DSC scan of as-deposited amorphous AIST is shown for a heating rate of 40 K/min. The two transitions (endo up) correspond to crystallization and melting of the material at an onset temperature of 451 K and 805 K, respectively.

7.3.3 Phase transitions in $\text{Ge}_3\text{Sb}_2\text{Te}_6$

A temperature scan of 37.25 mg as-deposited amorphous $\text{Ge}_3\text{Sb}_2\text{Te}_6$ has been performed at a heating rate of 5 K/min. This temperature scan is depicted in Fig. 7.6, but since the melting temperature of this compound is above the melting temperature of aluminum, it was not possible to access the liquid phase. Nevertheless, the crystallization process could be investigated. Its onset is at 441.1 K and releases a latent heat of 46.2 meV/atom. This leads to the formation of the meta-stable cubic phase [163], which is relevant for the transition in phase-change devices. A second, rather broad phase transition occurs at 614 K, which releases additional 7.5 meV/atom. This transition is related to the transition to the stable hexagonal phase. The results of this experiment are also included in Tab. 7.1.

A comparison of the results for AIST and $\text{Ge}_3\text{Sb}_2\text{Te}_6$ shows that the enthalpy changes upon crystallization are very similar.

7.3.4 Phase transitions in the $\text{GeTe-Sb}_2\text{Te}_3$ -system

For many materials, a calorimetric analysis of the phase-transitions has been performed by M. Klein [51] and the available data are compiled in Fig. 7.7, where some data points have been added for completeness. The calorimetric analyses of phase-transitions were per-

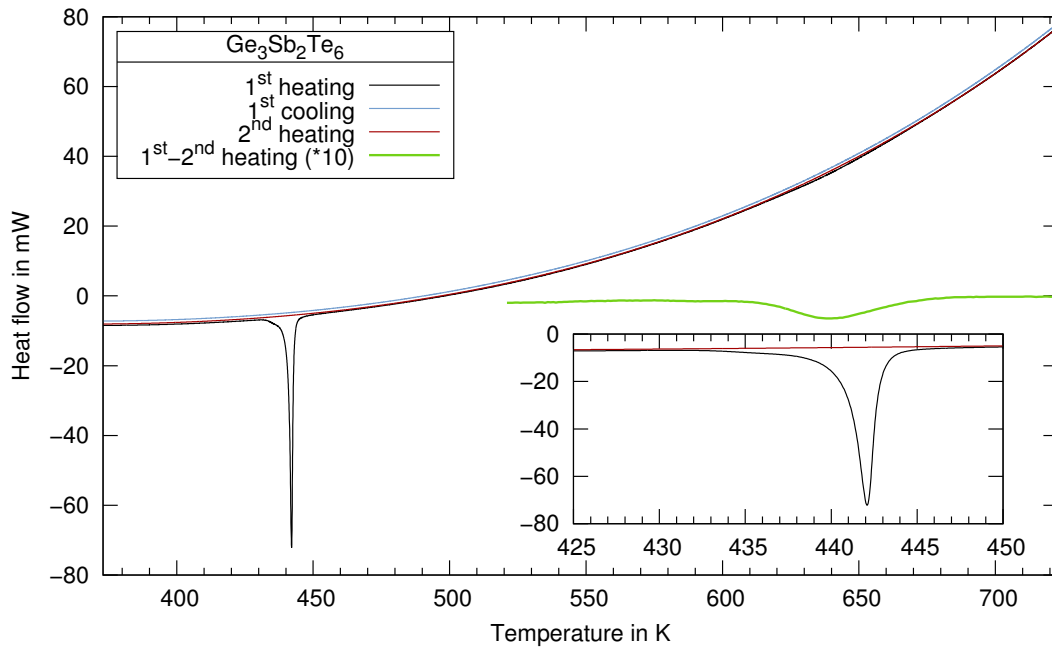


Figure 7.6: This DSC scan of amorphous $\text{Ge}_3\text{Sb}_2\text{Te}_6$ was obtained during heating with 5 K min^{-1} and the crystallization is clearly visible with an onset temperature of 441.1 K. The peak is located at 442.3 K and the total heat release amounts to 46.2 meV/atom. mass 37.25 mg. The second peak has 7.5 meV/atom and is located at 614 K onset and 640 K peak.

formed at heating rates of 10 K/min up to 450°C, including a re-scan. The resulting values are compiled in Tab 7.1 and in Fig. 7.7. Whereas the crystallization temperatures are well in line with literature data [164], the transition temperatures to the hexagonal phase deviate quite significantly. This deviation might originate from two facts: Yamada et al. prepared their samples by electron beam coevaporation [164], where the samples investigated here are prepared by sputter deposition from stoichiometric targets. Also the different film thickness (500 nm in the study by Yamada and 1500 nm here) might contribute a shift of the transition temperature.

The phase-diagram nicely shows the trend towards higher crystallization temperatures for GeTe-rich materials, which should allow for higher operation temperatures of the devices. This trend is nicely reproduced by the liquidus line, which is reproduced from literature [19]. In the original phase-diagram, only the phases GeSb_4Te_7 , GeSb_2Te_4 and $\text{Ge}_2\text{Sb}_2\text{Te}_5$ are drawn so that the additional phases $\text{Ge}_3\text{Sb}_2\text{Te}_6$ and $\text{Ge}_8\text{Sb}_2\text{Te}_{11}$ might be thermodynamically unstable against decomposition to $\text{Ge}_2\text{Sb}_2\text{Te}_5$ and GeTe. These less stable phases are therefore drawn as thinner lines in Fig. 7.7.

Table 7.1: Compilation of thermodynamic data of many glass-forming materials, including several phase-change materials. Values with (*) have been obtained by calculation. Scans with (+) were performed at 5 K/min. (#) The heats of crystallization are too small because the samples was only partly amorphous. All energies are given in meV/atom, except denoted otherwise. All entropies are given in $\mu\text{eV (atom K)}^{-1}$, except denoted otherwise. Molar masses are given in g/mol.

Compound	Molar mass	Crystallization			Melting			Cubic → Hex.	
		ΔH_{uc}	T_c	ΔS_{uc}	ΔH_m	T_m	ΔS_m	T_{ch}	ΔH_{ch}
Ge	72.6	117 [149]	750 K	32.3	-384 [165]	1211 K [166]	-317		
Si	28.1	124	960 K	34.7	-522 [165]	1687 K [166]	-309		
Sb ₂ Te ₃	125.3		393 K [167]					483 K ^a	
GeSb ₄ Te ₇	121.1	(#)	413 K	(#)	-179(12) [168]	880 K [168]	-169 [168]	501 K	
GeSb ₂ Te ₄	118.1	33.0(+) [51]	418 K[51]			886 K [169]	-146 [91]	547 K	10.9 [51]
Ge ₂ Sb ₂ Te ₅	114.1	34.3(+) [51]	428 K[51]					599 K	5.3[51]
Ge ₃ Sb ₂ Te ₆	111.5	46.2(+) [51]	441.1 K (+)					623 K	7.6
Ge ₈ Sb ₂ Te ₁₁	106.1	35 [51]	448 K					773 K ^b	
GeTe	100.1	46.7(+) [51]	483 K [51]		-74(14) [168]	985 K [168]	-74 [168]	793 K ^c	
In ₃ SbTe ₂	120.2					888 K [170]			
Sb ₂ Te	123.7	46.1(+) [51]	383 K[51] ([133], p. 94)			823 K [171]			
Ag ₄ In ₃ Sb ₆₇ Te ₂₆	122.5	47.2	451 K	35(20)		807 K [91]	-186, -212 [91]		
Ge ₁₂ Sb ₈₈	115.9					880 K [91]	-252 [91]		
Ge ₁₅ Sb ₈₅	114.4	51.0 (total)	514 and 604 K						
GeTe ₆	119.7	43.4(+) [51]	451 K / 484 K [51]		-153(10) [168]	655 K [168]	-185 [168]		
SnSe ₂	92.9				-221(9) (+) [168]	917 K [168]	-238 [168]		
GeSe	75.8				-109(10) [168]	947 K [168]	-115 [168]		

^amax. in C_p
^bextrapolated
^cextrapolated

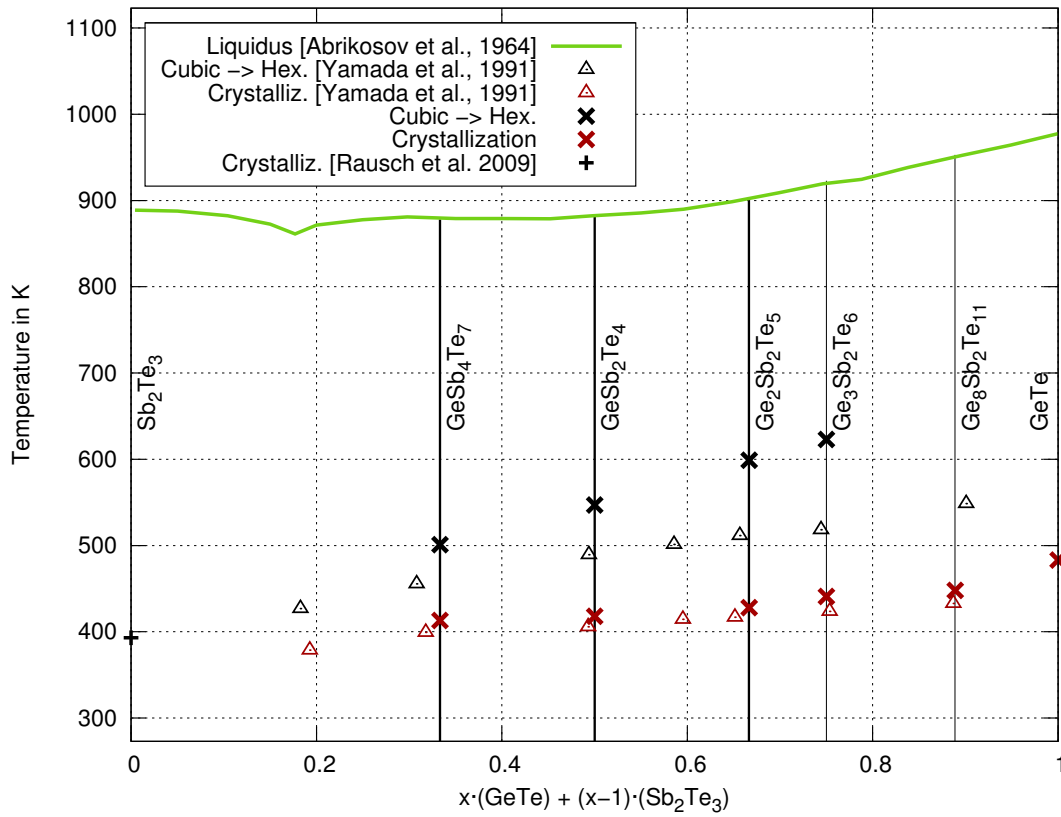


Figure 7.7: This partial phase diagram of GeTe-Sb₂Te₃ contains the crystallization temperatures of amorphous compounds and the transition temperatures for the cubic to hexagonal phase transition for those materials, which possess a meta-stable cubic phase. Additional data are included: Yamada et al. [164] (triangles), Abrikosov et al. [19] (liquidus line).

7.4 Measurements of specific heat/entropy

In the preceding section, the phase transitions have been investigated thermodynamically, resulting in values of $\Delta H_{ac}(T_c)$ and T_c . Still, the entropy difference at the crystallization temperature, $\Delta S_{ac}(T_c)$, is unknown. In Sec. 6.2.2, a strategy was presented to calculate this number based on the knowledge of the specific heats as a function of temperature for the crystalline phase and for the (undercooled) liquid. These measurements will be presented in the following.

Since the temperature range of the available calorimeter is limited to the temperature range below 863 K, only some phase-change materials can be molten. One such material is AIST, but unfortunately, all materials from the pseudobinary line between GeTe and Sb₂Te₃ melt at higher temperatures and are therefore inaccessible for this analysis. The resulting specific heats of AIST in the amorphous, crystalline and liquid phases are depicted in Fig. 7.8. The bright red stars denote the specific heat of the as-deposited amorphous phase, whereas the dark red crosses and the blue triangles denote a scan of the crystallized sample

over the full available temperature range. The data are in good agreement with the earlier results by Kalb et al. [25].

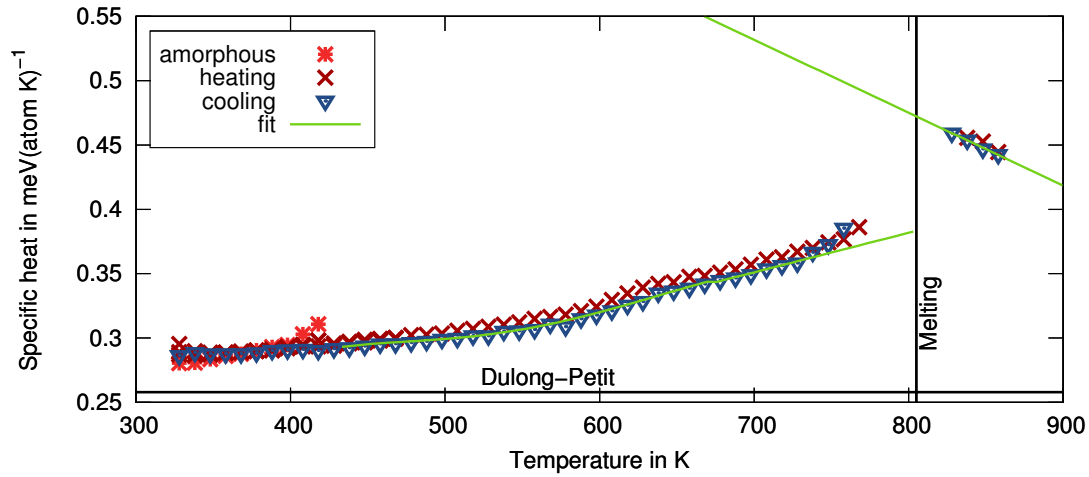


Figure 7.8: The specific heat of amorphous, crystalline (for heating and cooling) and liquid AIST is shown. Due to a low Debye temperature, the Dulong-Petit limit is always exceeded. Phase transitions occur upon crystallization at 451 K and at 807 K during melting.

A significant increase of specific heat above the general value by Dulong Petit occurs at higher temperature. This increase is usually observed at higher temperatures. During the melting transition, the extra heat release of the phase transition prevents an exact evaluation of the specific heat. In the liquid phase, an even higher specific heat is obtained, which decreases with temperature. These values can be fitted by a straight line $C_p = C_0 + \alpha T$, because its integral leads to Eq. 6.10. This fit has been applied and leads to the parameters $C_0 = 0.93(3) \text{ meV (atom K)}^{-1}$ and $\alpha = -5.6(3) \text{ meV (atom K}^2)^{-1}$. The data of Fig. 7.8 can be used to calculate entropy functions of temperature for each phase according to $S = \int C_p/T dT$. Only the absolute values of these entropies are still unknown. Starting from the liquid phase, it can be defined arbitrarily that $S(T_m) = 0$. This convention is applied in Fig. 7.9, where the entropies of all phases and the extrapolation of the liquid phase are included. Since there is no phase transition between the liquid and the undercooled liquid, these data can be extrapolated to very low temperatures. Since the latent entropy of fusion is also known, the entropy of the crystalline phase can be aligned to match the criterion $S(T_m) = 0$. Both curve intersect at the Kauzmann temperature, which turns out as 410(20) K. This value is reasonable, but the error contains only the experimental error of the specific heat measurement in the liquid phase. It is furthermore known, that the glass transition coincides with the crystallization (cf. Kalb [15]), so that the undercooled liquid is frozen to the glassy phase at the crystallization temperature. The entropy of the undercooled liquid at the glass transition therefore allows deriving the excess entropy of the amorphous phase, which is $35(20) \mu\text{eV (atom K)}^{-1}$ and contributes $-16(10) \text{ meV atom}^{-1}$ to the change of free enthalpy of crystallization, which is then reduced to $30(10) \text{ meV atom}^{-1}$. Unfortunately, the large error denies a useful comparison to other materials, but the preceding

analysis shows that this evaluation is feasible with precise data for the specific heat of the liquid phase.

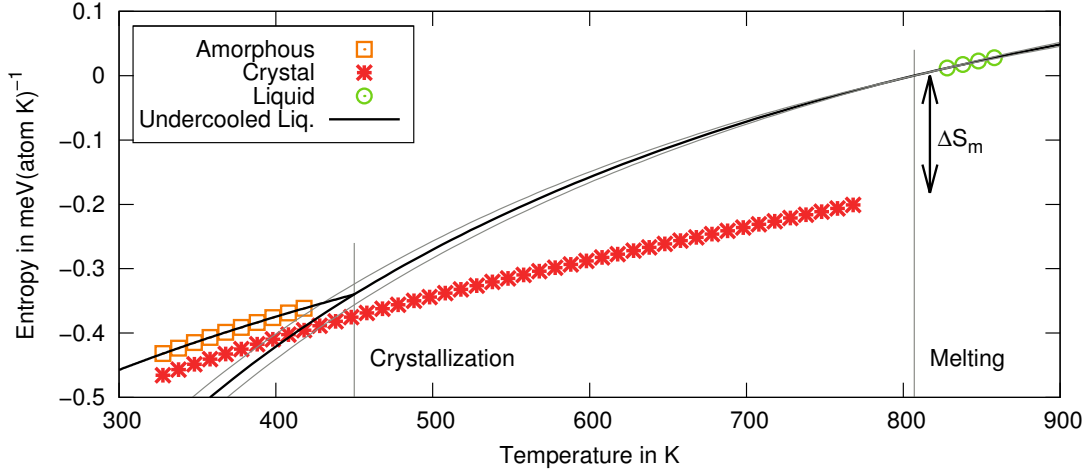


Figure 7.9: Entropy of AIST in the amorphous, crystalline and liquid phases with a reference value of $S(T_m) = 0$. The thin grey lines denote the 1σ statistical error for the extrapolation of the entropy in the undercooled liquid phase.

7.5 Comparison of GST and Sb₂Te-based phase-change materials

A pronounced substitutional disorder was revealed during the structural analysis of the metastable cubic phase of several GST phase-change materials. This disorder was shown to contribute a configurational entropy of approx. $40 \mu\text{eV}(\text{atom K})^{-1}$. At the crystallization temperature of approx. 420 K, this corresponds to a contribution to the free enthalpy G of $-17 \text{ meV}(\text{atom})^{-1}$, which is significant as compared to the change in enthalpy upon crystallization, $\Delta H_{ac} \approx 40 \text{ meV}(\text{atom})^{-1}$. This large configurational entropy reduces the free enthalpy of the meta-stable crystalline phase in those GST compounds, where such a disordered phase exists. The reduction of free enthalpy is even larger than the gain in enthalpy during the transition from the meta-stable to the stable phase (cf. Tab. 7.1) and therefore, this disorder is the reason for the existence of the meta-stable phase. It is natural to wonder, how this extra entropy of the crystalline phase enters the driving force of crystallization, $\Delta G_{ac} = \Delta H_{ac} - T\Delta S_{ac}$. Since $\Delta S_{ac} = S_a - S_c > 0$, the extra entropy of the crystalline phase reduces the entropy change upon crystallization and thereby increases the driving force of crystallization, ΔG_{ac} . It is therefore evident, that a significant entropy of the crystalline phase involved in the fast crystallization increases the driving force of crystallization and therefore increases the temperature dependence of nucleation and growth-rates, cf. Sec. 6.1.1.

Since such pronounced disorder was not observed for Sb₂Te-based phase-change materials like AIST, we can conclude that the entropy difference ΔS_{ac} is smaller for GST than

for Sb₂Te-based phase-change materials. Quite related to this analysis, it is worth returning to the observation of nucleation and growth dominated crystallization. Fig. 1.3 depicts TEM images of crystallized regions in AIST and in GST and it can be seen that crystallization takes place growth dominated in AIST, whereas GST crystallizes mostly by nucleation. It was further discussed that the formula for growth (cf. Eq. 6.2) is dominated by the activation barrier for the diffusion process, whereas nucleation is exponentially dependent on the change of free enthalpy per volume, $\Delta g_V > 0$. Additional surface effects $\Delta g_S < 0$ enter the fundamental equation for nucleation Eq. 6.1. Let us now discuss the influence of the large entropy of the crystalline phase of GST compounds. It was shown that it reduces the change in entropy Δs and thereby increases the change of free enthalpy $\Delta g_V = \Delta h_V - T_c \Delta s_V$. Since this is the driving force of nucleation, the larger entropy of crystalline GST as compared to crystalline AIST could explain the larger nucleation rate observed in this material. It is important to remember that also the temperature of crystallization T_c enters the equation, so that this comparison holds only for the crystallization using common heating rates some tens of K/min. At faster heating rates and higher crystallization temperatures, this situation might change. It should be pointed out as well, that the interface energies between the amorphous and crystalline regions might differ for both materials.

This result is well in line with the $T_g/T_m = T_{rg}$ -criterion, which was introduced in Sec. 1.4.1. As can be seen from Tab. 1.2, the value for T_{rg} is indeed lower for a GST compound, which is related to a larger nucleation rate by the original theory of Turnbull.

In conclusion, two arguments were presented, why the crystallization in GST compounds should be based on higher nucleation rates than that of e.g. AIST: The higher entropy of the crystalline phase of GST reduces the change in entropy upon crystallization and thereby increases the driving force of nucleation. This increase of the driving force has a more significant influence on the nucleation, where it enters exponentially than on the growth process, where it enters only linearly. Therefore, a large configurational entropy of the crystalline phase should favor nucleation dominated crystallization. The value for T_{rg} is also lower for GST, which is a criterion for nucleation dominated crystallization according to Turnbull.

One can speculate that materials with similarly large entropies of the crystalline phase will also crystallize via a large influence of nucleation. Indeed, also in In₃SbTe₂ and in the ternary GeTe-SnTe-systems, large configurational entropies were found based on the analysis of local atomic structures. Therefore, these materials might crystallize via faster nucleation than e.g. Sb₂Te or SnSe₂, whose crystalline structures contain only negligible configurational entropy – despite the usual thermally induced imperfections.

CHAPTER 8

Summary and conclusions

Atomic structure

The local atomic structure of several amorphous and crystalline phase-change materials has been investigated. The analysis of EXAFS and scattering data revealed that the atomic short range order changes significantly upon crystallization in all investigated materials, i.e. for GeSb_2Te_4 , $\text{Ge}_2\text{Sb}_2\text{Te}_5$, In_3SbTe_2 , Sb_2Te , AIST, GeTe and $\text{Ge}_{15}\text{Sb}_{85}$. In all these materials, the average nearest neighbor distance increased by 5% to 15%. This pronounced change in atomic distances goes along with an increase in the total coordination numbers, whereas the 8-N rule was found to hold for the amorphous phase of all materials except In_3SbTe_2 . In $\text{Ge}_2\text{Sb}_2\text{Te}_5$, e.g., the coordination number was found to increase from 2.78(3) to 5.23(5) in the crystalline phase. In conclusion, the 8-N rule is not obeyed in the crystalline phase of all investigated materials, where most atoms are in a 6-fold coordinated octahedral environment with the number of neighboring atoms being somewhat reduced due to the presence of intrinsic vacancies. This change in coordination number upon crystallization implies changes in the electronic structure as well. Indeed, the covalent bonds of the amorphous phase turn to resonant covalent bonds in the crystalline phase, since the valence orbitals are only half filled. Such an arrangement of atoms in the crystalline phase with perfect octahedral symmetry and half-filled bands is unstable against atomic displacements.

These atomic displacements are indeed observed in the crystalline phase of several of these compounds. It was shown that they are well described by a Peierls mechanism, which opens a gap in proportion to the amplitude of the atomic displacements. The octahedral atomic environment implies the formation of a rock-salt lattice, from which the atomic positions deviate randomly. The rock-salt structure of phase-change materials usually contains one sublattice, which is occupied by a single element (usually Te, but In in the case of In_3SbTe_2) and another sublattice, which is chemically disordered. This chemical disorder is referred to as substitutional disorder and induces static atomic displacements in particular

in GST compounds, because the local atomic charges deviate significantly: 0 for vacancies and 51 for Sb atoms. Also in In_3SbTe_2 and in ternary GeTe-SnTe compounds, such disorder was shown to exist.

Disorder

This atomic disorder is of particular interest, mainly because of two reasons: Firstly, a disorder induced metal-insulator transition has been reported to occur as a function of the annealing temperature of several GST-compounds, i.e. as a function of atomic disorder. Secondly, the disorder of the crystalline phase was shown to increase the driving force of crystallization since it leads to an increase of the change in free enthalpy upon crystallization. Therefore, the sources of atomic disorder in rock-salt like GeSb_2Te_4 have been investigated and several trends have been found, which reveal a gradually decreasing disorder: The amplitude of local atomic displacements reduces continuously within the cubic rock-salt phase. However, the resulting phase is still insulating. At a well defined transition temperature, the insulating cubic phase transforms into an insulating hexagonal phase, where the majority of vacancies is ordered on layers. This structure, however, was found to contain still significant sources of disorder: The atomic displacement parameters are much larger than what is expected for a single crystal and indeed, a remaining substitutional disorder on the Ge/Sb-sublattice was revealed for the metallic hexagonal phase by comparing DFT calculations to experimental data. This finding suggests that it is not the disorder of Ge and Sb atoms, which is responsible for the metal-insulator transition. Therefore, two sources of disorder remain, which could drive the metal-insulator transition: Stacking faults of the layers in the hexagonal phase or remaining atoms on the vacancy layers. The stacking faults were shown to decrease during the metal-insulator transition, whereas the second mechanism could not be evidenced due to the low fraction of atoms, which suffices to localize charge carriers. Already an occupation of the vacancy layers with 7% of the atoms is sufficient to localize charge carriers. This low fraction of atoms was below the detection limit of the experiments. The importance of the chemical ordering of the layers is further supported by the pronounced anisotropy of electronic conductivity, since significantly higher electronic conductivities (approx. a factor of 100) are found parallel to the layers than perpendicular to them (in e.g. Sb_2Te_3 or Bi_2Te_3 [172]).

Thermal vibrations

In common semiconductors, the variance of interatomic distances is larger in the amorphous phase than in the crystalline phase. In phase-change materials, however, it is larger in the crystalline phase of GeSb_2Te_4 and $\text{Ge}_2\text{Sb}_2\text{Te}_5$. This is rather surprising and might at first sight be linked to the large static atomic displacements. However, also the temperature dependence of the variance is larger in the crystalline phase, as was revealed by the comparison of XRD data for the crystalline phase and EXAFS data on the amorphous phase. This observation suggests that the interaction potentials of the crystalline phase are softer

than those of the amorphous phase. At the same time, it is known from literature, that the crystalline phase is elastically harder than the respective amorphous phase. This controversy was revealed by direct evidence of this vibrational softening from the density of phonon states. Indeed, the partial density of phonon states around Sb and Te shows that the interaction potentials (optic modes) soften upon crystallization, whereas macroscopically the material (acoustic modes) hardens. This surprising observation might be caused by the significantly larger coordination number of the crystalline phase, where the softness of the interaction potential is overcompensated by the larger number of bonds.

Thermodynamics of Crystallization

The phase transitions and the specific heat of phase-change materials have been investigated calorimetrically. It was found that the latent heats of crystallization ΔH are significantly lower than those of e.g. pure Ge. This observation is surprising, since one would expect a large driving force for crystallization ΔG in a material, which crystallizes more rapidly. Both quantities, ΔH and ΔG are related via the entropy change upon crystallization, ΔS , which has been measured calorimetrically by determining the specific heat of crystalline and liquid AIST. The specific heat of the liquid phase could be measured with good accuracy and was extrapolated over the undercooled liquid regime in order to obtain the residual entropy S_g . This number was obtained as $35(10) \mu\text{eV} (\text{atom K})^{-1}$, which is in good agreement with the values 32 and $35 \mu\text{eV} (\text{atom K})^{-1}$ for Ge and Si, respectively. For a material with residual entropy in the crystalline state, this entropy difference should be significantly smaller, since already the configurational entropy for a random configuration of Ge, Sb and vacancies on the second sublattice, the residual entropy of the crystalline phase would be about $42 \mu\text{eV} (\text{atom K})^{-1}$. This residual entropy of the crystalline phase increases the thermodynamic driving force of crystallization. An inspection of the equations of nucleation and growth revealed that the driving force enters linearly in the growth rate and exponentially in the nucleation rate. In conclusion, the large entropy of the crystalline phase could explain the larger nucleation rate of e.g. GeSb_2Te_4 . In conclusion, it was shown that a large atomic disorder in the crystalline phase and the highest possible ordering of the amorphous phase lead to the highest possible thermodynamic driving force of crystallization.

APPENDIX A

Drift in phase-change materials: A study of the model system GeTe-SnTe

One of the challenges towards the application of phase-change memories in consumer products is to find a strategy to control the resistance drift in these materials [18]. The magnitude of the resistance drift is measured by the dimensionless drift coefficient ν so that no drift occurs for $\nu = 0$. It refers to the change in electronic resistivity with time [173]. The magnitude of drift therefore defines a minimum difference in resistivity between the different states of resistivity in a device. Concludingly, the resistance drift limits the number of states, which can be reliably stored in one phase-change memory cell. Whereas the common phase-change material GeTe shows a significant drift, the substitution of Ge with Sn reduces this effect: GeTe shows a drift coefficient of $\nu = 0.122(2)$ at 323 K, whereas the drift coefficients of $\text{Ge}_3\text{Sn}_1\text{Te}_4$ and $\text{Ge}_2\text{Sn}_2\text{Te}_4$ are only 0.100(2) and 0.051(1), respectively [174]. Since resistance drift is linked to the structural relaxation of these materials [173], it is important to at least know their atomic structure. This knowledge might reveal a structural difference in the materials, which enables the development of design-rules to control resistance drift.

Based on earlier investigations of resistance drift and an observed trend of ν vs. stoichiometry in the GeTe-SnTe system [20][174], the atomic structure of amorphous GeTe, $\text{Ge}_3\text{Sn}_1\text{Te}_4$, $\text{Ge}_2\text{Sn}_2\text{Te}_4$ and of crystalline GeTe, $\text{Ge}_3\text{Sn}_1\text{Te}_4$, $\text{Ge}_2\text{Sn}_2\text{Te}_4$ and SnTe was determined using EXAFS analysis. Amorphous SnTe crystallizes below ambient temperature and is therefore not a potential phase-change material and was not investigated here. Samples of these compounds were deposited from stoichiometric targets using a DC magnetron sputtering setup described elsewhere [91]. The films had a thickness of some μm and did not show sharp reflections in x-ray diffraction so that the samples are in an amorphous phase. These films were deposited on borosilicate substrates and subsequently scratched using another slide of borosilicate slide. This method allowed the preparation of sufficient

amounts of amorphous material with only small contaminations of the sample with borosilicate. These contaminations are not relevant for EXAFS measurements due to the low energies of absorption edges in borosilicate and its low absorption coefficients. The samples were enriched with about 200 mg of cellulose and subsequently pressed to pellets of 13 mm diameter with a weight of 5-6 tons.

All EXAFS measurements on the GeTe-SnTe compounds were performed at beamline C at HASYLAB, DESY, Hamburg (cf. Sec. 2.7.1) using a cryostat to keep the samples at 10 K during the measurements.

A.1 Amorphous Phase

A.1.1 Amorphous GeTe

GeTe is the most prominent phase-change material from the system GeTe-SnTe. Since it is a binary material, the EXAFS data should be less complex than those of the intermediate ternary compounds and the results from the analysis of GeTe should simplify their evaluation. The analysis of EXAFS data on the binary data has already been presented in Sec. 4.3. In total, four distinct interatomic distances were found: One of them involved Ge-Ge distances only, whereas the other three were identified as Ge-Te distances. This arrangement of scattering paths at the Ge edge will be employed for the ternary materials as well.

A.1.2 Amorphous Ge_3SnTe_4

The next investigated material of the GeTe-SnTe system contains already a significant amount of Sn, which is incorporated instead of some Ge. The content of Sn turned out to be sufficient to obtain high quality data on all three K-edges, as can be seen from Fig. A.1, where EXAFS data of all edges are shown together with a fit. A detailed analysis of the fitting results in comparison to GeTe is presented in the following. At this point of the discussion, it would make sense to investigate the other binary end-point of the GeTe-SnTe system, amorphous SnTe, but unfortunately, amorphous SnTe crystallizes below ambient temperature at 180 K [175], and could not be prepared in the amorphous phase.

In order to fit all EXAFS data of amorphous Ge_3SnTe_4 , an additional element has to be included in the discussion, whose amplitude reduction factor S_0^2 is not yet known. It was obtained rather precisely from the analysis of crystalline SnTe in Chpt. A.3.2 and the factors S_0^2 are set to 0.67, 0.69 and 0.74 in the following for Ge, Sn and Te, respectively. The best fit has residua of 0.006, 0.008 and 0.013 for the three edges – again below the maximum for a reliable fit. The edge energy corrections obtained reasonable values of 8(2) eV, 5(1) eV and 7(2) eV for Ge, Sn and Te, respectively.

In the case of Ge_3SnTe_4 , the Ge K edge was analyzed first, using the same combination of scattering paths as for amorphous GeTe. Subsequently, the Sn K-edge was refined with the lowest number of scattering paths (i.e. free parameters) possible. It turned out that 2 scattering paths were already sufficient to obtain a residual of 0.008. Finally, the results of

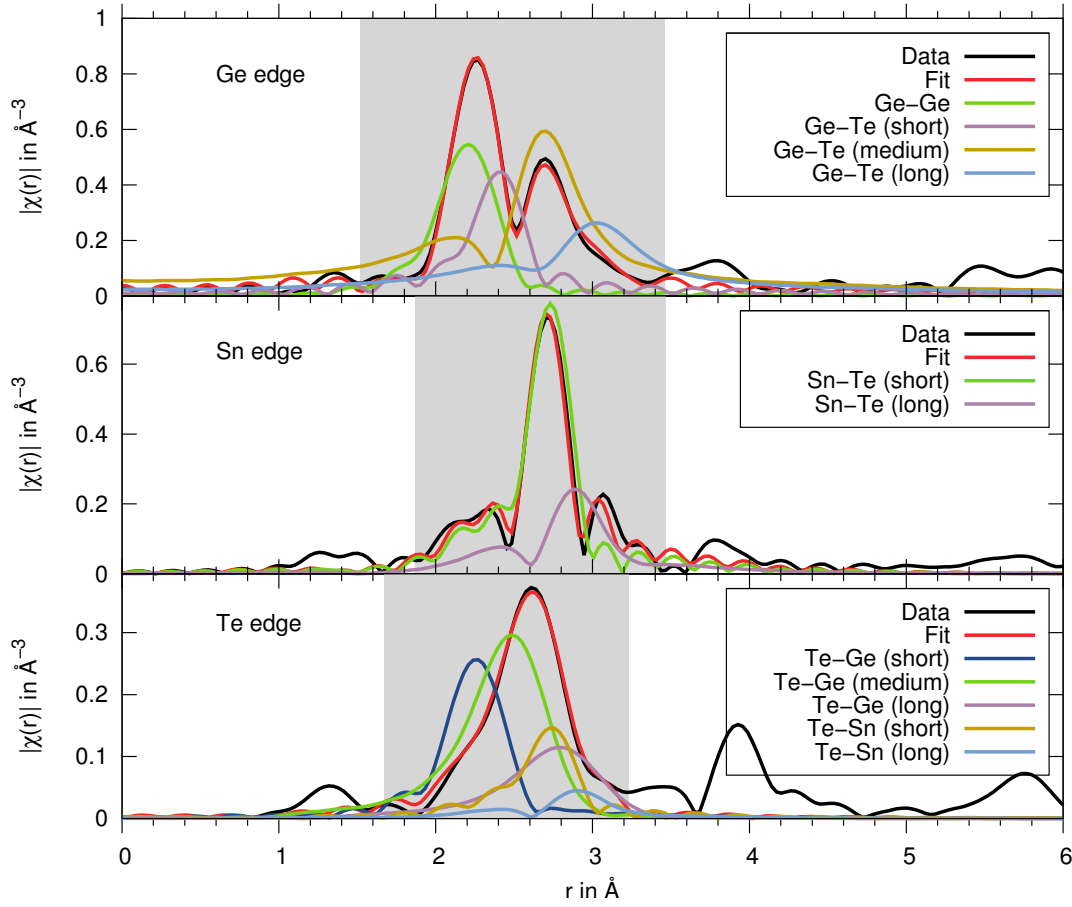


Figure A.1: Amorphous Ge_3SnTe_4 at 10 K: Fourier Transforms of measured and refined EXAFS spectra are shown. As compared to amorphous GeTe, the stronger influence from longer bonds around Ge can be seen in the data. They agree well with the bond lengths obtained from amorphous GeTe.

both refinements were transformed to the Te edge and checked for consistency. Since a good agreement between this transformation and the data of Te K-edge was obtained, a possible influence of Te-Te bonds is very unlikely and the resulting structural model was employed to refine all three K edges simultaneously. The fitting results are presented in Fig. A.1 and Tab. A.1.

The fit is based on the assumption that the same Ge-based atomic distances exist as in amorphous GeTe. These parameters were used as starting values for the fit and it leads to a stable result with similar atomic distances. While the Ge-Ge and Ge-Te (short) distances are in good agreement with amorphous GeTe, there is a difference in the bond lengths associated with the longer distances around Ge: In amorphous Ge_3SnTe_4 , the medium distance is significantly larger than that of amorphous GeTe and in good agreement with the short distance of crystalline GeTe.

At the Sn edge, two scattering paths are sufficient to refine the EXAFS data. The atomic distances related to these scattering paths can be compared only to the bond length of Sn-Te

Table A.1: EXAFS fitting parameters of amorphous Ge_3SnTe_4 at 10 K. The fitting model is based on the model employed for GeTe. Around Ge, almost the same sequence of bond lengths is observed. Constrained parameters are denoted by the same letter.

Scattering Path	N	Atomic distance r	Displacement Parameter σ^2
Ge-Ge	1.2(3)	2.49(1) Å	0.004(3) Å ²
Ge-Te (short)	0.8(3)	2.60(1) Å (a)	0.003(1) Å ² (a)
Ge-Te (medium)	2.0(5) (a)	2.84(1) Å (b)	0.011(2) Å ² (b)
Ge-Te (long)	2.0(5) (a)	3.15(1) Å (c)	0.016(1) Å ² (c)
Sn-Te (short)	2.4(2) (b)	2.98(1) Å (d)	0.004(1) Å ² (d)
Sn-Te (long)	2.4(2) (b)	3.13(2) Å (e)	0.010(2) Å ² (e)
Te-Ge (short)	0.6(1)	2.60(1) Å (a)	0.0027(5) Å ² (a)
Te-Ge (medium)	0.8(4) (c)	2.84(1) Å (b)	0.008(6) Å ² (b)
Te-Ge (long)	0.8(4) (c)	3.15(2) Å (c)	0.011(7) Å ² (c)
Te-Sn (short)	1.2(2) (d)	2.98(1) Å (d)	0.004(1) Å ² (d)
Te-Sn (long)	1.2(2) (d)	3.13(2) Å (e)	0.010(2) Å ² (e)

in crystalline SnTe. There (cf. Sec. A.3.2), the undistorted cubic rock-salt structure (β -phase) was obtained, where the unique bond length of 3.151(2) Å is revealed, which nicely corresponds to the long Sn-Te distance observed in amorphous Ge_3SnTe_4 . This shorter distance is only observed in amorphous ternary Ge-Sn-Te-systems. In principle, this shorter distance might as well originate from Sn-Sn instead of Sn-Te bonds, because the phase-shift induced upon backscattering at Sn or Te cannot be clearly distinguished. From a simultaneous refinement of all three edges (including the Te edge), it was found that the residual of the Te data increases from 0.012 to 0.020 if the Sn-Te (short) scattering path is replaced by a Sn-Sn scattering path. Therefore, the fit using two Sn-Te distances leads to a slightly better refinement and this result is presented here.

Like in amorphous GeTe, a simultaneous refinement of all absorption edges is presented here and the resulting coordination numbers will be discussed in the following. The total coordination numbers for the atoms in amorphous Ge_3SnTe_4 turn out as 6.0(9), 4.8(3) and 4.6(7), for Ge, Sn and Te, respectively. 33(6)% of the average interatomic distances around Ge are related to Ge-Ge distances, i.e. to phase-separated Ge.

A.1.3 Amorphous GeSnTe_2

Let us continue the series with amorphous GeSnTe_2 , a compound, which contains already the same amount of Sn as Ge. High quality EXAFS data have also been obtained for all three K-edges of this material and they are depicted in Fig. A.2, where a fit is included as well.

A detailed analysis of the fitting results in comparison to amorphous GeTe and Ge_3SnTe_4 is presented in the following.

The fit has been performed using the amplitude reduction factors S_0^2 like before, i.e. 0.67, 0.69 and 0.74 for Ge, Sn and Te, respectively. The best refinement, which is also shown in Fig. A.2 has a residual deviation of 0.006, 0.008, 0.012 at the Ge, Sn and Te edges, respectively and the fit can be considered reliable. The edge energy corrections at those edges turn out as 2.4(1) eV, 4.7(6) eV and 3.2(8) eV.

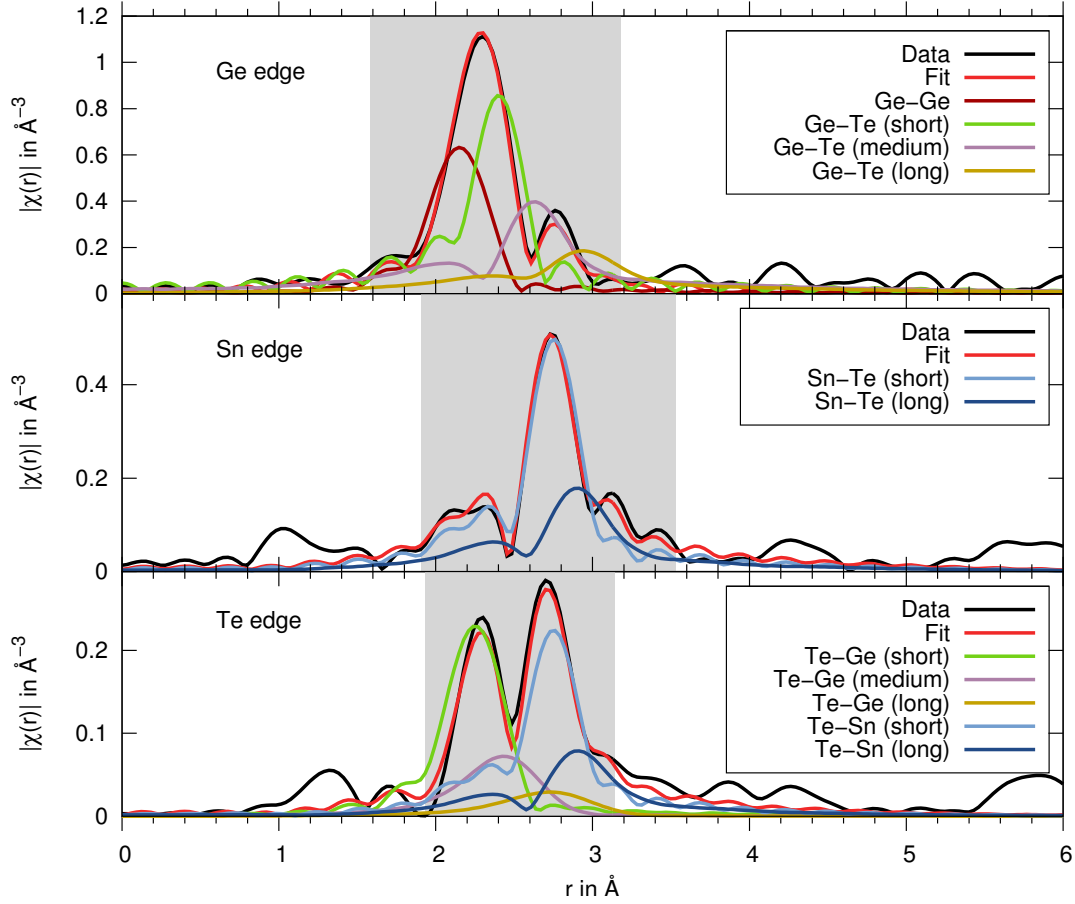


Figure A.2: Amorphous GeSnTe_2 at 10 K: Fourier Transforms of EXAFS spectra are shown together with their refinement. The data nicely reveal the dominance of heteropolar Ge-Te and Sn-Te bonds: The short distances of Ge-Te and the long distances of Sn-Te can be found at the Te edge as well. The refinement is based on the fitting model, that already turned out suitable for amorphous Ge_3SnTe_4 . The grey shaded areas denote the region that was taken into account during the least squares fitting.

The EXAFS data of the Ge edge are refined based on the same configuration of scattering paths as used for amorphous GeTe. The scattering paths for the Sn edge have been copied from the fit of amorphous Ge_3SnTe_4 . The Ge and Sn edges were refined and the model was tested at the Te edge for consistency. It turns out that the fitting model for the Ge

Table A.2: EXAFS fitting parameters of amorphous GeSnTe_2 at 10 K. The fitting model is based on the results of amorphous GeTe and Ge_3SnTe_4 . Values with an (*) were fixed to the values obtained for amorphous Ge_3SnTe_4

Scattering Path	N	Atomic distance r	Displacement Parameter σ^2
Ge-Ge	1.1(2)	2.46(1) Å	0.003 Å ² (*)
Ge-Te (short)	1.4(2)	2.61(1) Å (a)	0.003 Å ² (*)
Ge-Te (medium)	2.6(5) (a)	2.82(2) Å (b)	0.011 Å ² (*)
Ge-Te (long)	2.6(5) (a)	3.13(2) Å (c)	0.016 Å ² (*)
Sn-Te (short)	2.3(2) (b)	2.99(1) Å (d)	0.006(1) Å ² (d)
Sn-Te (long)	2.3(2) (b)	3.12(3) Å (e)	0.012(4) Å ² (e)
Te-Ge (short)	0.6(1)	2.61(1) Å (a)	0.003 Å ² (*)
Te-Ge (medium)	0.8(4)	2.82(2) Å (b)	0.011 Å ² (*)
Te-Ge (long)	0.8(4)	3.13(2) Å (c)	0.016 Å ² (*)
Te-Sn (short)	1.2(2)	2.99(1) Å (d)	0.006(1) Å ² (d)
Te-Sn (long)	1.2(2)	3.12(3) Å (e)	0.012(4) Å ² (e)

and Sn-edges is very suitable to predict the data at the Te edge so that all three edges could be refined simultaneously. Some of the displacement parameters, however, were copied and fixed to results of the refinement of Ge_3SnTe_4 , because otherwise very large error bars were obtained on these parameters.

The atomic distances at both, the Ge and the Sn edge are in good agreement with those observed for Ge_3SnTe_4 , so that these two ternary compounds are characterized by the same structural features – only with different contributions.

A.2 Conclusions for the structural relaxation during the drift

The resistance drift of the amorphous phase is a limiting factor for the increase of storage density and therefore should be as low as possible. Since drift occurs irreversibly and is based on structural relaxation in these materials, it might be related to specific atomic arrangements in the amorphous phase. It was already observed in the study of amorphous GeTe , that as many as four distinct atomic distances exist around Ge. The shortest of these distances were identified as Ge-Ge distances, whereas the longer distances are due to bonds between Ge and Te. The existence of Ge-Ge bonds is related to the different coordination numbers of Ge and Te and the absence of a sufficient amount of Te atoms to satisfy the covalent bonding associated with the 8-N rule. It is therefore not surprising that Ge-Ge bonds appear. The observation, that the resistance drift is lower after the substitution of Ge atoms by Sn suggests that the atomic structures related to the resistance drift are decreased in these compounds. The previous analysis of EXAFS data revealed that (a) the intermedi-

ate and long distances of Ge-Te in the ternary systems are in better agreement with those observed in crystalline GeTe and (b) the average number of Ge-Ge distances per Ge atom reduces from 1.7 in amorphous GeTe to 1.2 in Ge_3SnTe_4 and 1.1 in GeSnTe_2 . The fraction of short distances between Ge and Te did not show a clear trend with composition. It can be speculated that either (a) the local atomic displacements are more well-relaxed (i.e. the total energy is lower) in the ternary compounds or that (b) a continuing formation of Ge-Ge distances occurs within the amorphous state. Whatever the structural relaxation mechanism is, this analysis has shown that the Ge atoms favor a particularly large spread of interatomic distances, which vary from 2.45 Å to 3.15 Å i.e. by 29%. This influence of the Ge atoms will lead to a strong degeneracy of the amorphous state and will favor structural relaxation. Sn atoms on the other hand only form bonds between 2.99 Å and 3.12 Å, so that the variance of 4% is significantly smaller. In order to reduce the resistance drift effect it seems therefore beneficial to employ phase-change materials without Ge content.

A.3 Crystalline phase

A.3.1 Crystalline GeTe

As-deposited amorphous GeTe crystallizes at approx. 470 K into the rhombohedral β -phase. Taking into account the measured stoichiometry of the sample ($\text{Ge}_{53}\text{Te}_{47}$ [129, 8]), it is expected that some excess Ge will segregate upon crystallization. The amorphous powder was annealed in a tube furnace at 508 K in order to perform EXAFS measurements on the crystalline phase. These measurements were performed at 10 K sample temperature on both K edges. The resulting data have been treated by van Eijk [113] and only the most relevant results are given here for a direct comparison with the analysis of the GeTe-SnTe ternary compounds. The EXAFS data were fitted using a parametrized model according to the $R\bar{3}m$ space group and lattice parameters $a = 4.277(5)$ Å and $\alpha = 58.30(8)^\circ$ are obtained at 10 K. The atomic positions are slightly displaced from their rocksalt-like position ($u = 0.25$) to $\pm(u, u, u)^t$ with $u = 0.236(1)$. The fit is performed at both edges simultaneously and residuals of 0.031 and 0.024 are obtained for the Ge and Te edges, respectively, after fitting over a range of 2 to 6.5 Å. The amplitude reduction factors S_0^2 were obtained from the well-known crystal structure with 3 short (2.863 Å) and 3 long (3.127 Å) bonds around each atom. The S_0^2 are 0.67(6) (Ge) and 0.86(8) (Te) with corresponding edge energy shifts of 5.8(6) and 6.7(7) eV.

Furthermore, 6(4)% of the Ge atoms were found to segregate. It is well known that Ge segregates from the sputter deposited samples of GeTe [21] due to their Ge-rich stoichiometry $\text{Ge}_{53}\text{Te}_{47}$. The result of 6(4)% of the Ge atoms segregating is perfectly in line with the 6% excess Ge in this compound. Therefore, the so-formed GeTe is rather free of vacancies. The Ge-Ge distance of the segregated phase is obtained as 2.45(2) Å, which is obtained for both, amorphous and crystalline pure Ge. These results present a good basis for the treatment of the Ge edges of the ternary GeTe-SnTe compounds.

Table A.3: Crystalline SnTe at 10 K: Partial coordination numbers, atomic distances and displacement parameters are given. These were obtained from the least-squares fitting of EXAFS data. Numbers, which are equal due to crystallographic constraints (according to cubic rock-salt structure, $Fm\bar{3}m$) are denoted with the same letter in brackets. The lattice constant is $a = 6.302(4) \text{ \AA}$.

Scattering Path	N	Atomic distance r	Displacement Parameter σ^2
Sn-Te/Te-Sn	6	3.151(2) \AA (a)	0.0048(3) \AA^2
Te-Te	12	4.456(3) \AA (a)	0.0045(4) \AA^2
Sn-Sn	12	4.456(3) \AA (a)	0.0056(5) \AA^2
Sn-Te/Te-Sn	8	5.458(3) \AA (a)	0.008(1) \AA^2
Sn-Sn	6	6.302(4) \AA (a)	0.005(3) \AA^2 (b)
Te-Te	6	6.302(4) \AA (a)	0.005(3) \AA^2 (b)

Before the crystalline ternary compounds are discussed, the other end of the GeTe-SnTe system should be analyzed, because it can give valuable information on the fitting process at the Sn K-edge.

A.3.2 Crystalline SnTe

The EXAFS spectra of crystallized powder of SnTe were measured at 10 K at both K absorption edges in transmission geometry. The magnitude of their Fourier transforms are depicted in Fig. A.3, which shows that the data correspond to a well ordered crystalline structure, since peaks of different coordination shells are narrow and visible even beyond 6 \AA . The data were fitted with calculated scattering paths, which originate from a rocksalt structure ($Fm\bar{3}m$) of SnTe (β -SnTe) with a lattice constant of $a=6.303(4) \text{ \AA}$. Both edges were refined simultaneously using only a small number of 11 free parameters out of 86, which are contained in the data according to the criterion by Nyquist [84]. These 11 parameters consist of two edge corrections, two amplitude reduction factors, the lattice constant and 6 displacement parameters. The residua of the edges are 0.044 and 0.018, which corresponds to a good fit considering the low number of parameters. The amplitude reduction factors are 0.69(3) and 0.74(3) for Sn and Te, respectively. The edge corrections are 7.7(3) eV and 6.3(3) eV. The displacement parameters are summarized in Tab. A.3.

In addition, several multiple scattering paths were taken into account. If their total path length is below 6 \AA , their displacement parameter was constructed by adding the parameters of the contributing paths. Above 6 \AA , an additional displacement parameter was defined for all multiple scattering paths, which turned out to be 0.0040(7) \AA^2 .

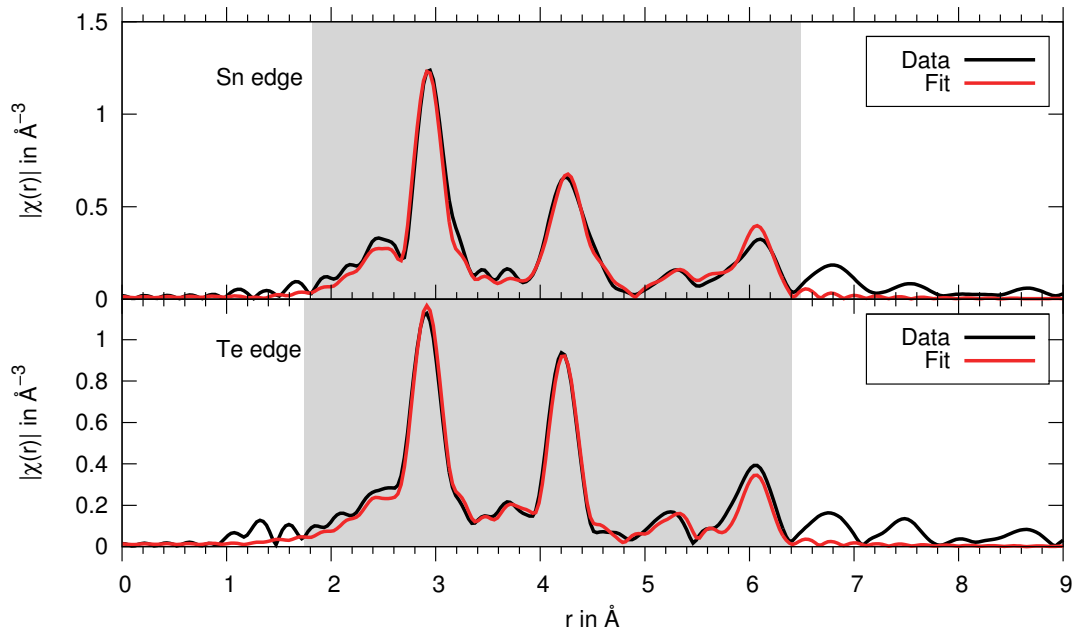


Figure A.3: Crystalline SnTe: Fourier Transforms of measured and refined EXAFS spectra from both K edges are shown. The fit is based on a rocksalt model of SnTe with a lattice constant of $a=6.303(4)$ Å. The various coordination shells can be clearly distinguished at both edges. They are not split to short and long bonds and therefore the local environment must be undistorted cubic at 10 K - well in line with findings in literature for samples with p-type charge carrier densities larger than $2 \cdot 10^{20} \text{ cm}^{-3}$ [176]. The grey shaded areas denote the region over which the least squares fitting was performed.

A.3.3 Crystalline Ge_3SnTe_4

As-deposited Ge_3SnTe_4 crystallizes into a cubic rock-salt like structure at 452 K (peak value after heating at 5 K/min) [177]. The crystalline phase has a density of 6.4 g/cm^3 [177] and contains some segregated Ge, as will be shown in this section. Like in $\text{Ge}_{15}\text{Sb}_{85}$, the excess Ge is probably segregated during the crystallization and forms an amorphous region [53]. This amorphous Ge crystallizes at 552 K (peak value after heating at 5 K/min) [177]. A detailed analysis of EXAFS data is presented in the following. The samples were prepared by sputter deposition on silica substrates and subsequently scratched to powder. This powder was crystallized at 488 K under Ar atmosphere and measured in transmission geometry over all three K absorption edges. The resulting data are shown together with the best refinement in Fig. A.4. The amplitude reduction factors of the fit were set to 0.67, 0.69 and 0.74 for the three edges of Ge, Sn and Te. The fitted edge energy corrections are $\Delta E = 4.5(3) \text{ eV}$, $5.1(3) \text{ eV}$ and 4.8 eV . All scattering paths of the fit are summarized with their parameters in Tab. A.4. The residuals of the fit are 0.012, 0.012 and 0.031.

An analysis of the individual local atomic environments reveals an interesting analogy between the amorphous and crystalline phases of Ge_3SnTe_4 : A splitting of bond lengths

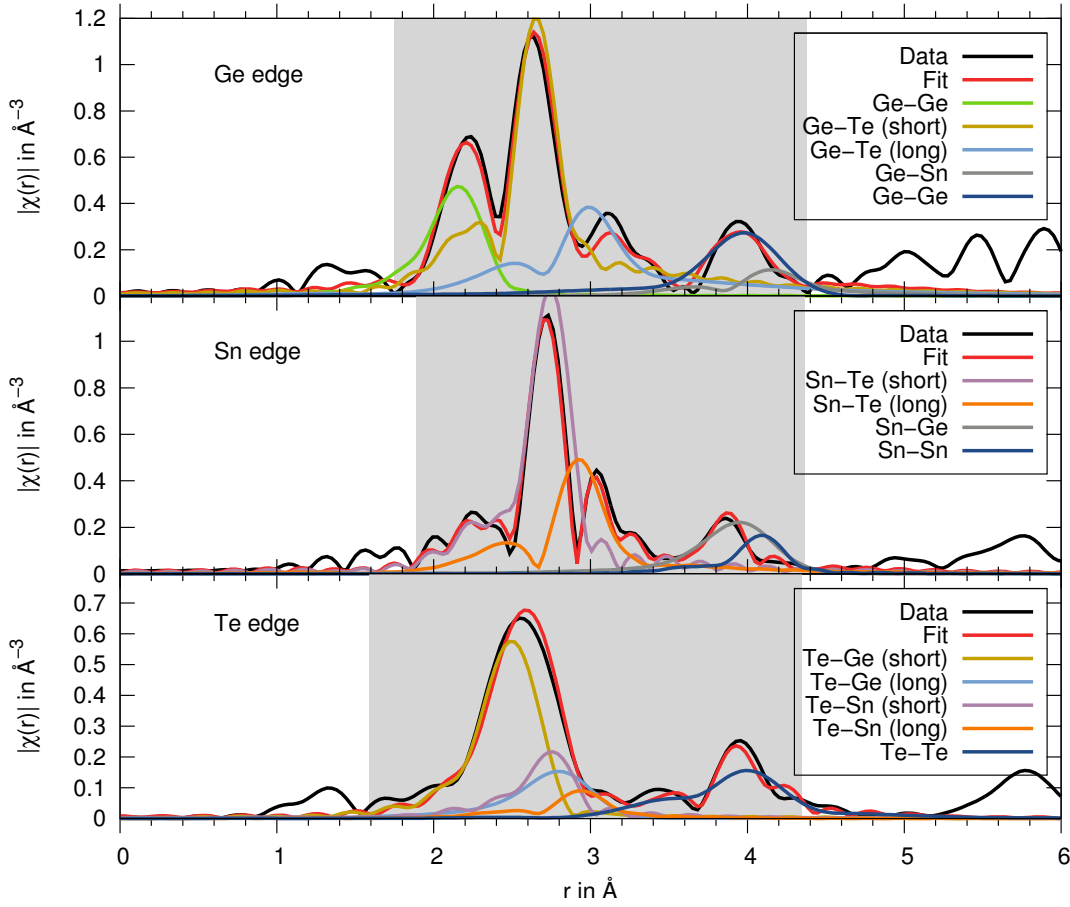


Figure A.4: Crystalline Ge_3SnTe_4 at 10 K: EXAFS data are shown together with a refinement of the first two coordination shells of the rock-salt lattice.

around Sn is observed not only in amorphous, but also in crystalline Ge_3SnTe_4 – although this splitting does not occur in crystalline SnTe , where a slight displacement of the atomic positions along the cubic $\{111\}$ directions could easily create such splittings. It is worth noting, that the resulting short and long bond lengths of Sn in crystalline Ge_3SnTe_4 are in very good agreement with those observed in the amorphous phase. This result shows that local atomic distortions prevail in crystalline GeTe-SnTe compounds, just like those observed in the meta-stable cubic phase of many $\text{GeTe-Sb}_2\text{Te}_3$ compounds. Both systems therefore possess a significant amount of substitutional disorder – in contrast to the binary materials GeTe and SnTe . It might therefore be worth investigating the GeTe-SnTe system further with regard to disorder induced localization effects, but since no vacancies are contained, no significant localization effects are expected.

The same substitutional disorder exists for the Ge atoms, which are also in a distorted coordination with short and long bonds. These Ge-Te bond lengths correspond well to those observed in crystalline GeTe . Since the transformation of these results to the Te edge gives a good agreement as well, all three edges were refined simultaneously. A fit of the second neighboring atoms has been performed as well, but although the resulting curves match the

Table A.4: Results from an EXAFS analysis of crystalline Ge_3SnTe_4 at 10 K. The short Ge-Ge distances are due to phase-separated Ge. Significant local atomic displacements are revealed by the splitting of short and long distances around both, Ge and Sn.

Scattering Path	N	Atomic distance r	Displacement Parameter σ^2
Ge-Ge	0.9(3)	2.44(1) Å	0.004(2) Å ²
Ge-Te (short)	2.6(2) (a)	2.839(3) Å	0.0044(5) Å ²
Ge-Te (long)	2.6(2) (a)	3.16(1) Å	0.011(1) Å ²
Ge-Ge	10.0(6) (c)	4.28(1) Å	0.015(2) Å ²
Ge-Sn	2.0(6) (c)	4.30(1) Å	0.012(2) Å ²
Sn-Te (short)	3.3(2) (b)	2.993(4) Å	0.0032(3) Å ²
Sn-Te (long)	3.3(2) (b)	3.17(1) Å	0.007(1) Å ²
Sn-Ge	10.0(6) (c)	4.28(1) Å	0.015(2) Å ²
Sn-Sn	2.0(6) (c)	4.33(2) Å	0.005(2) Å ²
Te-Ge (short)	2.2(2) (d)	2.839(3) Å	0.0044(5) Å ²
Te-Ge (long)	2.2(2) (d)	3.16(1) Å	0.011(1) Å ²
Te-Sn (short)	0.6(2) (e)	2.993(4) Å	0.0032(3) Å ²
Te-Sn (long)	0.6(2) (e)	3.17(1) Å	0.007(1) Å ²
Te-Te	12	4.23(2) Å	0.021(2) Å ²

experiments well, a ratio of 1/6 is obtained for the content of Sn to Ge atoms – instead of the expected value of 1/4, which only lies within the 2σ interval of the experimental value. This deviation suggests that although some Ge is segregated, there is still a larger fraction of Ge on the lattice than expected from the initial stoichiometry of the sample.

A quantitative evaluation of the coordination numbers gives a total coordination number of 6.1(4) around Ge, 6.6(3) around Sn and 5.6(3) around Te. These values suggest that the material does not contain a significant amount of vacancies – but the large errors of coordination numbers determined from an EXAFS analysis weaken this conclusion.

A.3.4 Crystalline GeSnTe_2

Crystalline GeSnTe_2 is known to crystallize to a rock-salt like cubic structure at 410 K (peak value after heating at 5 K/min) [177]. The density increases upon crystallization from 5.85(5) g cm⁻³ in the amorphous phase to 6.30(5) g cm⁻³ [177]. Additional reflections from crystalline pure Ge appear after heating the material further above 541 K. The samples for the EXAFS analysis were prepared by sputter deposition on silica substrates, scratching the obtained films to powder and heating the powder in a tube furnace up to 448 K. The three K absorption edges of the resulting crystalline powder were measured and the resulting data

are presented in Fig. A.5. During the fit, the amplitude reduction factors S_0^2 were set to 0.67, 0.69 and 0.74 for the Ge, Sb and Te edges, respectively. The best fit obtained is based on the scattering paths listed in Tab. A.5. It has residua of 0.013, 0.011 and 0.026 and the edge energy corrections are fitted as 5.6(6) eV, 6.8(3) eV and 4.2(3) eV.

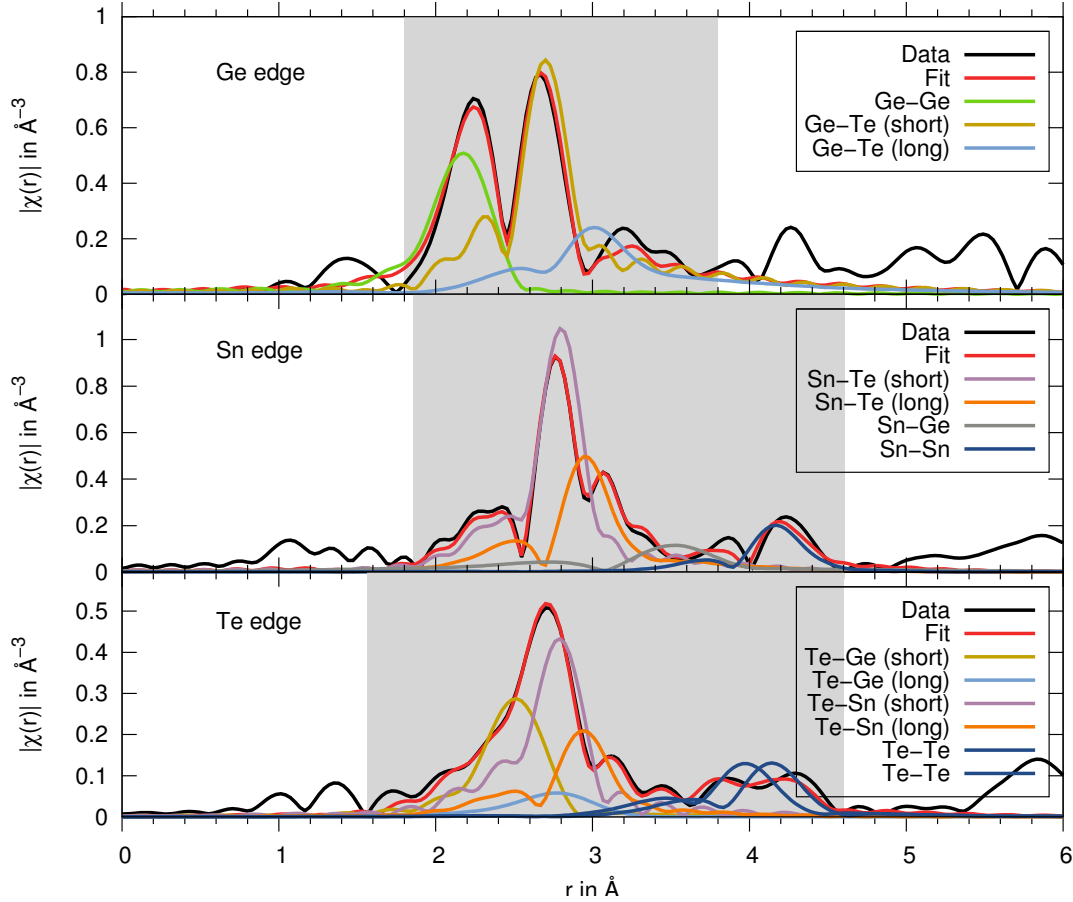


Figure A.5: The EXAFS data of the three K absorption edges of GeSnTe_2 are shown together with the best fit, which has an average residual of 0.017. The different contributions by short and long bonds can be seen at both, Ge and Sn edges. At the Ge edge, the additional influence of segregated Ge is visible (green curve). The Te edge is shown for consistency, since all three edges were refined using a constrained model.

The EXAFS refinement for crystalline GeSnTe_2 is based on the same model, that was used to refine the data of crystalline Ge_3SnTe_4 , except that here, the data for the Ge edge were for some reason not very clear above 3.8 Å and the peak at ≈ 4.2 Å could not be included in a stable fit. In a disordered crystal, the fitting of higher order coordination shells is very delicate, because these atomic distances are always influenced not only by the variance of bond lengths, but also by the variance of bond angles. Therefore, the higher order coordination shells were not refined at the Ge edge of crystalline GeSnTe_2 .

With an equal stoichiometric fraction of Ge and Sn, a perfectly ordered crystal could

Table A.5: Results of an EXAFS analysis of crystalline GeSnTe_2 at 10 K. The splitting of short and long distances around Ge and Sn atoms shows that local displacements exist. The short distances around Ge are due to the segregation of some Ge.

Scattering Path	N	Atomic distance r	Displacement Parameter σ^2
Ge-Ge	1.2(3)	2.46(1) Å	0.005(2) Å ²
Ge-Te (short)	2.0(2) (a)	2.860(5) Å	0.0045(7) Å ²
Ge-Te (long)	2.0(2) (a)	3.16(2) Å	0.014(4) Å ²
Sn-Te (short)	3.7(2) (b)	3.032(4) Å	0.0043(4) Å ²
Sn-Te (long)	3.7(2) (b)	3.18(1) Å	0.008(1) Å ²
Sn-Ge	20(4)	3.89(2) Å	0.031(4) Å ²
Sn-Sn	5(1)	4.37(1) Å	0.009(2) Å ²
Te-Ge (short)	1.1(2) (d)	2.860(5) Å	0.0045(7) Å ²
Te-Ge (long)	1.1(2) (d)	3.16(2) Å	0.014(4) Å ²
Te-Sn (short)	1.7(1) (e)	3.032(4) Å	0.0043(4) Å ²
Te-Sn (long)	1.7(1) (e)	3.18(1) Å	0.008(1) Å ²
Te-Te	12	4.22(2) Å	0.016(4) Å ²

be obtained. Instead, Sn-Ge and Sn-Sn distances are found at 4 Å at the Sn edge, so that substitutional disorder must prevail also in crystalline GeSnTe_2 . Further substitutional disorder is evidenced by the splitting of atomic distances around Ge and Sn. Those atomic displacements are even more pronounced as compared to Ge_3SnTe_4 , because in Ge_3SnTe_4 they were limited to the Ge/Sn sublattice, but in GeSnTe_2 also a distortion of the Te sublattice is observed: In Fig. A.5, a splitting of Te-Te distances is observed (cf. Te edge data at 4 Å).

Coordination numbers of GeSnTe_2 can be obtained from the parameters in Tab. A.5: The Ge atoms are on average 5.2(5)-fold coordinated, the Sn atoms 7.4(4)-fold and the Te atoms 5.6(4)-fold. Since the deviations of coordination numbers deviate in the same way as seen for crystalline Ge_3SnTe_4 , it seems that a deviation of the amplitude reduction factor S_0^2 might be involved, since this parameter was obtained from binary GeTe and SnTe. Due to the product $N \cdot S_0^2$ in the EXAFS equation, this factor influences the resulting coordination numbers directly.

In conclusion, local atomic displacements were revealed in all investigated ternary Ge-Sn-Te compounds, despite their cubic symmetry of the unit cell. These atomic displacements are due to the substitutional disorder, i.e. the structure of Ge atoms on the Ge/Sn sublattice does not possess translational symmetry. In addition, a phase separation of Ge atoms was observed in all compounds from the GeTe-SnTe system, which might be due to the excess Ge after sputter deposition.

APPENDIX B

Data compilation of phase-change materials

B.1 Density of phase-change materials

Many properties of phase-change materials can be obtained from ab-initio molecular dynamics (AIMD) simulations based on DFT calculations. This technique is usually performed to simulate the quenching process from the liquid phase and to obtain a structural model for the amorphous phase, from which further information can be derived. These simulations are usually performed under isochoric conditions, fixed to the atomic density of the amorphous phase. The atomic density is also crucial for the normalization of structure factors from neutron scattering, where it is necessary to subtract the correct amount of self-scattering and to normalize the data to exact coordination numbers. Experimentally, the atomic density can be derived from x-ray reflectivity measurements, which probes the electron density of smooth thin films of amorphous and crystalline phase-change materials. This value is obtained from the critical angle, under which total reflection is interrupted. If, in addition, the stoichiometry of the sample is known, the mass density can be calculated from the electron density. A list of these values is given in the following, which is a compilation of the values used in the data treatment of total neutron scattering and to some extent in AIMD simulations. The data are presented in Tab. B.1. In cases, where multiple references are given, the average values are printed. The error on the mass density from XRR is always given as 0.05 g cm^{-3} in the cited references. The number densities have been derived under the assumption that the stoichiometries correspond to the given values of the sputtering targets.

Table B.1: Collection of experimental values for the densities of phase-change materials, which are necessary to obtain absolute coordination numbers from the treatment of total neutron scattering data.

Material	Molar mass	Mass-density	Number density	Reference
as-deposited amorphous phase:				
Sb ₂ Te ₃	125.26 g mol ⁻¹	6.01(5) g cm ⁻³	0.02890 at. Å ⁻³	[178]
GeSb ₄ Te ₇	121.07 g mol ⁻¹	5.95(5) g cm ⁻³	0.02960 at. Å ⁻³	[163] (partly crystalline as dep.)
GeSb ₂ Te ₄	118.08 g mol ⁻¹	5.95(5) g cm ⁻³	0.03035 at. Å ⁻³	[163]
Ge ₂ Sb ₂ Te ₅	114.08 g mol ⁻¹	5.82(3) g cm ⁻³	0.03073 at. Å ⁻³	[163], [179], [180]
Ge ₃ Sb ₂ Te ₆	111.54 g mol ⁻¹	5.80(5) g cm ⁻³	0.03132 at. Å ⁻³	[163]
Ge ₈ Sb ₂ Te ₁₁	106.10 g mol ⁻¹	5.45(5) g cm ⁻³	0.03094 at. Å ⁻³	[163]
GeTe	100.11 g mol ⁻¹	5.50(2) g cm ⁻³	0.03309 at. Å ⁻³	[163], [179]
GeSe	75.79 g mol ⁻¹	4.60(5) g cm ⁻³	0.03656 at. Å ⁻³	[177]
GeBi ₂ Te ₄	143.00 g mol ⁻¹	6.91(5) g cm ⁻³	0.02910 at. Å ⁻³	[178]
SnSb ₂ Te ₄	124.66 g mol ⁻¹	6.15(5) g cm ⁻³	0.02971 at. Å ⁻³	[178]
Ge ₃ SnTe ₄	105.87 g mol ⁻¹	5.90(5) g cm ⁻³	0.03356 at. Å ⁻³	[177]
GeSnTe ₂	111.63 g mol ⁻¹	5.90(5) g cm ⁻³	0.03183 at. Å ⁻³	[177]
SnSe ₂	92.21 g mol ⁻¹	4.77 g cm ⁻³	0.03116 at. Å ⁻³	[58]
meta-stable crystalline phase:				
GeSb ₂ Te ₄	118.08 g mol ⁻¹	6.20(5) g cm ⁻³	0.03162 at. Å ⁻³	[163]
Ge ₂ Sb ₂ Te ₅	114.08 g mol ⁻¹	6.35(5) g cm ⁻³	0.03352 at. Å ⁻³	[163]
stable crystalline phase:				
GeSb ₂ Te ₄	118.08 g mol ⁻¹	6.50(5) g cm ⁻³	0.03315 at. Å ⁻³	[163]
Ge ₂ Sb ₂ Te ₅	114.08 g mol ⁻¹	6.60(5) g cm ⁻³	0.03484 at. Å ⁻³	[163]
GeTe	100.11 g mol ⁻¹	5.95(5) g cm ⁻³	0.03580 at. Å ⁻³	[163]
SnSe ₂	92.21 g mol ⁻¹	5.75 g cm ⁻³	0.03756 at. Å ⁻³	[58]
In ₃ SbTe ₂	120.23 g mol ⁻¹	7.00 g cm ⁻³	0.03507 at. Å ⁻³	[135]

B.2 Compilation of structural investigations of amorphous GST-based PCMs

Tab. B.2 contains a summary of the available information on the local atomic ordering in the amorphous $\text{Ge}_2\text{Sb}_2\text{Te}_5$ and GeSb_2Te_4 .

Table B.2: Most published studies of the atomic structure of amorphous GeSb_2Te_4 and $\text{Ge}_2\text{Sb}_2\text{Te}_5$ are summarized in this table with a special focus on the average coordination numbers and bond lengths. The AIMD simulations were most commonly performed on melt-quenched samples (MQ) and in one case, the sputter deposition process was simulated (AD) or an ideal glass (IG) of $\text{Si}_2\text{As}_2\text{Se}_5$ was simulated, subsequently replacing the atoms by Ge, Sb and Te. The experimental samples were prepared by sputter deposition (AD), by melt-quenching (MQ) or by ion bombardement (IB). The table shows that (1) the average bond lengths $\langle r \rangle$ obtained from AIMD simulations are by 5% to 3% larger than the experimental values and that (2) there is no significant deviation between the average bond lengths $\langle r \rangle$ in as-deposited or melt-quenched samples (compare entry 12 with 13 or 14 with 15 and 16).

No.	Compound	Method	N_{Ge}	N_{Sb}	N_{Te}	$\langle r \rangle$	Reference
1	$\text{Ge}_2\text{Sb}_2\text{Te}_5$ MQ	AIMD	4.2	3.7	2.9	2.855 Å	[124]
2	$\text{Ge}_2\text{Sb}_2\text{Te}_5$ MQ	AIMD	3.8	4.0	2.9	2.865 Å	[181]
3	$\text{Ge}_2\text{Sb}_2\text{Te}_5$ MQ	AIMD	4.1	3.7	2.8	2.805 Å	[182]
4	$\text{Ge}_2\text{Sb}_2\text{Te}_5$ MQ	AIMD	4.05	4.2	3.17	n/A	[183]
5	$\text{Ge}_2\text{Sb}_2\text{Te}_5$ MQ	AIMD	4.2	3.7	2.9	2.85 Å	[184]
6	GeSb_2Te_4 MQ	AIMD	3.5	3.8	2.9	n/A	[102]
7	$\text{Ge}_2\text{Sb}_2\text{Te}_5$ AD	AIMD	4.2	3.7	2.8	2.79 Å	[182]
8	$\text{Ge}_2\text{Sb}_2\text{Te}_5$ IG	AIMD	4.0	3.0	2.1	2.765 Å	[184]
9	$\text{Ge}_2\text{Sb}_2\text{Te}_5$ AD	EXAFS, XRD, ND	3.9	3.1	2.0	2.71 Å	[185]
10	GeSb_2Te_4 AD	EXAFS, XRD, ND	3.9	2.9	2.0	2.72 Å	[185]
11	$\text{Ge}_2\text{Sb}_2\text{Te}_5$ AD?	XRD, PDF	3.7	3.0	n/A	n/A	[33]
12	$\text{Ge}_2\text{Sb}_2\text{Te}_5$ MQ	EXAFS	n/A	n/A	n/A	2.73 Å	[31]
13	$\text{Ge}_2\text{Sb}_2\text{Te}_5$ AD	EXAFS	3.9	2.8	2.4	2.73 Å	[32]
14	$\text{Ge}_2\text{Sb}_2\text{Te}_5$ AD	EXAFS (Ge only)	n/A	n/A	n/A	2.62 Å (Ge-Te)	[123]
15	$\text{Ge}_2\text{Sb}_2\text{Te}_5$ MQ	EXAFS (Ge only)	n/A	n/A	n/A	2.62 Å (Ge-Te)	[123]
16	$\text{Ge}_2\text{Sb}_2\text{Te}_5$ IB	EXAFS (Ge only)	n/A	n/A	n/A	2.62 Å (Ge-Te)	[123]
17	GeSb_2Te_4 AD	EXAFS at 10 K	3.7(3)	3.2(3)	1.9(1)	2.75(1) Å	this work

Acknowledgements

Scientific progress throughout the history has been stimulated by the exchange of ideas and the discussion of the resulting challenges and opportunities. In particular the young generation of researchers requires this guidance in order to learn the various possible strategies for finding interesting and relevant questions, performing the experiments carefully but efficient, publishing, presenting and advertising the results and acquiring funding for various new projects. In Prof. Dr. M. Wuttig (RWTH Aachen), I have found such guidance and could enjoy and benefit from his support not only in scientific questions but also in positive spirit. For this I am very grateful. Of similar role was the influence by Dr. C. Bichara (CiNaM, Marseille), who fortunately invited me to visit him for extensive discussions to his lab. His questions and concise analysis have stimulated many of the investigations, which are now part of this thesis. I am also very grateful to Dr. M.-V. Coulet (Im2np, Marseille) for inviting me to participate in several fruitful experiments at ESRF and for her support and discussion on calorimetric questions. It was her idea and thorough planning, that enabled us to accomplish the coupled x-ray and calorimetric measurements. For these experiments, also the contribution by Dr. O. Mathon (ESRF), Dr. G. Aquilanti (Elettra, Trieste) and M. Sc. A. Bérangère (Im2np, Marseille) is acknowledged.

Great supporters of my work were also the former graduate students in our lab in Aachen, who generously shared their knowledge of various experimental setups. Here, I would like to mention Dr. P. Merkelbach, Dr. G. Bruns and Dr. M. Klein. To the former graduate student Dr. J. v. Eijk I am particularly indebted for allowing and motivating me to join her in revealing the atomic structure of phase-change materials. Therefore, she explained to me with great care the EXAFS technique in theory and practice and invited me to join for the first experiment at DESY, Hamburg. Thereby, I got in touch with the group of Prof. Dr. W. Bensch (CAU, Kiel) – in particular with Dipl.-Chem. S. Buller and B. Sc. T. Koch (both CAU, Kiel). We shared both, samples and beamtime in order to establish a team, which could perform the beamline experiments 24/7. It was them, who made the beamtimes with all its successes and unforeseen challenges a joyful experience. Drs. E. Welter and D. Zajac (both DESY, Hamburg) have taken great care in explaining the beamline CEMO at DORIS III to us and have helped us to increase the data quality to highest accuracy. I would like to thank Profs. Wuttig and Bensch in particular for choosing me as support for these experiments at DESY and also for allowing me to join the challenging projects at BESSY II, which led to the successful acquisition of NEXAFS data only by their continuous trust and effort. The local support by Dr. A. Vollmer (BESSY II, Berlin) and her immense technical experience and care only made the

experiments at SuriCat successful and enjoyable – even during late hours or weekends. I would like to thank Dr. T. Strunskus (CAU, Kiel) for sharing his experiments with UHV experiments and his support during the measurements.

It was Dr. P. Merkelbach who first invited me to join the neutron science community at ILL, where he was a great help during my later experiments. Our local contact Dr. H. Fischer (ILL, Grenoble) explained to us not only the instrument D4 and its particular challenges, but he also discussed with us in great detail the data treatment after neutron total scattering. Without his support, the interpretation of total scattering data would have remained significantly less sophisticated. I am also indebted to him for imparting his confidence in the capability of neutron scattering experiments, which has encouraged us to try measurements of the density of phonon states of phase-change materials. Dr. S. Rols (ILL) has made these measurements possible at his instrument IN4, which he has explained to us. I am particularly grateful for his kind invitation for a seminar talk at ILL and his big effort with the treatment of our data. Dr. M. Johnson (ILL) has helped us as local contact at ILL and has performed plenty of simulations in order to validate our measurements by various kinds of simulations. Similar measurements were performed by Dr. R. P. Hermann (FZ Jülich) at the ESRF. I am grateful to him for sharing with us his data and for explaining to us the challenging technique of nuclear inelastic scattering. Dr. T. Matsunaga and Dr. N. Yamada (both Panasonic, Osaka) have generously allowed us to combine their data on the atomic and vibrational properties of phase-change materials with our measurements of the density of phonon states and our interpretation.

Prof. Dr. R. Mazzarello (RWTH) with his PhD student M. Sc. Wei Zhang and Dr. J.-Y. Raty (Univ. of Liège) have performed several AIMD simulations related to my measurements and therefore I am grateful. In particular the simulations of the density of phonon states by Dr. J.-Y. Raty have allowed me to derive an explanation for my measurements. I would like to thank Prof. Dr. R. Mazzarello for his trust in my experimental input to his projects and for his offer to perform a joint project regarding the microscopic changes during the disorder-induced metal insulator transition. M. Sc. W. Zhang (RWTH) has helped me a lot to understand the features of my experimental data by performing various DFT-based atomic relaxations, from which I could calculate e.g. diffraction patterns in order to understand the influence of particular sources of disorder.

I was offered the privilege of using the Rutherford backscattering setup in Jülich for confirming the composition of deposited samples from our group. For this, I am grateful to Dr. D. Köhl (RWTH) and in particular to Dr. B. Holländer (FZ Jülich) for explaining to me the setup, the details of data treatment and for guiding me through the formal enrollment in Jülich.

Several graduate students have supported me not only during my experiments, but also after long hours in the lab. In this respect, I am particularly grateful to Dipl.-Phys. P. Rausch, who provided continuous ideas and topics for discussions e.g. on properties of the In_3SbTe_2 compounds. It was him, who made sure that our thinking does not become uninflected. Additional support was provided by Dipl.-Phys. S. Siegert, who joined me during an experiment at the ILL. He furthermore motivated me for our efforts on data treatment and encouraged experiments towards an understanding of the anharmonicity of crystalline phase-change materials. I am grateful to Dipl.-Phys. J. Luckas, who encouraged me on the importance of the atomic structure of the amorphous phase and stimulated several fruitful ideas to explain the resistance drift. I would also like to thank my students at RWTH, Dipl.-Phys. Anja König, M. Sc. Matthias Kaes and B. Sc. Franziska Schlich for their efforts in realizing my ideas for exciting measurements – however difficult they were.

For their support and their trust in the final accomplishment of this work, I am deeply indebted to Erhard G. Zalden and to Susann Schneider, who accompanied me during the ups and downs of this thesis.

Bibliography

- [1] Klaus Schwab. The Global Competitiveness Report 2010-2011. Technical report, World Economic Forum, 2010.
- [2] Lesley Adkins. *Empires of the Plain: Henry Rawlinson and the Lost Languages of Babylon*. St. Martin's Press, 2003.
- [3] LS Palmer. On the Dielectric Constant of the Water in Wet Clay. *Proceedings of the Physical Society. Section B*, 674, 1952.
- [4] G. E. Moore. Cramming more components onto integrated circuits. In: Electronics. *Electronics*, 38(8):114, 1965.
- [5] Mario Apicella. Fast, flexible, expensive. *InfoWorld*, (46):65, 2001.
- [6] Fahmida Y. Rashid. Mobile DRAM Market to Grow 71 Percent in 2011, iSuppli, 2011.
- [7] RD Pashley and SK Lai. Flash Memories: the best of two worlds. *Spectrum, IEEE*, 26(12):30, 1989.
- [8] G. Bruns, P. Merkelbach, C. Schlockermann, M. Salinga, M. Wuttig, T. D. Happ, J. B. Philipp, and M. Kund. Nanosecond switching in GeTe phase change memory cells. *Applied Physics Letters*, 95(4):3108, 2009.
- [9] Stanford R Ovshinsky. Reversible electrical switching phenomena in disordered structures. *Physical Review Letters*, 21(20):1450, 1968.
- [10] Simone Raoux, Jean L. Jordan-Sweet, and Andrew J. Kellock. Crystallization properties of ultrathin phase change films. *Journal of Applied Physics*, 103(11):114310, 2008.
- [11] M. Wuttig and N. Yamada. Phase-change materials for rewriteable data storage. *Nature materials*, 6(11):824–832, 2007.
- [12] H Philip Wong, Simone Raoux, Sangbum Kim, Jiale Liang, John P Reifenberg, Bipin Rajendran, Mehdi Asheghi, and Kenneth E Goodson. Phase Change Memory. *Proceedings of the IEEE*, 98(12):2201–2227, December 2010.
- [13] Alberto Gasperin. *Advanced Non-Volatile Memories: Reliability and Ionizing Radiation Effects*. PhD thesis, Università degli Studi di Padova, 2008.
- [14] H. Weintraub, M. Ashburner, P. N. Goodfellow, H. F. Lodish, C. J. Arntzen, P. W. Anderson, T. M. Rice, T. H. Geballe, A. R. Means, H. M. Ranney, T. R. Cech, R. R. Colwell, H. R. Bourne, B. Richter, I. M. Singer, P. Marrack, D. T. Fearon, A. Penzias, A. J. Bard, W. F. Brinkman, P. A. Marks, B. Vogelstein, K. W. Kinzler, J. M. Bishop, R. N. Zare, G. Schatz, S. J. Benkovic, H. B. Gray, J. S. Valentine, P. J. Crutzen, D. W. Choi, S. Nakanishi, S. M. Kosslyn, J. I. Brau-Man, D. C. Rees, W. J. Brill, J. Schell, R. Luhrmann, C. L. Will, W. Wulf, G. J. Vermeij, K. J. Arrow, N. J. Smelser, D. L. Anderson, and P. H. Abelson. Through the glass lightly. *Science*, 267:1609, 1995.

- [15] JA Kalb, M Wuttig, and Frans Spaepen. Calorimetric measurements of structural relaxation and glass transition temperatures in sputtered films of amorphous Te alloys used for phase change recording. *Journal of Materials Research*, 22(3):748, 2007.
- [16] T Morikawa, K Kurotsuchi, M Kinoshita, N Matsuzaki, Y Matsui, Y Fuiisaki, S Hanzawa, A Kotabe, M Terao, H Moriya, and Others. Doped In-Ge-Te phase change memory featuring stable operation and good data retention. In *Electron Devices Meeting, 2007. IEDM 2007. IEEE International*, pages 307–310. IEEE, 2007.
- [17] T. Ohta. Phase-Change Optical Memory Promotes the DVD optical disc. *Journal of Optoelectronics and Advances Materials*, 3(3):609, 2001.
- [18] N Papandreou, H Pozidis, T Mittelholzer, G F Close, M Breitwisch, C Lam, and E Eleftheriou. Drift-Tolerant Multilevel Phase-Change Memory. *Memory Workshop (IMW), 2011 3rd IEEE International*, pages 1–4, 2011.
- [19] N. Kh. Abrikosov and G. T. Danilova-Dobryakova. An Investigation of the structural diagram of Sb_2Te_3 -GeTe. *Izv. Akad. Nauk S.S.S.R., Neorg. Mater*, 1(2):204, 1965.
- [20] Daniel Krebs, RM Schmidt, J Klomfaß, and Jennifer Luckas. Impact of DoS changes on resistance drift and threshold switching in amorphous phase change materials. *Journal of Non-Crystalline Solids*, in press, 2012.
- [21] T. Siegrist, P. Jost, H. Volker, M. Woda, C. Schlockermann, P. Merkelbach, and M. Wuttig. Disorder-induced localization in crystalline phase-change materials. *Nature Materials*, 10(3):202, 2011.
- [22] Walter Kauzmann. The Nature of the Glassy State and the Behavior of Liquids at Low Temperatures. *Chemical Reviews*, 43(2):219–256, October 1948.
- [23] I. Gutzow and A. Dobrev. Structure, thermodynamic properties and cooling rate of glasses. *Journal of non-crystalline solids*, 129(1-3):266–275, 1991.
- [24] David Turnbull. Under what conditions can a glass be formed? *Contemporary Physics*, 10(5):473–488, September 1969.
- [25] J. Kalb, F. Spaepen, and M. Wuttig. Calorimetric measurements of phase transformations in thin films of amorphous Te alloys used for optical data storage. *Journal of Applied Physics*, 93(5):2389, 2003.
- [26] Frans Spaepen. The Identification of the Metallic Glass State. *Materials Research Society: Proceedings*, 57:161, 1986.
- [27] Oleg N Senkov and Daniel B Miracle. Correlation between thermodynamic and kinetic fragilities in nonpolymeric glass-forming liquids. *The Journal of chemical physics*, 128(12):124508, March 2008.
- [28] CA Angell, KL Ngai, GB McKenna, PF McMillan, and SW Martin. Relaxation in glassforming liquids and amorphous solids. *Journal of Applied Physics*, 88(6):3113, 2000.
- [29] M. Luis Ferreira Nascimento and C Aparicio. Viscosity of strong and fragile glass-forming liquids investigated by means of principal component analysis. *Journal of Physics and Chemistry of Solids*, 68(1):104–110, January 2007.
- [30] R. Zallen. *The Physics of Amorphous Solids*. Wiley, 1983.
- [31] Alexander V Kolobov, Paul Fons, Anatoly I Frenkel, Alexei L Ankudinov, Junji Tominaga, and Tomoya Uruga. Understanding the phase-change mechanism of rewritable optical media. *Nature Materials*, 3:703–708, 2004.
- [32] D. A. Baker, M. A. Paesler, G. Lucovsky, S. C. Agarwal, and P. C. Taylor. Application of Bond Constraint Theory to the Switchable Optical Memory Material $\text{Ge}_2\text{Sb}_2\text{Te}_5$. *Physical Review Letters*, 96(25):5–7, June 2006.
- [33] Shinji Kohara, K Kato, S Kimura, H Tanaka, T Usuki, K Suzuya, Y Moritomo, T Matsunaga, N Yamada, H Suematsu, Y Tanaka, and M Takata. Structural basis for the fast phase change of $\text{Ge}_2\text{Sb}_2\text{Te}_5$: Ring statistics analogy between the crystal and amorphous states. *Appl. Phys. Lett.*, 89(20):1910, 2006.
- [34] J. J. Sakurai. *Modern Quantum Mechanics*. Prentice Hall, 1993.

-
- [35] Manuel Bornhöfft. *TEM-Analyse eines lokal laserinduzierten Phasenübergangs zur Bestimmung der Kristallisationskinetik in Phasenwechselmaterialien*. Master thesis, RWTH Aachen, 2012.
- [36] L Pauling. *Nature of the Chemical Bond*. Cornell Univ. Press, New York, 1939.
- [37] K. Shportko, S. Kremers, M. Woda, D. Lencer, J. Robertson, and M. Wuttig. Resonant bonding in crystalline phase-change materials. *Nature Materials*, 7(8):653–658, 2008.
- [38] G. Lucovsky and R. White. Effects of Resonance Bonding on the Properties of Crystalline and Amorphous Semiconductors. *Physical Review B*, 8(2):660–667, July 1973.
- [39] Peter Littlewood. Structure and bonding in narrow gap semiconductors. *Critical Reviews in Solid State and Materials Sciences*, 11(3):229–285, 1983.
- [40] Ph Ghosez, J Michenaud, and X Gonze. Dynamical atomic charges: The case of ABO_3 compounds. *Physical Review B*, 58(10):6224–6240, 1998.
- [41] P Enders. Structure and Bonding in Cubic IV-VI Crystals III. On the Cubic to Rhombohedral Phase Transition. *Phys. Stat. Sol. (b)*, 121:461, 1984.
- [42] D. Lencer, M. Salinga, B. Grabowski, T. Hickel, J. Neugebauer, and M. Wuttig. A map for phase-change materials. *Nature Materials*, 7(12):972–977, 2008.
- [43] S R Elliott. Vibrational excitations in amorphous materials. In M. F. Thorpe and L. Tichý, editors, *Properties and applications of amorphous materials*. NATO Science Series.
- [44] W P Risk, C T Rettner, and S Raoux. Thermal conductivities and phase transition temperatures of various phase-change materials measured by the 3ω method. *Appl. Phys. Lett.*, 94(10):1906, 2009.
- [45] O Delaire, J Ma, K Marty, a F May, M a McGuire, M-H Du, D J Singh, a Podlesnyak, G Ehlers, M D Lumsden, and B C Sales. Giant anharmonic phonon scattering in PbTe. *Nature materials*, 10(8):614–9, January 2011.
- [46] A Pirovano, A.L. Lacaita, F Pellizzer, S.A. Kostylev, A. Benvenuti, and R Bez. Low-field amorphous state resistance and threshold voltage drift in chalcogenide materials. *Electron Devices, IEEE Transactions on*, 51(5):714–719, 2004.
- [47] Toshiyuki Matsunaga, Rie Kojima, Noboru Yamada, Kouichi Kifune, Yoshiki Kubota, and Masaki Takata. Structural Features of $\text{Ge}_1\text{Sb}_4\text{Te}_7$, an Intermetallic Compound in the $\text{GeTe-Sb}_2\text{Te}_3$ Homologous Series. *Chem. Mater.*, 20:5750–5755, 2008.
- [48] Toshiyuki Matsunaga and Noboru Yamada. Structural investigation of GeSb_2Te_4 : A high-speed phase-change material. *Physical Review B*, 69(10):1–8, March 2004.
- [49] Toshiyuki Matsunaga, Noboru Yamada, and Yoshiki Kubota. Structures of stable and metastable $\text{Ge}_2\text{Sb}_2\text{Te}_5$, an intermetallic compound in $\text{GeTe-Sb}_2\text{Te}_3$ pseudobinary systems. *Acta crystallographica. Section B, Structural science*, 60(Pt 6):685–91, December 2004.
- [50] Matthias Wuttig, Daniel Lüsebrink, Daniel Wamwangi, Wojciech Welnic, Michael Gillessen, and Richard Dronskowski. The role of vacancies and local distortions in the design of new phase-change materials. *Nature materials*, 6(2):122–8, 2007.
- [51] Michael Klein. *Crystallization Kinetics of Phase Change Materials for Novel Data Storage Concepts*. Dissertation, RWTH Aachen, 2009.
- [52] J Siegel, C N Afonso, and J Solis. Dynamics of ultrafast reversible phase transitions in GeSb films triggered by picosecond laser pulses. *Applied Physics Letters*, 75(20):3102–3104, 1999.
- [53] Peter Zalden, Christophe Bichara, Julia van Eijk, Carolin Braun, Wolfgang Bensch, and Matthias Wuttig. Atomic structure of amorphous and crystallized $\text{Ge}_{15}\text{Sb}_{85}$. *Journal of Applied Physics*, 107(10):4312, 2010.
- [54] M Anbarasu, Pascal Rausch, Peter Zalden, Hanno Volker, Jean-Yves Raty, Christophe Bichara, Riccardo Mazzarello, and Matthias Wuttig. Structure-property correlation of In_3SbTe_2 perspective of fourth family of phase change material. 2010.
- [55] Eun Tae Kim, Jeong Yong Lee, and Yong Tae Kim. Investigation of electrical characteristics of the
-

- $\text{In}_3\text{Sb}_1\text{Te}_2$ ternary alloy for application in phase-change memory. *physica status solidi (RRL) - Rapid Research Letters*, 3(4):103–105, 2009.
- [56] K Deneke and A Rabenau. Über die Natur der Phase In_3SbTe_2 mit Kochsalzstruktur. *Zeitschrift für anorganische und allgemeine Chemie*, 333(4-6):201–208, 1964.
- [57] Kyung-Min Chung. *Sn-Sb-Se based binary and ternary alloys for phase-change memory applications*. Phd thesis, RWTH Aachen, 2008.
- [58] Kyung-Min Chung, Daniel Wamwangi, Michael Woda, Matthias Wuttig, and Wolfgang Bensch. Investigation of SnSe , SnSe_2 , and Sn_2Se_3 alloys for phase change memory applications. *Journal of Applied Physics*, 103(8):083523, 2008.
- [59] P. Zalden. *Combined experimental and theoretical study of structure and electronic properties of the chalcogenide-free phase-change material $\text{Ge}_x\text{Sb}_{100-x}$* . Diploma thesis, RWTH Aachen, 2008.
- [60] T. Lee and S. Elliott. Ab Initio Computer Simulation of the Early Stages of Crystallization: Application to $\text{Ge}_2\text{Sb}_2\text{Te}_5$ Phase-Change Materials. *Physical Review Letters*, 107(14):1–5, September 2011.
- [61] D. Loke, T. H. Lee, W. J. Wang, L. P. Shi, R. Zhao, Y. C. Yeo, T. C. Chong, and S. R. Elliott. Breaking the Speed Limits of Phase-Change Memory. *Science*, 336(June):1566–1569, 2012.
- [62] Kurt Sköld and David L. Price, editors. *Methods of Experimental Physics, Vol. 23: Neutron scattering (Part A)*. Academic Press, Inc., 1986.
- [63] F. Hippert, Erik Geissler, Jean Louis Hodeau, Eddy Lelièvre-Berna, and Jean-René Regnard, editors. *Neutron and X-ray Spectroscopy*. Springer-Verlag, 2006.
- [64] Gordon Leslie Squires. *Introduction to the theory of thermal neutron scattering*. Cambridge University Press, 1978.
- [65] W. Reichardt. MUPHOCOR, a Fortran Program to Determine the Phonon Density of States from Neutron Scattering Experiments. *Primärberichte des Kernforschungszentrums Karlsruhe*, 1984.
- [66] VS Oskotski. Measurement of the phonon distribution function in polycrystalline materials using coherent scattering of slow neutrons into a solid angle. *Sov Phys Solid State*, 9(2):420, 1967.
- [67] D. L. Weaire. The Vibrational Density of States of Amorphous Semiconductors. In W. A. Phillips, editor, *Topics in Current Physics: Amorphous Solids*, chapter 2, pages 13–26. Springer-Verlag, 1981.
- [68] N. Ashcroft and D. Mermin. *Solid State Physics*. Harcourt College Publishers, 1976.
- [69] William Jones and Norman H. March. *Theoretical Solid State Physics, Volume 1: Perfect Lattices in Equilibrium*. Dover Publications, Mineola, 1985.
- [70] Hassel Ledbetter and Ming Lei. Elastic constants, Debye temperatures, and electron-phonon parameters of superconducting cuprates and related oxides. *Phase Transitions: A Multinational*, 23:61–70, 1990.
- [71] L. E. Kinsler. *Fundamentals of acoustics*. John Wiley and sons Inc., New York, 4th edition, 2000.
- [72] Je Lorenzo, R Currat, Aj Dianoux, P Monceau, and F Levy. Phonon density of states and low-temperature specific heat of quasi-one-dimensional $(\text{TaSe}_4)_2\text{I}$ and $(\text{NbSe}_4)_3\text{I}$. *Physical review. B, Condensed matter*, 53(13):8316–8322, April 1996.
- [73] T. Matsunaga, N. Yamada, R. Kojima, S. Shamoto, M. Sato, H. Tanida, T. Uruga, S. Kohara, M. Takata, P. Zalden, G. Bruns, I. Sergueev, H. C. Wille, R. P. Hermann, and M. Wuttig. Phase change materials: Vibrational softening upon crystallization and its impact on thermal properties. *Advanced Functional Materials*, 21(12):2232, 2011.
- [74] E. W. Kellermann. Theory of the Vibrations of the Sodium Chloride Lattice. *Philosophical Transactions of the Royal Society A: Mathematical, Physical and Engineering Sciences*, 238(798):513–548, May 1940.
- [75] Jens Als-Nielsen and Des McMorrow. *Elements of Modern X-ray Physics*. John Wiley and Sons Ltd., 1 edition, 2001.
- [76] H.E. Fischer, A.C. Barnes, and P.S. Salmon. Neutron and x-ray diffraction studies of liquids and glasses. *Reports on Progress in Physics*, 69:233, 2006.

-
- [77] A. Wannberg, A. Møllergård, P. Zetterström, R. Delaplane, M. Grönros, L.E. Karlsson, and RL McGreevy. SLAD: A neutron diffractometer for the study of disordered materials. *Journal of Neutron Research*, 8(2):133–154, 1999.
- [78] A Guinier. *X-ray diffraction in crystals, imperfect crystals, and amorphous bodies*. Dover Publications, Inc., 1994.
- [79] Warren. *X-ray Diffraction*.
- [80] Eric J. Mittemeijer and Udo Welzel. The "state of the art" of the diffraction analysis of crystallite size and lattice strain. *Zeitschrift für Kristallographie*, 223(9):552–560, September 2008.
- [81] G. Caglioti, A. Paoletti, and FP Ricci. Choice of collimators for a crystal spectrometer for neutron diffraction. *Nuclear Instruments*, 3(4):223–228, 1958.
- [82] E. Rimini, R. De Bastiani, E. Carria, M. G. Grimaldi, G. Nicotra, C. Bongiorno, and C. Spinella. Crystallization of sputtered-deposited and ion implanted amorphous $\text{Ge}_2\text{Sb}_2\text{Te}_5$ thin films. *Journal of Applied Physics*, 105(12):3502, 2009.
- [83] E Prokhorov, G Trapaga, and J González-Hernández. Structural and electrical properties of $\text{Ge}_1\text{Sb}_2\text{Te}_4$ face centered cubic phase. *Journal of Applied Physics*, 104(10):3712, 2008.
- [84] D C Koningsberger and R Prins, editors. *X-Ray Absorption*, volume 92. John Wiley & Sons Ltd, 1988.
- [85] Edmund Welter. EXAFS Beamline C: Experimental station. http://hasylab.desy.de/facilities/doris.iii/-beamlines/c_cemo/experimental_station/xafs_experiment/index_eng.html, 2007.
- [86] K Rickers, U Brüggmann, W Drube, M Herrmann, J Heuer, E Welter, H Schulte-Schrepping, and H Schulz-Ritter. New XAFS Facility for In-Situ Measurements at Beamline C at HASYLAB. *AIP Conference Proceedings*, 879:907, 2007.
- [87] K. Rickers, U. Brüggmann, W. Drube, M. Herrmann, J. Heuer, E. Welter, H. Schulte-Schrepping, and H. Schulz-Ritter. Compact Fixed-Exit uhv DCM for XAFS. In *Synchrotron Radiation Instrumentation; Part One*, volume 879, pages 907–910. American Institute of Physics, 2007.
- [88] D. Mills and V. Pollock. Stabilizing feedback system for synchrotron radiation monochromators. *Review of Scientific Instruments*, 51(12):1664–1668, 1980.
- [89] Konstantin Klementiev. XAFSmass software, 2011.
- [90] W T Elam, B D Ravel, and J R Sieber. A new atomic database for X-ray spectroscopic calculations. *Radiation Physics and Chemistry*, 63:121–128, 2002.
- [91] Johannes Andreas Kalb. *Crystallization kinetics in antimony and tellurium alloys used for phase change recording*. PhD thesis, RWTH Aachen, 2006.
- [92] M. Anbarasu, Pascal Rausch, Peter Zalden, Hanno Volker, Jean-Yves Raty, Christophe Bichara, Riccardo Mazzarello, and Matthias Wuttig. Structure-property correlation of In_3SbTe_2 : A perspective of fourth family of phase change material. Technical report, I. Physikalisches Institut (IA), RWTH Aachen, 2011.
- [93] JJ Rehr and Edward A. Stern. Multiple-scattering corrections to the extended x-ray absorption fine structure. *Physical Review B*, 14(10):4413, 1976.
- [94] Matthew Newville. Fundamentals of XAFS, 2004.
- [95] Matthew Newville. EXAFS analysis using FEFF and FEFFIT. *Journal of synchrotron radiation*, 8(2):96–100, 2001.
- [96] BK Teo and PA Lee. Ab initio calculations of amplitude and phase functions for extended X-ray absorption fine structure spectroscopy. *Journal of the American Chemical Society*, 1979.
- [97] M Newville, P Livins, Y Yacoby, J J Rehr, and E A Stern. Near-edge x-ray-absorption fine structure of Pb: A comparison of theory and experiment. *Physical Review B*, 47(21):14126–14131, June 1993.
- [98] S Shamoto, N Yamada, T Matsunaga, Th Proffen, J W Richardson Jr., J H Chung, and T Egami. Large displacement of germanium atoms in crystalline $\text{Ge}_2\text{Sb}_2\text{Te}_5$. *Appl. Phys. Lett.*, 86(8):1904, 2005.
- [99] G Bunker. Application of the ratio method of EXAFS analysis to disordered systems. *Nuclear Instru-*
-

- ments and Methods in Physics Research*, 207:437–444, 1983.
- [100] Giuseppe Dalba, N.D. Afify, and Francesco Rocca. X-ray absorption spectroscopy studies of glass structure. *Physics and Chemistry of Glasses-European Journal of Glass Science and Technology Part B*, 49(3):149–159, 2008.
- [101] J. M. Ziman. *Models of disorder*. Cambridge University Press, 1979.
- [102] Jean-Yves Raty, Céline Otjacques, Jean-Pierre Gaspard, and Christophe Bichara. Amorphous structure and electronic properties of the $\text{Ge}_1\text{Sb}_2\text{Te}_4$ phase change material. *Solid State Sciences*, 12(2):193–198, February 2010.
- [103] Wei Zhang, Alex Thiess, Peter Zalden, Jean-Yves Raty, Stefan Blügel, Matthias Wuttig, and Riccardo Mazzarello. Role of vacancies in metal-insulator transitions in crystalline phase-change materials. *Submitted to Nature Materials*, 2012.
- [104] Toshiyuki Matsunaga and Noboru Yamada. Crystallographic Studies on High-Speed Phase-Change Materials Used for Rewritable Optical Recording Disks. *Japanese Journal of Applied Physics*, 43(7B):4704–4712, July 2004.
- [105] I Friedrich, V Weidenhof, W Njoroge, P Franz, and M Wuttig. Structural transformations of $\text{Ge}_2\text{Sb}_2\text{Te}_5$ films studied by electrical resistance measurements. *Journal of Applied Physics*, 87(9):4130, 2000.
- [106] Juarez Da Silva, Aron Walsh, and Hosun Lee. Insights into the structure of the stable and metastable $(\text{GeTe})_m(\text{Sb}_2\text{Te}_3)_n$ compounds. *Physical Review B*, 78(22):1–10, 2008.
- [107] B. J. Kooi and J. Th. M. De Hosson. Electron diffraction and high-resolution transmission electron microscopy of the high temperature crystal structures of $\text{Ge}_x\text{Sb}_2\text{Te}_{3+x}$ ($x=1, 2, 3$) phase change material. *Journal of Applied Physics*, 92(7):3584, 2002.
- [108] O. Oeckler, M.N. Schneider, F. Fahnrbauer, and G. Vaughan. Atom distribution in SnSb_2Te_4 by resonant X-ray diffraction. *Solid State Sciences*, 13(5):1157, 2011.
- [109] S Caravati, M Bernasconi, T D Kühne, M Krack, and M Parrinello. First-principles study of crystalline and amorphous $\text{Ge}_2\text{Sb}_2\text{Te}_5$ and the effects of stoichiometric defects. *Journal of Physics: Condensed Matter*, 21(25):5501, June 2009.
- [110] C. Suryanarayana and M. Grant Norton. *X-Ray Diffraction: A Practical Approach*. Plenum Press, New York, 1998.
- [111] Jean-Yves Raty. Conductivity of disordered GeSb_2Te_4 by first principles calculations on 216 atoms. Technical report, 2011.
- [112] A. Filipponi and A. Di Cicco. Short-range order in crystalline, amorphous, liquid, and supercooled germanium probed by x-ray-absorption spectroscopy. *Physical Review B*, 51(18):12322, 1995.
- [113] Julia Maria van Eijk. *Structural Analysis of Phase-Change Materials using X-Ray Absorption Measurements*. PhD thesis, RWTH Aachen, 2011.
- [114] Julia van Eijk, Christophe Bichara, Peter Zalden, Carolin Braun, Saskia Buller, Wolfgang Bensch, and Matthias Wuttig. Differences in local atomic order of amorphous and crystalline $\text{Ge}_1\text{Sb}_2\text{Te}_4$ probed by X-Ray absorption spectroscopy. *submitted to Phys. Rev. B*, 2011.
- [115] Ch. Kittel. *Introduction to Solid State Physics*. 7 edition, 1996.
- [116] G. Dalba, P. Fornasini, M. Grazioli, and F. Rocca. Local disorder in crystalline and amorphous germanium. *Physical Review B*, 52(15):11034, 1995.
- [117] Stephan Kremers. *Optische Eigenschaften von Phasenwechselmaterialien für zukünftige optische und elektronische Speicheranwendungen*. PhD thesis, RWTH Aachen, 2009.
- [118] Philipp Merkelbach. *Crystalline Phase-Change materials: disorder, medium-range order and electrical switching*. PhD thesis, RWTH Aachen, 2011.
- [119] M Krack and M Parrinello. High Performance Computing in Chemistry. In J Grotendorst, editor, *High Performance Computing in Chemistry*, Vol. 25, pages 29–51. 2004.
- [120] GL Olson, JA Roth, LD Hess, and J Narayan. Kinetics of solid-phase crystallization in ion-implanted and

- deposited amorphous-silicon films. *US/Japan Seminar on Solid Phase Epitaxy and Interface Kinetics*, pages 20–24, 1983.
- [121] Marcio Nascimento and Edgar Zanzotto. Mechanisms and dynamics of crystal growth, viscous flow, and self-diffusion in silica glass. *Physical Review B*, 73(2):1–7, January 2006.
 - [122] J Orava, a L Greer, B Gholipour, D W Hewak, and C E Smith. Characterization of supercooled liquid $\text{Ge}_2\text{Sb}_2\text{Te}_5$ and its crystallization by ultrafast-heating calorimetry. *Nature materials*, 11(4):279–283, March 2012.
 - [123] E. Carria, a. M. Mio, S. Gibilisco, M. Miritello, F. D’Acapito, M. G. Grimaldi, and E. Rimini. Polymorphism of Amorphous $\text{Ge}_2\text{Sb}_2\text{Te}_5$ Probed by EXAFS and Raman Spectroscopy. *Electrochemical and Solid-State Letters*, 14(12):H480, 2011.
 - [124] J. Akola and R. Jones. Structural phase transitions on the nanoscale: The crucial pattern in the phase-change materials $\text{Ge}_2\text{Sb}_2\text{Te}_5$ and GeTe . *Physical Review B*, 76(23):1–10, 2007.
 - [125] V. Agafonov, N. Rodier, R. Céolin, R. Bellissent, C. Bergman, and J. P. Gaspard. Structure of Sb_2Te_3 . *Acta Crystallographica Section C Crystal Structure Communications*, 47(6):1141–1143, June 1991.
 - [126] A V Sapelkin, S C Bayliss, A. G. Lyapin, V V Brazhkin, and A. J. Dent. Structure of bulk amorphous GaSb : A temperature-dependent EXAFS study. *Physical Review B*, 56(18):531–535, 1997.
 - [127] D T Morelli, J P Heremans, and V Jovovic. Intrinsically Minimal Thermal Conductivity in Cubic I-V-VI₂ Semiconductors. *Physical review letters*, 101(08):035901–1, 2008.
 - [128] T Atake, R Abe, K Honda, and H Kawaji. Heat capacities of glassy and crystalline GeSe_2 . *Journal of Physics and Chemistry of Solids*, 61:1373–1377, 2000.
 - [129] F. Schlich and P. Zalden. The ferroelectric transition in GeTe . Technical report, RWTH Aachen, 2012.
 - [130] M Chen, KA Rubin, and RW Barton. Compound materials for reversible, phase-change optical data storage. *Applied physics letters*, 49(9):502, 1986.
 - [131] E. F. Steigmeier and G. Harbeke. Soft phonon mode and ferroelectricity in GeTe . *Solid State Communications*, 8:1275–1279, 1970.
 - [132] R. Abegg. Die Valenz und das periodische System. Versuch einer Theorie der Molekularverbindungen. *Zeitschrift für anorganische Chemie*, 39(1):330, 1904.
 - [133] S. Raoux and M. Wuttig, editors. *Phase Change Materials*. Springer, 2009.
 - [134] Beatriz Cordero, Verónica Gómez, Ana E Platero-Prats, Marc Revés, Jorge Echeverría, Eduard Cremades, Flavia Barragán, and Santiago Alvarez. Covalent radii revisited. *Dalton transactions*, (21):2832–2838, June 2008.
 - [135] Pascal Rausch. *Investigations of binary and ternary phase change alloys for future memory applications*. PhD thesis, RWTH Aachen, 2012.
 - [136] A. J. Strauss, M. D. Banus, and M. C. Finn. Pseudobinary InSb-InTe System. *Journal of The Electrochemical Society*, 113(5):458, 1966.
 - [137] I P Molodyan, S I Radautsan, D N Nasledov, and G V Sidorov. The Effective Mass of Electrons in $(\text{InSb})_x(\text{InTe})_{1-x}$ Crystals. *Physica Status Solidi*, 18(2):677, 1966.
 - [138] J. H. C. Hogg. The crystal structure of In_6Se_7 . *Acta Crystallographica Section B Structural Crystallography and Crystal Chemistry*, 27(8):1630–1634, August 1971.
 - [139] H J Deiseroth and H D Müller. Crystal structures of heptagallium decatelluride, $\text{Ga}_7\text{Te}_{10}$ and heptaindium decatelluride, $\text{In}_7\text{Te}_{10}$. *Zeitschrift für Kristallographie*, 210(1):57–58, 1995.
 - [140] I Park, J Jung, S Ryu, K Choi, B Yu, Y Park, S Han, and Y Joo. Thermomechanical properties and mechanical stresses of $\text{Ge}_2\text{Sb}_2\text{Te}_5$ films in phase-change random access memory. *Thin Solid Films*, 517(2):848–852, November 2008.
 - [141] R Ruffer and A I Chumakov. Nuclear inelastic scattering. *Hyperfine Interactions*, 128(1-3):255–272, July 2000.

- [142] H.-C Wille, Yu. V Shvyd'ko, E. E Alp, H. D Rüter, O Leupold, I Sergueev, R Rüffer, A Barla, and J. P Sanchez. Nuclear resonant forward scattering of synchrotron radiation from ^{121}Sb at 37.13 keV. *Europhysics Letters (EPL)*, 74(1):170–176, April 2006.
- [143] H C Wille, R P Hermann, I Sergueev, U Pelzer, A Möchel, T Claudio, R Rüffer, A Said, and Yu V Shvyd'ko. Nuclear forward and inelastic spectroscopy on ^{125}Te and $\text{Sb}_2\text{-}^{125}\text{Te}_3$. *Europhysics Letters*, 91(September):62001, 2010.
- [144] JB Hastings, DP Siddons, U. Van Bürck, R. Hollatz, and U. Bergmann. Mössbauer spectroscopy using synchrotron radiation. *Physical review letters*, 66(6):770–773, 1991.
- [145] S Kitao, T Mitsui, and M Seto. Nuclear Resonant Scattering of Synchrotron Radiation by ^{121}Sb and ^{149}Sm . *Journal of the Physical Society of Japan*, 69(3):683, January 2000.
- [146] J. W. Mullin. *Crystallization*. Butterworth-Heinemann, 4 edition, 2001.
- [147] Malte Jonathan Linn. *Kristallisationskinetik von Phasenwechselmaterialien unter dem Einfluss von Deckschichten*. PhD thesis, 2009.
- [148] J. W. Christian. *The Theory of Transformations in Metals and Alloys*. Pergamon Press, 1 edition, 1965.
- [149] D Turnbull. Thermodynamics of equilibrium and non-equilibrium of Ge and Si. *Le Journal de Physique Colloques*, 43(C1):259, 1982.
- [150] Schwabl. *Statistische Mechanik*. Springer, 3 edition, 2006.
- [151] Prabhat K. Gupta and John C. Mauro. The configurational entropy of glass. *Journal of Non-Crystalline Solids*, 355(10-12):595–599, May 2009.
- [152] Martin Goldstein. On the reality of the residual entropies of glasses and disordered crystals: counting microstates, calculating fluctuations, and comparing averages. *The Journal of chemical physics*, 134(12):124502, March 2011.
- [153] D W Denlinger, E N Abarra, Kimberly Allen, P W Rooney, M T Messer, S K Watson, and F Hellman. Thin film microcalorimeter for heat capacity measurements. *Review of Scientific Instruments*, 65(4):946, 1994.
- [154] I. Gutzow and J. Schmelzer. *The Vitreous State*. Springer, 1995.
- [155] R. Vink and G. Barkema. Configurational Entropy of Network-Forming Materials. *Physical Review Letters*, 89(7):1–4, July 2002.
- [156] R. L. C. Vink. *Computer Simulations Of Amorphous Semiconductors*. PhD thesis, Universiteit Utrecht, 2002.
- [157] Gerold Adam and Julian H. Bibbs. On the temperature dependence of cooperative relaxation properties in glass forming liquids. *The journal of chemical physics*, 43(1):139, 1965.
- [158] G. W. H. Höhne, W. F. Hemminger, and H.-J. Flammersheim. *Differential Scanning Calorimetry*. Springer, 2003.
- [159] Svein Stolen and Fredrik Gronvold. Critical assessment of the enthalpy of fusion of metals used as enthalpy standards at moderate to high temperatures. *Thermochimica Acta*, 327:1, 1999.
- [160] Mettler Toledo. Crucibles for Thermal Analysis, 2000.
- [161] Peter Zalden, G. Aquilanti, Carmelo Prestipino, Olivier Mathon, Berangere Andre, Matthias Wuttig, and Marie-Vanessa Coulet. Simultaneous calorimetric and quick-EXAFS measurements to study the crystallization process in phase change materials. *Journal of synchrotron radiation*, 2012.
- [162] L. Krusin-Elbaum, D. Shakhvorostov, C. Cabral, S. Raoux, and J. L. Jordan-Sweet. Irreversible altering of crystalline phase of phase-change GeSb thin films. *Applied Physics Letters*, 96(12):121906, 2010.
- [163] Sören Boyn. *Elektrische und optische Eigenschaften von kristallinen pseudo-binären GeSbTe Phasenwechselmaterialien*. Bachelor thesis, RWTH Aachen, 2009.
- [164] Noboru Yamada, Eiji Ohno, Kenichi Nishiuchi, Nobuo Akahira, and Masatoshi Takao. Rapid-phase transitions of $\text{GeTe-Sb}_2\text{Te}_3$ pseudobinary amorphous thin films for an optical disk memory. *Journal of*

- Applied Physics*, 69(5):2849–2856, 1991.
- [165] Enthalpy of Fusion. In *CRC Handbook of Chemistry and Physics*, pages 4–134.
 - [166] C. R. (n.d.). Hammond. Melting, Boiling, Triple, and Critical Point Temperatures of the Elements. In *CRC Handbook of Chemistry and Physics*, pages 4–134.
 - [167] Pascal Rausch and Michael Woda. Pascal Rausch, private communication, 2010.
 - [168] Daniel Kloeckner. *Kinetic and Electrical Properties of Chalcogenide Phase Change Alloys*. Diploma thesis, RWTH Aachen, 2007.
 - [169] Dominic Alexander André Lencer. *Kinetics, Structure and Lattice Dynamics of the Phase Change Alloy GeSb₂Te₄*. Diploma thesis, RWTH Aachen, 2006.
 - [170] R Blachnik B Legendre, B Gather. Ternäre chalcogenhaltige Systeme IX. Das Indium-Antimon-Tellur. *Zeitschrift für Metallkunde*, 71(H. 9):588–592, 1980.
 - [171] G Ghosh. The Sb-Te (Antimony-Tellurium) System. *Journal of Phase Equilibria*, 15(3):349–360, 1994.
 - [172] NikolaÄ Khristanov Abrikosov. *Semiconducting II-VI, IV-VI, and V-VI compounds*. Plenum Press, 1969.
 - [173] Mattia Boniardi and Daniele Ielmini. Physical origin of the resistance drift exponent in amorphous phase change materials. *Applied Physics Letters*, 98(24):243506, 2011.
 - [174] Rüdiger Matti Schmidt. *Widerstandsdrift in amorphen Phasenwechselmaterialien*. Diploma thesis, RWTH Aachen, 2010.
 - [175] R. W. Brown, A. R. Millner, and R. S. Allgaier. Properties of thin films of PbTe and SnTe deposited at temperature between 4.2 and 300K. *Thin Solid Films*, 5:157–168, 1970.
 - [176] M. Iizumi, Y. Hamaguchi, K.F. Komatsubara, and Y. Kato. Phase transition in SnTe with low carrier concentration. *J. Phys. Soc. Japan*, 38(2):443–449, 1975.
 - [177] Anja Herpers. *Eigenschaftstrends in Phasenwechselmaterialien bei Stöchiometrievariation*. Diploma thesis, RWTH Aachen, 2009.
 - [178] Michael Austgen. *Charakterisierung von Phasenwechselmaterialien abgeschieden auf gekühlten Substraten*. Diploma thesis, RWTH Aachen, 2007.
 - [179] Sarah Gindner. *Charakterisierung von neuartigen Phasenwechselmaterialien*. Diploma thesis, RWTH Aachen, 2008.
 - [180] P. Franz. *Untersuchungen zu den strukturellen Eigenschaften des Phasenwechselmediums Ge₂Sb₂Te₅*. Diploma thesis, RWTH Aachen, 1999.
 - [181] S. Caravati, M. Bernasconi, T. D. Kühne, M. Krack, and M. Parrinello. Coexistence of tetrahedral- and octahedral-like sites in amorphous phase change materials. *Applied Physics Letters*, 91(17):171906, 2007.
 - [182] J. Akola, J. Larrucea, and R. Jones. Polymorphism in phase-change materials: melt-quenched and as-deposited amorphous structures in Ge₂Sb₂Te₅ from density functional calculations. *Physical Review B*, 83(9):1–7, March 2011.
 - [183] Juarez L. F. Da Silva. Effective coordination concept applied for phase change (GeTe)_m(Sb₂Te₃)_n compounds. *Journal of Applied Physics*, 109(2):023502, 2011.
 - [184] E Cho, J Im, C Park, W J Son, D H Kim, H Horii, J Ihm, and S Han. Atomic and electronic structures of amorphous Ge₂Sb₂Te₅; melt-quenched versus ideal glasses. *Journal of physics. Condensed matter : an Institute of Physics journal*, 22(20):205504, May 2010.
 - [185] P. Jónvári, I. Kaban, J. Steiner, B. Beuneu, A. Schöps, and M. a. Webb. Local order in amorphous Ge₂Sb₂Te₅ and GeSb₂Te₄. *Physical Review B*, 77(3):081904, 2008.

Curriculum Vitae

Biographische Angaben von **Peter Erhard Zalden**

Geboren am 17. November 1982 in Münster, Deutschland

Deutsche Staatsangehörigkeit

Kontakt: peter@zalden.de

Bildungsgang

- | | |
|-------------|--|
| 1993 – 2002 | Gymnasium Hochdahl, Erkrath
Abschluss Abitur |
| 2002 – 2003 | Verpflichtender Wehrdienst mit Ausbildung zum Funkfernschreiber
Heinrich-Hertz Kaserne, Daun |
| 2003 – 2008 | Physikstudium an der RWTH Aachen University
Abschluss Diplom
Hauptfächer "Festkörperphysik" und "Neue Materialien und Bauelemente in der Informationstechnologie". Diplomarbeit "Combined experimental and ab-initio study of the chalcogenide-free phase-change material $\text{Ge}_x\text{Sb}_{1-x}$ " |
| 2008 – 2012 | Promotionsstudium an der RWTH Aachen University. Doktorarbeit "Phase-Change materials: Structure, vibrational properties and thermodynamics of crystallization" |

Publications

1. **Zalden, P.**, Bichara, C., van Eijk, J., Braun, C., Bensch, W., and Wuttig, M. (2010). Atomic structure of amorphous and crystallized $\text{Ge}_{15}\text{Sb}_{85}$. *Journal of Applied Physics*, 107(10), p.4312.
2. Austgen, M., Koehl, D., **Zalden, P.**, Kubart, T., Nyberg, T., Pflug, a, Siemers, M., et al. (2011). Sputter yield amplification by tungsten doping of Al_2O_3 employing reactive serial co-sputtering: process characteristics and resulting film properties. *Journal of Physics D: Applied Physics*, 44(34), p. 5501.
3. **Zalden, P.**, Bichara, C., Eijk, J. v., Hermann, R. P., Sergueev, I., Bruns, G., Buller, S., et al. (2011). Thermal and elastic properties of Ge-Sb-Te based phase-change materials. *MRS Proceedings*, 1338, mrss11-1338-r06-03.

4. Matsunaga, T., Yamada, N., Kojima, R., Shamoto, S., Sato, M., Tanida, H., Uruga, T., Kohara, S., Takata, M., **Zalden, P.**, Bruns, G., Sergueev, I., Wille, H. C., Hermann, R. P. and Wuttig, M. (2011). Phase change materials: Vibrational softening upon crystallization and its impact on thermal properties. *Advanced Functional Materials*, 21(12), p. 2232 – 2239. doi:10.1002/adfm.201002274.
5. van Eijk, J. M., Bichara, C., **Zalden, P.**, Braun, C., Buller, S., Bensch, W. and Wuttig, M. (2011). Differences in local order of amorphous and crystalline $\text{Ge}_1\text{Sb}_2\text{Te}_4$ probed by X-Ray absorption spectroscopy. submitted to *Physical Review B*.
6. **Zalden, P.** and Wuttig, M. (2012). The evolution of atomic ordering in phase-change materials. *Proceedings of the European Phase Change and Ovonic Symposium (EPCOS) 2012*.
7. Raty, J.-Y., Bichara, C., Mazzarello, R., Rausch, P., **Zalden, P.**, and Wuttig, M. (2012). Comment on "New Structural Picture of the $\text{Ge}_2\text{Sb}_2\text{Te}_5$ Phase-Change Alloy." *Physical Review Letters*, 108(23), p. 2011 – 2012.
8. Buller, S., Koch, C., Bensch, W., **Zalden, P.**, Sittner, R., Kremers, S., Wuttig, M., Schuermann, U., Kienle, L., Leichtweiss, T., Janek, J. and Schoenborn, B. (2012). Influence of partial substitution of Te by Se and Ge by Sn on the properties of the Blu-ray phase-change material $\text{Ge}_8\text{Sb}_2\text{Te}_{11}$. Submitted to *Chemistry of Materials*.
9. **Zalden, P.** Aquilanti, G., Prestipino, C., Mathon, O., André, B., Wuttig, M. and Coulet, M.-V. (2012). Simultaneous calorimetric and quick-EXAFS measurements to study the crystallization process in phase-change materials. *Journal of Synchrotron Radiation*, 19(5), p. 806 – 813.
10. **Zalden, P.**, Aquilanti, G., Prestipino, C., Mathon, O., Andre, B., Wuttig, M. and Coulet, M.-V. (2012). New insights on the crystallization process in $\text{Ge}_{15}\text{Sb}_{85}$ phase change material: a combined simultaneous calorimetric and quick-EXAFS measurement. Submitted to *Journal of Non-Crystalline Solids*
11. Zhang, W., Thiess, A., **Zalden, P.**, Zeller, R., Dederichs, P. H., Raty, J.-Y., Wuttig, M., Blügel, S. and Mazzarello, R. (2012). Structural transitions and disorder-driven meta-insulator transitions in crystalline phase-change material. *Nature Materials*, 11(11), p. 952 – 956.

Invited presentations

1. **Zalden, P.**, (*) Siegert, S., Raty, J.-Y., Rols, S., Fischer, H., Johnson, M. and Wuttig, M. (2011) Phase-Change materials: Property contrast and vibrational softening upon crystallization. Invited talk at the College 7 Seminar at ILL, Grenoble, France.
2. **Zalden, P.**, (*) Bichara, C. and Wuttig, M. (2012) The evolution of atomic disorder in crystalline phase-change materials. Invited talk at the European Phase Change and Ovonic Symposium (EPCOS) 2012 in Tampere, Finland.

International conferences

1. **Zalden, P.**, (*) Bichara, C., van Eijk, J. and Wuttig M. (2011) Thermal Properties of Ge-Sb-Te-based phase-change materials. Spring meeting of the Materials Research Society (MRS) 2011, San Francisco, US.

2. **Zalden, P.**, (*) Siegert, S., Raty, J.-Y., Rols, S., Fischer, H., Johnson, M. and Wuttig, M. (2012). Structure and Vibrational modes of $\text{Ge}_2\text{Sb}_2\text{Te}_5$. Spring meeting of the Materials Research Society (MRS) 2012, San Francisco, US.
3. Coulet, M.-V. (*) and **Zalden, P.** (2012). Combined simultaneous calorimetric and quick-EXAFS measurements to understand the crystallization process in phase-change materials. International Symposium on Non Oxide and New Optical Glasses, Saint-Malo, France.
4. **Zalden, P.**, Aquilanti, G., Prestipino, C., Mathon, O. and Coulet, M.-V. (*) (2012). New insights on the crystallization process of $\text{Ge}_{15}\text{Sb}_{85}$ phase-change material: a combined simultaneous calorimetric and quick-EXAFS measurement.

(*) presenting author

Conferences (presenting author is always first)

1. **Zalden, P.**, Lencer, D., Klein, M., Salinga, M. and Wuttig, M. (2008). Combined experimental and computational study of structure and electronic properties of the chalcogenide-free phase-change material $\text{Ge}_x\text{Sb}_{1-x}$. Frühjahrstagung der Deutschen Physikalischen Gesellschaft (DPG) 2008, Berlin.
2. **Zalden, P.**, Coulet, V., Bichara, C., Klein, M. and Wuttig, M. (2009). Kinetic and thermodynamic aspects of crystallization in the phase-change material $\text{Ge}_{15}\text{Sb}_{85}$. Frühjahrstagung der DPG 2009, Dresden.
3. König, A., **Zalden, P.**, Bruns, G. and Wuttig, M. (2010). Sb-Bi thin films investigated by structural and optical methods. Frühjahrstagung der DPG 2010, Regensburg.
4. **Zalden, P.**, van Eijk, J., Braun, C., Bensch, W., Micoulaut, M. and Wuttig, M. (2010). SnSe_2 : An XAS study on the atomic and electronic structure. Frühjahrstagung der DPG 2010, Regensburg.
5. Liepertz, S. C., Natarajan, G., Köhl, D., **Zalden, P.** and Wuttig, M. (2011). Influence of growth conditions on the crystallization behaviour of reactively magnetron sputtered amorphous molybdenum oxide films. Frühjahrstagung der DPG 2011, Dresden.
6. Kaes, M., **Zalden, P.**, van Eijk, J., Aquilanti, G., Pascarelli, S. and Wuttig, M. (2011) Trends in crystallization behavior of phase-change materials under high external pressure. Frühjahrstagung der DPG 2011, Dresden.
7. Siegert, K. S., Schlockermann, C., **Zalden, P.** and Wuttig, M. (2011) Thermal properties of phase change materials. Frühjahrstagung der DPG 2011, Dresden.
8. Schlich, F., **Zalden, P.** and Wuttig, M. (2012) The ferroelectric transition in the phase-change material GeTe. Frühjahrstagung der DPG 2012, Berlin.
9. Lange, F., Volker, H., **Zalden, P.** and Wuttig, M. (2012) The impact of phase segregation on the electrical properties of $\text{GeTe}_{1-x}\text{SnTe}_x$ alloys. Frühjahrstagung der DPG 2012, Berlin.